Research Annual Report 2018

科研工作年度报告

中国科学院紫金山天文台

“悟空”卫星成果“首次直接探测到电子宇宙射线能谱在1TeV附近的拐折”入选2018年度中国科学十大进展

2019年2月27日，由科技部基础研究管理中心举办的第14届“中国科学十大进展”遴选活动结果揭晓。由中国科学院紫金山天文台领导的暗物质粒子探测卫星“悟空”号（DAMPE）科学团队研究成果“首次直接探测到电子宇宙射线能谱在1TeV附近的拐折”成功入选。

“悟空”号卫星是我国首颗空间科学卫星，由中国科学院紫金山天文台提出，并联合中国科学技术大学、中国科学院近代物理研究所、中国科学院高能物理研究所、中国科学院国家空间科学中心等单位研制，瑞士和意大利的部分单位也参与了其硅子探测器的研制。卫星于2015年12月17日成功发射，2016年3月17日完成在轨交付，至今已开展超过三年的科学运行，获取了大量观测数据。

基于“悟空”号前530天的在轨测量数据，“悟空”号合作组以前所未有的高能量分辨率和低本底对25GeV—4.6TeV能量区间的电子宇宙线能谱进行了精确的直接测量。“悟空”号的结果首次清楚地直接测量到电子宇宙射线能谱在0.9TeV附近的拐折，此前只有地面实验间接测量给出过拐折存在的迹象。该拐折反映了宇宙中高能电子辐射源的典型加速能力，其精确的下降行为对于判定部分电子宇宙射线是否来自于暗物质起着关键性作用。此外，悟空号所获得的能谱在1.4TeV附近呈现出流量异常迹象，尚需进一步的数据来确认是否存在一个精细结构。

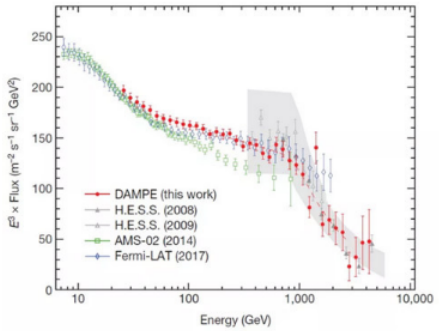

Purple Mountain Observatory CAS

中国科学院紫金山天文台

2018 科研工作年度报告

中国科学院紫金山天文台科技处

2019 年 10 月

Cover: Dark Matter Particle Explorer published its measurement of electrons and positrons in a very wide energy range

封面：首次直接探测到电子宇宙射线能谱在 1TeV 附近的拐折入选 2018 年中国科学十大进展

目 录

中国科学院紫金山天文台
科技处

地 址：南京市北京西路 2 号
邮 编：210008
电 话：+86-25-8333-2288, 2158
传 真：+86-25-8333-2288
电 邮：pmokjc@pmo.ac.cn
http://www.pmo.cas.cn

目 录 I

2018 年度科研工作总结 1

一、科研工作总体情况 1

ABSTRACT LIST OF PUBLICATIONS IN 2018 ..... **35**

I. DARK MATTER & SPACE ASTRONOMY **36**
Cosmic Gamma Ray Bursts, Neutron Stars, and Relevant Physics 36
（1）Short GRBs: Opening Angles, Local Neutron Star Merger Rate, and Off-axis Events for GRB/GW Association 36
（2）Neutrinos from Choked Jets Accompanied by Type-II Supernovae 36
（3）HESS J1640-465: A Gamma-Ray Emitting Pulsar Wind Nebula? 36
（4）Studies on Cosmic-Ray Nuclei with Voyager, ACE, and AMS-02. I. Local Interstellar Spectra and Solar Modulation 36
（5）The Diversity of Kilonova Emission in Short Gamma-Ray Bursts 37
（6）How Special Is GRB 170817A? 37
High-energy Solar physics 37
（7）Looking for the Gluon Condensation Signature in Protons Using the Earth-limb Gamma-Ray Spectra 37
（8）Determination of Differential Emission Measure from Solar Extreme Ultraviolet Images 37
（9）Spectroscopic Observations of a Current Sheet in a Solar Flare 38
（10）Space Solar Physics in China 38
（11）Photometric Solutions of Three Eclipsing Binary Stars Observed from Dome A, Antarctica 38
（12）Identifying Anticyclonic Vortex Features Produced by the Rossby Wave Instability in Protoplanetary Disks 38
（13）Properties of a Small-scale Short-duration Solar Eruption with a Driven Shock 38
（14）Confronting the DAMPE excess with the scotogenic type-II seesaw model 39
（15）Explaining the DAMPE data with scalar dark matter and gauged U(1)(Le- L mu) interaction 39
（16）Simplified TeV leptophilic dark matter in light of DAMPE data 39
（17）Two-stage Energy Release Process of a Confined Flare with Double HXR Peaks 39
（18）Non-LTE Calculations of the Fe I 6173 angstrom Line in a Flaring Atmosphere 40
Multi-Band Observation Solar Activity 40
（19）Non-damping oscillations at flaring loops 40
（20）High-resolution Observations of Flares in an Arch Filament System 40
（21）Observations of Electron-driven Evaporation in a Flare Precursor 40
（22）Two Kinds of Dynamic Behavior in a Quiescent Prominence Observed by the NVST 41

（23）Spectroscopic and imaging observations of small-scale reconnection events41
（24）Diagnosing the Magnetic Field Structure of a Coronal Cavity Observed during the 2017 Total Solar Eclipse 41
（25）Period Increase and Amplitude Distribution of Kink Oscillation of Coronal Loop 41
（26）High-resolution He I 10830 angstrom Narrowband Imaging for an M-class Flare. II. Multiple Hot Channels: Their Origin and Destination 42
（27）Magnetic Field Modeling of Hot Channels in Four Flare/Coronal Mass Ejection Events 42
（28）Studies of Isolated and Non-isolated Photospheric Bright Points in an Active Region Observed by the New Vacuum Solar Telescope 42
（29）Two Episodes of Magnetic Reconnections during a Confined Circular-ribbon Flare 42
（30）Vertical Oscillation of a Coronal Cavity Triggered by an EUV Wave 43
Acceleration and Radiation of High-Energy Cosmic Particles 43
（31）Impulsive radio and hard X-ray emission from an M-class flare 43
（32）超高能宇宙线从何而来? 43
（33）Where do the ultra-high energy cosmic rays come from? 43
Physics of Dark Matter Indirect Detection 44
（34）Detection of GeV Gamma-Ray Emission in the Direction of HESS J1731-347 with Fermi-LAT 44
（35）Fast gamma-Ray Variability in Blazars beyond Redshift 3 44
（36）Fermi-LAT Detection of a Transient gamma-Ray Source in the Direction of a Distant Blazar B3 1428+422 at z=4.72 44
（37）Search for gamma-ray emission from the nearby dwarf spheroidal galaxies with 9 years of Fermi-LAT data 45
（38）Study of the boxlike dark matter signals from dwarf spheroidal galaxies with Fermi-LAT data 45
（39）A model explaining neutrino masses and the DAMPE cosmic ray electron excess 45
（40）Massive black holes and tidal disruption events at the center of galaxies 45
（41）DES science portal: Computing photometric redshifts 45
（42）GW170817 and the Prospect of Forming Supramassive Remnants in Neutron Star Mergers 46
（43）M101: Spectral Observations of H II Regions and Their Physical Properties 46
（44）The flat-spectrum radio quasar 3C 345 from the high to the low emission state 46
（45）Constraints on the Composition, Magnetization, and Radiative Efficiency in the Jets of Blazars 47
（46）Searching for spectral oscillations due to photon-axionlike particle conversion using the Fermi-LAT observations of bright supernova remnants 47
（47）Two Transient X-Ray Quasi-periodic Oscillations Separated by an Intermediate State in 1H 0707-495 47
（48）What is dark matter? 47
（49）Constraints on the box-shaped cosmic ray electron feature from dark matter annihilation with the AMS-02 and DAMPE data 48
（50）Scalar dark matter explanation of the DAMPE data in the minimal left-right symmetric model 48
（51）Scalar dark matter interpretation of the DAMPE data with U(l) gauge Interactions 48
Laboratory for Dark Matter and Space Astronomy 48
（52）Effect of Alpha Beams on Low-frequency Electromagnetic Waves Driven by Proton Beams 49

（53）Fermi Large Area Telescope Detection of Gamma-Ray Emission from the Direction of Supernova iPTF14hls.....49
（54）Theoretical scaling law of coronal magnetic field and electron power-law index in solarmicrowave burst sources.....49
（55）On the knee of Galactic cosmic rays in light of sub-TeV spectral hardenings49
（56）Consistency test of the AMS-02 antiproton excess with direct detection data based on the effective field theory approach 49
（57）Revisit of cosmic ray antiprotons from dark matter annihilation with updated constraints on the background model from AMS-02 and collider data.....50
（58）A systematic Chandra study of Sgr A*: II. X-ray flare statistics 50
（59）Heart beats from the dark side.....50
（60）Electron acceleration by turbulent plasmoid reconnection 50
（61）Dark Matter Particle Explorer observations of high-energy cosmic ray electrons plus positrons and their physical implications.....51
（62）Interpretation of the DAMPE 1.4 TeV peak according to the decaying dark matter model.....51
（63）Prototype design of electronics readout system for solar gamma-ray spectrometer's high energy deposited.....51
（64）Dark Matter Particle Explorer and Its First Results 51
（65）The Design and Realization of the Payload Integrated Test System for DAMPE51
（66）空间间接探测暗物质粒子 52
（67）The X-ray binary system in the EP era 52
（68）The second-closest gamma-ray burst: sub-luminous GRB 111005A with no supernova in a super-solar metallicity environment.....52
（69）A Comprehensive Analysis of Fermi Gamma-Ray Burst Data. IV. Spectral Lag and its Relation to E-p Evolution 52
（70）Understanding the spectral hardenings and radial distribution of Galactic cosmic rays and Fermi diffuse gamma rays with spatially-dependent propagation.52
（71）Magnetic Reconnection at the Earliest Stage of Solar Flux Emergence 53
（72）Two Solar Tornadoes Observed with the Interface Region Imaging Spectrograph 53
（73）Two-zone Diffusion of Electrons and Positrons from Geminga Explains the Positron Anomaly 53
（74）Two-neutron halo state of B-15 around 3.48 MeV by a three-body model..53
（75）Performance of a scintillation detector array operated with LHAASO-KM2A electronics 54
（76）Calibration and Status of the 3-D Imaging Calorimeter of DAMPE for Cosmic Ray Physics on Orbit 54
（77）Internal alignment and position resolution of the silicon tracker of DAMPE determined with orbit data.....54
（78）Validation of Gean4 physics models for nuclear beams in extended media.54
（79）Dark Energy Survey year 1 results: Cosmological constraints from galaxy clustering and weak lensing 55
（80）Dark Energy Survey year 1 results: Galaxy clustering for combined probes .56
（81）New bounds on axionlike particles from the Fermi Large Area Telescope observation of PKS 2155-304 56
（82）Operation of the astronomical monitoring stations at Mt. Wumingshan.....56
（83）An algorithm to resolve gamma-rays from charged cosmic rays with DAMPE57
（84）用于空间天文的硅微条探测器原型样机研制 57
（85）Statistical Analysis on XMM-Newton X-Ray Flares of Mrk 421: Distributions of Peak Flux and Flaring Time Duration.....57
（86）Testing Relativistic Boost as the Cause of Gamma-Ray Quasi-periodic

Oscillation in a Blazar 57
（87）A 34.5 day quasi-periodic oscillation in gamma-ray emission from the blazar PKS 2247-131.....58
（88）Detection of gamma-ray emission from the Coma cluster with Fermi Large Area Telescope and tentative evidence for an extended spatial structure 58
UV/X-ray Astronomy Research Group 58
（89）Resonant Scattering Effect on the Soft X-Ray Line Emission from the Hot Interstellar Medium. I. Galactic Bulges 58
（90）Probing the dynamical state, baryon content, and multiphase nature of galaxy clusters with bright background QSOs 59
（91）Disc-corona interaction in the heartbeat state of GRS 1915+105.....59
II. ANTARCTIC ASTRONOMY RADIO ASTRONOMY.....60
Stellar Structure, Evolution and Pulsation 60
（92）Turbulent convection and pulsation stability of stars - III. Non-adiabatic oscillations of red giants.....60
Center for Antarctic Astronomy 60
（93）Late-time Flattening of Type Ia Supernova Light Curves: Constraints from SN 2014J in M82 60
（94）Observations of Turbulent Magnetic Reconnection within a Solar Current Sheet.....60
（95）Optical Observations of the Young Type Ic Supernova SN 2014L in M99 60
（96）Characterization of Type Ia Supernova Light Curves Using Principal Component Analysis of Sparse Functional Data 61
（97）Mapping Circumstellar Matter with Polarized Light: The Case of Supernova 2014J in M82 61
（98）The Scattering of FRBs by the Intergalactic Medium: Variations, Strength, and Dependence on Dispersion Measures.....61
（99）A Large-scale Survey of CO and Its Isotopologues toward the Rosette Molecular Cloud 62
（100）Molecular Gas toward the Gemini OB1 Molecular Cloud Complex. II. CO Outflow Candidates with Possible WISE Associations 62
（101）Introduction of Chinese Antarctic Optical Telescopes 62
（102）Optical observations of the 2002cx-like supernova 2014ek and characterizations of SNe Iax 62
（103）The first release of the AST3-1 Point Source Catalogue from Dome A, Antarctica 63
（104）Dark Energy Survey Year 1 results: cross-correlation redshifts - methods and systematics characterization 63
（105）Dark Energy Survey Year 1 Results: redshift distributions of the weak-lensing source galaxies.....64
（106）Rapidly evolving transients in the Dark Energy Survey.....65
Galaxy Cosmology and Dark Energy.....65
（107）The build up of the correlation between halo spin and the large-scale structure 65
（108）An Accurate Centroiding Algorithm for PSF Reconstruction.....65
（109）An Investigation of Intracluster Light Evolution Using Cosmological Hydrodynamical Simulations 66
（110）StarGO: A New Method to Identify the Galactic Origins of Halo Stars 66
（111）Prediction of Supernova Rates in Known Galaxy-Galaxy Strong-lens Systems66
（112）ELUCID. V. Lighting Dark Matter Halos with Galaxies 67
（113）Galaxy-Galaxy Weak-lensing Measurements from SDSS. II. Host Halo Properties of Galaxy Groups.....67
（114）Removing the Impact of Correlated PSF Uncertainties in Weak Lensing 67

（115）An Investigation of the Interstellar Environment of Supernova Remnant CTB87.....67
（116）Dynamic Equilibrium Sets of the Atomic Content of Galaxies across Cosmic Time.....68
（117）The Discrepancy between Einstein Mass and Dynamical Mass for SIS and Power-law Mass Models.....68
（118）The Spin Alignment of Galaxies with the Large-scale Tidal Field in Hydrodynamic Simulations.....68
（119）SDSS J0909+4449: A large-separation strongly lensed quasar at z similar to 2.8 with three images.....68
（120）Strong-lensing measurement of the total-mass-density profile out to three effective radii for z similar to 0.5 early-type galaxies.....69
（121）The correspondence between convergence peaks from weak lensing and massive dark matter haloes.....69
（122）The different growth pathways of brightest cluster galaxies and intracluster light.....69
（123）The large-scale environment from cosmological simulations I. The baryonic cosmic web (vol 473, pg 68, 2018).....69
（124）A high dust emissivity index β for a CO-faint galaxy in a filamentary Lyα nebula at z = 3.1.....70
（125）The magnification invariant of circularly-symmetric lens models.....70
（126）Alignment between Satellite and Central Galaxies in the SDSS DR7: Dependence on Large-scale Environment.....70
（127）Full-sky Ray-tracing Simulation of Weak Lensing Using ELUCID Simulations: Exploring Galaxy Intrinsic Alignment and Cosmic Shear Correlations.....70
（128）Statistical Test of Distance-Duality Relation with Type Ia Supernovae and Baryon Acoustic Oscillations.....71
（129）ELUCID. IV. Galaxy Quenching and its Relation to Halo Mass, Environment, and Assembly Bias.....71
（130）The BOSS Emission-line Lens Survey. V. Morphology and Substructure of Lensed Ly alpha Emitters at Redshift Z approximate to 2.5 in the BELLS GALLERY ...71
（131）The Strong Gravitationally Lensed Herschel Galaxy HLock01: Optical Spectroscopy Reveals a Close Galaxy Merger with Evidence of Inflowing Gas 72
Star Formation in Galaxies.....72
（132）A Survey of Atomic Carbon [C i] in High-redshift Main-sequence Galaxies.72
（133）Herschel Spectroscopy of the Taffy Galaxies (UGC 12914/12915=VV 254): Enhanced [C II] Emission in the Collisionally Formed Bridge.....72
（134）CO (7-6), [C I] 370 mu m, and [N II] 205 mu m Line Emission of the QSO BRI1335-0417 at Redshift 4.407.....73
（135）The MALATANG Survey: The L-GAS-L-IR Correlation on Sub-kiloparsec Scale in Six Nearby Star-forming Galaxies as Traced by HCN J=4 -> 3 and HCO+ J=4 -> 3 ..73
（136）Far-infrared Herschel SPIRE spectroscopy of lensed starbursts reveals physical conditions of ionized gas.....73
（137）Super-deblended Dust Emission in Galaxies. I. The GOODS-North Catalog and the Cosmic Star Formation Rate Density out to Redshift 6.....74
（138）Super-deblended Dust Emission in Galaxies. II. Far-IR to (Sub)millimeter Photometry and High-redshift Galaxy Candidates in the Full COSMOS Field.....74
（139）The Effect of Galaxy Interactions on Molecular Gas Properties 74
（140）The Herschel Bright Sources (HerBS): sample definition and SCUBA-2 observations.....75
（141）VALES - IV. Exploring the transition of star formation efficiencies between normal and starburst galaxies using APEX/SEPIA Band-5 and ALMA at low redshift 75
（142）JINGLE, a JCMT legacy survey of dust and gas for galaxy evolution studies - I.

Survey overview and first results.....75
Molecular Clouds and Star Formation.....76
（143）The Serpens filament at the onset of slightly supercritical collapse 76
（144）Magnetic Fields toward Ophiuchus-B Derived from SCUBA-2 Polarization Measurements 76
（145）Molecular line emission in NGC 4945, imaged with ALMA 77
（146）ALMA 26 Arcmin(2) Survey of GOODS-S at One Millimeter (ASAGAO): Average Morphology of High-z Dusty Star-forming Galaxies in an Exponential Disk (n similar or equal to 1) 77
（147）Kinetic temperature of massive star-forming molecular clumps measured with formaldehyde III. The Orion molecular cloud 1.....78
（148）A First Look at BISTRO Observations of the rho Oph-A core 78
（149）The Arizona Radio Observatory CO Mapping Survey of Galactic Molecular Clouds. VI. The Cep OB3 Cloud (Cepheus B and C) in CO J=2-1, (CO)-C-13 J=2-1, and CO J=3-2.....79
Galaxy formation and wide Field Sky Survey.....79
（150）A Machine-learning Method for Identifying Multiwavelength Counterparts of Submillimeter Galaxies: Training and Testing Using AS2UDS and ALESS.....79
（151）大视场巡天望远镜探测器响应与滤光片优化分析 80
（152）High-Speed Device-Independent Quantum Random Number Generation without a Detection Loophole.....80
（153）Upgrading SCUBA-2 with a newly designed thermal filter stack 80
High – energy time-domain astronomy 80
（154）Improved selection criteria for H II regions, based on IRAS sources 80
（155）ALMA twenty-six arcmin2 survey of GOODS-S at one millimeter (ASAGAO): Source catalog and number counts 81
（156）The first CCD photometric study of the open cluster NGC 744 81
（157）Gas distribution and Properties of the Milky Way.....81
（158）Millimeter & Sub-Millimeter Wave Laboratory 81
（159）Terahertz Superconducting Radiometric Spectrometer in Tibet for Atmospheric Science 82
（160）Sparse Millimeter-Wave InSAR Imaging Approach Based on MC.....82
（161）Verification of the transparency of polystyrene multi-layer insulation using terahertz time domain spectroscopy 82
（162）Terahertz Atmospheric Transmission Measured at Ali with a Fourier Transform Spectrometer.....82
（163）A Fully Integrated Heterodyne Receiver Based on a Hot Electron Bolometer Mixer and a Quantum Cascade Laser 82
（164）Characterization of a graphene-based terahertz hot-electron bolometer ..82
（165）High Sensitivity Terahertz Detection Module 82
（166）Characterization of NB and TiN superconducting CPW lines with thru-line calibration method 83
（167）The influence of Nb and Ti interface on DC characteristics of superconducting titanium transition edge sensors 83
（168）Dependence of Noise Temperature of Superconducting HEB Mixers on Frequency and Bath Temperature 83
（169）Performance of a 1.4 THz Twin-Slot Superconductivity Hot Electron Bolometer Mixer.....83
（170）Near-field measurements of the terahertz superconducting spectrometer for atmospheric observation 83
Telescope Technology Laboratory 83
（171）Analysis of a discrete-layout bimorph disk elements piezoelectric deformable mirror 83

（172）Research on the optimization of a bimorph piezoelectric deformable mirror based on zeroth-order method 84
（173）南极 5 m 太赫兹望远镜指向与调焦校准精度分析 84
Zhou Tao; Ye Zhoujun; Shi Yaohui; Liang Yanmin; Hao Xufeng; Qian Yuan 84
（174）Development of a compact readout system for optical CCD in Higashi-Hiroshima Observatory 84
（175）A comparative study of the thermal performance of primary mirror at the four typical sites 84
（176）The TOP-SCOPE Survey of Planck Galactic Cold Clumps: Survey Overview and Results of an Exemplar Source, PGCC G26.53+0.17 85
（177）Delingha millimeter wave Observation Station 86
（178）A comparison of the local spiral structure from Gaia DR2 and VLBI maser parallaxes 86
（179）德令哈 13.7m 望远镜谱线 OTF 观测系统 86
（180）Gas kinematics and star formation in the filamentary molecular cloud G47.06+0.26 86
（181）The spiral structure of the Milky Way 86
（182）A 95 GHz methanol emission survey toward eight small supernova remnants 87
（183）A challenge to identify an optical counterpart of the gravitational wave event GW151226 with Hyper Suprime-Cam(dagger) 87
III. APPLIED CELESTIAL MECHANICS AND SPACE OBJECT & DEBRIS RESEARCH 88
Center for Space Object and Debris Research 88
（184）An estimation of Envisat's rotational state accounting for the precession of its rotational axis caused by gravity-gradient torque 88
（185）On the lunar node resonance of the orbital plane evolution of the Earth's satellite orbits 88
（186）Deep Learning for Mid-term Forecast of Daily Index of Solar 10.6 cm Radio Flux 88
（187）卷帘快门 sCMOS 相机对空间碎片观测的影响研究 88
（188）高能光纤激光器光束合成技术 88
（189）云量分割在空间目标观测中的研究 89
（190）双行根数编目体系轨道误差研究 89
（191）云南天文台月球激光测距研究与试验 89
（192）Retrieval of atmospheric mass densities in lower thermosphere below 200 km from precise orbit of re-entry object CZ-3B R/B by analytical and numerical methods 89
（193）Beam combining of high energy fibre lasers 89
（194）Orbit error characteristic and distribution of TLE using CHAMP orbit data 90
Satellite Precise Orbit Determination and Application 90
（195）Influence of Ice Nuclei Parameterization Schemes on the Hail Process 90
（196）Numerical Study of a Southwest Vortex Rainstorm Process Influenced by the Eastward Movement of Tibetan Plateau Vortex 90
IV. PLANETARY SCIENCES AND DEEP SPACE EXPLORATION 90
Near Earth Object Survey and Solar System Bodies 91
（197）The GTC exoplanet transit spectroscopy survey IX. Detection of haze, Na, K, and Li in the super-Neptune WASP-127b 91
（198）基于 Fermi-LAT 数据的暗物质湮灭线谱搜寻及悟空号的伽马射线分析软件开发 91
（199）Na I and H alpha absorption features in the atmosphere of MASCARA-2b/KELT-20b 91
（200）The GTC exoplanet transit spectroscopy survey VIII. Flat transmission spectrum for the warm gas giant WASP-80b 92

（201）Detection of He I λ10830 Å absorption on HD 189733 b with CARMENES high-resolution transmission spectroscopy 92
（202）Tilting Styx and Nix but not Uranus with a Spin-Precession-Mean-motion resonance 92
（203）Transiting Exoplanet Monitoring Project (TEMP). IV. Refined System Parameters, Transit Timing Variations, and Orbital Stability of the Transiting Planetary System HAT-P-25 93
Ephemerial Astronomy and Astronomical Reference System 93
（204）Probing f(T) gravity with gravitational time advancement 93
（205）Solar system and binary pulsars tests of the minimal momentum uncertainty principle 93
（206）The nearby triple star HIP 101955 93
（207）Effects of a brane world on gravitational time advancement 94
（208）双星观测量计算方法的改进及应用 94
（209）Testing Photons Coupled to Weyl Tensor with Gravitational Time Advancement 94
The Sun and Solar System Plasmas 94
（210）Excitation of Ion Cyclotron Waves by Ion and Electron Beams in Compensated-current System 94
（211）Modulation of Ion and Electron Pitch Angle in the Presence of Large-amplitude, （）Low-frequency, Left-hand Circularly Polarized Electromagnetic Waves Observed by MMS 94
（212）Nonlinear Decay of Alfven Waves Driven by Interplaying Two- and Three-dimensional Nonlinear Interactions 95
（213）Two- and Three-dimensional Nonlinear Instabilities of Whistler Waves 95
（214）Nature of Magnetic Holes above Ion Scales: A Mixture of Stable Slow Magnetosonic and Unstable Mirror Modes in a Double-polytropic Scenario? 95
（215）Observations of Whistler Waves Correlated with Electron-scale Coherent Structures in the Magnetosheath Turbulent Plasma 96
（216）Two-dimensional Hybrid Simulations of Filamentary Structures and Kinetic Slow Waves Downstream of a Quasi-parallel Shock 96
（217）Polarization properties of low frequency electromagnetic cyclotron waves associated with magnetic clouds 96
（218）Statistical Study of Low-Frequency Electromagnetic Cyclotron Waves in the Solar Wind at 1 AU 96
（219）The Influence of IMF B-y on the Bow Shock: Observation Result 97
（220）Ion-Scale Kinetic Alfven Turbulence: MMS Measurements of the Alfven Ratio in the Magnetosheath 97
（221）Observation of Oblique Lower Band Chorus Generated by Nonlinear Three-Wave Interaction 97
Near Earth Object Telescope 97
（222）Transiting Exoplanet Monitoring Project (TEMP). I. Refined System Parameters and Transit Timing Variations of HAT-P-29b 97
（223）A Pilot Study of Asteroid Spin Rate Using the CNEOST at Xu-Yi Observatory 98
（224）Transiting Exoplanet Monitoring Project (TEMP). III. On the Relocation of the Kepler-9 b Transit 98
（225）New open cluster candidates discovered in the XSTPS-GAC survey 98
（226）Fundamentals of the orbit and response for TianQin 99
（227）Limits on radio emission from meteors using the MWA 99
（228）Dynamical properties and acceleration of hierarchical dust in the vicinity of comet 67P/Churyumov-Gerasimenko 99
Laboratory for Planetary Science and Deep Space Exploration 99
（229）Compositional Imprints in Density-Distance-Time: A Rocky Composition for

Close-in Low-mass Exoplanets from the Location of the Valley of Evaporation 100
（230）Study on Rotational Parameters for Asteroid 4179 Toutatis from Chang'e-2's Close Flyby 100
（231）云南保山地块香山组和丁家寨组沉积序列与碳同位素研究.....100
（232）基于二叉树的太阳系小天体数值历表建立方法 100
（233）基于调频广播信号的空间碎片探测方法 100
（234）小行星热物理及 Yarkovsky 效应和 YORP 效应的研究进展 101
（235）New Constraints on Turbulence and Embedded Planet Mass in the HD 163296 Disk from Planet-Disk Hydrodynamic Simulations 101
（236）Formation of S-type planets in close binaries: scattering-induced tidal capture of circumbinary planets.....101
（237）The formation mechanism of 4179 Toutatis' elongated bilobed structure in a close Earth encounter scenario 101
Laboratory for Astrochemistry and Planetary Sciences.....102
（238）Dating phosphates of the strongly shocked Suizhou chondrite 102
（239）Multiple impact events on the L-chondritic parent body: Insights from SIMS U-Pb dating of Ca-phosphates in the NWA 7251 L-melt breccia.....102
（240）The nature of the L chondrite parent body's disruption as deduced from high-pressure phases in the Sixiangkou L6 chondrite 102
（241）Petrogenesis of ore-bearing porphyry in non-subduction setting: a case study of the Eocene potassic intrusions in the western Yangtze Block 102
（242）Planetary Spectroscopy Group 103
（243）The Absolute Reflectance and New Calibration Site of the Moon 103
（244）风暴洋晚期玄武岩厚度及规模研究 103
（245）月球澄海玄武岩矿物成分研究 103
Mineralogy of Mare Frigoris.....103
（246）Geology, tectonism and composition of the northwest Imbrium region ..104
（247）Spectroscopic observations of the Moon at the lunar surface.....104
（248）The Thickness and Volume of Young Basalts Within Mare Imbrium 104
紫台历年发表论文情况.....106
学术报告.....106
专利 107
2018 年度发表科研论文、专著、专利一览表 109
国际合作与台内学术报告统计 111
中国 2018 年度“十大天文科技进展” 112

2018 年度科研工作总结

一、科研工作总体情况

1、概述

2018 年，紫台在研项目 373 项，其中新增 10 项；应结题项目 133 项，将于 2019 年 8 月底前完成结题。全年收到财务到账经费通知 219 笔，共计 2.23 亿元，比 2017 年增加 28.2%，其中项目合同经费 1.896 亿元（基础类 93%，应用类 7%），2018 年度在研项目实际入账 1.91 亿元。2018 年度应结题课题 152 项，延期课题 17 项，实际结题率 89%。2018 年度共清理课题账号 152。

2018 年，紫台共发表论文 297 篇，其中第一单位 138 篇，SCI 论文 249 篇，第一单位 SCI 论文 106 篇；著作 1 篇；申请专利 17 项，授权专利 6 项，软件登记 7 项。专利资助及奖励：专利资助 6.95 万。

2、 重要进展和重大成果

1），4 个重大突破

突破 1： 截至 2018 年 12 月 17 日，暗物质粒子探测卫星“悟空号”圆满完成了设计使命，在轨运行三年，观测约 17000 轨，获得约 56 亿高能粒子事例的科学数据。探测器各项指标完全正常，卫星工作表现优异，获批延寿 2 年。基于科技部国家重点研发计划“基于暗物质粒子探测卫星的科学研究”项目和“国家自然科学基金委员会-中国科学院空间科学卫星科学研究联合基金”专项支持下重点组织科学研究，继 2017 年第一批重大成果在《自然》杂志发表后，今年第二批成果也已完成投稿。“暗物质粒子探测卫星研究集体”获得 2018 年中科院杰出科技成就奖，“悟空”号暗物质粒子探测器获得 2018 年江苏省科技技术一等奖。

突破 2： 紫台作为国家重大科技基础设施建设十二五规划项目“中国南极天文台”的共建单位，2018 年继续开展前期预研和国家立项推进工作，根据中咨公司意见修改完善形成了新版项目建议书，将于近期再次提交国家发改委。紫台牵头承担科技部国家重点研发计划“射电技术方法前沿研究”项目继续开展南极天文台的关键技术攻关和前期研究。南极天文中心参与组织的第 35 次南极科考内陆天文科考任务正在实施中。

突破 3： 空间目标与碎片观测网持续运行，代表中科院参加了“天宫二号/神舟十一号”、“天宫二号/天舟一号”空间碎片预警监测任务，在危险空间碎片（特别是大椭圆空间碎片）的监测上发挥了重要作用；代表中科院参加了“天宫一号”目标飞行器再入大气层应对任务中，在再入预报和姿态分析上发挥了重要作用。先期预研项目“拓展望远镜系统”已于 2018 年 4 月在姚安站完成安装。空间碎片监测研究系统建设内容“光电篱笆”系统获批列入“国家军民融合工程项目”。

突破 4： 紫台作为院空间科学先导专项（二期）项目“先进天基太阳天文台（ASO-S）”的首席科学家单位、载荷研制单位和科学应用系统牵头单位，全力投入方案研制阶段，为转阶段做准备，并积极开展 ASO-S 相关科学研究，为未来重大科学产出做准备；目前先进天基太阳天文台（ASO-S）卫星工程正式启动，方案设计阶段进展良好。

2），5 个重点培育方向

培育 1：开展了太阳耀斑、CME、磁场、以及与 ASO-S 科学目标紧密相关的研究工作；利用短伽玛暴估算近邻宇宙的中子星并合率以及短暴与引力波事件成协概率；发现了超新星遗迹中高能粒子分布函数的演化规律；揭示了超新星遗迹高能粒子加速效率随时间的演化；发现最遥远的千兆电子伏辐射源候选体；紫台作为重要单位参加的先导 A 背景型号--小行星采样返回已立项；紫台作为首席科学家单位的项目--近邻宜居行星巡天计划(CHES)已经提交申请，预计不久将获批背景型号课题。

培育 2：紫台承担载人航天的高灵敏度太赫兹探测模块已进入方案阶段，按照总体计划，预计年底完成模样阶段，到目前为止，该项目已完成除制冷机外的原理样机，开展了超导薄膜氮化铌制备的技术攻关，预计明年将转入初样；南极 5 米太赫兹望远镜关键技术深化研究取得实质进展；“银河画卷计划”共计完成 954 个巡天单元；“银河画卷”展现了玫瑰星云分子云的千姿百态；发现银河系边缘的脉泽发射。

培育 3：空间目标与碎片中心代表中科院参加“天宫一号”再入大气层监测预报任务，组织所属设备采集了 500 多圈光学数据；运用多零点预报、精密定轨和卡尔曼滤波等多种预报技术，给出可靠的再入预报时间；基于激光联测的高精度数据求解出再入大气前的旋转状态。被中国载人航天工程办公室授予突出贡献证书；完成任务要求的软件现场测试；“人造天体的精密光学测量方法”项目获省部级科技进步二等奖。

培育 4：首次在系外行星大气中发现包括锂在内的多种碱金属；首次在系外行星大气中观测到大气逃逸形成的氦彗状尾；开展利用太阳系实验检验引力理论的工作；研究了地球磁鞘区大振幅阿尔文波的观测分析及其对粒子动力学的

影响；利用 MIRO 数据研究 67P 彗星彗发中水分子的早期分布；在国际上首次利用磷酸盐高压相进行 U-Pb 同位素定年，为小型天体间撞击事件年龄的获取提供新的途径；紫台 2018 年再次发现一个新的奇异小天体——2018 RR2，这是继 2010 年 3 月 10 日发现 2010 EJ104 后发现的又一个奇异小天体。

培育 5 提出了利用星系透镜系统寻找超新星的新方法；开展了 JCMT 大项目的近邻星系成图观测；首例引力波电磁对应体理论研究取得重要进展；紫台 2018 年与中科大合作的共建大视场巡天望远镜（WFST）项目已经启动，这一望远镜项目由中科院紫台大视场巡天望远镜团队预研多年，口径 2.5 米。本项目通过科教融合方式，获得中国科学技术大学“双一流”建设支持。

3），科技奖项和成果

2018 年获江苏省科学技术一等奖 1 项：“悟空”号暗物质粒子探测器，二等奖 1 项：人造天体的精密光学测量方法。

2018 年获评 2017 年度十大天文进展 3 项：暗物质粒子探测卫星发表首批科学成果、中国南极巡天望远镜团队追踪探测到引力波事件首例光学信号、“太赫兹超导阵列成像系统”研制成功。

以常进研究员为代表的“暗物质粒子探测卫星研究集体”获中国科学院 2018 年度杰出科技成就奖。

3、紫台在承担国家和科学院重大科技任务

本年度牵头申请国家重点研发计划一项，项目名称为“射电技术方法前沿研究”，并获得批准，这是紫台继 2016 年、2017 年后承担的第三项；2018 年通过验收由紫台牵头组织国家自然科学基金重大项目“极端台址环境下的天文望远镜关键技术方法研究”。2018 年获得基金委杰出青年基金项目一项（康熙）。

4、 院地合作

2018 年 1 月 6 日科学院正式发文通知，中国科学院天文大科学研究中心（简称“天文大科学中心”）正式运行。天文大科学中心是由中国科学院国家天文台、紫金山天文台、上海天文台共同建设。

2018 年 3 月 1 日，紫台和中国科技大学共建大视场巡天望远镜（WFST）项目启动。这一望远镜项目由中科院紫金山天文台 WFST 团队预研多年，通过科教融合方式，获得中国科学技术大学“双一流”建设支持。

2018 年 5 月三峡大学和中国科学院紫金山天文台签署了“共建三峡大学天文与空间科学研究中心”的共建协议，并于 2018 年 7 月签署了“三峡大学与中国科学院紫金山天文台关于联合培养研究生的补充协议”。2018 年 10 月，三峡大学与紫金山天文台在青海观测站联合共建大学生实习实训基地。

2018 年 9 月 14 日，紫金山天文台、国家天文台和盱眙县政府在盱眙站签订中国天泉湖天文论坛战略合作协议，三方希望能携手保护好珍贵的暗夜星空资源，通过论坛传播天文科普知识，提升公众科学素养，助推盱眙社会经济发展。

二、研究活动进展

Ⅰ. 暗物质与空间天文研究部

1-01 宇宙伽马暴、中子星及相关物理研究团组

主要进行高能爆发性天体的理论和观测研究，包括致密双星并合产生的引力波及电磁对应体；高能中微子、高能伽马光子、极高能宇宙射线；X 射线双星等领域，并取得了一定的成果。

利用双中子星并合事件研究中子星的状态方程。利用短伽玛暴估算近邻宇宙的中子星并合率以及短暴与引力波事件成协概率。我们把 GRB 170817A 与其他短暴进行了比较，得出结论这次引力波事件对应的短伽玛暴可能并不是独特的。

利用国内 80cm 望远镜、2.16 米望远镜获取一批 X 射线双星的测光和分光数据。处理和分析 KS 1947+300 这颗 Be/X 射线双星的观测数据。

研究总结了超新星爆发及遗迹演化过程产生中微子的各种可能机制，利用 II 型超新星的失败喷流模型成功解释了 IceCube 目前观测到的弥散中微子辐射，同时也解决了 Fermi LAT 团组提出的中微子源贡献的高能光子流量比普通理论预期低的问题。

我们结合了 IceCube 团组 2018 年 7 月最新公布的中微子事件 IceCube-170922A 与源 TXS 0506+056 成协的观测结果进行研究，提出了与 IceCube 团组不同的观点，指出存在另一中微子源 PKS 0502+049 的可能性。

中子星的状态方程是一个非常重要的基本问题，它决定了中子星的最大静止质量。双中子星并合事件 GW170817 提供了一个很好的机会来研究中子星的状态方程。我们研究了双中子星并合产物的性质，发现它强烈依赖于中子星的自转及中子星的质量分布。当中子星以开普勒速度旋转时，对多数较硬的状态方程，并合产物很可能会形成一个超大质量的中子星，而当自转较慢时，有较大的可能直接塌缩成黑洞。利用 GW170817 的数据，我们计算了静止中子星的最大质量，假设并合过程中抛射物质量是 0.03 太阳质量，并且中子星以开普勒速度旋转，则得到静止中子星的最大质量约为 2.19 太阳质量。(Ma et al. 2018, ApJ)

从引力波本身可以计算双中子星的并合率。既然短伽玛暴起源于双中子星并合，那么通过短暴也可以计算双中子星的并合率。而要准确计算短伽玛暴的爆发率，必须要知道短

伽玛暴喷流的张角大小。到目前为止有喷流张角数据的短伽玛暴数量还很少。我们通过仔细分析短伽玛暴的观测资料，在 GRB150424A 和 GRB160821B 这两个短暴中新发现了存在喷流拐折的证据，得到它们的喷流半张角都约为 0.1 弧度。通过系统分析近距离短暴，我们发现双中子星并合率很高，并且如果考虑偏轴效应(即短暴喷流不指向地球)，则双中子星并合的探测率能提高一个数量级，与引力波探测所得到的双中子星并合率一致，这极大的提高了伽玛暴 / 引力波成协事件的探测率 (Jin et al. 2018, ApJ) 。

与此次双中子星并合事件 GW170817 相关的短暴 GRB170817A 的能量很小，比典型的短暴能量小约四个量级，因此一个很有趣的问题是这个短暴与我们之前探测的短暴其物理起源是否相同。为此我们把 GRB170817A 与其他短暴进行了比较，看它的性质是不是很独特。结果发现如果把一些很亮的短暴如 GRB130603B 进行偏轴观测，则它的性质跟 GRB170817A 比较类似。另外我们还发现在现有的短暴数据中也有一些短暴的能量很小，跟 GRB170817A 类似，因此我们得出结论这次引力波事件对应的短伽玛暴可能并不是独特的，GRB170817A 很可能是一个偏轴的短暴。(Yue et al., 2018, ApJ)

宇宙射线与光子或物质发生反应可以产生中微子及相应的高能光子，基于这一理论，我们利用高能宇宙射线、中微子及高能光子等多信使手段来研究高能宇宙射线、中微子及高能光子的起源。IceCube 中微子探测器探测到显著超出大气中微子背景的弥散的高能中微子，同时 Fermi LAT 团组的研究指出来自中微子源的高能光子流量比理论预期低很多。其可能原因是这些中微子源很远，或者它们在高能光子频段很暗弱。基于这一问题，我们研究了 II 超新星的失败喷流。假设 II 型超新星爆炸时产生了喷流，在特定条件下，喷流无法冲出其前身星的氢包层，因此成为失败喷流。失败喷流可加速质子并与氢包层物质发生反应产生中微子和高能光子，然而其产生的高能光子无法逃逸出氢包层，但中微子可以逃逸出氢包层从而被我们观测到。我们的模型成功解释了 IceCube 目前观测到的弥散中微子辐射，同时也解决了 Fermi LAT 团组提出的来自中微子源的高能光子流量比普通理论预期低的问题。(He et al., 2018,ApJ)

至 2018 年 12 月 17 日，中国科学卫星系列首发星暗物质粒子探测卫星已成功运行三周年，期间不断累计观测数据。本团组的成员也参与了相关的数据分析等工作。

亮点工作

1) 利用短伽玛暴估算近邻宇宙的中子星并合率以及短暴与引力波事件成协概率。论文迄今已得到了 25 次引用。

2) 我们利用 II 型超新星的失败喷流模型成功解释了 IceCube 目前观测到的弥散中微子辐射，同时也解决了 Fermi LAT 团组提出的中微子源贡献的高能光子流量比普通理论预期低的问题。

1-02 太阳高能物理研究团组

2018 年度围绕台“十三五规划”135 重大突破方向 4 和重点培育方向 1 开展工作。经过前期一系列工作，先进天基太阳天文台（ASO-S）于 2017 年 12 月 29 日正式获中国科学院批复工程立项，ASO-S 方案设计阶段工作在 2018 年全面展开，取得预期进展，为接下来的转初样阶段打下坚实的基础。此外，团组在耀斑、CME、太阳磁场等方面也开展了颇有产出的研究工作。

亮点工作：

1)先进天基太阳天文台(ASO-S)卫星工程正式启动，方案设计阶段进展良好。

1) 先进天基太阳天文台（ASO-S）卫星工程正式启动

紫台是 ASO-S 首席科学家单位、ASO-S 科学应用系统总师单位、ASO-S 卫星系统 LST 载荷科学家和数据科学家单位、ASO-S 卫星系统 HXI 载荷主任设计师、载荷科学家、数据科学家单位。除了 HXI 硬件研制，其它紫台承担的 ASO-S 任务均落实在本团组。

2018 年 ASO-S 方案设计阶段工作全面展开，针对本团组承担的 ASO-S 任务，与 ASO-S 工程总体、项目办公室、卫星系统、地面支撑系统、以及各载荷研制单位密切配合，开展了卓有成效的工作，主要包括：

发挥首席科学家在 ASO-S 项目总体方面的作用：与 ASO-S 工程总体、项目办公室、卫星系统、地面支撑系统、以及各载荷研制单位密切配合，确保 ASO-S 项目总体按计划进程全面实施；以载荷科学家和数据科学家作为工作抓手，组织和参加数十次项目会议，牵头推进 ASO-S 国际合作和科学方面的准备工作；启动并实施首席科学家卫星科学准备项目及基金委天文联合基金重点项目，结合科学应用系统部分内容，在 6 个方面全面推进：ASO-S 任务规划和科学目标总体、FMG 磁场反演方法研究、LST 成像及谱线研究、HXI 图像重构研究、ASO-S 观测针对性科学研究、ASO-S 数据分析软件框架研究；组织国内空间天气预报相关部门召开了两次专题会，推进 ASO-S 拓展应用目标的落实；成功组织召开了 ASO-S 首次全国大会。

发挥科学应用系统牵头作用：全面启动了 ASO-S 科学应用系统研制任务，完成 ASO-S 卫星科学应用系统工程及管理系统建设，包括问题追踪（JIRA）、文档管理（Confluence）和版本控制（BitBucket）等集成软件；完成科学应用系统需求分析；完成科学应用系统对地面支撑系统需求分析；完成科学应用系统与地面支撑系统接口文件初稿；完成科学应用系统数据定义文档初稿等与科学应用系统相关的文档；完成了暗条自动识别与追踪程序的研制，推进了 CME 自动识别与入库软件的开发；分析了科学数据的计算和存储需求，与多家厂商进行了交流并调研了多套计算存储解决方案；讨论并初步明确了 ASO-S 数据分析软件框架

结构。

充分发挥载荷科学家作用 :载荷科学家是载荷研制满足科学需求的重要保证。在 LST 方面，完成 LST 探测芯片更改对科学目标影响分析文档并完成评审 ;完成 LST 科学指标及定标需求文档并完成评审；完成 LST 在轨定标方案第 1 版；完成 LST 工作模式和观测方案初稿；完成 LST 研制所需线偏振片进口 ;签订 LST 莱曼阿尔法波段滤光片进口合同；组织开展 LST 科学相关准备工作。在 HXI 方面 ,制定了 HXI 整个研制测试阶段的工作计划、内容和分工；全面展开光栅的数值模拟、基础成像算法研究和多种方法下的 HXI 成像模拟；基于大量模拟结果，改进 HXI 方案设计，其中光是光栅厚度的新方案就降低成本约一千五百万元人民币，大大缓解了硬件研制的压力；开展了 HXI 科学数据产品定义和内容、耀斑流量和观测指标的分析；制定 HXI 观测模式触发方案、HXI 光栅在轨定标方案；撰写 HXI 工作手册；开展广泛的国际合作与交流，与欧洲 SO/STIX 团队的合作获得国家自然科学基金重点国际合作项目支持。

2）太阳高能辐射和磁重联研究

等离子发射度计算 :利用极紫外辐射计算等离子体发射度是研究太阳爆发等活动背后物理过程的一个基础工具。但当前的多种方法在精确度方面无法满足研究需求。苏杨等改进了 Sparse 方法，使得精确度提高可达一个量级。该方法可仅适用 SDO 卫星 6 个 EUV 通道的图像便可较准确的求解出每个像素点的等离子发射度（在温度上的分布），即把观测量转换成物理量，进而可用来定量化研究。该工作为将来很多方面的研究突破奠定了基础。文章发表在 Su et al. ApJL, 856, 17, 2018。太阳耀斑硬 X 射线暴：耀斑中的粒子加速一直是太阳爆发研究和磁重联研究中的重点和难点。YOHKOH 卫星发现的环顶硬 X 射线源表明终止激波处是电子加速区，这是该卫星最著名的成果之一。但电子加速是否起始于 Masuda 源？苏杨等利用 RHESSI 和 SDO 的卫星资料，针对性的选取了长持续耀斑，详细分析了耀斑 cusp 结构中的 X 射线源和极紫外辐射，发现在 Masuda 源之上的高日冕区还存在一个新的硬 X 射线源 ,且该源同足点源联系密切。这表明，主加速区不在环顶之上的 Masuda 源，而是在重联出流区甚至更早的阶段。该工作即将投稿。

磁流体数值模拟太阳爆发:研究了在日珥/CME 爆发过程中，电流片的形成、结构与演化，以及耀斑环的形成与演化过程，指出 CME 从慢速上升相到快速上升相的转变对应于磁重联从 Sweet-Parker 机制到湍动磁重联的转变。基于 2.5 维磁流体模拟，计算了太阳爆发过程中 EUV 和软 X 射线辐射，研究了电流片与耀斑环辐射特性，指出耀斑软 X 射线峰值对应于重联率极大值，耀斑环和电流片中存在多种波和震荡， EUV 辐射准周期振荡与电流片中磁岛活动有关 (Zhao et al., submitted to ApJ)。

3）CME 及日冕研究

LST 科学方面: 利用 MHD 模拟(SWMF 和 Pagano et al.) 的 3 维数据结果合成日冕物质抛射的白光及 Ly-alpha 强度的 2 维图像来模拟 LST/SCI 观测; 进行白光日冕仪偏振方案的误差分析 (Feng et al., 2019, RAA), 并给出白光日冕仪在轨定标方案；使用 forward 软件包对未来 LST 所观测的 Lyman-alpha 波段的辐射进行了模拟，特别测试了不同的磁场对斯托克斯参量的影响。

研究了一个小尺度短时标爆发事件，这个 CME 和激波事件伴随有一个 M 级耀斑 ,研究发现 CME 的速度和加速度等运动学特征均超出了之前统计结果的最大值 ,利用二型暴的动态频谱图发现该 CME 驱动的激波形成高度异常的低，激波马赫数很高。该小尺度爆发与 James Chen 预测到的磁通量绳足点分离距离越小，CME 加速越快相一致。这是首次对小尺度短时标爆发事件的耀斑、CME 和激波进行的系统研究。(Ying et al. 2018, ApJ)。此外，发展了一种利用白光日冕图像计算日冕物质抛射的二维速度分布 ,并通过合成的白光图像来进行检验，应用于实际观测的事件中，进一步得到日冕物质抛射的动能和势能的能量分布图像 ,该论文即将投稿 (Ying et al.)。另一个进行中的工作是关于一个 jet 事件驱动的激波, 利用 STEREO 日冕仪的数据对其进行三维重构, 发现该激波具有弓激波特征, 并寻找其与普通的 CME 驱动激波的不同，论文正在准备中(Ying et al.)。卢磊等还开展对一个经典 CME 爆发事件的观测和数值模拟研究, 探讨其激波形成过程, 发现激波对应的二型暴主要存在与该 CME 与前一个 CME 相互作用期间, 目前已有初步结果。

4) 耀斑研究

太阳耀斑电流片的光谱诊断：利用 Hinode/EIS 光谱数据并结合 SDO/AIA 成像数据，分析了一个 X8.2 级耀斑中的电流片结构。结果显示：此电流片内部等离子体的温度高达千万度，Fe XXIV 谱线在电流片的地方显示出非常强的非热速度（高达 200 km/s），最强非热速度并非发生在电流片中心，而是在电流片的边缘；在电流片中心，非热速度和谱线强度成反比关系。求得电流片的厚度为 7 - 11 Mm。这些结果说明电流片内部存在精细结构 ,而其湍动过程很可能使得磁重联能够快速地进行 ,从而有效地耗散能量（Li Y. et al. 2018, ApJL, 853, 15 ）。电流片中湍动磁重联的观测：利用 SDO 上搭载的极紫外成像仪，分析了发生在 2017 年 9 月 10 日的一次 X 级耀斑事件，发现磁重联区的极紫外辐射强度的空间分布呈现一个幂律谱分布 ,出流辐射强度的时间变化同样呈现较好的幂律谱分布。基于观测估计的电流片长宽比（高达 200）也远远大于理论上得到的撕裂膜不稳定性发生的极限。此外，还利用极紫外光谱数据，观测到电流片中多条高温谱线甚至具有高达近 200 km/s 的非热速度。这些观测证据表明宏观上的电流片的确可能被分裂为更小的电流片结构，极有可能是由撕裂模不稳定性和湍流共同导致，从而提高了重联率（Cheng X. et al. ApJ, 866, 64 ）。耀斑大气中 Fe Ⅰ 6173 埃谱线的非局部热动平衡计算：对 Fe Ⅰ

6173 埃谱线进行了耀斑大气条件下的非局部热动平衡计算。结果显示，在初始宁静太阳大气中，Fe I 谱线线心明显增强，增强的辐射来源于光球层的辐射返回加热以及色球层的粒子束加热。由于在低色球层有向上的物质运动，这也导致了 Fe I 谱线呈现蓝不对称。而在黑子初始大气中，Fe I 谱线对耀斑加热响应更为显著，表现为线心发射以及非常明显的不对称性。这种线心辐射增强以及谱线不对称性都在 HMI 的观测中有所体现。通过计算偏振轮廓，发现斯托克斯 I 和 V 轮廓在耀斑加热时会发生变化。这也使得利用 Fe I 谱线轮廓测量磁场会受到影响。因此，我们在解释耀斑过程中的磁场瞬变现象时需要格外小心（Hong J. et al. 2018, ApJL, 857, 2）。

5）其它

今年团组国际合作比较活跃，邀请近十位外宾来访交流，包括聘请 ASO-S 国际顾问以及作为中科院高级来访专家在团组工作。团组成员参加了近 20 人次的国际会议和有关合作访问，包括：2018 年 COSPAR 大会、2018 年 IAU 大会、2018AGU 大会、第 17 届 RHESSI 年会、IRIS 年会、中瑞双边会等，以及赴德国、意大利有关单位交流 ASO-S 合作。在多个国际会议上做邀请报告或口头报告，并参与了一些国际会议的 SOC 组织工作（如 COSPAR、第二届中欧太阳物理会议）。此外，年内还依托太阳物理年会主办了首次全国 ASO-S 大会，以及一系列的 ASO-S 项目会议。ASO-S 项目进展应邀在 2018 年全国天文大会上做 45 分钟邀请报告。苏杨等申请的 NVST 望远镜观测项目成功在抚仙湖观测站进行了一周的观测，获得了暗条和磁龙卷的一系列观测数据。

1-03 太阳活动的多波段观测研究团组

在 2018 年度，本小组继续认真工作，结合本台“135”发展规划中的四个重大突破方向之一太阳物理，努力完成国家重点基金以及其他项目所设立的研究任务。在“太阳活动的高分辨率观测与研究”方面取得了研究进展。我们利用国际领先的探测设备的观测，主要是大熊湖天文台的古迪太阳望远镜(GST)、 太阳动力学卫星(SDO)、IRIS、和我国的云南抚仙湖一米真空望远镜(NVST)，从各个方面尤其是小的空间尺度上(亚角秒)深入研究了太阳活动。在既定科学目标方面取得重要进展。完成了重点基金项目“太阳活动的高分辨率观测与研究”《计划任务书》所设定的科学目标，重点基金项目顺利结题。2018 年 10 月 31 日，在本项目的支持下，利用 2018 年中国天文学会大会在昆明召开的机会，我们组织了一次"GST 偏振观测数据的磁场反演"研讨会。会上来自大熊湖天文台相关专业人员给参会学者讲解了磁场反演的程序， 并将程序和数据拷给参会学者实时处理，实时答疑，本次会议共有 80 多人参加，90 以上是年龄小于 35 岁的年轻学者。

亮点成果一：

我们也充分使用 IRIS 光谱的高分辨观测数据，详细研究了一个活动区的小尺度磁重联事件。这个磁重联事件在色球和过渡区表现为双向出流，在光球表现为磁场对消，在日冕则表现为极紫外增亮。综合起来，我们认为，微小尺度上(小于 0.1 个角秒)的底层大气重联同时产生了高温和低温物质的外流，由此加热了日冕。亮点成果二：在前兆阶段两个磁环重联形成不稳定的热通道(hot channel)，并在耀斑前由于不稳定开始缓慢膨胀，在膨胀阶段进一步产生 Torus 不稳定，从而产生爆发性耀斑。我们利用独特的 10830 埃高分辨率窄带成像从非常小的尺度上具体观测到了前兆阶段剪切磁环重联产生热通道的过程及其不稳定爆发的过程。尤其是我们首次发现，在同一个事件中三个耀斑前兆产生了三个热通道，只有二个爆发出去形成了耀斑双峰，这对耀斑的多峰结构首次给出了观测上的解释。

其他方面的进展有 利用美国大熊湖的地面 BBSO/GST 高分辨率观测以及空间卫星 SDO, IRIS 对活动区 12396 的多波段观测，宿英娜等发现该区域含有特殊的拱形暗条系结构，该结构四周环绕着时而增亮的准环形耀斑带。作者对该结构做了深入观测研究和磁场建模，结果表明该区域含有多条极性不同的磁通量绳，耀斑的各种宏观和精细结构均与该区域的复杂磁拓扑结构相关。 使用 SDO 成像和 IRIS 光谱的观测数据，我们研究了高温耀斑环中的无阻尼振荡现象。我们发现在耀斑环中存在 40 秒的准周期振荡，它可以被多种观测信号同时探测到，如 Fe XXI 的多普勒速度、谱线宽度、和峰值强度以及 GOES 1-8 A 的求导曲线和 Fermi 26-50 keV 的辐射流量。观测结果表明多普勒速度和谱线宽度的振荡相位是一致的，而与峰值强度的相位差是π/2。在观测中，40 s 的准周期振荡没有出现明显的衰减行为，研究认为这与耀斑环中的无阻尼 kink 振荡模式是一致的。根据 kink 振荡的模型可估算出耀斑环中的磁场强度大约为 120-170 G。同时根据磁场外推模型得到在耀斑环高度处的磁场强度约为 110-180 G。两种方法得到的磁场强度高度吻合，更进一步验证了耀斑环中 kink 振荡的解释。

使用 NVST 的高分辨率观测数据，我们研究了宁静日珥中的 K-H 不稳定性和小尺度振荡现象。我们观测到了由强剪切运动而导致的两组快速发展的涡旋结构，计算结果表明物质流的剪切速度远大于当地的声速，说明剪切运动能够产生足够强的边界恢复力从而克服表面约束力,进而产生 K-H 不稳定性。我们还在日珥的细丝结构中发现了小尺度的振荡现象，并且这些振荡的周期都是非线性变化的，振荡的幅度不足 1 Mm。观测结果表明这些小尺度的振荡都是日珥的本质行为，可能是由日冕中的 MHD 波驱动的。这两种动力学行为的尺度都很小，这主要得力于 NVST 的高分辨率观测数据。

我们报道了日冕喷流中亚角秒等离子体团的多波段观测。2014 年 8 月 24 日 04:55 UT 左右，活动区 12149 发生了一个 C5.5 级环形耀斑。伴随该耀斑发生了两次日冕喷流（jet1 和 jet2）。耀斑峰值时刻（05:02 UT）过后，jet2

底部出现了多个明亮而致密的等离子体团，被 IRIS/SJI 观测到。在 1330 埃波段中，这些等离子体团的大小在 0.45 角秒到 1.35 角秒之间，将近 84%比例是亚角秒的（即小于 1 角秒）。等离子体团尺寸的平均值和方差分别为 0.78 角秒和 0.19 角秒。速度在 10 到 220 公里每秒之间，有些在传播过程中减速、消失。三个等离子体团被 SDO/AIA 卫星在 EUV 波段观测到，速度和 UV 波段的几乎一致。我们认为，1330 埃波段观测到的属于等离子体团冷的部分（温度约 2.5 万度），EUV 波段观测到的属于热的部分（温度约几百万度）。我们的结论是：这些等离子体团是由日冕喷流底部或内部电流片的撕裂模不稳定性产生的。该研究结果对于深入理解日冕喷流内部精细结构和等离子体团在 UV 和 EUV 波段的关系具有重要的意义。

我们报道了环形耀斑中色球蒸发的多波段观测。2014 年 8 月 24 日，活动区 12149 发生了一个 C5.5 级耀斑。耀斑包含一个离散的环形耀斑带（直径约 1 角分）和里边的一个短耀斑带，它们在紫外、极紫外、软 X 射线波段，尤其是微波 17G 赫兹观测到。17G 赫兹光变曲线的峰值时刻(04:58 UT)和 1600 埃、软 X 射线流量求导（代替硬 X 射线）波段的峰值时刻一致，表征耀斑释放的能量在低层大气沉积（注入）的峰值时刻。紧接着，耀斑环中出现了汇聚运动和等离子体填充过程，在 AIA 131 埃和 XRT 两个滤光器(Be_thin, Be_med)中最明显，这是色球蒸发上升流的一个直接观测证据。通过与之前的理论模型进行比较，我们推断出大于 5×10^10 erg cm^-2 s^-1 能流密度可以解释观测到的现象。因为热传导加热不足以提供足够的能量，其他机制（如非热电子或阿尔芬波）可能起到重要的作用。

1-04 暗物质与空间天文台实验室

亮点工作

1）疑似超新星早期伽马射线辐射源的发现

2）ASO-S 太阳卫星正式立项批复，HXI 载荷研制工作紧张有序进行。

1. 疑似超新星早期伽马射线辐射源的发现

众所周知超新星的激波可以加速高能宇宙射线粒子，产生从射电到高能伽马射线的宽波段的辐射，形成绚丽的超新星遗迹。但一般的超新星遗迹通常在超新星爆发后很长时间(几百年以上)才能被观测到，在超新星爆发早期的粒子加速仍然只有一些理论上的猜测，缺乏观测证据。最近的超新星，位于大麦哲伦星云里的 1987A 在伽马射线波段还没有被观测到，这也一定程度上挑战了超新星的早期粒子加速图像。我们利用 Fermi 的观测数据，发现在一个超亮的奇特超新星 iPTF14hls 爆发大约 1 年以后在相应位置处出现一个伽马射线暂现源，其伽马射线辐射持续了大约 2 年时间，随后逐渐消失。该伽马射线可以解释为超新星激波加速的粒子和外围介质相互作用所产生。但因为伽马射线辐射较弱，和超新星光学以及别的波段观测结果之间的确切证认比较困难，目前只能当作一个疑似成协事件。

2. ASO-S 太阳卫星正式立项批复，HXI 载荷研制工作紧张有序进行

ASO-S 太阳卫星于 2018 年初正式立项批复，本团组承担三大有效载荷之一的 HXI 载荷研制任务，相关人员根据方案阶段工程研制计划，紧张有序的开展了相关工作。截止目前已完成了 HXI 分系统方案设计报告，关键技术攻关方案报告，分系统任务指标与定标需求，准直器、量能器、电控箱及热控各单机详细设计方案报告等工程研制文档的编写和评审；组织完成了光栅加工，准直器结构外协，溴化镧晶体，光电倍增管，量能器结构外协，电荷测量芯片，高压模块等重要外协采购项的招标采购流程，并按合同计划验收完成了方案阶段采购内容；验收合格并交付了用于方案阶段整星力学试验的准直器和量能器金属结构件产品。

1-05 宇宙高能粒子的加速和辐射研究团组

本年度参与高能所牵头的基于高海拔宇宙线观测站的科学研究的重大研发计划，负责这个研发计划的 4 个研究课题中有关宇宙线起源的第三课题研究。在超新星遗迹粒子加速研究方面取得两个重要成果，为完善宇宙线的超新星遗迹起源学说奠定基础。在太阳耀斑多波段观测方面也取得创新性成果，进一步揭示耀斑能量释放过程的多样性。

1）发现了超新星遗迹中高能粒子分布函数的演化规律

2）揭示了超新星遗迹高能粒子加速效率随时间的演化

在超新星遗迹粒子加速研究方面取得两个重要成果：1）发现超新星遗迹中高能粒子能谱分布一般表现为双幂律并且低能端谱指数和拐折能量随超新星遗迹年龄的增加而减小；2）超新星遗迹激波粒子加速效率随超新遗迹寿命的增加显著增长。基于这里个成果，宇宙线的超新星遗迹起源学说被分解成两部分内容：1）高能宇宙射线在年轻超新星遗迹中的加速和逃逸；2）决定宇宙线总能量的能量较低的高能粒子在年老超新星遗迹中的加速。围绕宇宙线的起源问题，和胡红波、王祥玉合作完成一篇综述文章。

在太阳耀斑和超新遗迹多波段研究方面也分别取得新发现。发表 SCI 论文各一篇。另外和袁强、鄢淑平合作在银河系中心黑洞和 X 射线双星光变研究上各发表一篇 SCI 论文。

1-06 暗物质间接探测的相关科学研究团组

长期服务于悟空号的科学需求。2018 年里我组织撰写完成了悟空号项目组的第三篇合作组论文“The on-orbit calibration of DArk Matter Particle Explorer”，这也是悟空号除了项目论文外的有一篇关键性基础文献。我还负责了该论文的投稿，文章已经在 Astropart. Phys.杂志在线发表(Ambrosi, G. et al./DAMPE collaboration. 2019, 106,

18)。本团组还积极的参加悟空号的宇宙线数据处理分析，岳川博士(DAMPE 骨干学者)负责完成了质子宇宙线的数据分析，该结果已经由我代表悟空号合作组正式投稿；我的博士研究生马鹏雄正在负责分析氦核宇宙线数据，力争在 2019 年正式发表之。我的博士研究生段凯凯与李翔、梁云峰一道正在优化悟空号的伽马射线分析软件，争取 2019 年发表首批伽马射线成果。

本团队 2018 年的关键性部署还包括悟空 2 号卫星项目的推进以及引力波数据处理小组的建立。悟空 2 号卫星项目是我和郭建华重点推进的预研项目，2018 年里我们先后组织了 3 次专家咨询会；凝炼了科学目标，并在技术方案方面形成了初步的共识。在引力波方面，2018 年我们的另一战略部署是成立了引力波数据处理学习小组，并派遣博士生(黄永嘉)去日本长期访学。目前该小组在引力波数据处理方面进展迅速，有望在 2019 年 LIGO O3 运行阶段把握重大机遇。

2018 年我们还继续从事暗物质间接探测（尤其是对悟空号电子数据的物理解读）、引力波天文、高能天体物理的理论研究，在 ApJL、ApJ、PRD、PLB 等国际主流天文/物理类期刊共发表论文 20 余篇。一名博士毕业生(梁云峰)的学位论文获得中国科学院优秀博士学位论文以及江苏省优秀博士学位论文，一名博士研究生（李尚）获得中国科学院院长奖(特别奖)、一名博士生获得研究生国家奖学金(马鹏雄)。

悟空号的相关研究：在 "悟空"号的宇宙线数据分析方面，本团组的岳川博士(DAMPE 骨干学者)负责完成了质子宇宙线的数据分析，该结果已经由我代表悟空号合作组正式投稿。我的博士研究生马鹏雄正在负责分析氦核宇宙线数据，力争在 2019 年正式发表之。悟空 2 号卫星项目是我和郭建华重点推进的预研项目，2018 年里我们先后组织了 3 次专家咨询会；凝炼了科学目标，并在技术方案方面形成了初步的共识。在暗物质间接探测方面我们拓宽了研究对象，除了重点研究 WIMP，还开始研究类轴子粒子。在类轴子粒子方面 2018 年我们发表了 2 篇 PRD 论文，对类轴子粒子的物理性质在部分参数空间予以了更强的限制（Xia, Z. Q. et al. 2018 PRD; Zhang, C. et al. 2018 PRD; Liang, Y. F. et al. arXiv:1804.07186）。在 WIMP 方面，我们主要是解释悟空号的电子宇宙线数据，部分工作有很好的国际反响(e.g., Fan, Y. Z. et al. 2018 PLB; Zu, L. et al. 2018 PRD)。我们也积极的分析 Fermi-LAT 矮星系的数据来寻找暗物质存在的迹象。系星系虽然总质量小（典型区间为 1 百万到 1 亿太阳质量），但由暗物质绝对主导(某些矮椭球星系的暗物质质量是恒星质量的上千倍)，几乎没有产生伽马射线辐射的高能天体物理过程。部分矮星系在天球面上分布于高银纬区域，周围没有明亮的伽马射线源。因此矮星系方向被认为是搜寻暗物质信号背景最为干净的区域，一直被寄予厚望。迄今为止，尚没有任何一个矮星系方向探测到可靠的伽马射线辐射，但个别矮星系方向有微弱的 GeV 辐射迹象。2018 年里我们对距离太阳系 50 kpc 之内的矮星系进行了系统的分析，发现现阶段最强的疑似伽马射线辐射信号来自于 Ret II, 尽管置信度依然不足以宣称为一个确定的探测，但是信号的强度在随着时间线性增长(见图 1)。如果解释为暗物质湮灭，该疑似伽马射线信号所需的参数空间也大致与银心 GeV 光子超(Zhou, B. et al. 2015 PRD)、AMS-02 的 GeV 反质子超出（Cui et al. 2017 PRL）一致。Fermi-LAT 目前工作状态良好，正在持续的产出数据，联合其它空间探测设备，可望最终的确认 Ret II 是否是一个伽马射线辐射源，并厘清其与暗物质的关系。

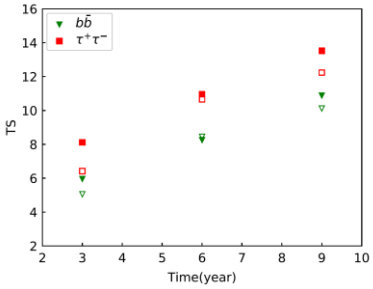

图 1: Reticulum II 方向疑似伽马射线辐射信号的置信度与时间的关系(图取自 Li, S. et al. 2018 PRD)

引力波相关研究: 2018 年我们成立包括 6 位成员的引力波数据处理学习小组，并派遣博士生(黄永嘉)去日本长期访学。目前该小组在引力波数据处理方面进展迅速，有望在 2019 年 LIGO O3 运行阶段把握重大机遇。理论研究方面，我们在利用引力波数据来限制中子星的最大引力质量方面取得进展，发现双中子星并合后形成的超大中子星的转动角动量的大小会显著的影响对最大引质量 Mmax 的估算，见图 2(Ma, P. X. et al. 2018 ApJ)。因此，要可靠的估算出 Mmax,我们需要一个先验的知道转动角动量的数值。我们还基于现有观测对于 Mmax 以及中子星最小半径的限制，解析给出了一个"双中子星引力质量之和"的上限值，高于此质量的双中子星系统的并合会产生黑洞而不是快速均匀自转的超重中子星（Shao, D. S. et al. 2018 submitted）。我们还提出了用 GW170817 晚期射电估算出的相对论性外流体的动能来限制中子星状态方程的方法(Wang, Y. Z. et al. arXiv:1811.02558).

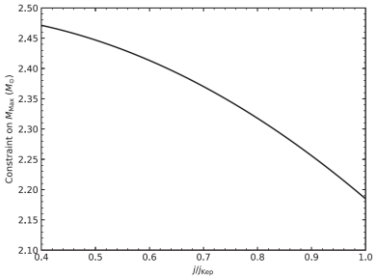

图 2: 基于 GW170817 数据得到的中子星最大引力质量的 90%上限与 j/jkep 的关系(图取自 Ma，P. X. et al. 2018 ApJ)。这里的 j 代表未塌缩超大质量中子星的无量纲角动量，jkep 代表开普勒运动速度下的无量纲角动量。

高能天体物理方面我们 2018 年重点关注了高红移宇宙的活动星系核并取得可喜的进展。早期宇宙一直是天文学家关心的热点领域，活动星系核作为宇宙中最明亮的稳定电磁波辐射源之一，是少许研究高红移宇宙的有效探针。耀变体，作为喷流对准地球的极端活动星系核子类，由于强的多普勒集束效应，主导了河外伽玛射线天空，是宇宙中高能粒子的重要加速源。来自于高红移耀变体的伽玛射线不仅仅对研究早期超大质量黑洞周围的极端环境有着重要的作用，它还能够对河外背景光模型起到强有力的限制。然而由于高红移耀变体的伽玛射线能谱比近邻源要显著偏软，且 sub-GeV 伽玛射线光子的空间分辨率比 GeV 光子的要差，探测来自于这一类源的微弱伽玛射线信号是一个巨大的挑战。近期，Fermi 卫星组分析了一千一百余个高红移耀变体的伽玛射线数据，发现了五个新的高红移伽玛射线耀变体，其中的最远的源红移达到了 4.3。虽然已知的伽玛射线耀变体的数目达到了三千余个，红移大于 3 的源的数目仍仅有 7 个。我们对这些高红移源的伽玛射线数据进行了深入分析，在其中 5 个源中发现了显著的长时标伽玛射线光变(Li, S. et al. 2018 ApJ)。这些时变信息不仅仅严格的限制了高红移耀变体的喷流速度及辐射区域位置，也对搜寻更高红移耀变体的伽玛射线辐射提供了新途径。考虑到高红移耀变体的剧烈光变，在其伽玛射线爆发期间时显然更容易探测到 GeV 辐射。受此启发，我们对红移 4.7 的耀变体 B3 1428+422 进行了分时段的 Fermi-LAT 数据分析。尽管 9 年的平均数据中没有显著的 GeV 辐射信号，但在 2012 年 8 月至 2013 年 5 月这段数据中发现了一个新的伽马射线瞬变源(见图 3)。这个瞬变源的伽玛射线谱很软，与已知的高红移耀变体的伽玛射线谱行为一致，对该瞬变源的定位结果与 B3 1428+422 一致，并且在该方向上不存在其它合适的候选体。这些结果表明所发现的 GeV 辐射来自于 B3 1428+422，尽管尚需射电、光学等多波段的长期监测予以最终确认。此前已知最远的 GeV 伽玛射线源是伽玛射线暴 GRB 080916C ，它的测光红移为 4.35，我们的工作(Liao, N. H. et al. 2018 ApJL)为打破这个记录提供了一个颇具竞争力的候选体。

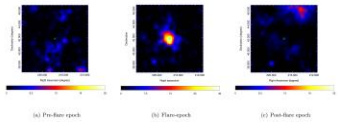

图 3 :不同时期 B3 1428+422 (z=4.7)方向上的伽马射线探测显著程度，绿色符号代表目标源射电坐标（图取自 Liao et al. 2018 ApJL)。

团组成员冯磊同国内理论物理学家合作，研究了胶子凝聚模型下质子核子碰撞产生的伽马射线能谱(Feng et al, Astrophys.J. 868 (2018) no.1, 2)，见图四。胶子凝聚是 QCD 模型的理论预言之一，在该模型下，核子碰撞的截面在胶子凝聚能段会极大的增强。在该模型下，核子碰撞产生的伽马射线的能谱会表现为特异的“尖峰”状结构，该“尖峰”结构的能量为 1-20TeV。弥散伽马射线的成分之一就是质子-质子碰撞，是寻找该结构的可能区域之一。另外我们提出 earth limb 的伽马射线成分单一，背景干净，是寻找该效应的理想区域。Fermi-LAT 卫星已经测量到 earth limb 的伽马射线，不过能量还不够高，只有 300GeV。DAMPE 的测量范围可以高达 10TeV，是理想的寻找该结构的探测器。

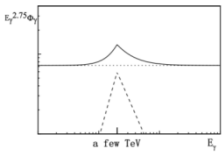

图四 :胶子凝聚模型预言的质子核子碰撞产生的伽马射线能谱

团组成员冯磊还同国内理论物理学家合作，系统的解读了 DAMPE 电子数据的物理意义。构建了解释该数据的理论模型。我们的模型有 Z’ 模型，DM cascade annihilation

模型等。相关论文已发表，包括：Guang Hua Duan*, Lei Feng* et al., "Simplified TeV leptophilic dark matter in light of DAMPE data"，Published in JHEP 1802 (2018) 107; Junjie Cao*, Lei Feng*, et al., "Explaining the DAMPE data with scalar dark matter and gauged U(1)Le−LμU(1) interaction"，Published in Eur.Phys.J. C78 (2018) no.3, 198。此外我们还利用 DAMPE 的数据限制了 box 型末态电子能谱的暗物质模型的参数，相关论文见：Lei Zu, Cun Zhang, Lei Feng* et al., "Constraints on box-shaped cosmic ray electron feature from dark matter annihilation with the AMS-02 and DAMPE data"，Phys.Rev. D98 (2018) no.6, 063010。

团组成员廖能惠积极参与 DAMPE 对耀变体 TXS 0506+056（PeV 中微子候选体）的伽玛射线耀发在 ATel 上的汇报（Xu, Zun-Lei, Liao Neng-Hui, Duan, Kai-Kai et al., ATel, 11246），这是 DAMPE 的第二个 ATel。除了研究高红移耀变体之外，廖能惠也与华中科大的研究者利用近期释放的 MHz 射电巡天数据，对活动星系核喷流的重要物理参量，例如功率，组分，磁化强度等，做了有力的限制（Fan, Xu-Liang*; Wu, Qingwen*; Liao, Neng-Hui*, 2018, ApJ, 861, 97）。廖能惠也积极参与与国内相关研究团组（云南天文台白金明研究员团组等）及国外意大利帕多瓦大学研究团组的合作，对著名耀变体 3C 454.3 和 3C 345 的多波段数据进行了详尽的分析，探究了其物理环境和辐射过程（Fan, Xu-Liang; Li, Shao-Kun; Liao, Neng-Hui, et al. 2018, ApJ, 856, 80；Berton, M.; Liao, N. H.; La Mura, G. et al. 2018, A&A, 614, 148）。与此同时，我还参与了本团组对 Seyfert 星系 1H 0707-495 的间歇性的准周期震荡行为的汇报（Zhang, Peng-fei; Zhang, Peng; Liao, Neng-hui et al. 2018, ApJ, 853, 193）。除了活动星系核之外，我们还对若干个有趣河内的伽玛射线源及来自于奇异超新星方向上的伽玛射线信号开展了研究，取得了一定的进展（Guo, Xiao-Lei; Xin, Yu-Liang; Liao, Neng-Hui et al. 2018, ApJ, 853, 2；Xin, Yu-Liang; Liao, Neng-Hui; Guo, Xiao-Lei et al. 2018, ApJ, 867, 55 ;Yuan, Qiang; Liao, Neng-Hui; Xin, Yu-Liang, et al. 2018, ApJ, 854, 18）。

1-07 紫外及 X 射线天文研究团组

本年度顺利完成天文联合重点项目中期考核，并展开科工局预研究项目的相关研究。在科学上，我们继续在高能弥漫天体领域进行研究，结合空间多波段研究工作，利用高分辨率的高能光谱进行谱线诊断并分析其物理起源；在致密星方面的研究，继续利用时变信息来研究吸积盘和冕的相互作用。在技术方面，我们完成了 HI 窄带成像仪的光学设计方案，正准备外协单位光学元器件方面的研制；紫外镀膜方面，合作单位也开展了样品薄膜的制备研究。

本年度顺利获得院对外合作重点项目，在紫外科学和技术国际交流方面得到资助；并获得天文联合基金一项。

亮点工作

1）通过时变信息研究吸积盘和冕的相互作用；

2）利用 Chandra 和 XMM-Newton 空间 X 射线望远镜，HST 的 COS 紫外光谱仪，和 SDSS/DSS 光学数据来研究不同重子的分布。

1、在近邻星系弥漫 X 射线辐射的研究工作。

a）通过电荷交换辐射限制星系超级风中冷气体团块的尺寸与形状，多为椭圆饼状。合作者文章已投递。

b）对旋涡星系，通过高分辨率光谱数据绘制纯热气体旋臂形态，并发现其中的电荷交换辐射。文章在撰写中。

c）构建全新共振散射光谱模型，并用以解释 M31 核球热气体的氧发射线的比值与形态。合作者文章已发表。

d）基于 M31 核球的深度观测，前所未有的高能谱分辨率与高空间分辨率的细节对其热气体给出限制。电荷交换辐射与共振散射机制都不能解释全部观测特征，而半个百万年前熄灭的 AGN 则能够解释。文章在最后修改即将投递。

e）为 M31 构建具体的包含动力学的非平衡光致电离光谱模型，这也将用于研究近邻宁静星系中的 AGN 出现频次与反馈影响。文章在修改中稍后投递。

f）对 M51 的核心区域光谱的分析表明，其外流中电荷交换辐射与非平衡光致电离辐射也许并存。学生的文章即将投递。

g）对近邻恒星形成星系样本的电荷交换辐射的研究正在进行。

2、高能致密星的研究：

把我们自己提出的时变分析方法应用到黑洞双星 GRS 1915+105 的 RXTE 观测数据，探索了一条通过时变信息研究吸积盘和冕的相互作用的途径（Yan et al. 2018）。

申请到了国家自然科学基金天文联合基金培育项目，计划将我们时变分析方法应用到"慧眼"卫星观测数据，以进一步研究黑洞吸积过程的重要细节。

3、宇宙缺失重子方面的研究：

为了研究星系团中的重子物质成分 .首先我们选出了一个特殊的星系团样本，每个星系团都有一个紫外亮的背景类星体 .然后我们利用这个样本去检索公开的天文多波段数据库，并且分析了数据库中包括 Chandra 和 XMM-Newton 空间 X 射线望远镜，HST 的 COS 紫外光谱仪，和 SDSS/DSS 光学数据来研究不同重子的分布。最后我们发现这些星系团都缺失重子，其中一部分缺失的重子可能在温气体和温热气体之中。然而数据库中 HST 的曝光时间太短，我们没有观测到紫外吸收线，只能推出一个上限，因而需要长时间的新观测来更好的限制温气体和温热气体的性质。

结果发表在 MNRAS 上（ http://adsabs.harvard.edu/abs/2018MNRAS.481.4111G ）

4、紫外技术方面的研究：

团组助理研究员在国家留学基金委国家公派访问学者项目的支持下，来德国图宾根大学参与 CAFE 项目微通道板（MCP）探测器的研发，学习了先进的 MCP 探测器的光阴极、MCP、阳极、电子学和密封等方面的设计理论和方法、设备和制造、测试和性能表征。

合作单位在镀膜方面进行了样本测试，进展良好。

Ⅱ．南极天文及射电天文研究部

2-01 恒星结构、演化和脉动的研究团组

1）我们理论的脉动极不稳定模同观测的半经验 Bedding-Kjeldson 标量关系符合得很好，给出了脉动红巨星一个全新的解释

之所以存在造父变星脉动不稳定带红端边界是因为对流的阻尼所致。所以长期以来，人们都将对流视为恒星脉动的一种纯碎阻尼机制。太阳 5 分钟振荡的湍流随机激发机制不仅成功解释了其有限的脉动振幅和振幅随频率的变化，而且其有限的线宽得到观测的强有力支持。一时间湍流随机激发理论变成低温红变星主流观点，将它推广到解释所有红巨星脉动的激发，甚至高光度的 OGLE 小振幅红巨星（OSARG）的激发。很明显，大变幅的 Mira 变星是无法用湍流随机激发机制来解释的。人们只能将它推之为一种至今未知的脉动激发机制。低温红变星的激发机制，长期以来一直是恒星脉动理论一个未解的难题。对这个问题我们一直持有与当今主流观点完全不同的看法。我们认为对流绝非单纯只是脉动的阻尼机制。对流引起恒星内部能量、动量的传递与交换和物质的混合，从而严重影响恒星的结构、演化与脉动稳定性。经过长达近半个世纪的研究，依据流体力学方程和湍流理论，我们发展了一种非局部和非定常的恒星对流理论，并成功地将它应用到恒星对流区结构，恒星演化和变星。即将最后的<Convection Theory and Relevant Problems in Stellar Structure, Evolution and Pulsation Stability>一文，对此作了一个全面的总结。利用我们的非局部和非定常的恒星对流理论，我们计算了红巨星径向和非径向非绝热脉动，并利用累积功对恒星对流与脉动的耦合进行了仔细的分析研究。我们的研究表明，对流绝非单纯的脉动阻尼机制。对流流与湍流粘滞性是脉动的阻尼机制，而湍流压却是脉动的激发机制。对流流的阻尼作用反比于振荡模的频率，是稳定低阶模和产生脉动不稳定区红端边界的主要机制。而湍流压的激发作用及湍流粘滞性的阻尼作用分别在 $\omega\tau_c \backsim 3\omega\tau_c/4$ 和 $3\omega\tau_c \backsim 1$ 达到极大。湍流粘滞性是高阶模振荡的主要机制，而湍流压是激发红变星脉动的重要机制。湍流压，湍流粘滞性及湍动热对流的激发和阻尼作用随着恒星的质量、光度、有效温度和振荡模的阶数变化。其综合的效果，时而表现得是脉动的激发机制，时而表现得是一种阻尼机制。对低光度红巨星，其低阶模是脉动稳定的，而中和高阶模是脉动不稳定的。恒星表现得像是典型的类太阳型恒星；随着恒星光度增高，极不稳定模向低阶模推进。到高光度红巨星，中高阶模都变得脉动稳定。只有少数低阶模变得脉动不稳定。高光度红巨星变得像典型的 Mira-like 型恒星。我们理论的脉动极不稳定模同观测的半经验 Bedding-Kjeldson 标量关系符合得很好，给出了脉动红巨星一个全新的解释。今年发表的<Turbulent convection and pulsation stability of stars - Ⅲ. Non-adiabatic oscillations of red giants>给 OGLE 亮红变星提出了一个完美的理论解释。

2-02 南极天文中心

（1）完成第三台南极巡天望远镜 AST3-3 的建造。AST3-3 搭配红外相机 KISS，将利用南极 Dome A 全球独一无二的红外观测条件在近红外 Kdark 波段进行观测。

1、完成第三台南极巡天望远镜 AST3-3 的建造。南极 Dome A 地区是地球上温度最低的区域之一（Dome A 已测到的最低温度是-82.5°C），红外背景辐射比通常站址低十倍以上，尤其在近红外 Kdark 波段（2.4μm）热背景比温带的天文站点低一百倍，这使得高灵敏度热红外观测成为可能。AST3-3 搭配了 2k×2k 的 KISS（Kunlun Infrared Sky Survey）红外相机，利用南极独一无二的红外观测条件，在 Kdark 波段开展观测。AST3-3 的光学设计与 AST3-1、AST3-2 相同，通光口径 500/680mm，视场 46×46arcmin。AST3-3 将利用南极极夜 135 天的连续全黑夜，对近红外波段的变源进行搜寻，其科学目标包括（1）超新星研究；（2）恒星形成和演化；（3）暂现源搜寻；（4）AGN 研究；（5）宇宙红外背景等。

2、完成南极中国之星小望远镜阵 CSTAR 的改造。CSTAR 原来为四台固定指向、通光直径 100mm 的小望远镜阵。新设计的 CSTAR 更换了新的 1k×1kCCD，加装了赤道仪，由两台通光直径 100mm 的望远镜为一组，一台 G 波段，一台全波段，将原来固定指向的 CSTAR 改造为可以指向跟踪的大视场巡天望远镜，并在盱眙观测站进行测试观测。

3、完成了南极能源支撑平台的设计制造和验收。自 2017 年 9 月至 2018 年 3 月，平台共进行了 4 次长期运行测试，测试期间无人值守，无外接电源，无人远程控制，基本能够模拟南极自动控制无人值守独立运行状态，外接负载功率不变。

4、2018 年 2 月 利用国内的天文望远镜设备 TNTS0.8 米、CNEOST 1 米、兴隆 2.16 米、丽江 2.4 米等，与澳大利亚斯威本大学 Jeffrey Cooke 教授的团队的 DWF 计划，利用全球数十台不同波段的望远镜，覆盖从射电到伽马射线的极宽波段，以及引力波和中微子等不同信使的探测器，对引力波光学对应体、快速射电暴开展联合观测。得到超过 15000 个暂现源候选体，其中包括几百个小行星，数个超新星（m>23.5），2 月 12 日 23:45（UT）探测到一个 FRB（FRB180212）。

5、发布了 AST3-1 的点源星表。AST3-1 在 2012 年巡天覆盖 2000 平方度的天区，以及整个大麦云和小麦云、挑选出来的系外行星场等。AST3-160 秒曝光达到了 19.3 等的巡天深度，亮星光变曲线精度 5mmag，达到了光子噪声的极限。这说明 AST3-1 对于搜索暗弱暂现源很有竞争力。

2-03 **星系宇宙学和暗能量研究团组**

本团组一直坚持面向星系宇宙学领域的前沿科学问题开展高质量的研究工作。本年度在星系形成模型、暗晕空间指向、弱引力透镜光线跟踪模拟、强引力透镜样本、星系并合数值模拟、星系图像处理等方面继续开展了深入研究；作为 HUBS 项目科学组成员，参与其科学白皮书的撰写工作。

1，首次提出了利用星系尺度的透镜现象寻找超新星的新方法。超新星作为宇宙中的标准烛光之一，在宇宙加速膨胀的发现方面做出了重要贡献，然而，高红移的超新星数量较少，主要是光度较低，而强引力透镜可以放大超新星的亮度，因此有望利用透镜原理发现更多的超新星。本工作(Shu et al., 2018, ApJ)中我们提出一种新的寻找超新星的策略，即对强引力透镜系统进行跟踪观测.利用 SDSS 的 128 个星系透镜系统，我们估计了观测到被透镜的超新星概率，并对 ZTF 和 LSST 寻找到超新星的概率进行了估计。

2，利用领先的弱引力透镜模拟数据研究了 shear peaks 方法在宇宙学中的应用。Shear peaks 作为独立的宇宙密度测量探针，在弱引力透镜宇宙学中有重要的应用。该方法需要解决的一个关键问题是需要统计那些 shear peaks 属于真实，那些属于噪声或大尺度结构投影效应。我们利用之前的模拟数据，比较了真实 shear 信号和数值模拟中暗晕的对应关系，对不同噪声水平的测量进行了估计。文章发表在 MNRAS（Wei et al. 2018, MNRAS）。

3, 继续开展了星系的空间指向。星系在空间分布并非随机的，而是在不同尺度上存在不同的空间指向排列现象，比如在小尺度上，卫星星系倾向于分布在中央星系的主轴附近，而且其信号强弱与中央星系的颜色和质量有关；在大尺度上，中央星系的主轴之间也存在相关性，中央星系跟大尺度环境之间也存在指向相关。2018 年，我们继续开展了星系空间指向的研究。在第一个工作中，我们利用领先的流体模拟数据，研究了星系指向和大尺度结构之间的关系，证实了观测上发现的星系指向与星系形态的依赖关系，研究成果发表在 ApJ（Wang et al. 2018a, ApJ）。在第二个工作中，我们利用 SDSS 的观测数据，研究了卫星星系排列对大尺度环境的依赖关系。我们首次发现，对于蓝色中央星系，其卫星星系的空间排列对大尺度环境有很强的依赖关系，该关系反应了卫星星系是如何从大尺度进入到星系中间的，对我们理解星系在小尺度上的各向异性分布非常重要。

4，开展了 PSF 的相关研究。点扩散效应(PSF)的对星系的模糊化是弱引力透镜剪切场测量主要污染项，围绕点扩散函数的精确测量和点扩散函数场的重构，我们深入开展了两项研究：1）用 Moffatlets 基函数和 EMPCA 算法。建立了新点扩散函数主成分算法，该算法同时具有传统 PCA 算法的灵活性和基函数分解的光滑性，所得主成分稳定、抗噪声能力强；2）提出并建立了利用星系图像限制点扩散函数的新算法，大大突破了传统限制，为点扩散函数场的精确重建提供了新的数据来源；基于精确的点扩散场，开展了包含反卷积过程的多次曝光图像叠加技术的研究，初步的测试表明该算法能在扣除点扩散函数影响的同时提高图像的分辨率和信噪比，其运算精度比传统的 Richardson-Lucy 算法更稳定，且速度有一个量级以上的提升。

2-04 **星系中的恒星形成研究团组**

在 2018 年度本团组紧密结合 135 指导方向，重点工作放到本职科研工作，在 2018 年发表文章 11 篇，IRAM 观测申请，作为 PI 成功申请到 NOEMA 观测时间。执行了科学院的外专外青计划项目，进行学术交流和讨论, 邀请了法国 IAS 的 Alex Beelen 博士，法国 IAP 的 Alain Omont 研究员，澳大利亚 Macquarie University 的副院长 Richard de Grijs 博士，法国 CEA 的 David Elbaz, Emanuele Daddi 教授，西班牙格林纳达大学的 Ute Lisenfeld 教授，SKA 的 Jeffrey F. Wagg 教授，肯塔基大学的 Yan, Renbin 教授, 密西根大学的李江涛博士，爱丁波大学的博士后张智昱，牛津大学博后柳莉杰博士, 法国冷原子研究所（IFRAF）主任 Nichele Leduc 博士和法国科学院（CNRS） 研究说主任 Elisabeth Giacobino 博士，等多位海外及国外专家来访。等 14 位国内外专家学者来访进行学术交流，并且本团组人员也多人次出访加州理工学院，意大利，法国，德国，韩国，西班牙，台湾地区，以及英国，奥地利等多地参加国际学术会议，到达美国夏威夷进行观测和学术合作交流。

正式签署了紫台与 IRAM 的合作协议，为相关课题的合作，进一步保障了将来 5 年的 IRAM 望远镜的观测时间。 3 月到德国参加国际会议，并作学术报告参加会议 "Interstellar Medium in the Nearby Universe"，并访问

ESO，与邀请者讨论合作项目 JCMT 的数据处理，和 ALMA 合作项目；4 月到意大利参加学术会议，并作学术报告“The star formation law in dense molecular gas”，到西班牙格林纳达参加会议；参加维也纳的 IAU 大会及 ApSS 期刊 50 周年庆祝。英国参加参加学术会议” The Wonders of Star Formation conference；访问马萨诸塞大学，纽约州立大学石溪分校，英国伦敦大学学院等。在贵州拉萨北京等国内城市参加学术会议，北京大学、云南天文台、云南大学等进行学术访问并作学术报告等；蒋雪健参加了 8 月份在拉萨举办的分子云与恒星形成研讨会并做学术报告；多次参与关于 60 米级下一代亚毫米波望远镜的科学研讨会。在南京举办了 40 余人的“重点研发项目”项目年度会议。

1）本年度的科研工作一方面是完成一篇 MALATANG 项目系列科学文章的发表

2）提出了一种新技术，用于从高度混合的图像中测量多波段的“超级分离”（super-deblended）光度测量，并将其应用于 GOODS 北场的赫歇尔和地面远红外（FIR）和（亚）毫米（mm）数据。

完成了 JCMT 大项目 MALATANG 中关于星系 NGC253 的数据处理和分析，探讨了致密气体发射在星系中心 kpc 尺度内的性质，发现致密气体的空间分布具有非常聚集于中心的性质。准备成文中。

本年度的科研工作一方面是完成一篇 MALATANG 项目系列科学文章的发表，另一方面是关于极亮红外类星体寄主星系的分子气体观测研究取得一些进展，目前正在准备 ALMA 观测数据的分析和文章撰写。此外，在 2018 年 3 月份的 IRAM 观测申请，作为 PI 成功申请到 NOEMA 观测时间，并于同年 10 月份前往法国 IRAM 总部 Grenoble 学习完成数据的处理和初步分析。

焦倩用 Herschel 空间望远镜对近邻星系中的[CI](1-0)和[CI](2-1)成图观测数据，结合 CO(1-0)、尘埃连续谱数据等，完成了在 kpc 分辨率上对于近邻星系[CI]示踪分子气体能力的研究分析，目前文章在准备投稿中。

姜燕参与的项目对 24 个 CHANG-ES 星系利用 IRAM 30 米进行 12CO（1-0）、13CO（1-0）、和 12CO（2-1）观测，目前观测完了 10 个源，并且都观测到了 12CO(1-0)、13CO（1-0）、和 12CO（2-1）三条谱线，只有少数源观测到了 C18O（1-0）发射。3 个源的数据已经处理完成。

进一步完善了之前关于 Perseus 分子云中年轻星体（YSO）的 LAMOST 光谱研究的工作。为了发挥 LAMOST 海量光谱数据的优势，我们进一步在 LAMOST 的光谱数据库中进行了搜寻，我们发现在 Perseus 分子云中还存在一批有发射线但是却没有被红外研究证认为 YSO 的源，这一部分工作也基本完成，正在充实之前的文章，并准备投稿。在认真检查过找出的光谱后，我们发现存在一些非常特殊的源，他们的光谱中只有发射线，并且发射线很强，对这些源的进一步分析以及对更大样本的搜寻工作正在进行中。

另外，我们开展了关于银河系分子云尺度上恒星形成定律的研究工作。主要研究已经存在的恒星对恒星形成过程的影响，因为对于河外星系的研究已经表明了当前的恒星形成活动不止受到气体含量的影响，也受到已经存在的恒星的引力势的影响。我们通过对银河系分子云尺度上的恒星形成定律的研究，来分析延展的施密特定律可以适用到什么样的尺度上，以此来了解恒星形成过程，以及恒星形成过程中的反馈作用。通过我们目前对近邻（500 pc 以内）的低质量恒星形成区的研究发现，考虑已存在的恒星之后，确实能让恒星形成定律的关系更为紧密。我们正在将这一结果扩展到更大的样本，包含更多的恒星形成环境（大质量恒星形成、小质量恒星形成）。

我们利用 WISE 尘泡巡天数据，在 30°≤ l ≤ 40°、距离≤ 5.5kpc 范围内筛选出了 18 个符合条件的电离氢区。借助 Herschel 空间红外望远镜的巡天项目 Hi-Gal 的数据证认了 171 个电离氢区致密分子云壳层附近的分子云团块。结合多波段望远镜巡天项目数据(2MASS, GLIMPSE, WISE, MIPSGAL, SCUBA2, ATLASGAL, BOLOCAM, MAGPIS, VGPS 等)统计了这些团块的物理性质,如团块的尘埃包层质量,尘埃温度,光度等等。通过速度-位置图、分子团块随归一化电离氢区半径的分布、演化轨迹图(L-M diagram)等方式，我们讨论了电离氢区对周围分子云核及下一代恒星形成的触发作用。另外，通过质量-半径关系图(Mass-Radius diagram)我们对 HII 区周围触发大质量恒星形成进行了简单讨论。

2-05 分子云与恒星形成研究团组

1）发现云云碰撞触发中低质量恒星形成的理想候选体

2）通过近红外偏振测量获得了环形分子壳层上的磁场方向和强度

1. “银河画卷”计划取得重要科学成果。云云碰撞是恒星触发形成的一种重要机制，然而迄今为止在观测方面可以用来深入研究该机制的候选对象并不是很多，而且已知的云云碰撞案例中绝大多数是伴随着大质量恒星形成的，却鲜有只触发中低质量恒星形成的例子。利用“银河画卷”谱线巡天数据发现：位于仙王座气泡（Cepheus bubble）边缘的分子云复合体 L1188 由两个几乎相互垂直的长条形分子云 L1188a 和 L1188b 组成，而且在两个分子云交叉的区域内的分子气体具备云云碰撞所可能表现的各种典型运动学特征。结合在交叉区域增强的年轻星分布特征，推断出其中的恒星形成很可能是通过发生在大约一百万年前的一场云云碰撞所触发的。进一步的研究还发现，该分子复合体中的云核都不足以形成大质量恒星，从而使 L1188 成为不可多得

的研究云云碰撞触发中低质量恒星形成的理想候选体，有待进一步高分辨率的研究。研究团队已经分别获得 IRAM-30 米和 JCMT-15 米毫米波望远镜的观测数据，将对其中的分子云核特性和恒星形成触发过程开展深入研究。论文发表在 Astrophysical Journal Letters 上。2017 年度分子云与恒星形成团组负责完成了“银河画卷”计划约 60 平方度天区的观测、数据检查和数据入库，为“银河画卷”计划的最终完成以及 2018 年度的科学研究奠定了良好基础。

2．大质量恒星形成研究取得重要进展。通过近红外偏振测量获得了环形分子壳层上的磁场方向和强度，发现磁场方向受到膨胀气体的挤压，形成与环形分子壳层平行的结构，磁场强度得到明显增强。研究结果显示，环形分子壳层上得到增强的磁场强度能够显著减弱由大质量恒星引起的触发恒星形成活动。论文发表在 ApJ。对位于 M17 中的一个热分子核的红外对应体进行了细致的研究。该热核的红外对应体与数个水脉泽斑相关，在其周围没有发现 I 型和 II 型甲醇脉泽。结合已经发表的 VERA 的三角视差观测发现这些水脉泽斑的自行运动相对于这个红外对应体呈现向外膨胀的运动，说明该区域可能存在分子外流以及盘吸积过程。这些观测证据说明热核的红外对应体很有可能是一个正在吸积物质的大质量原恒星。

3．原行星盘结构和演化研究取得系列重要成果。通过国际合作，对 HL Tau 原行星盘的 ALMA 和 VLA 观测资料做了细致的辐射转移模拟，限制了盘中尘埃亮环的性质并找到了早期行星形成过程的证据。论文发表在 A&A 杂志。通过细致的参量空间研究，分析了盘的张开程度和标高等关键结构参量如何改变能谱分布的整体形态，并以此提出了一个挑选发生尘埃生长和沉降原行星盘的实用判据。研究结果发表在 Ap&SS 杂志。成功申请到国际 IRAM 30 米望远镜对 Taurus 恒星形成区中 2 个原行星盘的毫米波观测，用于更好地限制盘的结构以及研究盘中早期行星形成过程。发展了用于分析即将到来的 JWST 原行星盘光谱数据资料的工具，研究盘的化学结构。

2-06 毫米波和亚毫米波技术实验室

主要包括：1）面向南极 5 米太赫兹望远镜的国家基金委重大基金项目“极端台址环境下的天文望远镜关键技术方法研究”相关课题、以及天文财政专项支持的相关课题通过结题验收；2）载人航天工程 2 米多功能光学设施的高灵敏度太赫兹探测模块初步完成关键技术攻关以及原理样机集成；3）国家重大科研仪器研制项目（课题）“多波段多大气成分主被动综合探测系统--太赫兹辐射波谱仪”通过结题验收；4）国家重点研发计划项目“射电技术方法前沿研究”启动实施，重点研发计划项目（课题）“光子数可分辨超导相变边缘单光子探测器及其读出电路”持续开展；5）中科院先导专项项目（课题）“阿里台址 CMB 观测条件评估与阿里 1 号辅助标定研究”持续开展，中科院重点支持仪器研发项目“超导探测器及系统研发团队”启动实施。

1）国家重点研发计划项目“射电技术方法前沿研究”成功立项并启动实施；

2）南极 5 米太赫兹望远镜关键技术深化研究取得实质进展。

1）南极 5 米太赫兹望远镜关键技术深化研究方面，完成了基于 Nb/NbN 混合超导隧道结的 450 微米波段和 350 微米波段超导 SIS 混频器的优化设计与芯片制备及初步性能表征；采用级联波束分离器本振信号分配技术和直流偏置复用技术，实现了 200 微米波段两像元超导 HEB 接收机的原理验证；完成了望远镜控制架构原型、低功耗大容量存储系统原型样机和低带宽条件下信息传输系统原型研制。此外，太赫兹量子级联激光器与超导 HEB 热电子混频器集成接收机技术实现了进一步突破，2.5 THz 实测噪声温度优于 1000 K（相当于 8 倍量子噪声极限），表征稳定性的 Allan 时间超过 5 秒。

2）载人航天工程 2 米多功能光学设施的高灵敏度太赫兹探测模块研制方面，完成太赫兹模块热接口件、电接口件研制以及与主光机的联调；完成针对法国 Air Liquide 公司的制冷机方案设计与接口协调；启动氮化铌超导隧道结混频器芯片制备关键技术攻关，实现氮化铌超导薄膜转变温度≥15K 的技术指标，并完成首批超导隧道结混频器芯片的制备；完成太赫兹模块原理样机研制与集成，初步开展原理验证测试。

3）国家重大科研仪器研制项目（部门推荐）“多波段多大气成分主被动综合探测系统”的“太赫兹超导辐射波谱仪”课题顺利通过结题验收。太赫兹超导辐射波谱仪于 2017 年 10 月运抵西藏羊八井观测站进行现场联调，2018 年 4 月基金委组织专家进行了现场技术指标测试，2018 年 6 月 13 日在北京通过了项目整体验收。该课题完成了项目任务书规定的研制内容，所有技术指标均验收合格。

4）国家重点研发划项目“射电技术方法前沿研究”启动实施，其中承担的课题 1 开展了 350 微米波段超导隧道结混频器芯片优化设计、0.78-1.55 THz 超宽带超导热电子混频器平面天线及集成透镜优化设计、以及 450 微米波段基于傅立叶分光器的 1×4 本振信号分配光栅研制与特性初步表征。国家重点研发计划项目（课题）“光子数可分辨超导相变边缘单光子探测器及其读出电路”方面，设计并制备了 1550 nm 光学腔体，理论仿真与实测结果吻合；研制了基于钛膜的超导相变边缘单光子探测器，并集成 1550 nm 波长介质反射镜，采用单模光纤正面对准，实测响应时间达微秒量级，实测系统探测效率达到 30 %。

5）中科院先导专项项目“阿里台址 CMB 观测条件评估与阿里 1 号辅助标定研究”课题方面，完成了太赫兹傅立叶光谱仪升级改造，包括阿里 CMB 台址大气透过率测试所需高温定标黑体维护与标定、太赫兹傅立叶光谱仪底座改造等。基于 MPI 型太赫兹傅立叶光谱仪实测了阿里 CMB 台址大气透过率，并与气象 MERRA2 卫星观测数据进行了比对分析。太赫兹傅立叶光谱仪实测结果显示：阿里 CMB 台址冬季最

低可沉降水汽含量（PWV）可优于 0.5 毫米，实测结果与气象 MERRA2 卫星观测数据很好吻合。此外，基于气象 MERRA2 卫星观测数据，系统分析了我国西部地区长周期（5 年以上）可沉降水汽含量（PWV）的分布规律。

6）顺利完成太赫兹超导探测器研制平台一期搬迁及设备调试，开展铌（Nb）超导隧道结器件制备，并重点开展了基于氮化铌（NbN）的超导隧道结混频器芯片和基于氮化钛（TiN）的超导动态电感探测器制备。

2-07 德令哈毫米波观测基地

13.7 米望远镜全年开机运行 321 天，其中对外开放课题观测 319 天。2018 年度新受理课题观测申请 26 件，安排国内外申请的课题观测 32 件，完成 CO、HCO+、CH3OH 等分子谱线的课题观测。2018 年度望远镜平均每天扫描 1.5 平方度的天区。2018 年度无论在设备运转、开放课题观测时间，还是在设备稳定运行、数据产出量方面，继续保持历史高位，数据质量则有更大提高。2018-2019 观测季节的开放课题观测从 2018 年 8 月 15 日开始。

基地运行的 13.7 米毫米波射电望远镜采用工业数字照相摄影测量系统，以 EL=52° 为基准位置，对天线面板进行测量，并根据测量结果，进行面板预置调整，调整后的天线面板精度 RMS 为 78μm（清洗了天线主面面板）。今年对主面方位和俯仰电机、高速箱、传动箱进行检修、加润滑油；对主面方位和俯仰大齿轮进行清洁、加润滑油；副面机械系统检修（电机、联轴节、减速箱、蜗轮蜗杆检查、加润滑油）。装配高速箱和传动箱时加入了电机电流监测环节，保证零件装配良好。方位 AZ2（北面）电机的传动箱输入轴更换新轴。对接收机系统所有设备进行了检修，部分老化设备进行了更换和更新。其中：①Beam3、Beam6 混频器采用新的 BiasT；②Beam3、Beam6、Beam8、Beam9 采用新混合电桥；③本振倍频器用 AFM-6-110-13（75~113GHz）倍频器换下使用 8 年的 AFM-x6-110（87~113 GHz）倍频器[15]。④结合杜瓦回温过程中出现的突变现象，更换部分 HEMT 放大器，Beam9（LSB）用 L003 型号 HEMT 换下 376D HEMT 放大器；⑤维护杜瓦内部分老化的偏置电缆、刚性电缆。⑥进行 TRX/IRR 测试，经过接收机噪声温度 Trx 测试和波束测量后，安装微波小车，以及天线调平衡等。⑦仪器除尘，FFTS 板卡芯片重新涂抹散热硅胶，更换制冷机，压缩机换气提高氦气纯度，压缩机前增加空调等。截止到 2018 年年底，“银河画卷计划”巡天工作完成 7364 个巡天单元（总共 10941 个单元，每个单元 30′×30′大小，完成 67.3%），包括 M17, Aqualia Rift, Cygnus X, W3/W4/W5, GEM OB1, Monoceros Nebula, Maddalena Cloud, 和 Califirnia Cloud 等比较有名的天体目标，对其中的分子云演化和恒星形成过程进行了研究，数据质量完全符合科学家的要求，彰显了“超导成像频谱仪系统+OTF 观测模式”的强大威力。

中国科学院紫金山天文台“银河画卷”巡天团队利用 13.7 米毫米波射电天文望远镜的 CO 分子谱线数据，对 Rosette 分子云进行了 CO J=1-0、13CO J=1-0、C18O J=1-0 三条谱线的观测研究。得到了目前为止对该区域最大尺度的分子云成图观测图像。该工作详细研究了大质量星团 NGC 2244 周围分子云的空间形态，物理性质和运动学特征，展示了该区域大质量恒星对周围分子云的反馈影响。此外，在 Rosette 分子云的背景上，我们还发现了 73 个速度更高的分子云团块，其中距离最远的为 11 kpc，位于外旋臂上。首次在这个区域发现了距离相近但物理性质完全不同的两组巨分子云，其中一块分子云的温度和线宽较高，研究显示这块分子云受到了电离氢区的反馈影响；而另一组分子云则未受到显著的反馈作用。该研究结果近日以“A Large-scale Survey of CO and Its Isotopologues toward the Rosette Molecular Cloud”为题发表在国际天文学期刊 ApJS 上（http://ads.bao.ac.cn/abs/2018ApJS..238...10L）。

中国科学院紫金山天文台研究团队利用 13.7 米毫米波射电天文望远镜的所获得的 CO 分子谱线搜寻了 Gem OB1 分子云复合体及其附近(银经为 180-190 度)的分子外向流，并且一共找到了 198 个分子外向流候选体。相关研究成果发表在 ApJS 上了，链接为 http://adsabs.harvard.edu/abs/2018ApJS..235...15L。这一成果为研究恒星形成提供了大量的样本，也同时为从大尺度上研究恒星形成与周围环境的相互作用奠定了基础。同时还注意到比较强的外向流多分布在 HII 区附近，另一方面 HII 区附近都有分子外向流的分布。这些反映 HII 区很有可能在与周围的环境作用的过程中促使新的恒星的形成。所有的这些都为大质量恒星形成及其与周围环境的相互作用的研究提供了一个大的样本并为此创造了条件。

中国科学院紫金山天文台“银河画卷”巡天团队利用 13.7 米毫米波射电天文望远镜的 CO 分子谱线数据，对银河系内的分子气体进行了广泛对研究和分析，得到恒星诞生与分子气体中，当恒星死亡时会对其周围的分子气体环境产生剧烈的影响。这些剧烈的天体物理过程是我们理解恒星演化、研究星际介质循环独一无二的对象。在分析 SNR W50（SS433）的时候，利用巡天数据，发现了距离银道面约 400 pc 的分子云与 W50 成协，并且与 SS433 的相对论性喷流的运动学性质一致；结合该天体的中子星 - 黑洞演化模型，计算出其演化时标约 10^5 年，与分子气体的运动学时标相当；进一步地，结合分子气体从高密、高温、高压环境下快速形成的理论，计算出该分子气体的形成时标小于等于 10^5 年，佐证了该团队的推断——该高银纬分子气体与 SS433 的相对性喷流相关。该文章发表在 ApJ 杂志上：http://adsabs.harvard.edu/abs/2018ApJ...863..103S。

南京大学研究团队利用 13.7 米毫米波射电望远镜在 Fermi-LAT 7.6 年的观测数据中，本课题利用中国科学院紫

金山天文台毫米波射电望远镜观测的 CO 分子谱线数据，对超新星遗迹（SNR）CTB 87 及其附近的分子云（MC）进行了形态学及动力学上的研究。通过对 13CO、12CO 同位素 J=1-0 谱线辐射的研究,发现在该超新星遗迹的东部及南部沿着视线方向存在分子云。结合对于分子云谱线的动力学分析的结果，该团队建议这个超新星遗迹与系统速度为 -60 到 -54km/s 的分子云成协。这一结果暗示了在该方向上看见的伽马射线辐射或许存在一定比例的强子起源成分。这有益于明晰宇宙线通过超新星遗迹激波加速的相关理论。同时，研究团队通过进一步结合 21cm HI 气体分布、WISE 红外观测，以及光学消光图像的结果，发现该超新星遗迹很可能位于一个由几十个 OB 星组成的 OB 星协吹出的巨大星风泡当中。相关的工作发表在 ApJ 杂志上(2018ApJ...859..173L)。

云南大学研究团队利用中国科学院紫金山天文台 13.7 米毫米波射电望远镜对位于金牛座的 L1495 纤维状分子云中的普朗克冷核进行了 CO 分子及其同位素 13CO 和 C18O 的谱线观测研究。基于紫金山天文台的 CO 及其同位素数据，研究了 L1495 分子云中 16 个普朗克冷核的性质。在这 16 个普朗克冷核中证认出了 30 个高密度的冷尘埃核。基于 13CO 的观测结果，发现所有的尘埃核都是湍动支撑的，且内部湍动几乎都为超音速湍动。C18O 的观测数据表明。在普朗克冷核中使用 C18O 计算得到的位力质量明显受到 CO 耗空效应的影响(即一氧化碳分子在致密的尘埃冷核中被冻结在尘埃颗粒表面)，所以不能很好的示踪尘埃冷核的内部结构。因此该团队认为在这种冷而致密的恒星形成早期环境中 C18O 并不能做为研究位力参数的有效工具。对所有观测到 C18O 发射的区域，基于 LTE 假设计算了其 C18O 的丰度，并与 non-LTE 假设下 "RADEX" 的计算结果进行比对，发现基本一致。基于两种计算的结果，发现 C18O 丰度与氢柱密度之间存在明显的反相关关系。这表明在类似于普朗克冷核这样的恒星形成极早期环境中，一氧化碳存在严重的 CO 耗空效应，这种效应在 L1495 的所有尘埃核中都被探测到。我们基于这些尘埃核的 C18O 丰度，计算得到了每一个尘埃核的 CO 耗空系数。根据每一个尘埃核所处的演化阶段，对其进行了分类，最后的结果发现 CO 耗空系数不仅仅与尘埃核的氢柱密度存在反相关关系，还与尘埃核所处的演化阶段之间存在着明显的反相关关系。这就表明 C18O 的丰度可以很好的示踪尘埃核所处的演化阶段。本课题相关的所有结果都已经发表在天体物理期刊 Astrophysical Journal 上（2018ApJ...856..141T ）。

围绕 13.7 米毫米波射电望远镜的建设、技术创新，成就出一批活跃在国际学科前沿的有影响的科研骨干。他们在使用基地望远镜的同时，积极申请其他国际一流望远镜，如德国 Effelsberg100m，日本 Nobeyama45m，美国的 VLA、VLBA 以及欧洲的 EVN 等的观测，做出了许多国际一流工作。

三峡大学是国家水利部和湖北省人民政府共建大学，教育部"卓越工程师教育培养计划"高校，水利电力特色与优势明显，是一所综合办学实力较强、享有一定社会声誉的综合性大学。为促进我国天文学及相关学科的发展和高层次天文研究人才的培养，经协商， 2018 年 10 月，三峡大学与紫金山天文台在青海观测站联合共建大学生实习实训基地，并完成了一批次三峡大学学生在本站的实习学习工作。

继续围绕着 1.2 米量子卫星专用望远镜，为中国科学技术大学"量子"团队和"天文"团队做好后勤保障工作，顺利完成了 1.2 米量子卫星专用望远镜镀膜工作，在交通、电力、网络等方面给予大力的支持，保障该望远镜各项科研工作顺利开展。

在中国 SONG 项目团队的精诚合作下，项目已经取得巨大进展：50BiN 双筒望远镜观测了包括疏散星团、食双星、超新星等； SONG 1 米望远镜与丹麦 SOONG 1 米望远镜成功实现了联合观测，对 Gamma Cephei，Gamma Per 等 10 余颗恒星进行联合时域观测，已完成数据处理，获得前期科学结果。完成西华师范大学天文系大学本科生 1 批次实习工作。

作为青海省爱国主义教育基地和科普教育基地，依靠 13.7 米射电望远镜、天文展板长廊、SONG 项目、1.2 米量子望远镜等设备宣传科普知识增强我站的综合实力和知名度，为提高全州地区及全省的科学文化素质、辐射带动旅游建设做出新的贡献。根据国家、台本部、青海省、海西州政府的要求积极参加各种科普活动。完成了澳门科学技术发展基金会组织的 "2018 青海-天文-地质科普夏令营" 活动；青海观测站科普部组织相关人员在德令哈市区举办了大型 "蓝血月" 活动。2018 累计接待科研院所、科技团组、夏令营、旅游团等 700 人次。

在台基建处领导的指导下，完成 2017 年度《青海观测站科研辅助用房修缮项目》验收、1.2 米量子卫星专用望远镜观测楼基建综合本验收、2019 年度《青海观测站专用道路及站区围墙改造项目》申报等基建工作。近几年通过修缮项目的实施，极大地提高了青海观测站的竞争实力，使得青海观测站科研平台基础能力有了大的提升，为观测站承担高水平的科学研究提供基础支撑保障。

2-08 星系形成与大视场巡天团组

在 2018 年，团组有固定成员两名，研究生 5 名，围绕星系形成和大视场巡天研究方向，面向 135 规划中的南极天文的大视场巡天科学需求，

1) 与中科大合作推进大视场巡天望远镜 (WFST) 项目，入选中科大双一流学科建设项目，通过科技融合方式共建；

2) 开展国内国际合作研究，培养人才队伍，培养毕业博士研究生 1 名，发表论文 12 篇 (见成果总结和文章列表)；

3) 面向南极天文台设备的科学目标需求，在星系形成研究方向，取国内外望远镜观测时间，开展前沿观测研究工作：

（a）上半年获取两个 z=2.24 的原初星系团结构的 JCMT/SCUBA2 850 微米成图观测，探测其中的亚毫米波星系。由于天气原因，只获得原定计划的 1/3 的数据；（b）与智利大学合作者 Valentino Gonzalez 副教授联合申请获得 Magellan 望远镜 4.5 晚和 Gemini 望远镜 24 小时的观测时间，用于证认 z=4.7 高红移[OII]发射线星系和 z>3 的宁静星系，研究其物理性质；（c）与智利大学合作者 Lira Paulina 教授联合申请获得 Gemini 望远镜 22 小时的观测时间，开展 z<1 的 heavily obscured QSOs 的光谱证认和研究工作；（d）获得东亚天文台 JCMT / SCUBA-2 的 2019 年上半年 29.5 小时观测时间，对高红移原初星系团的亚毫米波星系探测研究；

1. 安芳霞等（2018, ApJ, 862, 101）发展了一套利用机器学习的方法用来证认单天线探测到的亚毫米源的多波段对应体 （An F.X. et al. 2018, ApJ, 862, 101）：亚毫米星系是大质量，被尘埃遮蔽的星暴星系，是低红移处的大质量椭圆星系的前身星系。由于单天线亚毫米望远镜的分辨率非常低，一般为 10-30 角秒。这是对亚毫米源的准确多波段证认，是进行后续分析，以及研究其与其它星系演化关系的瓶颈。我们利用目前最大的亚毫米、毫米干涉阵（ALMA）探测到的高分辨率的亚毫米星系以及 UDS 场的多波段数据发展了一套机器学习的方法用来证认单天线探测到的亚毫米源的多波段对应体。我们首先利用 ALMA 探测到的亚毫米星系以及其多波段的特性建立了一个训练样本，我们结合机器学习的方法来分辨训练样本中亚毫米星系和非亚毫米星系的区别。我们首先利用训练样本对我们的方法做了一个自我测试，发现我们的方法可以证认出 87%的 ALMA 探测到的亚毫米星系。接着我们将方法应用到另外一个完全独立的，同时具备单天线亚毫米观测以及 ALMA 观测的场（ECDFS），证认出了 80%的 ALMA 探测到的亚毫米星系。这说明我们的方法可以成功证认单天线亚毫米源的多波段对应体。我们计划将我们的方法应用于那些还没有被亚毫米干涉阵观测或者不在亚毫米干涉阵观测范围内的单天线亚毫米观测样本，从而得到一个统计上足够大的亚毫米星系对应体的样本用来研究亚毫米星系的形成与演化以及它和其它天体的演化关系。

2. 大视场巡天望远镜的探测器响应和滤光片优化（Shi D.D. et al. 2018, 天文学报，59, 22）：大视场巡天望远镜(Wide Field Survey Telescope, WFST)是采用主焦式光学设计、2.5 m 口径、具备强大巡天能力的望远镜，可以开展大规模图像巡天，用于刻画银河系和近邻宇宙的组成和结构、普查太阳系天体和外部构成、开展时域天文监测等科学研究工作. 结合大视场巡天望远镜光学系统的透过率、西藏阿里站址的大气透过率和冒纳凯阿台址的天光发射谱，比较不同电荷耦合器件(Charge Coupled Device, CCD)量子响应曲线、读出噪声和不同曝光时间情况下，不同类型天体在 u、g、r、i、z 和 w 波段的能谱响应，分析各个波段测光信噪比，优化确定 CCD 响应曲线和用于太阳系天体巡天的白光滤光片(w)设计. 分析结果显示: 蓝敏 CCD 对探测超新星等高能爆发暂现源有优势，但在 r、i、z 波段效率降低，从而降低这些波段的巡天探测灵敏度. 光学宽带 CCD 响应曲线兼顾蓝端和红端能谱响应，在相同观测时间内，可以实现比蓝敏 CCD 更高的巡天灵敏度. 采用宽带 CCD 响应曲线，结合估算的 WFST 系统光学成像效率及站址的天光和消光，计算给出了巡天观测对太阳系天体(G2V 恒星光谱)、椭圆星系(E)、漩涡星系(Sbc/Scd)、不规则星系(Im)、类星体、I 型和Ⅱ型超新星的探测灵敏度. 通过调节 w 波段的带宽和中心波长，可以实现对不同类型天体的能谱响应信噪比最大化. 综合比较，确定 w 滤光片的优化设计波长范围为 367-795 nm. 最后，计算给出了各波段长期巡天图像数据叠加的探测灵敏度随曝光时间的变化曲线.

3. 大质量恒星形成星系气体内流和外流的演化研究（Pan Z.，et al 2019， in press）:像银河系这般的大质量恒星形成星系如何从早期宇宙演化至今是星系形成演化的核心课题。这一工作研究了近邻宇宙中银河系质量（1010.7 太阳质量）大小的恒星形成星系的气体内流速率和外流速率从红移 1.3 以来的演化。假设前身星系在不同红移时都是一个典型的恒星形成星系，我们就可以回推银河系在不同红移时应该有多大的质量。根据星系的质量—恒星形成率关系，我们可以推断前身星系的分子氢气体质量。我们发现银河系的恒星质量增长要显著慢于恒星+气体总质量的增长。有了恒星+气体总质量随时间的增长曲线，我们可以得到星系的净吸积率随时间的演化。我们发现在最近的 30 亿年里，星系的净吸积率要比恒星形成率低 5-12 倍，这说明星系气体吸积率的显著降低是恒星形成熄灭的主要原因。我们还发现恒星死亡带来的气体回馈对维持星系的恒星形成率起到显著作用。

4. 恒星形成星系尘埃遮蔽普适关系的研究（Qin J.，et al 2019, MNRAS, submitted）：宇宙中尘埃在重子物质中的质量占比只有约 5%左右，但是由尘埃在远红外波段的热辐射占宇宙所有天体电磁辐射能谱总能量的一半。研究尘埃热辐射与星系中恒星形成活动参数等的关联规律，对认识星系形成和演化意义重大。这一工作中，我们用一个近邻恒星形成星系样本研究星系尘埃遮蔽参数（红外与紫外光度比值 IRX）与星系的恒星质量、恒星形成率、金属丰度、红外光度、半光半径等参数的相关关系，验证 IRX 与这些参数及红外光度面密度相关，这些相关关系很大程度上是由星系恒星质量主导的标度关系（scaling relation）衍生的。由于盘星系的投影造成视线方向消光变化进而影响紫外光度，几何参数轴比 b/a 也与 IRX 存在相关。 通过分析发现，IRX 的变化由红外光度、半光半径、轴比和金属丰度共同参与的多参数幂律关系决定，与恒星质量无关。我们同时发现高红移的各类恒星形成星系同样满足这一 IRX 幂律关系，表明这一相关关系具有普适性，可以作为星系尘埃成分的基本标度关系，成为星系演化图象的关键组成部分。我们发现的这一尘埃遮蔽普适关系表明，星系中 IRX 由恒星形成率、星系尺度

和金属丰度共同决定，与星系恒星质量无关。金属丰度在IRX的相关关系中发挥决定性的因素。

2-09 高能时域天文团组

本团组围绕我台 135 规划三大突破之一“中国南极昆仑站天文台”（在建）和 5 个重点培育方向“高能天体物理”，本年度主要从事伽玛射线暴、引力波事件、快速射电暴、脉冲星的相关研究，以及开展了宇宙学方面的研究工作。作为第一完成人的“高精度检验相对论基本假设”和作为共同完成人的“引力波电磁对应体观测与理论取得重要进展”和“TG-2 POLAR 伽马暴偏振测量”，均入选科技部 973 项目“伽玛射线暴与相关前沿物理研究”项目结题验收的 3 个代表性成果。

国际学术交流与科研合作：（a）借助中澳天文联合研究中心和 SKA 国际合作平台，通过博士研究生国际合作培养计划，选派张松波同学赴西澳大学，在国际射电天文研究中心(ICRAR) 的科学主任 Lister Staveley-Smith 教授指导下，利用帕克斯望远镜（Parkes）、澳大利亚平方公里阵列（ASKAP），默奇森射电阵列（MWA）等，开展 SNR 1987A 脉冲星搜索、已知脉冲星单脉冲、旋转射电瞬变源（RRAT）、快速射电暴（FRB）和射频干扰（RFI）观测与研究工作。（b）邀请美国宾州州立大学博士生杨光 5 月 21-24 日来访并做题为“What drives the growth of black holes?”学术报告；邀请美国里海大学博士生药新雨 6 月 27-29 日来访并做题为“Precovery of TESS Single Transits with KELT”学术报告；邀请瑞典斯德哥尔摩大学李亮博士生 7 月 3 日至 8 月 10 日来访合作交流；邀请意大利 ICRANet 天体物理实验室李亮博士 11 月 5 日至 12 月 4 日来访合作交流。（c）本年度本团组与国际合作发表 SCI 论文 13 篇。

1、首例引力波电磁对应体理论研究取得重要进展（亮点工作一）

2017 年 8 月 17 日，激光干涉引力波天文台（LIGO）探测到首例双中子星并合引力波事件，随后又探测到伴随的短伽玛暴 GRB 170817A 与多波段余辉辐射以及千新星。这是继 2015 年 9 月人类首次直接探测到引力波之后，历史上第一次发现引力波的电磁对应体，是多信使天文学的重大里程碑。同时，其电磁对应体 GRB 170817A 的发现，对于长期以来广泛被接受的短伽玛暴起源于双中子星并合的理论给出了直接的证据。吴雪峰及其合作者对首例双中子星并合引力波事件进行了系统深入的数据处理、分析和理论研究。我们对该引力波事件的电磁对应体，即伽玛暴 GRB 170817 和多波段余辉，进行了数据分析和理论解释，发现 GW170817 具有结构化喷流，并合产物更可能是一颗典型磁场强度、大质量、毫秒自转的中子星，相关工作发表在 Nature Communications（1 篇）、ApJL（1 篇）和 ApJ（2 篇）。

吴雪峰及其合作者对该引力波事件在伽玛射线波段的瞬时辐射展开了全面的分析和研究。通过分析光度变化的精细结构和能谱，发现这是一个光度异常低的短伽玛暴，提出这样的观测只能由偏轴的结构化喷流或类似结构产生，同时还指出这一超低光度的短伽玛暴预示着由双子星并合产生的伽玛暴的发生率远高于人们之前的预期（Zhang et al., 2018, Nature Communications, 9, id. 447）。短伽玛暴辐射机制的研究，一直是伽玛暴研究领域中非常重要的前沿热点课题。GRB 170817A 有一个显著特征，即瞬时辐射明显分成主脉冲与弱的尾巴两个时期，且弱的尾巴时期的辐射能谱呈现为近似黑体的形状。基于上述特征，蒙延智、吴雪峰及其合作者提出了来自结构化喷流的偏轴观测的光球辐射模型来解释这个暴瞬时辐射的能谱特征，很好地解释了这些特征（Meng, Geng, Zhang, Wei, Xiao, Liu, Gao, Wu*, et al., 2018, ApJ）。另外，吴雪峰、蒙延智及其合作者对于 170817A 在 X 射线、光学以及射电波段的余辉晚期增亮，发现可以用来自于暴中心的长寿命中子星的包含正、负电子对的星风与更早的抛出物之间的相互作用来比较好地解释（Geng, Lin, Dai, Huang, Wu, Li, Li & Meng, 2018, ApJL）。尽管目前国际上对于 GW170817 的并合产物还未有定论，但是我们结合 GW170817 的引力波与多波段电磁数据（伽马射线、X 射线、光学和射电），对并合产物的性质进行了限制。我们发现，如果 GW170817 的并合产物为中子星，则此中子星需要满足高速旋转（毫秒周期），且磁场不能太大（小于 10^12 G）（Ai, Gao, Dai, Wu, Li, Zhang & Li, 2018, ApJ）。

2、伽玛暴及余辉的研究进展

开展了“三胞胎”伽玛暴 GRB 160625B 的观测与理论研究（Zhang, et al 2018, Nature Astronomy, 2, 69）。GRB 160625B 的伽玛射线波段的光变曲线，完美诠释了伽玛暴γ波段辐射的完整组成：前兆辐射、瞬时辐射和延展辐射。吴雪峰和合作者通过对 GRB 160625B 时间分辨谱和多波段观测数据的详尽分析，指出这类由前兆辐射、瞬时辐射和延展辐射按照演化序列构成的完整伽玛暴可能具有一定的普遍性，因此 GRB 160625 可能是对人们深刻理解伽玛暴物理的一个非常关键的“原型”伽玛暴。

对伽玛暴 GRB 081221 瞬时辐射进行了详细数据分析和理论研究，发现该暴的瞬时辐射起源于光球的多色黑体辐射（Hou, Zhang, Meng, Wu, et al., 2018, ApJ）。伽玛暴的辐射机制是发生在光球的热辐射还是来自光薄处的同步辐射，是伽玛暴研究中极其重要却未被彻底解决的疑难问题。吴雪峰、蒙延智及其合作者通过对 GRB 081221 的时间积分光谱以及时间分辨光谱进行了详细分析，发现这个暴的光谱可以用光球辐射来更好地加以解释。这个暴的时间积分光谱可以用多色黑体来很好地拟合，不同的温度被认为来自不同的辐射半径或者观测角度。而这个暴的时间分辨光谱也可以用多色黑体来很好地拟合，甚至时间间隔取得足够小的话，可以用一系列的单色黑体来很好地拟合。这个工作是目前对

伽玛暴光球辐射从数据上和理论上研究的非常详细的一个案例，是对相当一部分伽玛暴瞬时辐射起源于光球的一个重要观测支持。

提出伽玛暴低能谱指数可以用冷却电子的同步辐射解释（Geng, Huang, Wu, Zhang, & Zong, 2018, ApJS）。吴雪峰和合作者开发了一个数值计算程序，用给定的初始参数计算电子分布的演化，综合考虑三个冷却过程（即绝热、同步辐射和逆康普顿冷却）和衰减磁场的影响。我们通过探索合理参数空间，给出了一系列结果。我们的结果表明伽玛暴低能谱指数较硬可以归因于内激波模型中同步自康普顿冷却，或者在磁化喷流中衰变的同步辐射冷却。这两种机制可以通过观察一些伽玛暴中孤立短脉冲的低能谱来区分。

基于ROTSE-III观测得到的伽玛暴光学余辉早期辐射流量上限开展伽玛暴喷流性质和暴周环境的限制（Cui, Zou, Wei, Zheng, & Wu*, 2018, MNRAS）。伽玛暴的早期余辉携带了非常重要的信息，包括伽玛暴相对论喷流的初始速度（洛伦兹因子）、伽玛暴暴周环境的密度分布（均匀介质、星风）和大小。吴雪峰、魏俊杰和合作者基于伽玛暴外激波的正反模型，对 ROTSE-III 观测到的 36 个伽玛暴早期光学辐射流量上限，给出了相对论喷流初始洛伦兹因子的范围限制，以及介质种类和密度大小限制。

利用 Swift 卫星观测到的伽玛暴 X 射线平台对伽玛暴中心引擎进行限制（Li, Wu*, Lei, Dai, Liang, & Ryde, 2018, ApJS）。X 射线平台是 Swift 上天后的重要发现，一般认为起源于中心引擎的持续能量注入。伽玛暴中心引擎主要有 2 类：快速旋转的黑洞，和快速自转的强磁场中子星（磁星）。吴雪峰和合作者系统地分析了 101 个 Swift/XRT 观测到的伽玛暴 X 射线平台，并假设 2×1052 尔格作为磁星能提供的最大能量，超过这个能量，则伽玛暴的中心引擎更有可能是黑洞。在这 101 个伽玛暴中，我们发现 9 个伽玛暴的 X 射线平台相各向同性辐射能量和动能都超过了 2×1052 尔格，因此这 9 个伽玛暴的中心引擎是黑洞；发现 69 个伽玛暴的 X 射线平台相各向同性动能超过了 2×1052 尔格，但各向同性辐射能量没有超过，考虑到动能依赖于模型假设，因此这 69 个伽玛暴的中心引擎有可能是黑洞；剩下 23 个伽玛暴的 X 射线平台相各向同性辐射能量和动能都不超过 2×1052 尔格，因此这 23 个伽玛暴的中心引擎可能是磁星。

提出对伽玛暴 X 射线耀发偏振探测可以探索磁场位形（Geng, Huang, Wu, Song, & Zong, 2018, ApJ）。X 射线耀发发生在伽玛暴结束之后，一般持续 100-1000 秒，其物理起源仍然是未知的，目前仅探测到光变曲线和能谱信息。X 射线偏振探测是未来国际空间天文的一个重要发展态势。吴雪峰和合作者假设 X 射线耀发来自相对论激波的同步辐射，在理论上详细研究了 X 射线耀发的偏振行为，发现 X 射线耀发上升阶段的线偏振度要高得多，而在衰变阶段偏振演化是由曲率效应所决定。因此，未来测量 X 射线耀发的偏振将为探测辐射区磁场结构提供一个有用的工具，甚至可能有助于检验曲率效应，有关磁场位形信息可以进一步帮助我们了解伽玛暴喷流的物理特性。

伽玛暴多波段光学余辉光谱色指数的大样本研究（Li, Wang, Shao, Wu, Huang, Zhang, Ryde & Yu, 2018, ApJS）。吴雪峰和合作者基于 70 个伽玛暴多波段光学余辉的大样本数据分析，系统研究了色指数的时间演化，并将样本分为 25 个伽玛暴组成的金样本，和 45 个伽玛暴组成的银样本。在金样本中，我们发现 96%的色指数不会随时间变化。但是，在更多数的伽玛暴中，色指数在短时间内发生变化。其中，73%的色指数的改变可能起源于同步辐射冷却频率穿过观测频率，12%则由于早期尘埃消光，5%起源于反向激波辐射向正向激波辐射过渡，最后 10%则是超新星浮现造成。

在伽玛暴双成分喷流模型框架下对光学余辉及其偏振进行了详细的理论研究（Lan, Wu & Dai, 2018, ApJ）。伽玛暴被广泛认为起源于双致密星并合或大质量恒星的核心塌缩。由这些系统驱动的喷流可能有两个成分：一个内部的、窄的喷流和一个外部的、宽的喷流。这样的双成分喷流与周围介质相互作用，在宽、窄喷流分别产生了一个反向激波和一个正向激波。在窄喷流中的反向激波区域磁场可能是混合型，即既有规则磁场，也有随机磁场。兰迷香、吴雪峰及其合作者研究了一个 2 维的“混合”磁场，发现对于这样的 2 维“混合”磁场，其中的同步辐射的偏振度的演化和纯的规则磁场中的情形类似。这种 2 维“混合”磁场实际上就是大尺度规则磁场，只是其磁场位形不同于传统的环形磁场或平行磁场。双成分喷流同步辐射的偏振方位角可以逐渐改变也可以突然改变 90 度。一般的偏振方位角 90 度的改变发生在偏振度从衰减相到增加相的演变时刻。这一理论研究结果，对未来伽玛暴余辉偏振观测提供理论支撑。

3、快速射电暴的起源研究

提出了快速射电暴的原初双黑洞模型（Deng, Cai, Wu, & Liang 2018, PRD）。原初黑洞被认为是宇宙极早期密度涨落的产物，长期以来被当作暗物质的候选体之一。邓灿敏、吴雪峰及其合作者提出，原初双黑洞形成之后可能会带上一定数量的电荷（或磁荷），原初双黑洞由于引力波辐射导致并合，带荷的原初双黑洞并合过程中会产生电磁辐射。如果双黑洞的质量在 1028 克的量级，那么产生的电磁辐射正好处在 GHz 射电波段，这种信号与目前天文上观测到的快速射电暴信号很相似。而且，只需要质量为 1028 克的原初黑洞占暗物质含量的十万分之一就有可能解释目前观测到的快速射电暴的高发生率，这是大多数传统的天体物理模型难以达到的。此外，本工作还讨论了这类双黑洞并合产生 GHz 引力波辐射探测前景。目前国际上已经有几个团队在讨论建造 GHz 引力波探测器。因而，很可能在将来能同时观测到原初双黑洞的引力波辐射和电磁波辐射。因此，这一工作也为将来的这种多信使观测提供理论支持。

4、脉冲星的搜寻和应用（亮点成果二）

对超新星 SN 1987A 遗迹的可能脉冲星进行了系统搜寻（Zhang, Dai, Hobbs, Staveley-Smith, Manchester, Russell, Zanardo, & Wu, 2018, MNRAS）。张松波、吴雪峰及其合作者分别利用 64 米帕克斯望远镜的 20 厘米多波束接收机和 10/50 厘米接收机观测了超新星 1987A 的遗迹，以期搜寻其中可能存在的超新星爆发后生成的脉冲星。这一工作同时利用周期性搜寻和单脉冲搜寻的方法，对获得的数据进行详细的处理，其中周期性搜寻并没有获得明显的脉冲星存在的证据，但是在 1.4 GHz 和 3 GHz 频段分别获了现今最好的流量限制：31 Jy 和 21 Jy。 而单脉冲搜寻是第一次运用到 SN 1987A 遗迹脉冲星的搜寻中，我们发现了 4 个脉冲星单脉冲信号候选体（信噪比大于 7），其中 2 个在二次搜寻中获得了信噪比略低的信号（信噪比大于 6.5）。我们将利用帕克斯望远镜最新的超宽带接收机对已有的结果进行进一步的检验。

利用河外射电脉冲星的统计样本更可靠地限制光子静止质量（Wei & Wu, 2018, JCAP）。光子静止质量是否为零是物理学领域长期关注的基本问题之一。限制光子静止质量的最直接方法是探测光速的频率依赖性，但是该方法依赖于假设不同频率光子之间的观测到达时间差都是由于光子静止质量不为零造成的。实际上，观测时间延迟除了有来自光子静止质量不为零效应的贡献之外，还有等离子体效应的贡献。众所周知，低频射电信号在等离子体介质中传播会导致光子的到达时间对光子频率有一定的依赖性，到达时间正比于频率的负二次方，即所谓的等离子体效应。而光子静止质量不为零也会导致相同的色散关系，我们很难区分光子静止质量不为零效应和等离子体效应。这两种效应之间的简并会影响人们对光子静止质量限制结果的可靠性。魏俊杰和吴雪峰提出了一种基于大样本的统计方法来扣除等离子体效应造成的时间延迟。通过分析河外射电脉冲星的统计样本，他们得到了光子静止质量上限的最可靠限制(~10-48 千克）。此外，我们还指出该统计方法也适用于未来已知红移的快速射电暴样本。

5、宇宙学的研究进展

提出引力波和快速射电暴成协事件作为升级版的标准汽笛开展宇宙学研究（Wei, Wu & Gao, 2018, ApJL）。一些理论模型预言当双中子星绕转距离足够近，通过双星之间的磁层相互作用产生快速射电暴。如果快速射电暴产生于双中子星并合过程，那么快速射电暴有可能和引力波事件成协。魏俊杰、吴雪峰及其合作者讨论了引力波和快速射电暴成协系统作为宇宙学探针的可能性。我们提出通过结合引力波信号的光度距离 DL 信息和快速射电暴的色散量 DM 信息，即 DL×DM，可以构造升级版的标准汽笛。传统的标准汽笛方法（即 DL 方法）和 DM 方法都依赖于哈勃常数的定标，而 DL×DM 方法具有不依赖于哈勃常数的优势。通过蒙特卡罗模拟，我们证实相比单独的 DL 或 DM 方法，DL×DM 方法可以更有效地限制宇宙学模型。借助 DL×DM 方法，未来仅需要大概探测到 100 例引力波和快速射电暴成协事件就可以精确限制宇宙学参数。此外，即使引力波和快速射电暴成协事件不存在的话，该方法仍然适用于发生在同一红移处的引力波和快速射电暴。

基于引力波观测开展对宇宙曲率测定的相关研究（Wei 2018, ApJ）。宇宙曲率Ωk 是现代宇宙学的一个基本参数。宇宙到底是开放的、平坦的、还是闭合的，与宇宙的演化、暗能量的特征等许多重要问题是息息相关的。然而，由于宇宙曲率和暗能量状态方程之间的强简并，人们很难同时限制这两个参数。一般而言，科学家们要么是在分析暗能量时把曲率参数取定为零，要么是在限制曲率参数时假设特定的暗能量模型（比如宇宙学常数模型）。值得强调的是，即使曲率参数的真实值非常小，平坦宇宙的假设仍然可能会导致暗能量状态方程的不正确重构；而宇宙学常数的假设也有可能会导致平坦的ΛCDM 模型和非平坦的暗能量 w(z)模型之间的混淆。为了克服假设曲率为零的缺陷，最近有人提出了一种宇宙学模型无关的新方法，即通过结合最新的 Ia 型超新星数据和哈勃参数 H(z)直接得到宇宙曲率参数的观测限制。但是，从超新星的视星等得到光度距离需要知道来自光变曲线校准方法的三个“讨厌”参数大小，而这三个参数并不能严格确定。这些“讨厌”参数的不确定性会影响 Ia 型超新星数据对平坦宇宙的检验结果。而引力波作为宇宙学探针的最大优势是它可以独立给出光度距离信息，即引力波的距离定标不需要依赖于任何其它的距离阶梯，它可以实现自我定标（self-calibrating）。因此，相比 Ia 型超新星，引力波信号可以更好地被用来测量曲率参数。魏俊杰基于高斯重构的模型无关方法，联合未来的引力波观测数据（模拟下一代引力波探测器对引力波信号的探测前景）和现有的哈勃参数 H(z)观测数据测量宇宙曲率Ωk，发现相比其它模型无关的检验方法，利用引力波数据的方法可以更有效地限制曲率参数。

利用 Ia 型超新星观测检验宇宙学模型（Melia, Wei, Maier & Wu, 2018, EPL）。魏俊杰、吴雪峰及其合作者利用 JLA 613 颗 Ia 型超新星数据检验不同的宇宙学模型。由于包含统计误差和系统误差的超新星协方差矩阵依赖于表征超新星光度的几个“讨厌”自由参数，我们提出应该采用最大似然估计法来同时限制宇宙学参数和“讨厌”参数，并发现当 Rh = ct 模型和 wCDM 模型做比较时，现有的超新星数据倾向于支持 Rh = ct 模型；而当 Rh = ct 模型和平坦的ΛCDM 模型做比较时，则结果刚好相反，超新星数据倾向于支持平坦的ΛCDM 模型。

利用 kSZ2 - 21 cm 互相关测量宇宙再电离的不均匀性（Ma, Helgason, Komatsu, Ciardi & Ferrara, 2018, MNRAS）。马清波及其合作者研究了如何利用动力学 Sunyaev–Zel' dovich 效应（kSZ）和 21 厘米信号的互相关来研究宇宙再电离的不均匀性。由于 kSZ 效应正比于重

子物质在视线方向上的速度，kSZ-21 cm 的互相关在小尺度上会互相抵消，因此我们注重研究了 kSZ 平方和 21 厘米信号的互相关，结果表明当宇宙的电离率较低时（ <0.7），kSZ2 的扰动由稀有的电离泡主导，从而和 21 厘米信号产生了正的相关关系，而当电离度较高时，kSZ2-21 cm 的互相关由中性氢主导，因此互相关为负。在实际的观测中，可以利用维纳滤波去除宇宙微波背景 CMB 观测中的背景噪声，利用这个技术我们发现未来的SKA和地基CMB实验可以以很高的信噪比观测到真实的 kSZ2-21 cm 互相关信号。

研究了 X 射线背景和 21 厘米信号的互相关关系（Ma, Ciardi, Eide & Helgason, 2018, MNRAS ）。马清波及其合作者使用高精度流体动力学数值模拟研究了高红移辐射源，比如 X 射线双星、吸积中心黑洞、激波加热的星际介质，对 X 射线背景的贡献。马清波等发现这些源对 X 射线背景的贡献仅有几个百分点 ,因此很难直接用 X 射线背景的观测来研究宇宙再电离。随后利用辐射转移模拟计算了这些辐射源对中性氢的电离和加热效应，并利用相应的结果计算了 21 厘米信号和 X 射线背景的互相关。这种互相关可以用于证实 21 厘米信号的起源以及研究再电离时期 X 射线辐射源的性质。该工作还发现这种互相关在宇宙再电离的早期为正，而在再电离的晚期为负 ,而正负之间的转换依赖于 X 射线源的性质以及研究的宇宙尺度。利用 SKA 和未来的 X 射线巡天计划，这种互相关的信噪比最高可以达到 5。

6、时域巡天观测数据处理方法的研究

余波开展了时域巡天大数据的图像处理研究，他对国际同行根据统计学原理提出的图像相加和相减方法提出 zogy 图像处理方法和代码基础上，从理论上提出了更加一般的方法，并编写了代码，目前正在分析测试和优化中。根据已得到的结果，大致有如下进展：（ 1 ）首先，从另外的角度（卡方方法 ）简化了 zogy 新方法的推导；（ 2 ）使用卡方方法和直接概率计算得到了噪声水平不均匀情况下的图像加减方法；（ 3 ）给出了减图时不需要图像对齐重采样的处理方法；（ 4 ）在理想情况下测试了上述方法的可行性；（ 5 ）编写了处理实际图像的代码并进行初步测试。

2-10 银河系气体分布与性质研究团组

在 2018 年度 ,团组工作紧密围绕我台 135 的重点突破方向“南极天文”和重点培育方向“宇宙中的恒星形成与太赫兹技术”。全体成员作为主力参加到我台德令哈 13.7 米毫米波望远镜“银河画卷”巡天中，负责银道面不同天区的观测、数据处理、结果分析等工作。团组成员基于“银河画卷”巡天，并结合国内外多波段望远镜，开展银河系气体分布与性质的研究，在星际分子云与恒星形成、超新星遗迹、遥远外臂上恒星形成等前沿领域取得科研成果。

此外，陈学鹏研究员参加了中国科大天文与空间科学学院的“射电天文”的联合授课；协助台领导，多次组织国内和台内毫米波与亚毫米波天文会议，凝炼该领域关键科学问题，积极开展国家重大科技基础设施“60 米级亚毫米波望远镜”的项目建议工作。苏扬博士负责“银河画卷”巡天计划的观测时间分配工作，安排协调各天区负责人的巡天观测时间和进度。孙燕博士申请并获批 2018 年度“中国科学院青年创新促进会”会员和“中国科学院优秀博士论文”。

成果名称：发现银河系边缘的脉泽发射（Sun Y. et al. 2018, ApJ, 869，148 ）

具体内容 :为了更好地理解大质量恒星形成这一关键科学问题，团组孙燕博士等人利用国际一流的射电望远镜（上海天文台天马 65m 和德国 Effelsberg-100m 望远镜），对基于“银河画卷”CO 巡天发现的约 200 个位于银河系外臂上的分子云进行了 H2O, CH3OH, OH 脉泽搜寻。通过脉泽巡天，孙燕博士等人在 5 个分子云中发现了脉泽发射，其中包括距离太阳最遥远的甲醇脉泽（约 21 kpc ）和最遥远的羟基脉泽（约 18 kpc ）。这些脉泽的发现证明了在银河系边缘存在着剧烈的大质量恒星形成活动（见图 1 ）。较低的脉泽探测率表明在银河系边缘低气体密度和金属丰度的环境下有较低的恒星形成率，为长期以来的理论模型提供了直接的观测证据。课题组的发现有助于我们进一步理解大质量恒星形成的物理化学环境以及银河系的恒星形成历史，并为后续的研究提供了宝贵的观测样本。

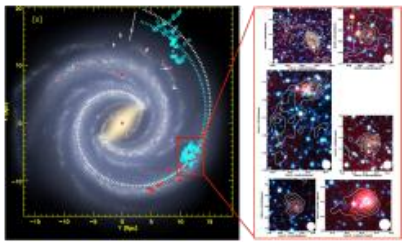

图 1：左图为银河系旋臂示意图，青色圆圈代表了通过“银河画卷”CO 巡天发现的银盘边缘的分子云；右图观测发现的具有脉泽（绿色圆圈）发射的 6 个分子云，彩色为在红外发射和白色轮廓图为 CO 强度图。

成果名称：SS 433/W50 的大尺度星际环境：激波扰动促进分子气体快速形成(Su Y. et al. 2018, ApJ, 863 ,103)

具体内容 :图 2 左展示了射电展源 SNR W50 包裹着其中心明亮的强力引擎 microquasar SS 433，射电辐射（黑色等高线图）表现出明显的双瓣结构，与 SS 433 的相对性喷流直接相关。原子气体表现出特殊的双极空腔型结构和破碎的壳层结构（灰色强度图），分子气体在相对性喷流的顶端增强（红色+蓝色等高线图 ）。其中红/蓝色直线分别代表 SS 433 相对性喷流远离/接近观测者的运动学特征，这些喷流的特征与周围环境气体的运动学性质一致，表明二者具有物理相关性。

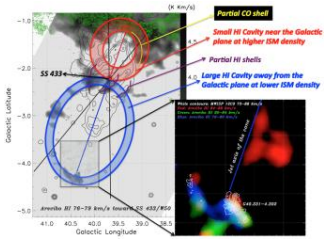

右下角图示展现了远离银盘的气体 G40.331−4.302 的性质：原子气体和分子气体都表现出蓝移的运动学特征，与朝向观测者的 SS 433 喷流在空间和运动学性质上吻合。利用 HI+CO 气体的运动学性质推算出气体的距离为 4.9kpc，与由 SS 433 喷流的自行测算得到的距离一致，确认了二者的物理联系。MC G40.331−4.302 位于银盘下方约 370 pc，远远大于内银盘分子气体垂直于银道面的分布（例如，CO 气体的半高全宽 FWHM=90--100 pc）。这是目前银河画卷 CO 巡天发现的距离内银盘最远的分子气体。利用激波扰动星际介质的模型，我们发现 G40.331−4.302 内约 10^3 太阳质量的分子气体会在 10^5 年内大量形成，分子气体的形成时标与 SS 433 的双星演化时标，SNR W50 的演化时标，HI 和 CO 的蓝移气体的运动学时标相当。

2-11 天文望远镜技术实验室

重点围绕 5m 太赫兹望远镜(DATE5)和大视场巡天望远镜（WFST）关键技术预研展开工作，主要包括：自适应光学、面向 DATE5 的热控及防霜方案研究、天线近场全息测量研究等。申请成功并开始执行国家重点研发计划项目“射电技术方法前沿研究”，本团组主持其课题 2“大型及高精度天线关键技术和方法研究”。

碳纤维复合材料面板取得阶段性进展

碳纤维面板的热变形特性研究取得阶段性进展。在优质低固化收缩率、低热膨胀系数树脂材料国际上对我国禁运的环境下，通过多参数优化方法设计了一套全碳纤维材料的面板结构，采用国产树脂及 M55J 碳纤维，夹芯采用点阵结构，试制了原型面板并完成了面形精度测试。在常温（+20℃）下的面形精度为 7.2μm rms，低温（-40℃）下的面形精度为 7.3μm rms，初步实现了接近“零膨胀”的热变形特性。

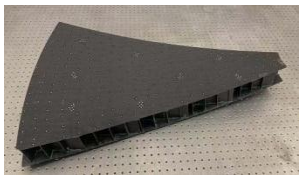

图 1 全碳纤维夹层结构原型面板

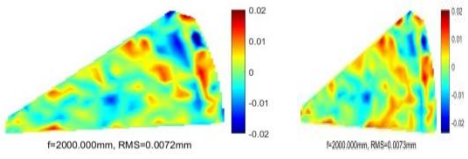

图 2 面形误差分布，(左图)常温+20℃时，(右图)低温-40℃时

近场全息测量研究取得重要进展

开展了斜轴式太赫兹天线近场全息测量过程中系统性误差修正方法及仿真研究，包括近场波束扫描过程中光程差的精确修正、波束旋转效应修正、极化修正、以及天线副面衍射效应修正等。在此基础上，针对 1.2m 斜轴式太赫兹天线，在 100GHz 频段开展了近场全息测量实验，取得如下测量结果：a）重复测量误差优于 2μm rms；b）全息测量结果与摄影测量结果一致，例如在某状态下，用两种方法相继测得的面形误差分别为 25.9μm 和 26.3μm rms，且误差分布一致；c）能够正确检测单块面板人为调整偏移量；d）在反射面人为调乱的大面形误差（55μm rms）初始状态下，用近场全息测量方法，经过 2~3 轮测量调整，反射面迅速收敛到其受限面形精度（22μm rms，受限于被测天线各面板加工精度、面板切向无法调整、热变形等因素）。相关论文即将投稿。

自适应光学研究方面取得重要成果，面向高分辨成像需求，在国际上提出高空间分辨率的连续镜面分立式双压电片变形镜，为突破自适应光学的瓶颈（在提高压电变形镜变形量的同时拓展其控制带宽）提供了新的解决方案。应用力学、光学、电学、控制等多科学思想与方法建构了该类压电变形镜精确的数学理论模型，并给出了其各个支撑单元的影响函数及其性能评估。研究工作得到了国际同行专家的积极评价，相关结果发表在天文仪器 Top 期刊 Journal of Astronomical Telescopes, Instruments, and Systems, 2018, 4(2): 029001。

WFST 相关研究取得进展，面向 WFST 建设需求，建构了 WFST 主镜在极端台址环境（高海拔低气压昼夜大温差）下温度模型，并选择国际上四个典型台址实测气象数据作为输入，模拟分析了极端台址环境对 WFST 主镜成像质量的影响，揭示极端台址环境对 WFST 主镜性能影响规律。研究工作得到国际同行专家认可，相关成果发表在国际知名的光学期刊 Optik, 2018, 174, 727-738。

DATE5 热控方案及其缩比模型热控实验研究

分别与重庆大学和南京航空航天大学合作，完成了 DATE5 望远镜热学模型建模以及热力学仿真分析，以及 DATE5 望远镜整体热控方案的详细设计。完成了 DATE5 望远镜缩比或局部模型的研制，开展了模拟南极极端台址环境的热力学实验。

射电望远镜波前测量中的非相干方法研究，提出了一种基于波前扰动的面形测量和调整方法，该方法是一种非相干面形测量方法，通过多种主动扰动状态下的天线增益测量反演面形误差分布。本年度完成了该方法的模拟仿真以及测量流程优化，并在 1.2m 口径 DATE5 缩比天线上开展了初步实验验证，获得了理想的实测结果。3mm 波段实验结果表明，调整后的天线面形精度优于 λ/100。

斜轴式望远镜指向误差模型关键参数提取实验研究

基于 1.2 米口径 DATE5 缩比天线，开展了斜轴式望远镜指向误差模型的实验研究。该研究旨在理解斜轴式机架系统的

特有运动特性和指向误差规律，为南极 5 米太赫兹望远镜工程建设储备技术基础。本研究创新性地采用数字摄影测量技术来研究各种轴系误差和天线结构变形对指向的影响。初步实验结果表明，指向测量的均方根重复精度达到1~2角秒。其它

开展了 60 米口径亚毫米波望远镜的前期预研工作，完成了望远镜光学设计以及初步性能估算，联合国内天线制造商开展了天线概念设计，编写了《60 米亚毫米波望远镜天线技术方案及可行性分析报告》；成功举办了“大型亚毫米波望远镜天线关键技术研讨会”。

完成了修缮项目“望远镜测试场与实验室条件改造”。主要内容包括：1200 平方米山坡地整平和硬化，钢筋混凝土望远镜安装基础，轨道电动移动工作房和极端环境实验室条件改造。该项目已顺利通过验收。

参与紫外光谱仪项目 CAFE 的预研工作，完成了 HI Lyman-α 窄带成像光谱仪的光学设计。该光学设计采用大色散光栅光谱仪与大视场成像光学相结合，在 Lyman 紫外波段实现了大视场中等分辨率的光谱成像功能。完成了光学设计的公差分析及各光学元件的加工图纸，开展了关键器件如球面光栅、主次镜等的加工方案论证和原理样机研制准备工作。

参与 921 项目“高灵敏度太赫兹探测模块”的研制，作为准光与定标组件的负责人，完成了该组件方案设计、原理样机研制以及主要性能测试。

参与大视场巡天望远镜建设的前期准备工作，编写了望远镜总体技术指标要求，完成了光学性能的复核计算及公差分析，为望远镜询价以及招标提供技术支撑。

团组人员作为骨干成员参加中日合作项目“西藏阿里天文台 HinOTORI 50cm 望远镜”，完成了前期安装调试，并在今年的 10 月进行了现场及远程的试观测，在此基础上获得了一些望远镜的技术参数及性能指标。刘伟在国家留学基金资助下留学日本广岛大学攻读博士学位，完成了基于 Linux 操作平台的滨松可见光探测器的读出电路设计，并在东京大学天文中心进行了整体系统测试；完成了对金牛座变星 AA Tau 的 2018 年春季观测，获得了可见光和近红外六个波段的偏振数据。

本团组主持的 2015-2016 年度院天文财政专项项目“DATE5 望远镜集成与测量、热控与防霜、多波束接收机技术研究”顺利通过验收。

本团组牵头，促成紫金山天文台与南京航空航天大学合作申办江苏省研究生工作站事宜，已获得设站批复，且已有一名硕士研究生进站。

2-12 基于 SKA 的宇宙学研究团组

(1)Use the Planck data to detect the velocity dispersion of kinetic Sunyaev-Zeldovich effect at 2.8 sigma, constrain the scale of homogeneity.

(2) Forecast the measurement of cosmological parameters with future FRB data

(3) Stack the pairs of Luminous Red Galaxies and detect the signal of filaments at 5.3 sigma

(4) Build up computational pipeline to analyze the effect of 1/f noise in single-dish 21-cm intensity mapping experiment (SKA-I)

1) A Search for Warm/Hot Gas Filaments Between Pairs of SDSS Luminous Red Galaxies

2）Planck intermediate results. LIII. Detection of velocity dispersion from the kinetic Sunyaev-Zeldovich effect

今年我在紫金山天文台的主要工作在于人才引进。之前面试了 3 位申请人。目前已经确认了一位印度学者 Dr. Chandreyee Sengupta 来紫金山天文台任副研究员。她的主要研究方向是 HI 星系巡天，主要是研究小尺度上的星系的 HI 丰度。她的研究可以很好的和南非 MeerKAT 项目以及和中国 FAST 项目结合起来。

另外在今年我们也邀请了几位在海外正在做博士后的，SKA 宇宙学方向的中国学者前来访问。李毅超（南非 UWC 大学博士后），陈天悦（英国曼彻斯特大学博士后），施迪夫（南非 UKZN 大学，英国 Durham 大学博士后）。他们都是这个领域的正在快速成长的青年力量。他们在海外目前的博士后工作经验为 1-2 年，将在未来的 1-3 年的时间内申请人才计划。（百人计划的窗口）同时今年我们还吸引了一位学者 Vimal Simha 通过紫金山天文台申请 PIFI 国际博士后项目，申请结果尚不知晓。

III．应用天体力学和空间目标与碎片研究部

3-01 空间目标与碎片观测研究中心

2018 年度团组在科研、重大设备研制、完成国家任务以及观测网的持续运行等各方面开展了大量工作，主要有：

（1）院观测网持续运行，目标管理能力持续增长，圆满完成多项国家任务，特别是“天宫一号”再入大气层监测预报任务，为国家对外发布再入简报提供了依据；

（2）“30 厘米拓展”已在姚安站完成安装调试，目前正在开展同步轨道巡天试验；“广角 LB”已完成外场安装；“××卫星地面应用系统”，完成全部六个软件的研制和配置型测试，已进入在轨试运行阶段；参加 “国家 JM 融合工程项目”的论证，即将批复立项。

（3）完成光学特性测量仿真实验室的建设和调试，并通过验收；

（4）“人造天体的精密光学测量方法”项目获省部级科技进步二等奖（单位排名第一，已公示）；

（5）继续开展空间目标运动理论与应用研究，集中在特殊轨道（同步轨道、半同步轨道、Molniya 和 Tundra 型轨道）动力学特征及其长期演化规律研究、编目技术、陨落期预报方法、天文定位、识别方法、大气模型改进、碰撞预警、空间碎片测光方法、空间碎片旋转规律、暗弱目标探测方法以及空间碎片精确定位方面的研究；

（6）2018 年度，团组在研课题共计 55 项，并完成了其中 12 项课题的结题与验收工作，新申请到课题 15 项，包括：国防科工局空间碎片专题 4 项、973 项目子项 1 项、自然基金 13 项、航天领域预研基金 3 项、院重点部署 2 项、修购 1 项等。

2、亮点工作：

1）中心代表中科院参加“天宫一号”再入大气层监测预报任务，组织所属设备采集了 500 多圈光学数据；运用多零点预报、精密定轨和卡尔曼滤波等多种预报技术，给出可靠的再入预报时间；基于激光联测的高精度数据求解出再入大气前的旋转状态。被中国载人航天工程办公室授予突出贡献证书。

2）“人造天体的精密光学测量方法”项目获省部级科技进步二等奖

（1）2018 年中心参加了多项国家任务，并得到了各方好评。主要有：

① “天宫一号”再入大气层监测预报；

② “龙江一号”应急观测；

③ “中卫 1C”卫星应急观测；

④ “北斗 14”卫星应急观测；

⑤ 遥感 3 号等五颗卫星测光试验；

⑥ 美国同步卫星重点观测。

特别是：中心代表中科院参加“天宫一号”再入大气层监测预报任务，组织所属设备采集了 500 多圈光学数据；运用多零点预报、精密定轨和卡尔曼滤波等多种预报技术，给出可靠的再入预报时间；基于激光联测的高精度数据求解再入大气前的旋转状态。被中国载人航天工程办公室授予突出贡献证书。

Ⅳ．行星科学和深空探测研究部

4-01 近地天体探测和太阳系天体研究团组

（1）开展了行星系统起源演化的动力学研究，以及太阳系天体自转演化及其相关动力学演化过程研究。通过哈密顿方程，对海王星质量的行星进行分析研究，当两个轨道均为近圆时，一阶平运动共振在中等倾角处出现强度低谷。同时用数值模拟方法研究了一阶平运动共振强度随轨道倾角的变化。此文章投 RAA，第二轮审稿意见已经回复。对系外行星系统 Kepler-9b、c 近 2:1 共振状态分析：Kepler-9b、c 经过最新的 TTV 联测，各轨道根数已达到<1%的精度，参照近年发表的系列工作，利用二阶哈密顿方程，分析了 Kepler-9b、c 当前所处的共振状态，发现此两行星正好处于共振区与近共振区的分界处，由此推测了其可能经历的演化历史。在天体自转演化及相关动力学方面，研究了冥王星卫星 Styx 和 Nix 的自转轴倾角在现构型下的状态及其轨道迁移过程中自转轴的可能演化历史，在本研究工作中，发现了一种新的可快速激发自转轴倾角的机制——自转-进动-平运动共振，共振角中包含一阶、二阶或三阶平运动共振角，从而表现为在对应平运动共振附近发生自转轴倾角的激发，这一现象可以很好地解释利用 mass-spring 模型得出的数值结果，发表合作论文 1 篇。

（2）开展了彗星观测和测光研究，研究了三颗主带彗星 176P/LINEAR (118401)、238P/Read 和 288P/300163 的活动性。结果表明，彗星 176P/LINEAR (118401)是不活动的（在近日点之前），彗星 238P/Read 和 288P/300163 均处于活动状态。主带彗星的动力学特征与主带小行星相同，它们的活动性需要热量进入到岩层下部使水冰挥发驱动，一般到达近日点附近或过近日点之后才会产生活动性，我们的研究结果进一步证实了这个结论。同时，我们得到了三颗彗星的彗核半径和反映尘埃活动性的 Afρ值。文章已投稿，二审稿意见已经回复。

（3）对去年建立的太阳系小天体轨道和基本物理参数数据库进行了维护和更新，目前包含的彗星总数达到了 3532 颗，小行星总数达到了 780341 颗，并实现了轨道的可视化演示的功能，网址更新为：http://www.astorb.com。用户可以通过 PC 端（包括手机客户端）输入网址后查看任意一颗小行星和彗星的实时轨道（日心黄道系），并且通过修改时间参数，可以查看该天体的任意时刻的位置信息（包括相位角），从而对该小天体的可观测性做出迅速的判断。针对彗星这类特殊天体，用户还可以对其参数进行修改，能够实时更新彗星的相关物理参数。

（4）开展系外行星大气的观测研究，对多颗较高温度的系外气态巨行星进行观测普查，利用凌星现象获取它们的大气透射谱，进而根据光谱特征分析得到大气组成成分。本年度的进展包括（但不限于）：确认热木星 WASP-80b 的透射谱无宽带光谱特征，很可能存在光学厚的高空云层，该行星是罕见的宿主恒星为 M 型矮星的热木星；在超级海王星 WASP-127b 上发现霾、水和多种碱金属；在极高温热木星 KELT-20b 上分辨出热成层中的钠原子以及氢包层；在热木星 HD 189733b 上发现了延展的氦包层；在土星质量的热

木星 WASP-69b 上发现了延展的氦包层，并确认存在大气逃逸，发表论文 5 篇。

承担天文学院到中国科大教学任务，到合肥教课，带学生赴盱眙观测基地教学实习；开展面向太阳系小天体深空探测的一些科学问题研讨；团组 4 人共承担科学基金（国家基金、联合基金和省基金)5 项。5 人次出国进行国际交流与合作，开展系外行星大气观测研究和太阳系小天体动力学合作研究，其中，史建春访问日本期间，利用东广岛天文台的 Kanata 望远镜在 2018 年 8 月 6-8 日对彗星 21P、37P 和 64P 进行了成像观测和偏振观测，获取到了三颗彗星在多个波段的光学、红外和偏振观测数据，同时向日本同行学习了彗星偏振观测数据的处理方法和流程，就进一步开展彗星方面的观测和合作交流进行了讨论。

对多颗较高温度的系外气态巨行星进行观测普查，利用凌星现象获取它们的大气透射谱，进而根据光谱特征分析得到大气组成成分。

1）公转周期较短的系外行星的大气在吸收了主星的高强度辐射后很可能出现大气逃逸的现象。开普勒望远镜所观测到的短周期行星所呈现的半径或者质量随轨道距离的分布很可能与此过程相关。利用位于西班牙 Calar Alto 天文台 3.5 米望远镜上拥有极高光谱分辨率（ R~80,400 ）的 CARMENES 光谱仪，我们观测了一颗土星质量的系外行星 WASP-69b，发现它在近红外 1083 纳米附近的亚稳态氦三重线上的半径显著大于其它波长，并且远远大于可见光的半径。细致分析后，我们发现该额外吸收来自行星大气中的氦，并且存在 3.58 km/s 的净蓝移，结合光变曲线在氦线线心上存在 22 分钟的延迟出凌，说明这颗行星存在大气逃逸的现象，并且形成了一个彗星状的尾巴。氢和氦是宇宙中最丰富、也是最轻的元素，非常适合用于研究大气逃逸过程。此前的大气逃逸只能利用空间望远镜在紫外观测氢的莱曼 alpha 线，有很大的观测局限性，而这项工作表明，地基的高谱分辨率光谱设备有能力分辨行星大气的氦三重线，将有望应用到大量的样本上，让我们从观测上更加有效地理解大气逃逸的过程。这项工作发表在 Science 杂志上。

2）一直以来，碱金属原子吸收线被认为是晴空条件下高辐照系外行星大气在可见光波段的典型特征。然而，实际观测中几乎只探测到过钠吸收线的窄线心，钾吸收线的发现也仍然存在争议。我们利用 10.4 米 GTC 的低分辨率光谱仪 OSIRIS 观测了一颗极其低密度的系外超级海王星，其质量为海王星 3 倍、而半径却达到了木星 1.4 倍。观测获取的凌星透射光谱显示，这颗行星的大气中含有钠原子、钾原子、锂原子和水分子，钠和钾各自的共振双线的压力致宽线翼首次同时被分辨出来，此外，约 52%的区域被云霾覆盖，存在小颗粒气溶胶引发的瑞利散射。分析表明，三种碱金属的丰度都显著超过太阳丰度。锂元素是首次在系外行星上探测到，这很可能成为研究行星形成过程的探针之一。该工作发表在 A&A 杂志上，并召开 Press Release 一次。

4-02 历算和天文参考系团组

“超越经典太阳系实验检验：引力时间提前”是本团组的一个亮点工作。尽管广义相对论已通过四大经典实验检验，然而许多引力理论也同样满足和符合这些实验检验。有别于广义相对论四大经典实验，引力时间提前表明在特定构型下，测量观测者与遥远探测器之间往返光信号的原时时间间隔，其数值会小于平直时空下的结果，尤为重要的是不同引力理论下的引力时间提前会存在明显差别。本项研究工作以一些修改引力理论为例，说明不同理论下引力时间提前的差别性以及可探测阈值，并针对未来有望实现的光频率标准和行星激光测距，就在相对论引力时间提前检验中可开展的研究与实践给出展望与总结。有关研究成果已经发表在 PLB、CQG 等本领域国际重要 SCI 期刊上。

继续开展三星系统运动学和动力学研究。利用三体模型给出了邻近的具有低等级构形的三星系统 LHS 1070 新动力学状态参数，解决了长期以来有关该系统的困惑：即此前的双二体模型解既不稳定又不符合近年来的高精度观测。此外，该系统两颗子星的质量接近氢燃烧极限，因此获取它们的高精度质量对小质量恒星经验质光关系及其对金属丰度的依赖关系具有重要作用，在我们早前已发表工作的基础上已着手进一步开展这方面的研究工作。

结合研究生培养，继续开展多类天体运动理论和天文参考系等方面的研究工作。

给出了牛顿双恒星运动学观测量计算的严格模型，并通过实例验证了在目前观测精度下部分系统运动学拟合研究中使用严格模型的必要性。

发展了一种在通过密切接近确定小行星质量拟合研究中模型参数的选取方法，该方法能够有效地提高小行星质量确定的精度,利用该方法大大提高了小行星 349 的质量，由此限制了这颗小行星的物理性质，有关工作已收到 AJ 正面的审稿意见，目前正着手稿件的修改工作。此外，与 349 有密切接近的小质量小行星的历表研制工作也有了初步结果。

在大行星和天然卫星历表，以及河外射电源位置稳定性方面也分别取得了进一步的阶段性成果。

本年度开展的另两项工作是 :完成了有关海司航保局“电子航海天文历”项目验收的相关工作，项目顺利通过验收；完成了“太阳系高精度光学观测平台”的建设、试观测和设备验收工作，并成功地对各类太阳系天体和双恒星系统等开展了观测研究工作，目前已完成项目验收准备工作，并向院里提交了验收申请。

4-03 太阳和太阳系等离子体团组

本年度我们团组以紫台“一三五”规划中固本开源、持续发展的科学理念为指导，继续发挥本团组特色和优势研究开展科研工作。围绕规划中培育方向之一“高能天体物理、太阳物理与空间天文探测技术”，本团组就太阳和空间环境中射电、高能粒子现象与丝状结构的相关物理问题作基础理论研究，并且获得重要的研究进展。团组本年度发表 SCI 论文 11 篇，其中第一完成单位 6 篇，非第一完成单位 5 篇。重要的研究成果主要有以下几个方面：1）针对近年来空间等离子体卫星观测中的离子回旋频率附近的回旋电磁波现象这一热点问题，通过理论解析工作结合数值计算，对于回旋电磁波的不同激发机制进行了系统的研究和比较分析，不仅为太阳风中回旋电磁波的激发提供了理论依据，同时也为太阳风中的质子束流减速问题提供了合理的物理解释；2）通过对 MMS 卫星在地球磁鞘区观测的大振幅阿尔文波事件的分析，发现大振幅波可以导致离子投掷角的周期性变化，并对带电粒子动力学产生重要影响；3）基于二维数值模拟对空间无碰撞准平行激波激波下游的丝状结构进行了研究，通过结合理论进行分析，基本确认了这些丝状结构来自于下游的动力学慢波。

太阳风中束流不稳定性研究

研究在质子束流激发回旋波的情况下，考虑 alpha 束流对回旋波的影响。结果表明：alpha 束流的漂移速度能影响回旋波的阈值，实频和生长率。具体来说，随着 alpha 的漂移速度增加，左手和右手波的生长率都是先减少后增加，并且，alpha 漂移速度的变化对左手波影响更大。另外，通过比较两种波的阈值，发现右手波有低的速度阈值，同时太阳风中束流的漂移速度比左手和右手波的速度阈值都低，因此我们的理论结果可以解释太阳风中束流减速问题。

联合二维和三维非线性作用机制驱动阿尔文波非线性演化

针对低频阿尔文波非线性波波相互作用，其主要机制有阿尔文波-阿尔文波非线性相互作用和阿尔文波-慢波非线性相互作用。这两种机制都致使阿尔文波能量向不同尺度阿尔文波传输。以前研究分别考虑这两种机制，讨论非线性波波作用导致阿尔文波非线性演化问题，我们首先同时考虑了这两种机制对阿尔文波演化的影响。

基于相互作用的波需满足共振条件要求，存在三种阿尔文波非线性衰减方式：（channel Ⅰ）阿尔文波衰减为正向传播慢波和反向传播阿尔文波；(channel Ⅱ)阿尔文波衰减为正向传播慢波和正向传播阿尔文波；(channel Ⅲ)阿尔文波衰减为反向传播慢波和正向传播阿尔文波。我们结果发现：（1）在 channel Ⅰ中，非常大磁流体尺度（约万倍离子尺度）阿尔文波非线性不稳定性由二维非线性作用机制控制，激发宽带阿尔文波扰动。当波尺度约小于千倍离子尺度，三维非线性作用机制更重要，激发离子尺度扰动。（2）在 channel Ⅱ中，三维非线性作用机制为主，激发 45 度传播的、离子尺度的扰动。（3）channel Ⅲ仅在离子尺度触发，激发的波的尺度也是离子尺度。以上结果表明离子尺度波动很容易被激发。这些离子尺度波动携带了平行方向的电场扰动，可以有效地捕获和能化日冕和太阳风中离子。

大振幅电磁离子回旋波对离子和电子投掷角分布的调制

利用 MMS 卫星，发现了地球磁鞘 flank 区域中大振幅电磁离子回旋波事件，波振幅约为 1-2 nT。该事件中背景磁场约为 15 nT，因而，波的相对振幅可达 0.1 量级。我们发现该大振幅波可引起离子投掷角的周期性变化。电子投掷角分布中出现丝状分布特征，其时间尺度约为电磁离子回旋波周期。同时，一部分电子被约束在投掷角约为 90 度处。我们观察结果表明了大振幅波对带电粒子动力学的影响。

4-04 行星科学与深空探测实验室

2018 年度，行星科学与深空探测实验室的科研人员在思想上、行动上与党中央保持一致，坚持贯彻党的八项规定和“唯实、求真、协力、创新”的优良院风，保持廉洁的工作作风，坚决拥护紫金山天文台台领导的各项正确方针和举措。团组认真密切结合我台 135 重点工作布局，针对 2017 年度既定科研计划良好有序地展开各项工作，取得了重要的科研进展。

2018 年度本团组围绕“小行星深空探测”这一主题展开各项工作，取得如下科研进展：（1）提出了 4179 Toutatis 延长型接触双小行星的一种形成机制；（2）提出了 Bennu 等赤道隆起的小行星形状的形成机制；（3）建立三维模型研究 67P 彗发水分子分布；（4）开展了其他与深空探测相关的研究，对七块玻璃陨石进行了高精度钾同位素分析，尤其是对一块完整的海南玻璃陨石精细剖面上进行了钾和锌同位素对比分析，为月球的撞击起源提供了有力的证据。2018 年，《中科院空间科学背景型号（第一批）-小天体探测及采样返回》项目通过论证后正式启动， 本团组领衔承担子课题二-目标小天体的光谱特征与轨道演变相关科研任务。在目标小天体的遴选方面,我们筛选了 9 颗近地小行星和 1 颗主带彗星作为潜在的探测对象，向西班牙的 10.4 米 GTC 望远镜提出了观测申请，拟通过使用近红外低分辨率光谱设备 EMIR 观测获取这些候选对象的光谱，从而初步分析其可能的组成和性质，目前获得了 Filler 模式的观测时间。围绕实验室平台建设，本团组组织开展了“有机组分分析仪”实验平台修购专项的申请工作，并获得项目资助。季江徽研究员领衔的由中科院紫金山天文台和中国空间技术研究院科研人员组成的中国科学院小行星深空探测创新交叉团队，围绕国家小天体探测任务积极开展学术活动，在 4 月 23 日-25 日参加了关于太阳系小天体探测的 PSI-QianLab 2018 Workshop，就小天体探测科学目标和有效载荷及探测对象特性等开展研讨。12 月 25 日参加探月中心组织的深空探测科学研究项目论证会议，参与后续工程相关的科学问题研究课题撰写。这些工作都为推动国内小行星深空探测奠定了坚实基础。

2018 年度本团组在系外行星科学的基础研究取得了重要进

展：研究了大气逃逸对行星半径和密度分布的影响；研究了 LkCa15 系统的气体和尘埃分布研究了盘模型对共振构型的影响，获得了一种进入近共振构型的可能机制。对多行星系统的稳定性进行了研究，获得了相关的稳定区域及突破共振所需的条件。提出了解释极短周期行星的两种可能形成机制与一种热木星本地形成的理论。通过数值模拟揭示原行星盘中旋涡结构证据，研究原行星盘中的开尔文-亥姆霍兹不稳定性，揭示原行星盘中旋涡产生的旋臂结构的特征。本团组研究论文（Jin .et al. 2016， ApJ）入选 IOP 出版社中国高引用论文（共 17 篇），该项成果基于行星和原行星盘的相互作用成功解释了 ALMA 观测到的 HL Tau 系统中明暗相间的环结构。此外，团队积极参与中国科学院战略性先导科技专项(A 类) 空间科学空间科学（二期） “近邻宜居行星巡天计划（CHES）”项目，开展了 CHES 科学目标深化论证等工作，于 2018 年 11 月 16 日召开系外行星空间探测科学目标论证会， 争取推动背景型号立项。

2018 年度本团组围绕小行星深空探测和行星科学的前沿研究，开展了卓有成效的国际合作：与美国加州大学圣克鲁兹分校 Lin.D.N.C 教授合作开展了系外行星的动力学研究；与美国耶鲁大学王松虎博士开展短周期系外行星形成研究；与美国洛斯阿拉莫斯国家实验室 Li Hui 教授与莱斯大学 Andrea Isella 助理教授合作深入开展了原行星盘研究；与德国马普太阳系研究所 Ladislav Rezac 博士合作开展了彗发三维辐射转移模型研究；与美国罗切斯特大学 Alice Quillen 教授合作开展了小天体碰撞与形貌特征成因研究。

2018 年度本团组在行星科学与深空探测前沿领域积极推进国内合作。2018 年 12 月 26 日至 28 日，中科院行星科学重点实验室在宜兴成功举办了“中国天文学会行星科学与深空探测前沿研讨会暨中科院行星科学重点实验室 2018 年学术年会”。来自南京大学、北京大学、中国地质大学（武汉）、中科院国家空间科学中心、紫金山天文台、上海天文台、国家天文台、云南天文台、中国空间技术研究院等 21 家单位，100 多位专家学者参加了会议。会议主题涵盖了我国未来深空探测计划与最新进展、太阳系小天体探测与物理化学特征、月球与火星和行星际空间、系外行星探测与大气及其动力学与演化、行星遥感与深空探测技术等前沿领域。此次会议为国内外学者提供学术交流与合作的平台，同时也推动国内行星科学与深空探测研究与发展。另外，季江徽研究员受邀参加第 634 次香山科学会议-“小行星监测预警、安全防御和资源利用的前沿科学问题与关键技术”，作“小行星研究中的几个前沿科学问题”邀请报告；受邀参加第 639 次香山科学会议-“太阳系边际探测的前沿关键问题”，参加科学讨论。

本年度我们共(完成)发表了 26 篇研究论文，其中发表 SCI 论文 10 篇（包括 3 篇 ApJ，5 篇 MNRAS），国内核心期刊 3 篇，已完成论文 10 篇。本年度实验室积极开展学术交流活动，团组成员参加国内外学术会议 30 余人次，邀请国内外专家来访 7 人次来紫台做学术报告，包括 1 次台级学术报告。近年来我们的研究成果逐渐为国际同行所关注，这表明我们团队在国际行星科学领域上已显出一定的影响力。

小天体深空探测方面：

揭示 4179 Toutatis 小行星可能的形成机制

4179 Toutatis 具有奇特的形状和非常缓慢的自转，地面雷达和嫦娥二号光学图像均显示该小行星具有延展型的密接双小行星结构（由两个瓣组成），且连结处位于身体的长轴上。据推测该小行星的形成机制源于一次两部分结构的低速撞击。如果 Toutatis 的母体是一颗近地双小行星，在近距离飞越地球的过程中，由于地球的引力改变了该双小行星的相互轨道，并有可能影响该系统主星和卫星的自转和形状。假设该系统为双同步自旋双小行星，卫星相对主星的距离为 4 倍主星半径，并且两部分均考虑为由无粘附力作用下的自引力球形粒子聚合体所构成。利用 pkdgrav 程序，考虑了软球离散元模型。结果表明，在合适的参数下，这种机制很容易形成密接双小行星，但发现两者之间的相互碰撞很难用来解释主星延展型结构。然而，在飞越距离约为 1.4-1.5 倍地球半径情况下，获得一组与目前 Toutatis 形状相似的密接双小行星，表明该机制可解释 Toutatis 目前的形状（Hu et al., 2018，MNRAS）。

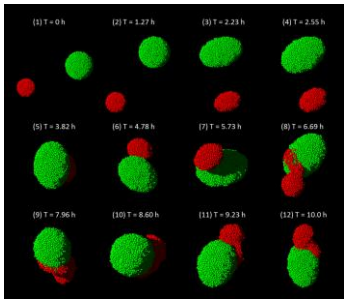

图 1：4179 Toutatis 小行星的形成过程

利用 MIRO 数据研究 67P 彗星彗发中水分子的早期分布

建立了一套包括三维形状输入、热物理模型、三维彗发模型、三维辐射转移模型、观测数据模拟和谱线反演等功能的三维程序分析 MIRO 的观测数据，分析了观测初期彗发中水分子的分布情况，得到了 Hapi 区域相比表面其他地方大概高出 10 个量级的活动性（Zhao et al., 2018， A&A, submitted）。

图 2 :Imhotep 活动性较强时水分子柱密度的空间分布

提出了 Bennu 等赤道隆起的小行星形状的形成机制

利用基于 REBOUND 程序包建立的 mass-spring 软件，模拟了小行星撞击产生地震波的过程，提出撞击激发全球振

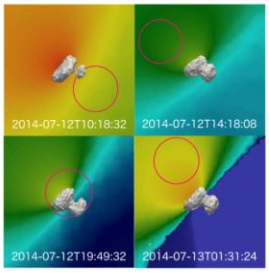

动从而导致赤道隆起的动力学机制，对不同尺度和物质成分及结构的小行星受到不同程度撞击后的命运理论进行了完善（Quillen, Zhao，Chen et al., 2019 ,Icarus）。

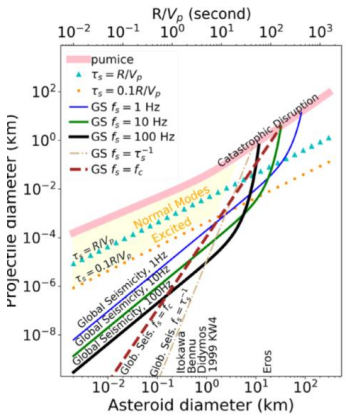

图 3：不同半径小行星受到不同尺度石头撞击后的动力学命运

67P 表面尘埃上升机制的研究

利用彗核表面热物理模型、重力场和自转相关的动力学研究了不同气体彗发带动不同尺度尘埃粒子离开彗核表面的动力学和热物理过程(Skorov, Reshetnyk, Rezac, Zhao et al., 2018, MNRAS)。

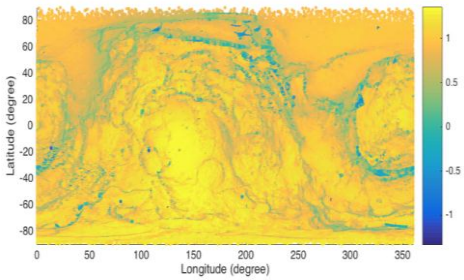

图 4： 67P 表面重力加速度分布

研究不同形状和自转状态彗核挥发性的影响

结合彗核表面热物理模型和彗核轨道及自转运动，研究不同形状和不同指向对彗核挥发性计算的影响，说明在研究彗核活动性和挥发率的问题下需考虑彗核活动和指向等参数（Marshall et al., 2018, MNRAS, submitted）。

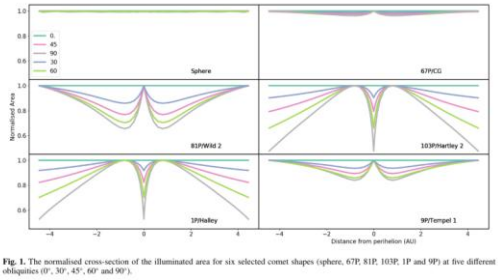

Fig. 1. The normalised cross-section of the illuminated area for six selected comet shapes (sphere, 67P, 81P, 103P, 1P and 9P) at five different obliquities (0°, 30°, 45°, 60° and 90°).

图 5：不同形状和指向对近日点前后彗核活动性的影响

基于二叉树的太阳系小天体数值历表建立方法

在小天体深空探测任务中，经常需要调用力模型较完备的精确小天体数值历表，然而由于部分小天体可能有较大的轨道偏心率及存在近距离飞越大行星的可能,导致传统的等区间分段切比雪夫多项式插值方法不适用于构建这些小天体的数值历表. 在传统方法基础上采用结合误差自适应的二分法对原始轨道进行分段，并采用二叉树结构来组织所有的分段区间，能解决历表读取中的系数反查问题. 以大偏心率近地小行星 4179 Toutatis 和 3200 Phaethon、大偏心率彗星 2P/Encke 以及将近距离飞越地球的 99942 Apophis 小行星为例，通过数值仿真证实了该算法的有效性. 由于该方法没有对小天体的轨道性质做任何要求，因此能够作为构建太阳系小天体数值历表的通用方法，可应用于大量目标小天体的精确轨道设计中（胡寿村等，2018 ,天文学报)。

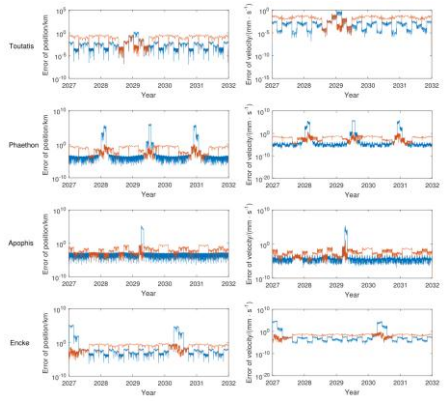

图 6 :传统方法(蓝色)与新方法(橙色)生成的历表位置和速度误差的对比。

系外行星研究方面：

1. 近距双星系统中S型行星的可能机制——P型行星散射引起的潮汐俘获

尽管目前人们已经在双星系统中探测到很多 S 型的行星，但是尚未在双星间距小于 5 au 的近距双星系统中探测到此类行星。而在观测上近距双星是普遍存在的。最近有系列研究提出在近距双星中探测此类行星的方法，并且下一步的探测项目如 PLATO 等完全可以探测此类行星。而行星形成理论一般认为在近距双星中“本地”形成这种行星是及其困难的。我们提出、检验了此类行星形成的一种可能机制。我们系统研究了 P 型行星之间的散射和后期行星与恒星之间的潮汐作用，研究潮汐作用是否可以将散射的行星俘获。研究表明这种机制是非常有效的。最大的俘获概率达到 10%以上，这和单恒星系统中通过散射——潮汐俘获机制形成热木星的几率相当。行星被俘获的概率和双星的轨道构型有关：双星的偏心率越小，质量比越小，则俘获的几率越大。我们还发现逆行行星可以在这一机制下自然形成，这是潮汐俘获和“本地”形成渠道的特征性区别。我们的研究结果为下一步探测此类行星提供了选源依据(Gong & Ji, 2018,MNRAS)。

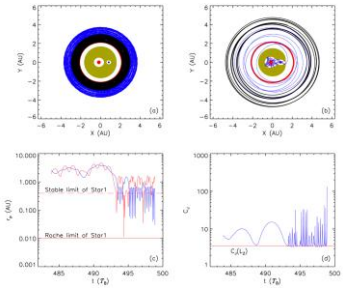

图 7：散射—潮汐俘获机制。（a）旋转坐标系中，不考虑行星之间的作用，2 颗 P 型行星轨道长期稳定。（b）考虑二者之间作用时，系统会发生散射，初始在外面的行星被恒星 1 俘获。（c）两颗行星到恒星 1 距离的演化。（d）被俘获行星的雅可比常数随时间的演化。

大气逃逸对行星半径和密度分布的影响

系统地研究了大气逃逸对行星演化的影响，指出短周期系外行星在 2 个地球半径处的分布低谷是对应岩石行星的特征，并基于此研究提出 Kepler 空间望远镜发现的低质量行星大多是岩石行星（Jin & Mordasini，2018， ApJ）。

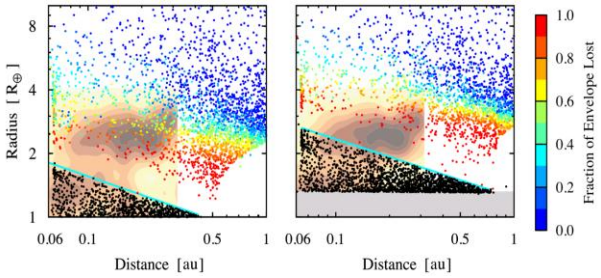

图 8：模拟结果和 Kepler 数据的比较。左：岩石行星族群的半径分布；右：含水 75%的行星族群的半径分布。图中表明 Kepler 行星的半径分布符合岩石行星族群的情况。

行星之间进入近共振构型的形成机制研究

针对目前 Kepler 计划观测到的多行星系统中轨道周期的分布情况发现，大部分的行星在演化过程中进入共振后会脱离共振到达近共振构型。我们提出了一种可能的形成机制解释这一过程。行星在进入共振后将嵌在一起迁移，而此时若气体盘仍存在时，行星由于进入共振而被激发的偏心率则会被抑制，与此同时行星将会有小幅度的轨道迁移过程，从而脱离共振到达目前的近共振构型。通过大量的数值计算，我们从统计上发现该机制可以解释目前的近共振构型的形成(Wang et al. 2018, in prep.)。

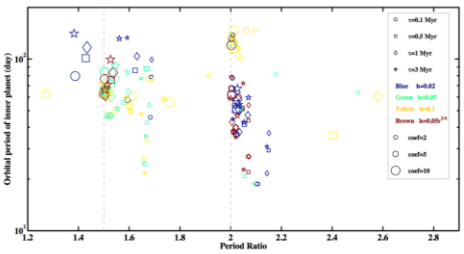

图 9：通过数值模拟获得的行星的周期比分布结果

多行星系统稳定性研究

目前发现的多行星系统中有很多是处于共振或者近共振构型，尤其是随着 Trappist-1 系统的发现，在该系统中七颗行星两两之间轨道周期处于简单的整数比，因此共振构型可能是多行星系统长期稳定存在的一个构型。我们考虑了气体盘的存在下行星的轨道迁移过程，检验了多行星系统的稳定需要的条件。我们发现气体盘的消散时标较长的情况下系统更容易稳定，但是共振构型行系统的稳定区域较小。当系统中存在行星较快或者较高的质量损失时系统可能由稳定状态变为不稳定(Wang et al. 2018, in prep.)。

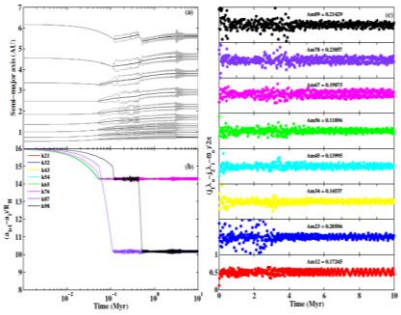

图 10：九颗行星系统的演化过程，在此情况下系统将稳定超过 10 百万年

极短周期行星的形成

目前发现的系外行星中有一部分行星非常靠近中心恒星，称之为极短周期行星，我们提出了极短周期的两种可能形成机制。一种是解释以 WASP-47 系统为代表的系统中行星的形成：行星初始形成在共振构型中，在潮汐作用下最接近中心恒星的行星的偏心率将会被压制，同时行星的轨道将会内迁，同时由于长期混沌效应行星的偏心率会被不断激发，不断的偏心率压制过程将会形成极短周期行星。另一种解释机制是行星在靠近恒星的过程中可能存在质量损失，当质量损失足够大的情况下将破坏系统的稳定性同时激发行星的偏心率，偏心率被压制的过程中可以形成极短周期行星(Wang et al. 2018, in prep.)。

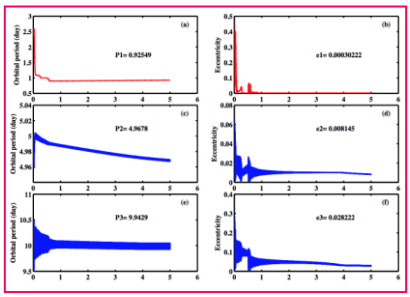

图 11：WASP-47 系统的形成演化过程

原行星盘方面研究：

通过数值模拟揭示原行星盘中旋涡结构证据

在该项研究中，通过流体动力学模拟，辐射转移计算，ALMA 图像处理，生成模拟的 12CO 气体分子的发射谱线，计算 12CO 分子的径向速度分布，确认了旋涡在原行星盘反气旋速度场的痕迹。这项研究对未来 ALMA 寻找原行星盘中的旋涡结构有重要意义(Huang et al. 2018, ApJ)。

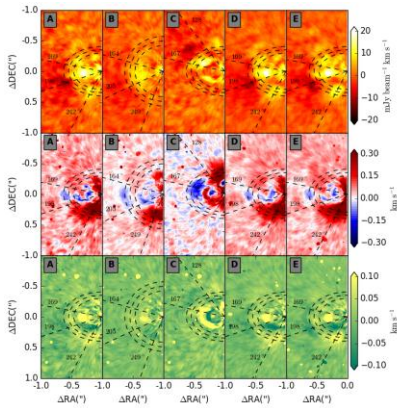

图 12：通过对比原行星盘中 12CO J=3-2 光谱发射线强度分布，速度分布和速度弥散的红移和蓝移部分，证实了反气旋的旋涡结构可以通过 ALMA 未来的观测进一步确认。

通过数值模拟研究原行星盘中的开尔文-亥姆霍兹不稳定性

基于流体动力学模拟，尘埃辐射转移计算，ALMA 图像处理，研究原行星盘中的开尔文-亥姆霍兹不稳定性，研究原行星盘中的环状结构的特性(Huang et al. 2018, in prep.)。

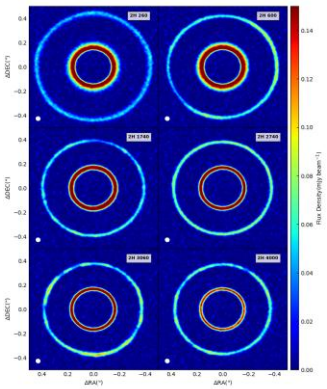

图 13：通过原行星盘中的尘埃与气体的相互作用，产生开尔文-亥姆霍兹不稳定性，从而使得原行星盘中的某些环状结构变得凹凸不平，为将来的 ALMA 观测提供指示。

原行星盘中旋涡产生的旋臂结构特征

通过流体动力学模拟不同的参量，触发罗斯贝波不稳定性，产生旋涡结构，旋涡产生旋臂结构，发现其旋臂结构与行星产生的旋臂结构并不相同(Huang et al. 2018, in prep.)。

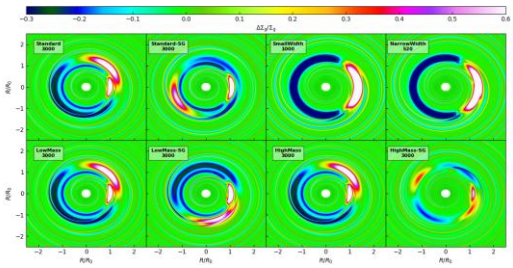

图 14：通过不同参数的流体力学模拟，确认原行星盘中的旋涡结构也能产生旋臂结构，特性与行星产生旋臂结构并不相同。旋涡产生的旋臂结构与质量并无直接关系，并且能产生多达 4,6 和 8 条旋臂。

原行星盘中旋涡产生的旋臂结构特征

参与了 HD 163296 系统的拟合工作，发现 HD 163296 系统观测到的尘埃、CO 的同位素分布可以通过行星和盘的相互作用来解释。理论模型指出，该系统气体盘的粘滞度在盘的内部必须非常低，而在盘的外部则相对较高。（Liu et al. 2018,ApJ）。

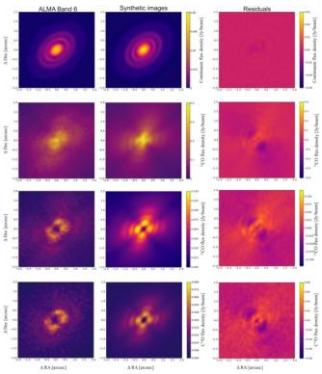

图 15：模拟结果和 HD 163296 系统的比较。从上至下四行分别给出了尘埃、12CO、13CO 和 C18O 的观测图像，理论模型拟合的图像，以及二者的残差。

天体化学方面:

对玻璃陨石开展了高精度钾同位素分析

玻璃陨石是小行星撞击地球表面过程中高温高压还原条件下产生的，记录了地球大规模撞击历史，研究它可以分析撞击蒸发事件中中等挥发性元素（如 K 和 Zn）的表现。利用高精度钾同位素测试方法，分析了来自三个不同散落区的七个玻璃陨石的钾同位素成分。所有玻璃陨石的钾同位素成分分布范围窄（δ41KBSE: −0.10 ± 0.03‰ 至 0.16 ± 0.04‰），与不同构造背景的地球玄武岩代表的均一的全岩硅酸盐地球无异。同时，对一块完整的海南玻璃陨石进行了精细剖面的钾和锌同位素对比分析，锌同位素变化大（δ66Zn: −0.39 ± 0.02‰ 至 2.38 ± 0.03‰），而钾在误差范围内没有明显变化（图 16）。对三个中等挥发性元素（K, Zn, Cu）的热化学计算表明，Cu 和 Zn 比 K 容易蒸发得多，可以产生较大的分异。相对地，亲石元素 K 由于非常低的活度系数倾向于留在硅酸盐溶体中，因此钾同位素几乎不分异。根据多个挥发性元素同位素体系在玻璃陨石和月球样品之间的对比，认为月球 Cu 和 Zn 元素亏损以及同位素分异是岩浆脱气或陨石撞击形成的，而钾元素在同样的过程中保持稳定。因此，月岩记录的钾同位素分异可能保留了月球形成事件中的同位素特征(Jiang et al.,2018, GCA, under review)。

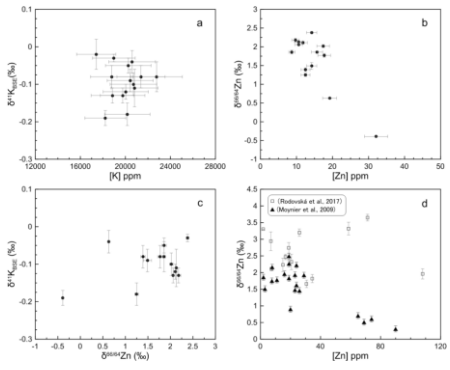

图 16：海南玻璃陨石的高精度钾和锌同位素对比分析。钾元素和钾同位素无相关性（a），而锌呈现明显的负相关（b）

使用 MWA 探测空间碎片

在对流星的观测过程中，发现了其他的射电暂现现象，主要是低轨道卫星对调频广播信号的反射。通过将反射信号与卫星轨道进行对比确认，探测到的最小卫星为立方卫星（cubesat），轨道高度为 600 km，大小为数十厘米。这证明了利用 FM 广播信号来探测空间碎片是可行的。图 17 按时间先后顺序从左向右排列，每张图像的积分时间为 2 秒。黄色圆圈代表根据卫星轨道根数推算出的卫星在 2 秒积分时间开始时的位置。为了减小背景辐射产生的噪声，这里给出的是相邻图像相减之后的结果 (Zhang et al.,2018, MNRAS) 。

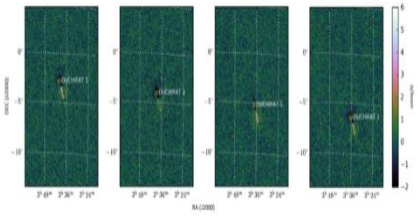

图 17. 默奇森宽场阵列探测到的立方卫星 Duchifat-1。

4-05 天体化学和行星科学实验室

本年度天体化学实验室在球粒陨石的矿物岩石学、太阳系小天体撞击年代学、灶神星陨石的热演化和冲击变质历史、中铁陨石的岩石成因学、以及铁陨石的碳同位素组成等学科方向上开展了广泛和深入的研究工作，取得了大量的第一手分析数据和成果，已在国际一流天体化学和矿物学杂志上发表 SCI 论文三篇。本年度获得国家自然科学青年基金一项，澳科大国家重点实验室开放课题一项，中科院留学基金一项。实验室李晔博士与丹麦自然历史博物馆合作开展铁陨石的碳同位素组成研究，廖世勇副研究员与瑞典 Lund 大学合作开展地球的陨石通量历史研究。李晔博士在中科院留学基金资助下前往加州大学洛杉矶分校开展为期一年的交流学习，与该校 Wasson 教授和 Rubin 教授建立了良好的合作关系。通过与国内外同行加强学术交流和合作，青年科研人员的研究工作水平得到了显著提升。

1. 小型天体之间的撞击事件可能无法产生充足的热量使全岩同位素时钟重置，因而难以获得其准确撞击年龄。通过原位微区手段测定陨石中局部冲击熔融脉中磷酸盐高压相 U-Pb 同位素组成，为解决这一难题提供途径。我们在国际上首次利用磷酸盐高压相进行 U-Pb 同位素定年，为小型天体间撞击事件年龄的获取提供新的途径，相关工作已发表在国际一流矿物学杂志 American Mineralogist 上。

2. 通常认为冲击之后的持续高温是造成同位素重置的决定性因素。然而，寺巷口陨石磷灰石 U-Pb 同位素体系受重置程度与高压相变程度具有显著的正相关，表明受到冲击过程中极端 P-T-t 条件的影响。我们将同位素分析技术与多种矿物学分析手段结合，验证磷灰石 U-Pb 同位素体系受冲击过程中极端 P-T-t 条件的影响，相关工作已发表在国际一流陨石学杂志 Meteoritics and Planetary Science 上。

3. 对 L 群普通球粒陨石 NWA 7251 进行了详细的岩石学、矿物学以及同位素年代学研究，结果显示以 NWA 7251 为代表的 L 群球粒陨石经历了两期重要的冲击变质作用，第一期发生在 44.6 亿年前，与成月事件相关；另一期发生在~500 Ma 年前，与 L 群球粒陨石母体碰撞裂解有关。相关工作已发表在国际一流陨石学杂志 Meteoritics and Planetary Science 上。

4. 对罕见的 LL7 型普通球粒陨石 NWA 11004 进行了详细的岩石学、矿物学、地球化学以及同位素年代学研究，发现 NWA 11004 记录有目前最古老的冲击变质事件，此次事件导致其发生高度重结晶以及部分熔融。

5. 在灶神星陨石 NWA 6594 中发现存在 4524±2Ma 的一期独立热事件，证实其与样品的热变质作用有关。该事件明显晚于 4550±10Ma 的成岩年龄，表明其与岩浆喷发堆叠过程无关，而更可能由后期岩浆侵入体加热导致。灶神星壳的热变质过程可能与持续的岩浆侵入活动关系密切。相关成果在 Meteoritics & Planetary Science 审稿中。

6. 中铁陨石作为一种罕见的石铁陨石，对于认识太阳系早期行星的形成和演化历史具有重要的科学意义。通过对尤溪陨石开展矿物岩石学、全岩化学和同位素地质年代学研究，证实了其硅酸盐相与灶神星陨石具有成因上的关联，通过对形成于金属相-硅酸盐相两相混合事件的磷酸盐进行 U-Pb 定年，确定了该陨石母体的形成年龄为~3.9 Ga，且两相混合导致硅酸盐母体发生了一系列的热变质。相关成果即将投稿。

4-06 近地天体望远镜 团组室

2018 年全年保持了近地天体望远镜的正常运行，共计获得了 163 天观测数据。建设了近地天体望远镜数据库南京点的数据库硬件系统，实现了数据库硬件裸容量 120TB，提供了后续观测热数产品数据的存储、备份和发布能力。实现了原始数据和定标数据的实时发布。2018 年度产生的新增原始数据容量为 11.5TB。

近地天体望远镜团组 2018 年的工作主线是围绕近地天体望远镜开展的观测，通过继续开展太阳系天体巡天观测，共计获得 250751 个(次)太阳系小天体的 990266 个观测数据，在全球台站观测量据第 8。2018 年度共发现了 549 个新小行星，其中 22 个小行星获得了正式编号。2018 年共监测了 415 个近地小行星的 2095 个位置数据，截止目前近地天体望远镜总计监测了 1977 个（次）近地小行星，得到了 10455 个位置数据。2018 年近地天体望远镜发现了 3 个新的近地小行星，均为 Apollo 型近地小行星。其中 2018 DH1 是一个 Apollo 型潜在威胁小行星（轨道根数：a=2.10AU,e=0.60,i=1.99,q=0.84AU）。截止目前近地天体望远镜已经发现了 18 个新的近地小行星。2018 年近地天体望远镜发现了 1 个新的半人马小天体 2018 RR2（轨道根数：a=21.43AU,e=0.64,i=40.23,q=7.69AU）。继续开展大样本小行星光变巡天，发现了一批超快自转小行星候选体和双小行星候选体，并利用已有的部分小行星样本开展了自转特性的统计分布研究。为后续开展近地天体监测预警网的建设，开展小行星地面观测研究和小行星深空探测的地基观测，开展大样本太阳系天体物理性质的观测研究，提供了有力的支撑。2018 年我国加入国际小行星预警网，近地天体望远镜作为其中的主干设备，赵海斌为技术专家。

近地天体望远镜开展了时域巡天计划，继续开展“紫台-清华超新星巡天计划”（PMO & Tsinghua Supernova Survey，PTSS），目前超新星搜索方面已经完成 SDSS-r，SDSS-i，VR 等 3 个波段北天绝大部份天区的模板建设和全自动瞬变源数据处理软件，本年度共计发现超新星候选体目标 31 个。开展了利用西藏阿里的小型望远镜开展时域巡天的数据处理系统建立（CSNS）。同时逐步释放变源星表，为我国的变源相关研究的团队提供了共享数据。与国家天文台合作开展银道面窄波段巡天观测计划（Narrow Band Survey，NBS），已经完成 SDSS-r’，SDSS-i’波段的 25000 平方度的巡天覆盖。近地天体望远镜开展了引力波源电磁对应体的搜索巡天观测。

本年度近地天体望远镜发现了 3 个新的近地小行星，均为 Apollo 型小行星，其中 2018 DH1 是一个 Apollo 型潜在威胁小行星（轨道根数：a=2.10AU,e=0.60,i=1.99,q=0.84AU）。截止目前近地天体望远镜已经发现了 18 个新的近地小行星。2018 年我国加入联合国和平利用外层空间委员会下设的国际小行星预警网络（IAWN），近地天体望远镜作为我国该领域的主干设备。

2018 年 9 月 8 日近地天体望远镜发现一个新的半人马小天体 2018 RR2，这是继 2010 年发现 2010 EJ104 后发现的

又一个奇异小天体，是目前近地天体望远镜在最远距离上发现的新的太阳系小天体。

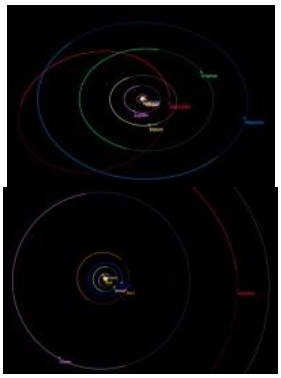

图 1. 2018 RR2 的轨道和大行星轨道图

2018 年共监测了 415 个近地小行星的 2095 个位置数据，截止目前近地天体望远镜总计监测了 1977 个（次）近地小行星，得到了 10455 个位置数据。开展太阳系小天体巡天观测，共计获得 250751 个(次)太阳系小天体的 990266 个观测数据，在全球观测量据第 8。2017 年度共发现了 549 个新小行星，其中 22 个小行星获得了正式编号。

开展了大样本小行星光变巡天，2018 年度共计获得了完成 800 多平方度天区观测，获得 1.14 万颗小行星的 3.8 万条光变曲线，从中找到一批具有特殊光变曲线的目标候选体，包括 6 个超快速自转的小行星候选体和 7 个具有双轨道同步小行星候选体。

近地天体望远镜开展了时域巡天计划，组织开展了“紫台-清华超新星巡天计划”（PTSS），完成和继续更新北天 SDSS-r，SDSS-i，VR 等 3 个波段天区的模板库建设和全自动瞬变源数据处理软件，本年度共计发现超新星候选体目标 31 个。

完成了近地天体望远镜数据库系统南京点的硬件建设，此数据库硬件裸容量为 120TB，提供了观测热数据的异地存储、备份和发布能力，提供了原始数据和定标数据的实时发布。2018 年度产生的新增原始数据容量为 11.5TB。

大力推进设备的共享观测，开展了 LIGO 引力波天文台光学电磁对应体的巡天搜索。接受开放观测项目包括反银心方向窄带巡天观测、Fast rotate asteroid 搜索、引力波事件对应体 Li-Paczynski 巨新星观测研究、中微子事件光学对应体搜索、主带活动彗星观测等。完成了转发式卫星导航试验系统盱眙站分系统运行。

4-07 行星光谱学研究团组（筹）

本年度发表学术论文 7 篇。6 月份在乌克兰太阳系天体观测国际会议做了邀请报告。入选嫦娥四号核心科学家团队。鉴于行星光谱与遥感是深空探测所需技术，包括月球、火星、小行星乃至地球都有广泛应用，团组开展了多个课题研究，包括重点研发《红外基准载荷测月应用》、863 项目《月亮定标技术》、中科院重点培育《数字月球图》以及重点实验室主任季江徽研究员牵头的《小行星背景型号》等。向科工局建议了本世纪最长月食前后利用我国高分卫星进行调姿对月观测计划并得到批准，首次获得了中波月球图，承担了高分、天宫、军星等多颗卫星对月定标，在对月定标领域建立了影响，还有多颗卫星已受邀负责对月定标，今后将在该领域显示领军单位作用。

（1）对雨海西北部开展了物质成分、定年、构造、地质图、火山喷发规模等系统性研究，获得了多项成果及新认识。综合利用光谱、地形、雷达等多源数据绘制了最为详细的地质图，提出将爱拉托迅纪玄武岩细分为上爱拉托迅纪（UEm）和下爱拉托迅纪（LEm）的新观点。提出了新类型的高地—铁镁质高地（MH）的概念。识别出高地广泛分布橄榄石、斜方辉石等铁镁质矿物，首次明确发现了橄长岩，绘制了玄武岩厚度分布图，识别出大量年轻构造（<10 Ma），说明月球的构造活动持续到很年轻，并非过去所认为的月球在 31 亿年前就已经死亡。该成果作为 Icarus 封面文章并受央视报导（http://m.cas.cn/kyjz1/201804/t20180402_4640676.html）。

（2）嫦娥三号红外光谱数据处理、分析与应用。对国际上首次在月球表面测试的光谱开展了深入的处理与分析，校正了近红外探测器与短波红外探测器之间的差异，为用户提供高质量光谱数据。获得了月球绝对亮度，揭示了国际上其他探测器测量存在的偏差，指出美国 LROC WAC 数据定标偏大偏红并得到认可，促进了美国卫星定标。提出了嫦娥三号着陆点作为国际新的月球定标点。与现今常用的定标点（如 Apollo16、MS2）相比具有时代年轻、地形平坦、受污染少、具有原位测试数据等多种优势。此外，还在多方面纠正了过去研究的错误观点，例如：

（a）太空风化。过去认为太空风化导致光谱变红。广泛采用的著名的月壤 TiO2 含量反演模型基于此观点。我们的研究认为风化导致光谱变蓝而非变红。该发现具有重要的意义。意味着月壤风化模型、TiO2 反演模型等都需要改写。

（b）飞船着陆后月表变亮原因。过去所有观点都认为是火箭吹拂导致月表变平坦使得月表变亮。我们认为是化学原因（太空风化）而非物理原因（表面平坦）。火箭吹拂掉表皮极薄、极暗的风化层，并提出了真实月表风化模型。该研究也揭示了 Apollo 月球样品并不代表月球真实的太空风化特征，并提出了今后采集极表皮月壤样品的建议。

（c）近红外光谱抬升因素。过去发表在 Nature Commun 文章认为近红外谱段抬升是因为矿物在 2μm 附近吸收所致，

并据此解译矿物。我们认为是温度原因。这是因为月表无大气，白天温度很高，近红外谱段就体现了热效应。首次利用短波红外波段获得了月壤温度，发现月表实际温度高于模型模拟的温度，揭示了月壤微尺度具有显着的温度效应。

综上所述，尽管嫦娥三号月球车红外光谱仪仅获得 4 条光谱，在 EPSL、GRL、AJ、RAA 发表四篇颠覆过去观点的成果。

（3）向科工局建议高分卫星对月观测。向科工局建议 7 月 27 日世纪最长月全食前后利用我国高分静止地球卫星对月观测的建议得到批准。科工局协调数据接收、二六、卫星总体等单位负责观测，本团组负责制定观测计划、观测时间、相机曝光时间和后去数据处理应用等。获取了±30o、90o 以及满月月图，其中中波红外月图为国际上首次。目前负责数据的处理与应用在进展中。

三、学术交流与合作

1、国际合作与交流概况

2018 年，紫台人才培养方面，执行中美联合培养博士生 3 人、中英联合培养博士生 1 人。中国科学院国际人才计划项目方面，执行“国际访问学者”2 项、“国际博士后”1 项，新立项国际人才计划项目 2 项、科学院国际特别交流项目 1 项、台湾青年学者计划 1 项。

紫台主办/承办的国际会议共 3 场，分别是“第二届东亚天文统计学国际会议”、“第四届中澳天体物理学研讨会”和“关于举办第 18 届中美前沿科学研讨会的请示”。

ABSTRACT LIST OF PUBLICATIONS IN 2018

I. Dark Matter & Space Astronomy

Cosmic Gamma Ray Bursts, Neutron Stars, and Relevant Physics

第 1 条，共 248 条

Short GRBs: Opening Angles, Local Neutron Star Merger Rate, and Off-axis Events for GRB/GW Association

Jin, ZP (Jin, Zhi-Ping); Li, X (Li, Xiang); Wang, H (Wang, Hao); Wang, YZ (Wang, Yuan-Zhu); He, HN (He, Hao-Ning); Yuan, Q (Yuan, Qiang); Zhang, FW (Zhang, Fu-Wen); Zou, YC (Zou, Yuan-Chuan); Fan, YZ (Fan, Yi-Zhong); Wei, DM (Wei, Da-Ming)
ASTROPHYSICAL JOURNAL
卷: 857 期: 2 文献号: 128
The jet breaks in the afterglow light curves of short gamma-ray bursts (SGRBs), rarely detected so far, are crucial for estimating the half-opening angles of the ejecta (theta(j)) and hence the neutron star merger rate. In this work, we report the detection of jet decline behaviors in GRB 150424A and GRB 160821B, and find theta j similar to 0.1 rad. Together with five events reported before 2015 and three others "identified" recently (GRB 050709, GRB 060614, and GRB 140903A), we have a sample consisting of nine SGRBs and one long-short GRB with reasonably estimated theta(j). In particular, three Swift bursts in the sample have redshifts z <= 0.2, with which we estimate the local neutron star merger rate density to be similar to 1109(-657)(+1432) Gpc(-3) yr(-1) or 162(-83)(+140) Gpc(-3) yr(-1) if the narrowly beamed GRB 061201 is excluded. Inspired by the typical theta(j) similar to 0.1 rad found currently, we further investigate whether the off-beam GRBs (in the uniform jet model) or the off-axis events (in the structured jet model) can significantly enhance the GRB/GW association. For the former, the enhancement is at most moderate, while for the latter the enhancement can be much greater and a high GRB/GW association probability of similar to 10% is possible. We also show that the data of GRB 160821B may contain a macronova/kilonova emission component with a temperature of similar to 3100 K at similar to 3.6 days after the burst and more data are needed to ultimately clarify.

第 2 条，共 248 条

Neutrinos from Choked Jets Accompanied by Type-II Supernovae

He, HN (He, Hao-Ning); Kusenko, A (Kusenko, Alexander); Nagataki, S (Nagataki, Shigehiro); Fan, YZ (Fan, Yi-Zhong); Wei, DM (Wei, Da-Ming)
ASTROPHYSICAL JOURNAL
卷: 856 期: 2 文献号: 119
The origin of the IceCube neutrinos is still an open question. Upper limits from diffuse gamma-ray observations suggest that the neutrino sources are either distant or hidden from gamma-ray observations. It is possible that the neutrinos are produced in jets that are formed in core-collapsing massive stars and fail to break out, the so-called choked jets. We study neutrinos from the jets choked in the hydrogen envelopes of red supergiant stars. Fast photo-meson cooling softens the neutrino spectrum, making it hard to explain the PeV neutrinos observed by IceCube in a one-component scenario, but a two-component model can explain the spectrum. Furthermore, we predict that a newly born jet-driven type-II supernova may be observed to be associated with a neutrino burst detected by IceCube.

第 3 条，共 248 条

HESS J1640-465: A Gamma-Ray Emitting Pulsar Wind Nebula?

Xin, YL (Xin, Yu-Liang); Liao, NH (Liao, Neng-Hui); Guo, XL (Guo, Xiao-Lei); Yuan, Q (Yuan, Qiang); Liu, SM (Liu, Si-Ming); Fan, YZ (Fan, Yi-Zhong); Wei, DM (Wei, Da-Ming)
ASTROPHYSICAL JOURNAL
卷: 867 期: 1 文献号: 55
HESS J1640-465 is an extended TeV gamma-ray source, and whether its.-ray emission is from the shell of a supernova remnant (SNR) or a pulsar wind nebula (PWN) is still under debate. We reanalyze the GeV gamma-ray data in the field of HESS J1640-465 using eight years of Pass 8 data recorded by the Fermi Large Area Telescope. An extended GeV gamma-ray source positionally coincident with HESS J1640-465 is found. Its photon spectrum can be described by a power law with an index of 1.42 +/- 0.19 in the energy range of 10-500 GeV and smoothly connects with the TeV spectrum of HESS J1640-465. The broadband spectrum of HESS J1640-465 can be well fit by a leptonic model with a broken power-law spectrum of electrons with an exponential cut off at similar to 300 TeV. The spectral properties of HESS J1640-465 are broadly consistent with the characteristics of other sources identified as PWNe, such as the correlations between high-energy luminosity ratios and the physical parameters of pulsar, including the spin-down luminosity E. and the characteristic age T-c. All of these pieces of evidence support that the.-ray emission of HESS J1640-465 may originate from the PWN powered by PSR J1640-4631 rather than the shell of the SNR G338.3-0.0.

第 4 条，共 248 条

Studies on Cosmic-Ray Nuclei with Voyager, ACE, and AMS-02. I. Local Interstellar Spectra and Solar Modulation

Zhu, CR (Zhu, Cheng-Rui); Yuan, Q (Yuan, Qiang); Wei, DM (Wei, Da-Ming)
ASTROPHYSICAL JOURNAL
卷: 863 期: 2 文献号: 119
The acceleration of cosmic-ray particles and their propagation in the Milky Way and the heliosphere tangle with each other, leading to complexity and degeneracy of the modeling of Galactic cosmic rays (GCRs). The recent measurements of the GCR spectra by Voyager-1 from outside of the heliosphere gave the first direct observation of GCRs in the local interstellar (LIS) environment. Together with the high-precision data near the Earth taken by the Advanced Composition Explorer (ACE) and AMS-02, we derive the LIS spectra of helium, lithium, beryllium, boron, carbon, and oxygen nuclei from a few MeV n(-1) to TeV

n(-1), using a non-parameterization method. These LIS spectra are helpful in further studying the injection and propagation parameters of GCRs. The nearly 20 years of data recorded by ACE are used to determine the solar modulation parameters over solar cycles 23 and 24, based on the force-field approximation. We find general agreements of the modulation potential with the results inferred from neutron monitors and other cosmic-ray data.

第 5 条，共 248 条

The Diversity of Kilonova Emission in Short Gamma-Ray Bursts

Gompertz, BP (Gompertz, B. P.); Levan, AJ (Levan, A. J.); Tanvir, NR (Tanvir, N. R.); Hjorth, J (Hjorth, J.); Covino, S (Covino, S.); Evans, PA (Evans, P. A.); Fruchter, AS (Fruchter, A. S.); Gonzalez-Fernandez, C (Gonzalez-Fernandez, C.); Jin, ZP (Jin, Z. P.); Lyman, JD (Lyman, J. D.); Oates, SR (Oates, S. R.); O'Brien, PT (O'Brien, P. T.); Wiersema, K (Wiersema, K.)
ASTROPHYSICAL JOURNAL
卷: 860 期: 1 文献号: 62
The historic first joint detection of both gravitational-wave and electromagnetic emission from a binary neutron star merger cemented the association between short gamma-ray bursts (SGRBs) and compact object mergers, as well as providing a well-sampled multi-wavelength light curve of a radioactive kilonova (KN) for the first time. Here, we compare the optical and near-infrared light curves of this KN, AT 2017gfo, to the counterparts of a sample of nearby ($z < 0.5$) SGRBs to characterize their diversity in terms of their brightness distribution. Although at similar epochs AT 2017gfo appears fainter than every SGRB-associated KN claimed so far, we find three bursts (GRBs 050509B, 061201, and 080905A) where, if the reported redshifts are correct, deep upper limits rule out the presence of a KN similar to AT 2017gfo by several magnitudes. Combined with the properties of previously claimed KNe in SGRBs this suggests considerable diversity in the properties of KN drawn from compact object mergers, despite the similar physical conditions that are expected in many NS-NS mergers. We find that observer angle alone is not able to explain this diversity, which is likely a product of the merger type (NS-NS versus NS-BH) and the detailed properties of the binary (mass ratio, spins etc.). Ultimately disentangling these properties should be possible through observations of SGRBs and gravitational-wave sources, providing direct measurements of heavy element enrichment throughout the universe.

第 6 条，共 248 条

How Special Is GRB 170817A?

Yue, C (Yue, Chuan); Hu, Q (Hu, Qian); Zhang, FW (Zhang, Fu-Wen); Liang, YF (Liang, Yun-Feng); Jin, ZP (Jin, Zhi-Ping); Zou, YC (Zou, Yuan-Chuan); Fan, YZ (Fan, Yi-Zhong); Wei, DM (Wei, Da-Ming)
ASTROPHYSICAL JOURNAL LETTERS
卷: 853 期: 1 文献号: L10
GRB 170817A is the first short gamma-ray burst (GRB) with direct detection of the gravitational-wave radiation and also the spectroscopically identified macronova emission (i.e., AT 2017gfo). The prompt emission of this burst, however, is underluminous in comparison with the other short GRBs with known redshift. In this work, we examine whether GRB 170817A is indeed unique. We first show that GRB 130603B/macronova may be the on-axis "analogs" of GRB 170817A/AT 2017gfo, and the extremely dim but long-lasting afterglow emission of GRB 170817A may suggest a low number density (similar to 10(-5) cm(-3)) of its circumburst medium and a structured outflow. We then discuss whether GRB 070923, GRB 080121, GRB 090417A, GRB 111005A, and GRB 170817A form a new group of very nearby underluminous GRBs originated from neutron star mergers. If the short events GRB 070923, GRB 080121, and GRB 090417A are indeed at a redshift of similar to 0.076, 0.046, 0.088, respectively, their isotropic energies of the prompt emission are similar to 10(47) erg and thus comparable to the other two events. The non-detection of optical counterparts of GRB 070923, GRB 080121, GRB 090417A, and GRB 111005A, however, strongly suggests that the macronovae from neutron star mergers are significantly diverse in luminosities or, alternatively, there is another origin channel (for instance, the white dwarf and black hole mergers). We finally suggest that GW170817/GRB 170817A are likely not alone and similar events will be detected by the upgraded/upcoming gravitational-wave detectors and the electromagnetic monitors.

High-energy Solar physics

第 7 条，共 248 条

Looking for the Gluon Condensation Signature in Protons Using the Earth-limb Gamma-Ray Spectra

Feng, L (Feng, Lei); Ruan, JH (Ruan, Jianhong); Wang, F (Wang, Fan); Zhu, W (Zhu, Wei)
ASTROPHYSICAL JOURNAL
卷: 868 期: 1 文献号: 2
A new type of gamma-ray spectrum is predicted in a general hadronic framework by taking into account gluon condensation (GC) effects in proton. The result presents a power law with a sharp break in the gamma-ray spectra at the TeV band. We suggest probing this GC signature in Earth-limb gamma-ray spectra using the Dark Matter Particle Explorer and the Calorimetric Electron Telescope in orbit.

第 8 条，共 248 条

Determination of Differential Emission Measure from Solar Extreme Ultraviolet Images

Su, Y (Su, Yang); Veronig, AM (Veronig, Astrid M.); Hannah, IG (Hannah, Iain G.); Cheung, MCM (Cheung, Mark C. M.); Dennis, BR (Dennis, Brian R.); Holman, GD (Holman, Gordon D.); Gan, WQ (Gan, Weiqun); Li, YP (Li, Youping)
ASTROPHYSICAL JOURNAL LETTERS
卷: 856 期: 1 文献号: L17
The Atmospheric Imaging Assembly (AIA) on board the Solar Dynamic Observatory (SDO) has been providing high-cadence, high-resolution, full-disk UV-visible/extreme ultraviolet (EUV) images since 2010, with the best time coverage among all the solar missions. A number of codes have been developed to extract plasma differential emission measures (DEMs) from AIA images. Although widely used, they cannot effectively constrain the DEM at flaring temperatures with AIA data alone. This often results in much higher X-ray fluxes than observed. One way to solve the problem is by adding more constraint from other data sets (such as soft X-ray images and fluxes). However, the spatial information of plasma DEMs are lost in many cases. In this Letter, we present a different approach to constrain the DEMs. We tested the sparse inversion code and show that the default settings reproduce X-ray fluxes that could be too high. Based on the tests with both simulated and observed AIA data, we provided recommended settings of basis functions and tolerances. The new DEM solutions derived from AIA images alone are much more consistent with

(thermal) X-ray observations, and provide valuable information by mapping the thermal plasma from similar to 0.3 to similar to 30 MK. Such improvement is a key step in understanding the nature of individual X-ray sources, and particularly important for studies of flare initiation.

第 9 条，共 248 条

Spectroscopic Observations of a Current Sheet in a Solar Flare

Li, Y (Li, Y.); Xue, JC (Xue, J. C.); Ding, MD (Ding, M. D.); Cheng, X (Cheng, X.); Su, Y (Su, Y.); Feng, L (Feng, L.); Hong, J (Hong, J.); Li, H (Li, H.); Gan, WQ (Gan, W. Q.)
ASTROPHYSICAL JOURNAL LETTERS
卷: 853 期: 1 文献号: L15
The current sheet is believed to be the region of energy dissipation via magnetic reconnection in solar flares. However, its properties, for example, the dynamic process, are not fully understood. Here, we report a current sheet in a solar flare (SOL2017-09-10T16:06) that was clearly observed by the Atmospheric Imaging Assembly on board the Solar Dynamics Observatory as well as the EUV Imaging Spectrometer on Hinode. The high-resolution imaging and spectroscopic observations show that the current sheet is mainly visible in high-temperature (> 10 MK) passbands, particularly in the Fe XXIV. 192.03 A. line with a formation temperature of similar to 18 MK. The hot Fe XXIV. 192.03 angstrom. line exhibits very large nonthermal velocities up to 200 km s(-1) in the current sheet, suggesting that turbulent motions exist there. The largest turbulent velocity occurs at the edge of the current sheet, with some offset with the strongest line intensity. At the central part of the current sheet, the turbulent velocity is negatively correlated with the line intensity. From the line emission and turbulent features we obtain a thickness in the range of 7-11 Mm for the current sheet. These results suggest that the current sheet has internal fine and dynamic structures that may help the magnetic reconnection within it proceed efficiently.

第 10 条，共 46 条

Space Solar Physics in China

Gan Weiqun; Fan Quanlin
Chinese Journal of Space Science
卷: 38 期: 5 页: 662-664
The activities of Chinese space solar physics in 2016-2018 can be divided into two categories: prestudy projects and mission-level projects. Both projects were undertaken smoothly. Especially the ASO-S, after several years' promotion, finally got formal approval at the end of 2017. This paper describes in brief the status of all related projects.

第 11 条，共 248 条

Photometric Solutions of Three Eclipsing Binary Stars Observed from Dome A, Antarctica

Liu, N (Liu, N.); Fu, JN (Fu, J. N.); Zong, W (Zong, W.); Wang, LZ (Wang, L. Z.); Uddin, SA (Uddin, S. A.); Zhang, XB (Zhang, X. B.); Zhang, YP (Zhang, Y. P.); Cang, TQ (Cang, T. Q.); Li, G (Li, G.); Yang, Y (Yang, Y.); Yang, GC (Yang, G. C.); Mould, J (Mould, J.); Morrell, N (Morrell, N.)
ASTRONOMICAL JOURNAL
卷: 155 期: 4 文献号: 168
Based on spectroscopic observations for the eclipsing binaries CSTAR 036162 and CSTAR 055495 with the WiFeS/2.3 m telescope at SSO and CSTAR 057775 with the Mage/Magellan I at LCO in 2017, stellar parameters are derived. More than 100 nights of almost-continuous light curves reduced from the time-series photometric observations by CSTAR at Dome A of Antarctic in i in 2008 and in g and r in 2009, respectively, are applied to find photometric solutions for the three binaries with the Wilson-Devinney code. The results show that CSTAR 036162 is a detached configuration with the mass ratio q = 0.354 +/- 0.0009, while CSTAR 055495 is a semi-detached binary system with the unusual q = 0.946 +/- 0.0006, which indicates that CSTAR 055495 may be a rare binary system with mass ratio close to one and the secondary component filling its Roche Lobe. This implies that a mass-ratio reversal has just occurred and CSTAR 055495 is in a rapid mass-transfer stage. Finally, CSTAR 057775 is believed to be an A-type W UMa binary with q = 0.301 +/- 0.0008 and a fill-out factor of f = 0.742(8).

第 12 条，共 248 条

Identifying Anticyclonic Vortex Features Produced by the Rossby Wave Instability in Protoplanetary Disks

Huang, PH (Huang, Pinghui); Isella, A (Isella, Andrea); Li, H (Li, Hui); Li, ST (Li, Shengtai); Ji, JH (Ji, Jianghui)
ASTROPHYSICAL JOURNAL
卷: 867 期: 1 文献号: 3
Several nearby protoplanetary disks have been observed to display large-scale crescents in the (sub) millimeter dust continuum emission. One interpretation is that these structures correspond to anticyclonic vortices generated by the Rossby wave instability within the gaseous disk. Such vortices have local gas overdensities and are expected to concentrate dust particles with a Stokes number around unity. This process might catalyze the formation of planetesimals. Whereas recent observations showed that dust crescents are indeed regions where millimeter-size particles have abnormally high concentration relative to the gas and smaller grains, no observations have yet shown that the gas within the crescent region counterrotates with respect to the protoplanetary disk. Here we investigate the detectability of anticyclonic features through measurement of the line-of-sight component of the gas velocity obtained with ALMA. We carry out 2D hydrodynamic simulations and 3D radiative transfer calculations of a protoplanetary disk characterized by a vortex created by the tidal interaction with a massive planet. As a case study, the disk parameters are chosen to mimic the IRS. 48 system, which has the most prominent crescent observed to date. We generate synthetic ALMA observations of both the dust continuum and (CO)-C-12 emission around the frequency of 345 GHz. We find that the anticyclonic features of the vortex are weak but can be detected if both the source and the observational setup are properly chosen. We provide a recipe for maximizing the probability of detecting such vortex features and present an analysis procedure to infer their kinematic properties.

第 13 条，共 248 条

Properties of a Small-scale Short-duration Solar Eruption with a Driven Shock

Ying, BL (Ying, Beili); Feng, L (Feng, Li); Lu, L (Lu, Lei); Zhang, J (Zhang, Jie); Magdalenic, J (Magdalenic, Jasmina); Su, YN (Su, Yingna); Su, Y (Su, Yang); Gan, WQ (Gan, Weiqun)
ASTROPHYSICAL JOURNAL
卷: 856 期: 1 文献号: 24
Large-scale solar eruptions have been extensively explored over many years. However, the properties of small-scale events with associated shocks have rarely been investigated. We present analyses of a small-scale, short-duration event originating from a small region. The impulsive phase of the M1.9-class flare lasted only four minutes. The kinematic evolution of the CME hot channel reveals some exceptional characteristics, including a very short duration of the main

acceleration phase (<2 minutes), a rather high maximal acceleration rate (similar to 50 km s(-2)), and peak velocity (similar to 1800 km s(-1)). The fast and impulsive kinematics subsequently results in a piston-driven shock related to a metric type II radio burst with a high starting frequency of similar to 320 MHz of the fundamental band. The type II source is formed at a low height of below 1.1. R-circle dot less than similar to 2 minutes after the onset of the main acceleration phase. Through the band-split of the type II burst, the shock compression ratio decreases from 2.2 to 1.3, and the magnetic field strength of the shock upstream region decreases from 13 to 0.5 Gauss at heights of 1.1-2.3 R-circle dot. We find that the CME (similar to 4 x 10(30) erg) and flare (similar to 1.6 x 10(30) erg) consume similar amounts of magnetic energy. The same conclusion for large-scale eruptions implies that small-and large-scale events possibly share a similar relationship between CMEs and flares. The kinematic particularities of this event are possibly related to the small footpoint-separation distance of the associated magnetic flux rope, as predicted by the Erupting Flux Rope model.

第 14 条，共 248 条

Confronting the DAMPE excess with the scotogenic type-II seesaw model

Ding, R (Ding, Ran); Han, ZL (Han, Zhi-Long); Feng, L (Feng, Lei); Zhu, B (Zhu, Bin)
CHINESE PHYSICS C
卷: 42 期: 8 文献号: UNSP 083104
The DArk Matter Particle Explorer (DAMPE) has observed a tentative peak at E similar to 1.4 TeV in the cosmic-ray electron spectrum. In this paper, we interpret this excess in the scotogenic type-II seesaw model. This model extends the canonical type-II seesaw model with dark matter (DM) candidates and a loop-induced vacuum expectation value of the triplet scalars, v(Delta), resulting in small neutrino masses naturally even for TeV scale triplet scalars. Assuming a nearby DM subhalo, the DAMPE excess can be explained by DM annihilating into a pair of triplet scalars which subsequently decay to charged lepton final states. Spectrum fitting of the DAMPE excess indicates it potentially favors the inverted neutrino mass hierarchy. We also discuss how to evade associated neutrino flux in our model.

第 15 条，共 248 条

Explaining the DAMPE data with scalar dark matter and gauged U(1)(Le- L mu) interaction

Cao, JJ (Cao, Junjie); Feng, L (Feng, Lei); Guo, XF (Guo, Xiaofei); Shang, LL (Shang, Liangliang); Wang, F (Wang, Fei); Wu, PW (Wu, Peiwen); Zu, L (Zu, Lei)
EUROPEAN PHYSICAL JOURNAL C
卷: 78 期: 3 文献号: 198
Inspired by the peak structure observed by recent DAMPE experiment in e(+)e(-) cosmic-ray spectrum, we consider a scalar dark matter (DM) model with gauged U(1)(Le-L mu) symmetry, which is the most economical anomaly-free theory to potentially explain the peak by DM annihilation in nearby subhalo. We utilize the process chi chi -> Z'Z' -> l (l) over barl'(l) over bar' , where chi, Z', l(()')()) denote the scalar DM, the new gauge boson and l(()')()) = e, mu, respectively, to generate the e(+)e(-) spectrum. By fitting the predicted spectrum to the experimental data, we obtain the favored DM mass range m(chi) similar or equal to 3060(-100)(+80) GeV and Delta m = m(chi) - m(Z') less than or similar to 14 GeV at 68% Confidence Level (C.L.). Furthermore, we determine the parameter space of the model which can explain the peak and meanwhile satisfy the constraints from DM relic abundance, DM direct detection and the collider bounds. We conclude that the model we consider can account for the peak, although there exists a tension with the constraints from the LEP-II bound on m(Z') arising from the cross section measurement of e(+)e(-) -> Z'* -> e(+)e(-).

第 16 条，共 248 条

Simplified TeV leptophilic dark matter in light of DAMPE data

Duan, GH (Duan, Guang Hua); Feng, L (Feng, Lei); Wang, F (Wang, Fei); Wu, L (Wu, Lei); Yang, JM (Yang, Jin Min); Zheng, R (Zheng, Rui)
JOURNAL OF HIGH ENERGY PHYSICS
期: 2 文献号: 107
Using a simplified framework, we attempt to explain the recent DAMPE cosmic e(+) + e(-) flux excess by leptophilic Dirac fermion dark matter (LDM). The scalar (Phi(0)) and vector (Phi(1)) mediator fields connecting LDM and Standard Model particles are discussed. We find that the couplings P circle times S, P circle times P, V circle times A and V circle times V can produce the right bump in e(+) + e(-) flux for a DM mass around 1.5 TeV with a natural thermal annihilation cross-section < sigma v > similar to 3 x 10(-26)cm(3)/s today. Among them, V circle times V coupling is tightly constrained by PandaX-II data (although LDM-nucleus scattering appears at one-loop level) and the surviving samples appear in the resonant region, m(Phi 1) similar or equal to 2m(chi). We also study the related collider signatures, such as dilepton production pp -> Phi(1) -> l(+) l(-), and muon g - 2 anomaly. Finally, we present a possible U(1)(X) realization for such leptophilic dark matter.

第 17 条，共 248 条

Two-stage Energy Release Process of a Confined Flare with Double HXR Peaks

Ning, H (Ning, Hao); Chen, Y (Chen, Yao); Wu, Z (Wu, Zhao); Su, Y (Su, Yang); Tian, H (Tian, Hui); Li, G (Li, Gang); Du, GH (Du, Guohui); Song, HQ (Song, Hongqiang)
ASTROPHYSICAL JOURNAL
卷: 854 期: 2 文献号: 178
A complete understanding of the onset and subsequent evolution of confined flares has not been achieved. Earlier studies mainly analyzed disk events so as to reveal their magnetic topology and the cause of confinement. In this study, taking advantage of a tandem of instruments working at different wavelengths of X-rays, EUVs, and microwaves, we present dynamic details about a confined flare observed on the northwestern limb of the solar disk on 2016 July 24. The entire dynamic evolutionary process starting from its onset is consistent with a loop-loop interaction scenario. The X-ray profiles manifest an intriguing double-peak feature. From the spectral fitting, it has been found that the first peak is nonthermally dominated, while the second peak is mostly multithermal with a hot (similar to 10 MK) and a super-hot (similar to 30 MK) component. This double-peak feature is unique in that the two peaks are clearly separated by 4 minutes, and the second peak reaches up to 25-50 keV; in addition, at energy bands above 3 keV, the X-ray fluxes decline significantly between the two peaks. This, together with other available imaging and spectral data, manifest a two-stage energy release process. A comprehensive analysis is carried out to investigate the nature of this two-stage process. We conclude that the second stage with the hot and super-hot sources mainly involves direct heating through a loop-loop reconnection at a relatively high altitude in the corona. The uniqueness of the event characteristics and the complete dataset make the study a nice addition to present literature on solar flares.

第 18 条，共 248 条

Non-LTE Calculations of the Fe I 6173 angstrom Line in a Flaring Atmosphere

Hong, J (Hong, Jie); Ding, MD (Ding, M. D.); Li, Y (Li, Ying); Carlsson, M (Carlsson, Mats)
ASTROPHYSICAL JOURNAL LETTERS
卷: 857 期: 1 文献号: L2
The Fe I 6173 angstrom line is widely used in the measurements of vector magnetic fields by instruments including the Helioseismic and Magnetic Imager (HMI). We perform non-local thermodynamic equilibrium calculations of this line based on radiative hydrodynamic simulations in a flaring atmosphere. We employ both a quiet-Sun atmosphere and a penumbral atmosphere as the initial one in our simulations. We find that, in the quiet-Sun atmosphere, the line center is obviously enhanced during an intermediate flare. The enhanced emission is contributed from both radiative backwarming in the photosphere and particle beam heating in the lower chromosphere. A blue asymmetry of the line profile also appears due to an upward mass motion in the lower chromosphere. If we take a penumbral atmosphere as the initial atmosphere, the line has a more significant response to the flare heating, showing a central emission and an obvious asymmetry. The low spectral resolution of HMI would indicate some loss of information, but the enhancement and line asymmetry are still kept. By calculating polarized line profiles, we find that the Stokes I and V profiles can be altered as a result of flare heating. Thus the distortion of this line has a crucial influence on the magnetic field measured from this line, and one should be cautious in interpreting the magnetic transients observed frequently in solar flares.

Multi-Band Observation Solar Activity

第 19 条，共 248 条

Non-damping oscillations at flaring loops

Li, D (Li, D.); Yuan, D (Yuan, D.); Su, YN (Su, Y. N.); Zhang, QM (Zhang, Q. M.); Su, W (Su, W.); Ning, ZJ (Ning, Z. J.)
ASTRONOMY & ASTROPHYSICS
卷: 617 文献号: A86
Context. Quasi-periodic oscillations are usually detected as spatial displacements of coronal loops in imaging observations or as periodic shifts of line properties (i.e., Doppler velocity, line width and intensity) in spectroscopic observations. They are often applied for remote diagnostics of magnetic fields and plasma properties on the Sun.
Aims. We combine the imaging and spectroscopic measurements of available space missions, and investigate the properties of non-damping oscillations at flaring loops.
Methods. We used the Interface Region Imaging Spectrograph (IRIS) to measure the spectrum over a narrow slit. The double-component Gaussian fitting method was used to extract the line profile of Fe xxi 1354.08 angstrom at the "OI" spectral window. The quasi-periodicity of loop oscillations were identified in the Fourier and wavelet spectra.
Results. A periodicity at about 40 s is detected in the line properties of Fe xxi 1354.08 angstrom, hard X-ray emissions in GOES 1-8 angstrom derivative, and Fermi 26-50 keV. The Doppler velocity and line width oscillate in phase, while a phase shift of about pi/2 is detected between the Doppler velocity and peak intensity. The amplitudes of Doppler velocity and line width oscillation are about 2.2 km s(-1) and 1.9 km s(-1), respectively, while peak intensity oscillates with amplitude at about 3.6% of the background emission. Meanwhile, a quasi-period of about 155 s is identified in the Doppler velocity and peak intensity of the Fe xxi 1354.08 angstrom line emission, and AIA 131 angstrom intensity.
Conclusions. The oscillations at about 40 s are not damped significantly during the observation; this might be linked to the global kink modes of flaring loops. The periodicity at about 155 s is most likely a signature of recurring downflows after chromospheric evaporation along flaring loops. The magnetic field strengths of the flaring loops are estimated to be about 120-170 G using the magnetohydrodynamic seismology diagnostics, which are consistent with the magnetic field modeling results using the flux rope insertion method.

第 20 条，共 248 条

High-resolution Observations of Flares in an Arch Filament System

Su, YN (Su, Yingna); Liu, R (Liu, Rui); Li, SW (Li, Shangwei); Cao, WD (Cao, Wenda); Ahn, K (Ahn, Kwangsu); Ji, HS (Ji, Haisheng)
ASTROPHYSICAL JOURNAL
卷: 855 期: 2 文献号: 77
We study five sequential solar flares (SOL2015-08-07) occurring in Active Region 12396 observed with the Goode Solar Telescope (GST) at the Big Bear Solar Observatory, complemented by Interface Region Imaging Spectrograph and SDO observations. The main flaring region is an arch filament system (AFS) consisting of multiple bundles of dark filament threads enclosed by semicircular flare ribbons. We study the magnetic configuration and evolution of the active region by constructing coronal magnetic field models based on SDO/HMI magnetograms using two independent methods, i.e., the nonlinear force-free field (NLFFF) extrapolation and the flux rope insertion method. The models consist of multiple flux ropes with mixed signs of helicity, i.e., positive (negative) in the northern (southern) region, which is consistent with the GST observations of multiple filament bundles. The footprints of quasi-separatrix layers (QSLs) derived from the extrapolated NLFFF compare favorably with the observed flare ribbons. An interesting double-ribbon fine structure located at the east border of the AFS is consistent with the fine structure of the QSL's footprint. Moreover, magnetic field lines traced along the semicircular footprint of a dome-like QSL surrounding the AFS are connected to the regions of significant helicity and Poynting flux injection. The maps of magnetic twist show that positive twist became dominant as time progressed, which is consistent with the injection of positive helicity before the flares. We hence conclude that these circular shaped flares are caused by 3D magnetic reconnection at the QSLs associated with the AFS possessing mixed signs of helicity.

第 21 条，共 248 条

Observations of Electron-driven Evaporation in a Flare Precursor

Li, D (Li, Dong); Li, Y (Li, Ying); Su, W (Su, Wei); Huang, Y (Huang, Yu); Ning, ZJ (Ning, Zongjun)
ASTROPHYSICAL JOURNAL
卷: 854 期: 1 文献号: 26
We investigate the relationship between the blueshifts of a hot emission line and the nonthermal emissions in microwave and hard X-ray (HXR) wavelengths in the precursor of a solar flare on 2014 October 27. The flare precursor is identified as a small but well-developed peak in the soft X-ray and extreme-ultraviolet passbands before the GOES flare onset,

which is accompanied by a pronounced burst in microwave 17 and. 34 GHz and in HXR 25-50 keV. The slit of the Interface Region Imaging Spectrograph (IRIS) stays on one ribbon-like transient during the flare precursor phase, which shows visible nonthermal emissions in Nobeyama Radioheliograph and RHESSI images. The IRIS spectroscopic observations show that the hot line of Fe XXI 1354.09. angstrom (log T similar to 7.05) displays blueshifts, while the cool line of Si IV 1402.77 angstrom (log T similar to 4.8) exhibits redshifts. The blueshifts and redshifts are well correlated with each other, indicative of an explosive chromospheric evaporation during the flare precursor phase combining a high nonthermal energy flux with a short characteristic timescale. In addition, the blueshifts of Fe XXI 1354.09 angstrom are well correlated with the microwave and HXR emissions, implying that the explosive chromospheric evaporation during the flare precursor phase is driven by nonthermal electrons.

第 22 条，共 248 条

Two Kinds of Dynamic Behavior in a Quiescent Prominence Observed by the NVST

Li, D (Li, Dong); Shen, YD (Shen, Yuandeng); Ning, ZJ (Ning, Zongjun); Zhang, QM (Zhang, Qingmin); Zhou, TH (Zhou, Tuanhui)
ASTROPHYSICAL JOURNAL
卷: 863 期: 2 文献号: 192
We present high-resolution observations of two kinds of dynamic behavior in a quiescent prominence using the New Vacuum Solar Telescope, i.e., Kelvin-Helmholtz instabilities (KHIs) and small-scale oscillations. The KHIs were identified as rapidly developed vortex-like structures with counterclockwise/clockwise rotations in the Ha red-wing images at +0.3 angstrom, which were produced by the strong shear-flow motions on the surface/interface of prominence plumes. The KHI growth rates are estimated to be similar to 0.0135 +/- 0.0004 and similar to 0.0138 +/- 0.0004. Our observational results further suggest that the shear velocities (i.e., supersonic) of the mass flows are fast enough to produce the strong deformation of the boundary and overcome the restraining surface tension force. This flowdriven instability might play a significant role in the process of plasma transfer in solar prominences. The smallscale oscillations perpendicular to the prominence threads are observed in the Ha line-center images. The oscillatory periods changed nonmonotonically and showed two changing patterns, in which one first decreased slowly and then started to increase, while the other grew fast at the beginning and then started to decrease. Both of these thread oscillations with changing periods were observed to be unstable for an entire cycle, and they were local in nature. All our findings indicate that the small-scale thread oscillations could be magnetohydrodynamic waves in the solar corona.

第 23 条，共 248 条

Spectroscopic and imaging observations of small-scale reconnection events

Li, D (Li, Dong); Li, LP (Li, Leping); Ning, ZJ (Ning, Zongjun)
MONTHLY NOTICES OF THE ROYAL ASTRONOMICAL SOCIETY
卷: 479 期: 2 页: 2382-2388
We present spectroscopic and imaging observations of small-scale reconnection events on the Sun. Using Interface Region Imaging Spectrograph (IRIS) observations, one reconnection event is first detected as IRIS jets with fast bidirectional velocities in the chromosphere and transition region, which are identified as non-Gaussian broadenings with two extended wings in the line profiles of SiIV, C II and MgIIk. The magnetograms under the IRIS jets from helioseismic and magnetic images simultaneously exhibit magnetic flux cancellation, supporting the idea that the IRIS jets are driven by magnetic reconnection. Atmospheric Imaging Assembly images also show an extreme ultraviolet (EUV) brightening shortly after the underlying IRIS jets, i.e. in the 131-, 171-, 193-, 211- and 94-angstrom channels, implying that the overlying EUV brightening in the corona is caused by the IRIS jets in the chromosphere and transition region. We also find another three reconnection events, which show the same features during this IRIS observation. Our observational results suggest that small-scale reconnection events might contribute to coronal heating. A new result is that the process of magnetic reconnection is detected from the photosphere through the chromosphere and transition region to the corona.

第 24 条，共 248 条

Diagnosing the Magnetic Field Structure of a Coronal Cavity Observed during the 2017 Total Solar Eclipse

Chen, YJ (Chen, Yajie); Tian, H (Tian, Hui); Su, YN (Su, Yingna); Qu, ZQ (Qu, Zhongquan); Deng, LH (Deng, Linhua); Jibben, PR (Jibben, Patricia R.); Yang, ZH (Yang, Zihao); Zhang, JW (Zhang, Jingwen); Samanta, T (Samanta, Tanmoy); He, JS (He, Jiansen); Wang, LH (Wang, Linghua); Zhu, YJ (Zhu, Yingjie); Zhong, Y (Zhong, Yue); Liang, Y (Liang, Yu)
ASTROPHYSICAL JOURNAL
卷: 856 期: 1 文献号: 21
We present an investigation of a coronal cavity observed above the western limb in the coronal red line Fe X 6374 angstrom using a telescope of Peking University and in the green line Fe XIV 5303 angstrom using a telescope of Yunnan Observatories, Chinese Academy of Sciences, during the total solar eclipse on 2017 August 21. A series of magnetic field models is constructed based on the magnetograms taken by the Helioseismic and Magnetic Imager on board the Solar Dynamics Observatory (SDO) one week before the eclipse. The model field lines are then compared with coronal structures seen in images taken by the Atmospheric Imaging Assembly on board SDO and in our coronal red line images. The best-fit model consists of a flux rope with a twist angle of 3.1 pi, which is consistent with the most probable value of the total twist angle of interplanetary flux ropes observed at 1 au. Linear polarization of the Fe XIII 10747 angstrom line calculated from this model shows a "lagomorphic" signature that is also observed by the Coronal Multichannel Polarimeter of the High Altitude Observatory. We also find a ring-shaped structure in the line-of-sight velocity of Fe XIII 10747 angstrom, which implies hot plasma flows along a helical magnetic field structure, in the cavity. These results suggest that the magnetic structure of the cavity is a highly twisted flux rope, which may erupt eventually. The temperature structure of the cavity has also been investigated using the intensity ratio of Fe XIII 10747 angstrom and Fe X 6374 angstrom.

第 25 条，共 248 条

Period Increase and Amplitude Distribution of Kink Oscillation of Coronal Loop

Su, W (Su, W.); Guo, Y (Guo, Y.); Erdelyi, R (Erdelyi, R.); Ning, ZJ (Ning, Z. J.); Ding, MD (Ding, M. D.); Cheng, X (Cheng, X.); Tan, BL (Tan, B. L.)
SCIENTIFIC REPORTS
卷: 8 文献号: 4471
Coronal loops exist ubiquitously in the solar atmosphere. These loops puzzle astronomers over half a century. Solar magneto-seismology (SMS) provides a unique way to constrain the physical parameters of coronal loops. Here, we study the evolution of oscillations of a coronal loop observed by the

Atmospheric Imaging Assembly (AIA). We measure geometric and physical parameters of the loop oscillations. In particular, we find that the mean period of the oscillations increased from 1048 to 1264s during three oscillatory cycles. We employ the differential emission measure method and apply the tools of SMS. The evolution of densities inside and outside the loop is analyzed. We found that an increase of density inside the loop and decrease of the magnetic field strength along the loop are the main reasons for the increase in the period during the oscillations. Besides, we also found that the amplitude profile of the loop is different from a profile would it be a homogeneous loop. It is proposed that the distribution of magnetic strength along the loop rather than density stratification is responsible for this deviation. The variation in period and distribution of amplitude provide, in terms of SMS, a new and unprecedented insight into coronal loop diagnostics.

第 26 条，共 248 条

High-resolution He I 10830 angstrom Narrowband Imaging for an M-class Flare. II. Multiple Hot Channels: Their Origin and Destination

Wang, Y (Wang, Ya); Su, YN (Su, Yingna); Shen, JH (Shen, Jinhua); Yang, X (Yang, Xu); Cao, WD (Cao, Wenda); Ji, HS (Ji, Haisheng)
ASTROPHYSICAL JOURNAL
卷: 859 期: 2 文献号: 148
In this paper, we report our second-part result for the M1.8 class flare on 2012 July 5, with an emphasis on the initiation process for the flare-associated filament eruption. The data set consists of high-resolution narrowband images in He 110830 angstrom and broadband images in TiO 7057 angstrom taken at Big Bear Solar Observatory with the 1.6 m aperture Goode Solar Telescope. EUV images in different passbands observed by the Atmospheric Imaging Assembly on board the Solar Dynamics Observatory are used to distinguish hot plasma from cool plasma structures during the flare process. High-resolution 10830 angstrom images clearly show that, below the horizontal fibrils, which correspond to the filament's spine in full-disk Ha images, a sheared arch filament system (AFS) lies across the penumbra and surrounding satellite sunspots, between which continuous shearing motion is observed. Before the eruption, three microflares occurred successively and were followed by the appearance of three EUV hot channels. Two hot channels erupted, producing two flaring sites and two major peaks in GOES soft X-ray light curves; however, one hot channel's eruption failed. The 10830 angstrom imaging enables us to trace the first two hot channels to their very early stage, which is signified by the rising of the AFS after the first two precursors. Continuous flux emergence and localized flare-associated cancellation are observed under the AFS. In addition, EUV ejections were observed during the formation of the EUV hot channels. These observations support the fact that the hot channels are the result of magnetic reconnections during precursors.

第 27 条，共 248 条

Magnetic Field Modeling of Hot Channels in Four Flare/Coronal Mass Ejection Events

Liu, T (Liu, Tie); Su, YN (Su, Yingna); Cheng, X (Cheng, Xin); van Ballegooijen, A (van Ballegooijen, Adriaan); Ji, HS (Ji, Haisheng)
ASTROPHYSICAL JOURNAL
卷: 868 期: 1 文献号: 59
We investigate the formation and magnetic topology of four flare/coronal mass ejection events with filament-sigmoid systems, in which the sigmoidal hot channels are located above the filaments and appear in pairs before eruption. The formation of hot channels usually takes several to dozens of hours, during which two J-shaped sheared arcades gradually evolve into sigmoidal hot channels and then keep stable for tens of minutes or hours and erupt, while the low-lying filaments show no significant change. We construct a series of magnetic field models and find that the best-fit preflare models contain magnetic flux ropes with hyperbolic flux tubes (HFTs). The field lines above the HFT correspond to the high-lying hot channel, whereas those below the HFT surround the underlying filaments. In particular, the continuous and long field lines representing the flux rope located above the HFT match the observed hot channels well in three events. However, for the SOL2014-04-18 event, the flux bundle that mimics the observed hot channel is located above the flux rope. The flux rope axis lies in a height range of 19.8 and 46 Mm above the photosphere for the four events, among which the flux rope axis in the SOL2012-0712 event has a maximum height, which probably explains why it is often considered as a double-decker structure. Our modeling suggests that the high-lying hot channel may be formed by magnetic reconnections between sheared field lines occurring above the filament before eruption.

第 28 条，共 248 条

Studies of Isolated and Non-isolated Photospheric Bright Points in an Active Region Observed by the New Vacuum Solar Telescope

Liu, YX (Liu, Yanxiao); Xiang, YY (Xiang, Yongyuan); Erdelyi, R (Erdelyi, Robertus); Liu, Z (Liu, Zhong); Li, D (Li, Dong); Ning, ZJ (Ning, Zongjun); Bi, Y (Bi, Yi); Wu, N (Wu, Ning); Lin, J (Lin, Jun)
ASTROPHYSICAL JOURNAL
卷: 856 期: 1 文献号: 17
Properties of photospheric bright points (BPs) near an active region have been studied in TiO lambda 7058 angstrom images observed by the New Vacuum Solar Telescope of the Yunnan Observatories. We developed a novel recognition method that was used to identify and track 2010 BPs. The observed evolving BPs are classified into isolated (individual) and non-isolated (where multiple BPs are observed to display splitting and merging behaviors) sets. About 35.1% of BPs are non-isolated. For both isolated and non-isolated BPs, the brightness varies from 0.8 to. 1.3 times the average background intensity and follows a Gaussian distribution. The lifetimes of BPs follow a lognormal distribution, with characteristic lifetimes of (267 +/- 140). s and (421 +/- 255). s, respectively. Their size also follows log-normal distribution, with an average size of about (2.15 +/- 0.74). x. 10(4) km(2) and (3.00 +/- 1.31). x 10(4) km(2) for area, and (163 +/- 27) km and (191 +/- 40) km for diameter, respectively. Our results indicate that regions with strong background magnetic field have higher BP number density and higher BP area coverage than regions with weak background field. Apparently, the brightness/size of BPs does not depend on the background field. Lifetimes in regions with strong background magnetic field are shorter than those in regions with weak background field, on average.

第 29 条，共 248 条

Two Episodes of Magnetic Reconnections during a Confined Circular-ribbon Flare

Li, T (Li, Ting); Yang, SH (Yang, Shuhong); Zhang, QM (Zhang, Qingmin); Hou, YJ (Hou, Yijun); Zhang, J (Zhang, Jun)
来源出版物: ASTROPHYSICAL JOURNAL
卷: 859 期: 2 文献号: 122
We analyze a unique event with an M1.8 confined circular-ribbon flare on 2016 February 13, with successive formations of two circular ribbons at the same location. The

flare had two distinct phases of UV and extreme ultraviolet emissions with an interval of about 270 s, of which the second peak was energetically more important. The first episode was accompanied by the eruption of a mini-filament and the fast elongation motion of a thin circular ribbon (CR1) along the counterclockwise direction at a speed of about 220 km s(-1). Two elongated spinerelated ribbons were also observed, with the inner ribbon co-temporal with CR1 and the remote brightenings forming similar to 20 s later. In the second episode, another mini-filament erupted and formed a blowout jet. The second circular ribbon and two spine-related ribbons showed similar elongation motions with that during the first episode. The extrapolated three-dimensional coronal magnetic fields reveal the existence of a fan-spine topology, together with a quasi-separatrix layer (QSL) halo surrounding the fan plane and another QSL structure outlining the inner spine. We suggest that continuous null-point reconnection between the filament and ambient open field occurs in each episode, leading to the sequential opening of the filament and significant shifts of the fan plane footprint. For the first time, we propose a compound eruption model of circular-ribbon flares consisting of two sets of successively formed ribbons and eruptions of multiple filaments in a fan-spine-type magnetic configuration.

第 30 条，共 248 条

Vertical Oscillation of a Coronal Cavity Triggered by an EUV Wave

Zhang, QM (Zhang, Q. M.); Ji, HS (Ji, H. S.)
ASTROPHYSICAL JOURNAL
卷: 860 期: 2 文献号: 113
In this paper, we report our multiwavelength observations of the vertical oscillation of a coronal cavity on 2011 March 16. The elliptical cavity with an underlying horn-like quiescent prominence was observed by the Atmospheric Imaging Assembly on board the Solar Dynamics Observatory. The width and height of the cavity are 150 '' and 240 '', and the centroid of cavity is 128 '' above the solar surface. At similar to 17: 50 UT, a C3.8 two-ribbon flare took place in active region 11169 close to the solar western limb. Meanwhile, a partial halo coronal mass ejection erupted and propagated at a linear speed of similar to 682 km s(-1). Associated with the eruption, a coronal extremeultraviolet (EUV) wave was generated and propagated in the northeast direction at a speed of similar to 120 km s(-1). Once the EUV wave arrived at the cavity from the top, it pushed the large-scale overlying magnetic field lines downward before bouncing back. At the same time, the cavity started to oscillate coherently in the vertical direction and lasted for similar to 2 cycles before disappearing. The amplitude, period, and damping time are 2.4-3.5 Mm, 29-37 minutes, and 26-78 minutes, respectively. The vertical oscillation of the cavity is explained by a global standing MHD wave of fast kink mode. To estimate the magnetic field strength of the cavity, we use two independent methods of prominence seismology. It is found that the magnetic field strength is only a few Gauss and less than 10 G.

Acceleration and Radiation of High-Energy Cosmic Particles

第 31 条，共 248 条

Impulsive radio and hard X-ray emission from an M-class flare

Zhang, P (Zhang, Ping); Guo, Y (Guo, Yang); Wang, L (Wang, Lu); Liu, SM (Liu, Siming)
ASTRONOMY & ASTROPHYSICS
卷: 615 文献号: A48
Context. Impulsive radio and hard X-ray emission from large solar flares are usually attributed to a hard distribution of high-energy electrons accelerated in the energy dissipation process of magnetic reconnection.
Aims. We report the detection of impulsive radio and hard X-ray emissions produced by a population of energetic electrons with a very soft distribution in an M-class flare: SOL2015-08-27T05: 45.
Methods. The absence of impulsive emission at 34 GHz and hard X-ray emission above 50 keV and the presence of distinct impulsive emission at 17 GHz and lower frequencies and in the 25-50 keV X-ray band imply a very soft distribution of energetic electrons producing the impulsive radio emission via the gyro-synchrotron process, and impulsive X-rays via bremsstrahlung.
Results. The spectrum of the impulsive hard X-ray emission can be fitted equally well with a power-law model with an index of similar to 6.5 or a super-hot thermal model with a temperature as high as 100 MK. Imaging observations in the extreme-UV and X-ray bands and extrapolation of the magnetic field structure using a nonlinear force-free model show that energetic electrons trapped in coronal loops are responsible for these impulsive emissions.
Conclusions. Since the index of the power-law model is nearly constant during the impulsive phase, the power-law distribution or the super-hot component should be produced by a bulk energization process such as the Fermi and betatron acceleration of collapsing magnetic loops.

第 32 条，共 46 条

超高能宇宙线从何而来?

胡红波，王祥玉，刘四明
科学通报
宇宙线是来自外太空的唯一物质样本,携带着粒子物理、高能天体物理、宇宙物质组成及其演化的丰富信息.已知的宇宙线粒子最高能量约为3×10~(20) eV."宇宙线是如何被加速的?""其起源天体是什么?""在这样的高能情况下,已知的物理学规律是否还能适用?"等这些都是有待解决的重大科学问题.为此人们通过多种实验手段在空间和地上开展宇宙线的多信使研究.在过去的几十年里,宇宙线、伽马射线和中微子观测取得了丰富的成果:(1)宇宙线能谱、成分和各向异性的测量精度达到了史无前例的水平,极高能宇宙线的偶极各向异性表明这些粒子来自银河系之外；(2)空间实验发现了3000 多个 GeV 伽马源,地面实验发现了近 200 个 TeV 源,它们大多为高能电子源,有几个已被认证为强子源；(3)冰立方实验发现了近百个高能中微子,它们的各向同性分布暗示着河外起源.这些新结果为解决宇宙线的起源问题和发展相关的粒子加速理论奠定了基础.新一代更高灵敏度的实验装置的建设和运行正在开启宇宙线粒子天体物理研究的新篇章。

第 33 条，共 46 条

Where do the ultra-high energy cosmic rays come from?

Hu Hongbo; Wang Xiangyu; Liu Siming
Chinese Science Bulletin
卷: 63 期: 24 页: 2440-2449
Cosmic rays are the only sample of matter coming from outer

space. They carry rich information about particle physics, high-energy astrophysics, composition and evolution of the Universe. The highest energy of cosmic rays detected so far is about 3*10~(20) eV. How are the cosmic rays accelerated?What kind of astronomic sources do the cosmic rays originate from?Are the fundamental physics laws still valid in such high-energy scales? are all important scientific problems waiting to be addressed. To answer these questions, various space and ground experiments have been carried out to explore the nature of cosmic rays in a multi-messenger approach. The past few decades have witnessed great achievements in high-energy cosmic ray, gamma ray, neutrino observations, and detection of gravitational wave. (1) The cosmic ray spectra, composition, and anisotropy have been measured with unprecedented precision leading to better understanding of cosmic ray acceleration and transport and stricter constraints on properties of potential candidates of dark matter particles, and the dipole anisotropy of ultrahigh energy cosmic rays indicates that they have an extragalactic origin. (2) Space borne experiments have discovered more than 3000 sources in the GeV range, and the ground based experiments have uncovered more than 200 sources at TeV energies. Most of these sources are high-energy electron accelerators, and a few of them are identified as the accelerators of cosmic ray nuclei. Diffuse gamma-ray emission associated with galactic disks and jets and/or outbursts of Active Galactic Nuclei is also measured with better spatial and energy resolutions, which can be used to study cosmic ray transport in the interstellar/galactic/cluster medium. (3) With the IceCube experiment, about 100 high-energy neutrino events have been recorded and their isotropic distribution suggests an extragalactic origin. (4) The first gravitational wave event with simultaneous multi-wavelength observations has been detected opening the epoch of gravitational wave astronomy. Strong gravitational wave events represent the most catastrophic energy release in the Universe and can be important cosmic ray sources. These new results established the foundation to address the origin of cosmic rays and to develop theories of particle acceleration and transport. The study of cosmic ray transport has gone beyond the diffusion approximation to study the effect of magnetic field fluctuations on small scale anisotropy of cosmic rays and comprehensive numerical modelings of cosmic ray transport in the Galaxy are advanced with multi-wavelength observations. Diffusive particle acceleration by strong shocks of supernova remnants (SNRs) is also advanced based on multi-wavelength observations and cosmic ray measurements. The scenario of SNR origin of Galactic cosmic rays is being quantified with testable predictions. Although there are still uncertainties in amplification of magnetic field by cosmic rays and cosmic ray scattering by turbulent plasmas, sophisticated numerical codes are being developed to address these issues. Successful construction and operation of new generation cosmic ray and gamma-ray experiments will open a new chapter of the astro-particle physics study.

Physics of Dark Matter Indirect Detection

第 34 条，共 248 条

Detection of GeV Gamma-Ray Emission in the Direction of HESS J1731-347 with Fermi-LAT

Guo, XL (Guo, Xiao-Lei); Xin, YL (Xin, Yu-Liang); Liao, NH (Liao, Neng-Hui); Yuan, Q (Yuan, Qiang); Gao, WH (Gao, Wei-Hong); Fan, YZ (Fan, Yi-Zhong)
ASTROPHYSICAL JOURNAL
卷: 853 期: 1 文献号: 2
We report the detection of GeV gamma-ray emission from supernova remnant HESS J1731-347 using 9 yr of Fermi Large Area Telescope data. We find a slightly extended GeV source in the direction of HESS J1731-347. The spectrum above 1 GeV can be fitted by a power law with an index of Gamma = 1.77 +/- 0.14, and the GeV spectrum connects smoothly with the TeV spectrum of HESS J1731-347. Either a hadronic-leptonic or a pure leptonic model can fit the multiwavelength spectral energy distribution of the source. However, the hard GeV gamma-ray spectrum is more naturally produced in a leptonic (inverse Compton scattering) scenario, under the framework of diffusive shock acceleration. We also searched for the GeV gamma-ray emission from the nearby TeV source HESS J1729-345. No significant GeV gamma-ray emission is found, and upper limits are derived.

第 35 条，共 248 条

Fast gamma-Ray Variability in Blazars beyond Redshift 3

Li, S (Li, Shang); Xia, ZQ (Xia, Zi-Qing); Liang, YF (Liang, Yun-Feng); Liao, NH (Liao, Neng-Hui); Fan, YZ (Fan, Yi-Zhong)
ASTROPHYSICAL JOURNAL
卷: 853 期: 2 文献号: 159
High-redshift blazars are one of the most powerful sources in the universe and gamma-ray variability carries crucial information about their relativistic jets. In this wor gamma we present results of the first systematical temporal analysis of Fermi-LAT data of all known seven gamma-ray blazars beyond redshift 3. Significant long-term.-ray variability is found from five sources in monthly gamma-ray light curves, in which three of them are reported for the first time. Furthermore, intraday gamma-ray variations are detected from NVSS J053954-283956 and NVSS J080518+ 614423. The doubling variability timescale of the former source is limited as short as less than or similar to 1 hr (at the source frame). Together with variability amplitude over one order of magnitude, NVSS J053954-283956 is the most distant gamma-ray flaring blazar so far. Meanwhile, intraday optical variability of NVSS J163547+ 362930 is found based on an archival PTF/iPTF light curve. Benefiting from the multi-wavelength activity of these sources, constraints on their Doppler factors, as well as the locations of the gamma-ray radiation region and indications for the SDSS high redshift jetted active galactic nuclei deficit are discussed.

第 36 条，共 248 条

Fermi-LAT Detection of a Transient gamma-Ray Source in the Direction of a Distant Blazar B3 1428+422 at z=4.72

Liao, NH (Liao, Neng-Hui); Li, S (Li, Shang); Fan, YZ (Fan, Yi-Zhong)
ASTROPHYSICAL JOURNAL LETTERS
卷: 865 期: 2 文献号: L17
We report the detection of a transient gamma-ray source in the direction of B3 1428+422 (z = 4.72) by analyzing the 110-month Fermi-LAT. Pass 8 data. The new transient gamma-ray source is far away from the Galactic plane and has a rather soft spectrum, in agreement with being a high redshift blazar. We suggest that the newly discovered transient is the gamma-ray counterpart of B3 1428+422, which could be the most distant GeV source detected so far. The detection of a group of such distant gamma-ray blazars will be helpful in reconstructing the evolution of the luminosity function and studying the extragalactic background light at such high redshifts.

第 37 条，共 248 条

Search for gamma-ray emission from the nearby dwarf spheroidal galaxies with 9 years of Fermi-LAT data

Li, S (Li, Shang); Duan, KK (Duan, Kai-Kai); Liang, YF (Liang, Yun-Feng); Xia, ZQ (Xia, Zi-Qing); Shen, ZQ (Shen, Zhao-Qiang); Li, X (Li, Xiang); Liao, NH (Liao, Neng-Hui); Feng, L (Feng, Lei); Yuan, Q (Yuan, Qiang); Fan, YZ (Fan, Yi-Zhong); Chang, J (Chang, Jin)
PHYSICAL REVIEW D
卷: 97 期: 12 文献号: 122001
In this work, we search for gamma-ray emission from nearby Milky Way dwarf spheroidal galaxies (dSphs) and candidates with the publicly available Pass 8 data of Fermi-LAT. Our sample includes 12 sources with the distances < 50 kpc. Very weak gamma-ray excesses (similar to 2 sigma) are found in some dSphs/candidates, consistent with those reported in the previous literature. Intriguingly, the peak test statistic (TS) value of the weak emission from Reticulum II rises continually. If interpreted as dark matter (DM) annihilation, the peak TS value is 13.5 for the annihilation channel of chi chi -> tau(+)tau(-) and the DM mass of m(chi) similar to 16 GeV. The combination of all these nearby sources yields a more significant (with local significance >4 sigma) gamma-ray signal.

第 38 条，共 248 条

Study of the boxlike dark matter signals from dwarf spheroidal galaxies with Fermi-LAT data

Li, S (Li, Shang); Liang, YF (Liang, Yun-Feng); Xia, ZQ (Xia, Zi-Qing); Zu, L (Zu, Lei); Duan, KK (Duan, Kai-Kai); Shen, ZQ (Shen, Zhao-Qiang); Feng, L (Feng, Lei); Yuan, Q (Yuan, Qiang); Fan, YZ (Fan, Yi-Zhong)
PHYSICAL REVIEW D
卷: 97 期: 8 文献号: 083007
The observation of a special spectral feature in the gamma-ray data would be one of the best ways to identify dark matter (DM). The box-shaped gamma-ray spectra could be generated by the decay of intermediate particles produced by DM annihilation or decay. It provides another kind of signal that can be relatively easily distinguished from astrophysical backgrounds besides the linelike signals. Dwarf spheroidal galaxies are expected to be dominated by DM and may be one of the most promising targets for indirect DM searches. In this paper, we study the box-shaped DM signals with Fermi-LAT observations of dwarf spheroidal galaxies. We analyze 106 months of Fermi-LAT data to derive the upper limits on the annihilation cross section or the decay timescale of DM. In addition, we compare the results for different sample selections and DM density distributions. We expect that more dwarf spheroidal galaxies will be found and the sensitivity of box-shaped gamma-ray signal searches will be significantly improved in the future.

第 39 条，共 248 条

A model explaining neutrino masses and the DAMPE cosmic ray electron excess

Fan, YZ (Fan, Yi-Zhong); Huang, WC (Huang, Wei-Chih); Spinrath, M (Spinrath, Martin); Tsai, YLS (Tsai, Yue-Lin Sming); Yuan, Q (Yuan, Qiang)
PHYSICS LETTERS B
卷: 781 页: 83-87
We propose a flavored U(1)(e mu) neutrino mass and dark matter(DM) model to explain the recent DArk Matter Particle Explorer (DAMPE) data, which feature an excess on the cosmic ray electron plus positron flux around 1.4 TeV. Only the first two lepton generations of the Standard Model are charged under the new U(1)(e mu) gauge symmetry. A vector-like fermion psi, which is our DM candidate, annihilates into e(+/-) and mu(+/-) via the new gauge boson Z' exchange and accounts for the DAMPE excess. We have found that the data favors a psi mass around 1.5 TeV and a Z' mass around 2.6 TeV, which can potentially be probed by the next generation lepton colliders and DM direct detection experiments. (C) 2018 The Authors. Published by Elsevier B.V.

第 40 条，共 46 条

Massive black holes and tidal disruption events at the center of galaxies

Liu Zhu; Yuan Weimin; Sun Hui; Li Shuo; Liu Fukun; Chen Xian; Lu Youjun; Wang Tinggui; Lei Weihua; Zhong Shiyan; Yuan Feng; Wang Junfeng; Li Zhuo; Li Lixin; Fan Yizhong; Zhou Hongyan
Scientia Sinica Physica, Mechanica & Astronomica
卷: 48 期: 3 页: 039503-1-039503-13
When a star enters the tidal radius of a massive black hole (BH) at the center of a galaxy, the tidal force will rip the star apart. The BH may accrete the debris of the star and produce energetic flare. This phenomenon is now commonly known as Tidal Disruption Event (TDE). The characteristics of its spectra as well as variability are dependent on the properties of the central BH and the disrupted star, so that we can study their parameters, accretion process and jet, and the property of circumnuclear environment by confirming and systematically studying the BH in quiescent galaxies. TDE may also provide important clues on the existence of intermediate BH as well as supermassive BH binary. However, the study of TDE is hindered by relatively small sample size (especially in X-ray band) and low quality of data due to the low incident rate. The Einstein Probe (EP), which covers the 0.5-4 keV soft X-ray energy band, has a large field of view as well as high sensitivity, making it perfect to detect TDE. We expect that EP will detect several tens to about one hundred TDE every year, of which around 10 or even more are TDE with relativistic jet. This will result in a homogeneously selected completely TDE sample, which is important for investigating the statistical property of TDE. It makes it possible to investigate the existence and statistical property of BH, explore the growth and evolution of BH, discovery the intermediate BH as well as supermassive BH binaries.

第 41 条，共 248 条

DES science portal: Computing photometric redshifts

Gschwend, J (Gschwend, J.); Rossel, AC (Rossel, A. C.); Ogando, RLC (Ogando, R. L. C.); Neto, AF (Neto, A. F.); Maia, MAG (Maia, M. A. G.); da Costa, LN (da Costa, L. N.); Lima, M (Lima, M.); Pellegrini, P (Pellegrini, P.); Campisano, R (Campisano, R.); Singulani, C (Singulani, C.); Adean, C (Adean, C.); Benoist, C (Benoist, C.); Aguena, M (Aguena, M.); Kind, MC (Kind, M. Carrasco); Davis, TM (Davis, T. M.); de Vicente, J (de Vicente, J.); Hartley, WG (Hartley, W. G.); Hoyle, B (Hoyle, B.); Palmese, A (Palmese, A.); Sadeh, I (Sadeh, I); Abbott, TMC (Abbott, T. M. C.); Abdalla, FB (Abdalla, F. B.); Allam, S (Allam, S.); Annis, J (Annis, J.); Asorey, J (Asorey, J.); Brooks, D (Brooks, D.); Calcino, J (Calcino, J.); Carollo, D (Carollo, D.); Castander, FJ (Castander, F. J.); D'Andrea, CB (D'Andrea, C. B.); Desai, S (Desai, S.); Evrard, AE (Evrard, A. E.); Fosalba, P (Fosalba, P.); Frieman, J (Frieman, J.); Garcia-Bellido, J (Garcia-Bellido, J.); Glazebrook, K (Glazebrook, K.); Gerdes, DW (Gerdes, D. W.); Gruendl, RA (Gruendl, R. A.); Gutierrez, G (Gutierrez, G.); Hinton, S (Hinton, S.); Hollowood, DL (Hollowood, D. L.); Honscheid, K (Honscheid, K.); Hoormann, JK (Hoormann, J. K.); James, DJ (James, D. J.); Kuehn, K (Kuehn, K.); Kuropatkin, N (Kuropatkin, N.); Lahav, O (Lahav, O.); Lewis, G (Lewis, G.); Lidman, C (Lidman, C.); Lin, H (Lin, H.); Macaulay, E (Macaulay, E.); Marshall, J (Marshall, J.);

Melchior, P (Melchior, P.); Miguel, R (Miguel, R.); Moller, A (Moller, A.); Plazas, AA (Plazas, A. A.); Sanchez, E (Sanchez, E.); Santiago, B (Santiago, B.); Scarpine, V (Scarpine, V); Schindler, ZH (Schindler, Z. H.); Sevilla-Noarbe, I (Sevilla-Noarbe, I); Smith, M (Smith, M.); Sobreira, F (Sobreira, F.); Sommer, NE (Sommer, N. E.); Suchyta, E (Suchyta, E.); Swanson, MEC (Swanson, M. E. C.); Tarle, G (Tarle, G.); Tucker, BE (Tucker, B. E.); Tucker, DL (Tucker, D. L.); Uddin, S (Uddin, S.); Walker, AR (Walker, A. R.)
ASTRONOMY AND COMPUTING
卷: 25 页: 58-80
A significant challenge facing photometric surveys for cosmological purposes is the need to produce reliable redshift estimates. The estimation of photometric redshifts (photo-zs) has been consolidated as the standard strategy to bypass the high production costs and incompleteness of spectroscopic redshift samples. Training-based photo-z methods require the preparation of a high-quality list of spectroscopic redshifts, which needs to be constantly updated. The photo-z training, validation, and estimation must be performed in a consistent and reproducible way in order to accomplish the scientific requirements. To meet this purpose, we developed an integrated web-based data interface that not only provides the framework to carry out the above steps in a systematic way, enabling the ease testing and comparison of different algorithms, but also addresses the processing requirements by parallelizing the calculation in a transparent way for the user. This framework called the Science Portal (hereafter Portal) was developed in the context the Dark Energy Survey (DES) to facilitate scientific analysis. In this paper, we show how the Portal can provide a reliable environment to access vast datasets, provide validation algorithms and metrics, even in the case of multiple photo-zs methods. It is possible to maintain the provenance between the steps of a chain of workflows while ensuring reproducibility of the results. We illustrate how the Portal can be used to provide photo-z estimates using the DES first year (Y1A1) data. While the DES collaboration is still developing techniques to obtain more precise photo-zs, having a structured framework like the one presented here is critical for the systematic vetting of DES algorithmic improvements and the consistent production of photo-zs in future DES releases. (C) 2018 Elsevier B.V. All rights reserved.

第 42 条，共 248 条

GW170817 and the Prospect of Forming Supramassive Remnants in Neutron Star Mergers

Ma, PX (Ma, Peng-Xiong); Jiang, JL (Jiang, Jin-Liang); Wang, H (Wang, Hao); Jin, ZP (Jin, Zhi-Ping); Fan, YZ (Fan, Yi-Zhong); Wei, DM (Wei, Da-Ming)
ASTROPHYSICAL JOURNAL
卷: 858 期: 2 文献号: 74
The gravitational wave data of GW170817 favor the equation of state (EoS) models that predict compact neutron stars (NSs), consistent with the radius constraints from X-ray observations. Motivated by such remarkable progress, we examine the fate of the remnants formed in NS mergers and focus on the roles of the angular momentum and the mass distribution of the binary NSs. In the mass-shedding limit (for which the dimensionless angular momentum equals the Keplerian value, i.e., j = j(Kep)), the adopted seven EoS models, except for H4 and ALF2, yield supramassive NSs in more than half of the mergers. However, for j less than or similar to 0.7 j(Kep), the presence or absence of a non-negligible fraction of supramassive NSs formed in the mergers depends sensitively on both the EoS and the mass distribution of the binary systems. The NS mergers with a total gravitational mass less than or similar to 2.6M(circle dot) are found to be able to shed valuable light on both the EoS model and the angular momentum of the remnants if supramassive NSs are still absent. We have also discussed the uncertainty on estimating the maximum gravitational mass of nonrotating NSs (M-max) due to the unknown j of the precollapse remnants. With the data of GW170817 and the assumption of the mass loss of 0.03 M-circle dot, we have M-max < (2.19, 2.32) M-circle dot (90% confidence level) for j = (1.0, 0.8) j(Kep), respectively.

第 43 条，共 248 条

M101: Spectral Observations of H II Regions and Their Physical Properties

Hu, N (Hu, Ning); Wang, EC (Wang, Enci); Lin, ZS (Lin, Zesen); Kong, X (Kong, Xu); Cheng, FZ (Cheng, Fuzhen); Fan, Z (Fan, Zou); Fang, GW (Fang, Guangwen); Lin, L (Lin, Lin); Mao, YW (Mao, Yewei); Wang, J (Wang, Jing); Zhou, X (Zhou, Xu); Zhou, ZM (Zhou, Zhiming); Zhu, YN (Zhu, Yinan); Zou, H (Zou, Hu)
ASTROPHYSICAL JOURNAL
卷: 854 期: 1 文献号: 68
By using the Hectospec 6.5 m Multiple Mirror Telescope and the 2.16 m telescope of the National Astronomical Observatories, of the Chinese Academy of Sciences, we obtained 188 high signal-to-noise ratio spectra of H II regions in the nearby galaxy M101, which is the largest spectroscopic sample of H II regions for this galaxy so far. These spectra cover a wide range of regions on M101, which enables us to analyze two-dimensional distributions of its physical properties. The physical parameters are derived from emission lines or stellar continua, including stellar population age, electron temperature, oxygen abundance, etc. The oxygen abundances are derived using two empirical methods based on O3N2 and R-23 indicators, as well as the direct T-e method when [O III] lambda 4363 is available. By applying the harmonic decomposition analysis to the velocity field, we obtained a line-of-sight rotation velocity of 71 km s(-1) and a position angle of 36 degrees. The stellar age profile shows an old stellar population in the galaxy center and a relatively young stellar population in outer regions, suggesting an old bulge and a young disk. The oxygen abundance profile exhibits a clear break at similar to 18 kpc, with a gradient of -0.0364 dex kpc(-1) in the inner region and -0.00686 dex kpc(-1) in the outer region. Our results agree with the "inside-out" disk growth scenario of M101.

第 44 条，共 248 条

The flat-spectrum radio quasar 3C 345 from the high to the low emission state

Berton, M (Berton, M.); Liao, NH (Liao, N. H.); La Mura, G (La Mura, G.); Jarvela, E (Jarvela, E.); Congiu, E (Congiu, E.); Foschini, L (Foschini, L.); Frezzato, M (Frezzato, M.); Ramakrishnan, V (Ramakrishnan, V.); Fan, XL (Fan, X. L.); Lahteenmaki, A (Lahteenmaki, A.); Pursimo, T (Pursimo, T.); Abate, V (Abate, V.); Bai, JM (Bai, J. M.); Calcidese, P (Calcidese, P.); Ciroi, S (Ciroi, S.); Chen, L (Chen, L.); Cracco, V (Cracco, V.); Li, SK (Li, S. K.); Tornikoski, M (Tornikoski, M.); Rafanelli, P (Rafanelli, P.)
ASTRONOMY & ASTROPHYSICS
卷: 614 文献号: A148
We report simultaneous observations at different energy bands in radio, optical, UV, X-rays and gamma rays of the flat-spectrum radio-quasar 3C 345. We built the light curve of the source at different frequencies from 2008, the beginning of the Fermi all-sky survey, to 2016, using new data and public archives. In particular we obtained several optical spectra, to study the behavior of emission lines and the continuum in different activity states and to derive the black hole mass. 3C 345 showed two flaring episodes in 2009, which occurred

simultaneously in gamma ray, optical/UV and X-rays, and were later followed in radio. The source shows an inverse Compton dominated spectral energy distribution, which moved from higher to lower frequencies from the high to the low state. The reverberation of emission lines during one outburst event allowed us to constrain the location of production of gamma rays very close to the broad-line region, and possibly in the jet-base. We report the observation of an increased accretion after the outburst, possibly induced by the decrease of magnetic held intensity with respect to the low state.

第 45 条，共 248 条

Constraints on the Composition, Magnetization, and Radiative Efficiency in the Jets of Blazars

Fan, XL (Fan, Xu-Liang); Wu, QW (Wu, Qingwen); Liao, NH (Liao, Neng-Hui)
ASTROPHYSICAL JOURNAL
卷: 861 期: 2 文献号: 97
The composition and energy dissipation in jets are two of the fundamental questions of jet physics that are not fully understood. In this paper, we attempt to constrain the composition, magnetization, and radiative efficiency for blazars with the recently released low-frequency radio catalog of the TIFR GMRT Sky Survey at 150 MHz.. The jet power estimated from the low-frequency radio emission is much lower than that derived from spectral energy distribution fitting assuming one proton per electron. Assuming the jet power estimated from low-frequency radio emission is physical, the fraction of electron/positron pairs can be constrained with n(pairs)/n(p) similar to 10. By comparing the power carried by the magnetic field and radiation with the jet power estimated from the low-frequency radio emission, we find both the relatively high magnetization parameter of sigma similar to 0.5 and the radiative efficiency of eta similar to 0.4 in the dissipation region of blazars. These results suggest that magnetic reconnection processes may play an important role in the energy dissipation of blazars. We also explore the connection between these three parameters (n(pairs)/n(p), sigma, and eta) and the black hole mass, disk luminosity, and Eddington ratio. No significant correlation is found, except that sigma shows a possible correlation with disk luminosity.

第 46 条，共 248 条

Searching for spectral oscillations due to photon-axionlike particle conversion using the Fermi-LAT observations of bright supernova remnants

Xia, ZQ (Xia, Zi-Qing); Zhang, C (Zhang, Cun); Liang, YF (Liang, Yun-Feng); Feng, L (Feng, Lei); Yuan, Q (Yuan, Qiang); Fan, YZ (Fan, Yi-Zhong); Wu, J (Wu, Jian)
PHYSICAL REVIEW D
卷: 97 期: 6 文献号: 063003
Axionlike particles (ALPs) are one promising type of dark matter candidate particle that may generate detectable effects on gamma-ray spectra other than the canonical weakly interacting massive particles. In this work we search for such oscillation effects in the spectra of supernova remnants caused by the photon-ALP conversion, using the Fermi Large Area Telescope data. Three bright supernova remnants, IC443, W44, and W51C, are analyzed. The inclusion of photon-ALP oscillations yields an improved fit to the gamma-ray spectrum of IC443, which gives a statistical significance of 4.2 sigma in favor of such spectral oscillation. However, the best-fit parameters of ALPs (m(a) = 6.6 neV, g(a gamma) = 13.4 x 10(-11) GeV-1) are in tension with the upper bound (g(a gamma) < 6.6 x 10(-11) GeV-1) set by the CAST experiment. It is difficult to explain the results using the systematic uncertainties of the flux measurements. We speculate that the "irregularity" displayed in the spectrum of IC443 may be due to the superposition of the emission from different parts of the remnant.

第 47 条，共 248 条

Two Transient X-Ray Quasi-periodic Oscillations Separated by an Intermediate State in 1H 0707-495

Zhang, PF (Zhang, Peng-fei); Zhang, P (Zhang, Peng); Liao, NH (Liao, Neng-hui); Yan, JZ (Yan, Jing-zhi); Fan, YZ (Fan, Yi-zhong); Liu, QZ (Liu, Qing-zhong)
ASTROPHYSICAL JOURNAL
卷: 853 期: 2 文献号: 193
In the narrow-line Seyfert 1 galaxy 1H 0707-495, recently a transient quasi-periodic oscillation (QPO) signal with a frequency of similar to 2.6 x 10(-4) Hz has been detected at a high statistical significance. Here, we reanalyze the same set of XMM-Newton data observed on 2008 February 4 with the weighted-wavelet Z-transform method. In addition to confirming the previous findings, we also find another QPO signal with a frequency of similar to 1.2 x 10-4 Hz in a separated X-ray emission phase at the significance level of similar to 3.7 sigma. The signal is also found fitting an autoregressive model though at a lower significance. The frequency ratio between these two signals is similar to 2: 1. The analysis of other XMM-Newton measurements of 1H 0707-495 also reveals the presence of the similar to 2.6 x10(-4) Hz (similar to 1.2 x 10(-4) Hz) QPO signal on 2007 May 14 (2010 September 17) at the significance level of similar to 4.2 sigma (similar to 3.5 sigma). The QPO frequency found in this work follows the fQPO-MBH relation reported in previous works spanning from stellar mass to supermassive black holes. This is the first observation of two separated transient X-ray QPO signals in active galactic nuclei, which sheds a new light on the physics of accreting supermassive black holes.

第 48 条，共 46 条

What is dark matter?

Bi Xiaojun; Fan Yizhong; Yue Qian; Zhou Yufeng
Chinese Science Bulletin
卷: 63 期: 24 页: 2413-2421
This study aims to review the early history of dark matter study, such as observational evidence from galactic rotational curves, gravitational lensing, and the cosmic microwave background, among others. The observation of the bullet clusters, which strongly supports the existence of dark matter rather than the theory of modified gravity, is discussed. The N body simulations also suggest the existence of cold non-relativistic dark matter and the existence of a universal form of the dark matter density distribution profile. We introduce a standard mechanism of thermal freeze-out for dark matter relic abundance, i.e., an explanation of how the dark matter particles that were kept in thermal equilibrium in the early stages of the universe are later unable to stay in equilibrium due to the expansion of the universe. The typical dark matter candidates are the so-called WIMPs (weakly interacting massive particles). Popular WIMP candidates include the lightest supersymmetric particles such as neutralinos. Other WIMP candidates such as the lightest T odd particles in the little Higgs models and the lightest KK (Kluza-Klein) modes in the universal extra dimension models are also discussed. Non-WIMP dark matter candidates such as axions are briefly discussed. The basic ideas and methods of dark matter detection, such as underground direct detection, which involves dark matter scattering off target nuclei, and indirect detection in space, which involves dark matter annihilation or decay in galaxies, are reviewed with a focus on recent experimental developments. For underground direct detection,

we begin with the basic formulas for elastic dark matter nuclei scattering and the general features of nuclear number dependence. Three types of observables are discussed: (1) direct recoil events, (2) solar modulation of the recoil events, and (3) directional effects or the day-night differences of the events. Then, we focus on the experiments studying low-mass dark matter below 10 GeV, such as SuperCDMS (super cryogenic dark matter search) and CDEX (China dark matter experiment), among others, with a special focus on the CDEX experiment, which uses point contact germanium detectors. Experiments studying high-mass dark matter using liquid argon, such as Xenon, PandaX (particle and astrophysical xenon detector), and DarkSide are also discussed. Directional detection experiments, such as DRIFT (directional recoil identification from tracks) and MIMAC (MIcro-tpc MAtrix of Chambers), are briefly discussed. For indirect detection experiments in space, we first introduce the basic theory of dark matter signals in cosmic rays and then discuss the importance of the propagation effects of high-energy cosmic rays, such as electrons, positrons, protons, antiprotons, and heavier cosmic ray nuclei. The uncertainties originating from various sources are also discussed. We then review recent experimental results, such as that from Fermi LAT (Fermi large area telescope) and AMS-02(Alpha magnetic spectrometer 02), with a focus on the most recent dark matter particle explorer (DAMPE) experiments. As nearby sources may contribute to CRE (cosmic ray electron) structures at high energies, the recently released DAMPE results on the CRE flux, which hinted at a narrow excess at energy of 1.4 TeV, is discussed in some detail. In general, a spectral structure with a narrow width appears to reveal the space time distribution of the sources. Future perspectives of heavier cosmic-ray nuclei, such as anti-deuteron and anti-helium, are also reviewed.

第 49 条，共 248 条

Constraints on the box-shaped cosmic ray electron feature from dark matter annihilation with the AMS-02 and DAMPE data

Zu, L (Zu, Lei); Zhang, C (Zhang, Cun); Feng, L (Feng, Lei); Yuan, Q (Yuan, Qiang); Fan, YZ (Fan, Yi-Zhong)
PHYSICAL REVIEW D
卷: 98 期: 6 文献号: 063010
Precise measurements of spectra of cosmic ray electrons and positrons can effectively probe the nature of dark matter (DM) particles. In a class of models where DM particles initially annihilate into a pair of intermediate particles which then decay into standard model particles, box-shaped spectra can be generated. Such spectra are distinct from astrophysical backgrounds and can probably be regarded as characteristic features of the DM annihilation. In this work, we search for such a feature in the total electron plus positron spectrum measured by AMS-02 and DAMPE. No significant evidence for such a DM annihilation component has been found. The 95% confidence level upper limits of the velocity-weighted annihilation cross section are derived, which range from similar to 10(-26) cm(3) s(-1) for DM mass of 50 GeV to similar to 10(-23) cm(3) s(-1) for DM mass of 10 TeV.

第 50 条，共 248 条

Scalar dark matter explanation of the DAMPE data in the minimal left-right symmetric model

Cao, JJ (Cao, Junjie); Guo, XF (Guo, Xiaofei); Shang, LL (Shang, Liangliang); Wang, F (Wang, Fei); Wu, PW (Wu, Peiwen); Zu, L (Zu, Lei)
PHYSICAL REVIEW D
卷: 97 期: 6 文献号: 063016
The left-right symmetric model (LRSM) is an attractive extension of the Standard Model (SM) that can address the origin of parity violation in the SM electroweak interactions, generate tiny neutrino masses, accommodate dark matter (DM) candidates, and provide a natural framework for baryogenesis through leptogenesis. In this work, we utilize the minimal LRSM to study the recently reported DAMPE results of the cosmic e(+)e(-) spectrum, which exhibits a tentative peak around 1.4 TeV, while satisfying the current neutrino data. We propose to explain the DAMPE peak with a complex scalar DM chi in two scenarios: (1) chi chi* -> H1++lH1-- -> l(i)(+)l(i)(+)l(j)(_)l(j)(-), and (2) chi chi* -> Hk++Hk-- -> l(i)(+)l(i)(+)l(j)(-)l(j)(-) accompanied by chi chi* -> H1+H1- -> l(i)(+)v(l1)l(-)v(lj), with l(i,j) = e, mu, tau and k =1, 2. We fit the theoretical prediction of the e(+)e(-) ethorne-spectrum to relevant experimental data to determine the scalar mass spectrum favored by the DAMPE excess. We also consider various constraints from theoretical principles and collider experiments, as well as DM relic density and direct search experiments. We find that there is ample parameter space to interpret the DAMPE data while also passing the constraints. On the other hand, our explanations usually imply the existence of other new physics at an energy scale ranging from10(7) to 10(11) GeV. Collider tests of our explanations are also discussed.

第 51 条，共 248 条

Scalar dark matter interpretation of the DAMPE data with U(l) gauge Interactions

Cao, JJ (Cao, Junjie); Feng, L (Feng, Lei); Guo, XF (Guo, Xiaofei); Shang, LL (Shang, Liangliang); Wang, F (Wang, Fei); Wu, PW (Wu, Peiwen)
PHYSICAL REVIEW D
卷: 97 期: 9 文献号: 095011
Recently, the Dark Matter Particle Explorer (DAMPE) experiment released the new measurement of the total cosmic e(+) e(-) flux between 25 GeV and 4.6 TeV, which indicates a spectral softening at around 0.9 TeV and a tentative peak at around 1.4 TeV. We utilize a scalar dark matter (DM) model to explain the DAMPE peak by XX -> Z'Z' -> l (l) over barl'(l) over bar 'l with an additional anomaly-free gauged U (l) family symmetry, in which X, Z'and l(('')) denote, respectively, the scalar DM, the new gauge boson, and l(('')) = e, mu, tau, with m(x) similar to m(z)' similar to 2 x 1.5 (TeV). We first illustrate that the minimal framework Gsm X U(l)(Y') with the above mass choices can explain the DAMPE excess, which, however, be excluded by LHC constraints from the Z' searches. Then, we study a nonminimal framework G(SM) X U(l)(Y') x U(i)(Y") in which U(l)(Y") mixes with U(l)(Y'). We show that such a framework can interpret the DAMPE data and at the same time survive all other constraints including the DM relic abundance, DM direct detection, and collider bounds. We also investigate the predicted e(+) e(-) spectrum in this framework and find that the mass splitting Delta m = m(x) - m(z") should be less than about 17 GeV to produce the peaklike structure.

Laboratory for Dark Matter and Space Astronomy

第 52 条，共 248 条

Effect of Alpha Beams on Low-frequency Electromagnetic Waves Driven by Proton Beams

Xiang, L (Xiang, L.); Wu, DJ (Wu, D. J.); Chen, L (Chen, L.)
ASTROPHYSICAL JOURNAL
卷: 869 期: 1 文献号: 64
Electromagnetic waves (EMWs) below or near the proton gyrofrequency can be left-hand (LH) or right-hand (RH) polarized waves, which are believed to be fundamentally important in the energization of plasma particles. Proton and alpha beams that are associated with EMW activities are ubiquitous in space and astrophysical plasmas. Based upon linear Vlasov theory, we study the effect of alpha beams on the LH and RH instabilities driven by both the presence of proton and alpha beam populations in a compensated-current system. The results show that the thresholds, real frequencies, and growth rates of both instabilities are highly sensitive to the density and drift velocity of alpha beams. In particular, alpha beams with v(He) < v(He)(L(R)min) inhibit two kinds of instabilities; where v(He)(L(R)min) is the drift velocity of alpha beams with minimum values of growth rates, while for v(He) < v(He)(L(R)min) both the growth rates are enhanced with the density or drift velocity of alpha beams, especially for the LH waves. We also investigate the competition between the LH and RH instabilities. The RH waves have a lower threshold and higher growth rate than the LH waves. Additionally, a comparison of the approximate analytical solutions with the exact numerical calculations based on WHAMP indicates that the analytical results are in good agreement with the numerical calculations. A possible application to EMW activities with respect to the formation and evolution of ion beams in the solar wind is briefly discussed.

第 53 条，共 248 条

Fermi Large Area Telescope Detection of Gamma-Ray Emission from the Direction of Supernova iPTF14hls

Yuan, Q (Yuan, Qiang); Liao, NH (Liao, Neng-Hui); Xin, YL (Xin, Yu-Liang); Li, Y (Li, Ye); Fan, YZ (Fan, Yi-Zhong); Zhang, B (Zhang, Bing); Hu, HB (Hu, Hong-Bo); Bi, XJ (Bi, Xiao-Jun)
ASTROPHYSICAL JOURNAL LETTERS
卷: 854 期: 2 文献号: L18
The remnant of a supernova explosion is widely believed to be the acceleration site of high-energy cosmic-ray particles. The acceleration timescale is, however, typically very long. Here, we report the detection of a variable gamma-ray source with the Fermi Large Area Telescope, which is positionally and temporally consistent with a peculiar supernova, iPTF14hls. A quasi-stellar object SDSS J092054.04+504251.5, which is probably a blazar candidate according to the infrared data, is found in the error circle of the gamma-ray source. More data about the gamma-ray source and SDSS J092054.04+504251.5 are needed to confirm their association. On the other hand, if the association between the gamma-ray source and the supernova is confirmed, this would be the first time detecting high-energy gamma-ray emission from a supernova, suggesting very fast particle acceleration by supernova explosions.

第 54 条，共 248 条

Theoretical scaling law of coronal magnetic field and electron power-law index in solarmicrowave burst sources

Huang, Y (Huang, Y.); Song, QW (Song, Q. W.); Tan, BL (Tan, B. L.)
ASTROPHYSICS AND SPACE SCIENCE
卷: 363 期: 4 文献号: 79
It is first proposed a theoretical scaling law respectively for the coronal magnetic field strength B and electron power-law index delta versus frequency and coronal height in solar microwave burst sources. Based on the non-thermal gyro-synchrotron radiation model (Ramaty in Astrophys. J. 158:753, 1969), B and delta are uniquely solved by the observable optically-thin spectral index and turnover (peak) frequency, the other parameters (plasma density, temperature, view angle, low and high energy cutoffs, etc.) are relatively insensitive to the calculations, thus taken as some typical values. Both of B and delta increase with increasing of radio frequency but with decreasing of coronal height above photosphere, and well satisfy a square or cubic logarithmic fitting.

第 55 条，共 248 条

On the knee of Galactic cosmic rays in light of sub-TeV spectral hardenings

Guo, YQ (Guo, Yi-Qing); Yuan, Q (Yuan, Qiang)
CHINESE PHYSICS C
卷: 42 期: 7 文献号: 075103
More than fifty years after the discovery of the knee in the cosmic ray (CR) spectra, its physical origin remains a mystery. This is partly due to the ambiguity of the energy spectra of individual components. Recently, direct measurements from several space experiments found significant spectral hardenings of CR nuclei at similar to 200 GV. A joint modeling of the direct and indirect measurements may help to understand the experimental systematics and the physics of the knee. In this work, we update the phenomenological "poly-gonato" model to include the spectral hardenings, with a changing spectral index of gamma+beta.logE. This modification gives a reasonable description of the CR spectra in a wide energy range. However, the fits to different data sets give different results. We find that the fit to the AMS-02 and CREAM data slightly favors a relatively low energy knee of the light components. In such a case, the expected all-particle spectra under-shoot the data, which may require an extra component of CRs. The fits to AMS-02 data and the light component (H+He) data from the Tibet AS gamma/ARGO-YBJ/WFCTA and KASCADE experiments give consistent results with the all-particle spectra. We further propose a possible physical realization of such a "modified poly-gonato" model of spectral hardenings by means of spatially-dependent diffusion of CRs. We find reasonably good agreement between the model predictions and the data for CR spectra, the secondary-to-primary ratios, and the amplitude of anisotropies.

第 56 条，共 248 条

Consistency test of the AMS-02 antiproton excess with direct detection data based on the effective field theory approach

Cui, MY (Cui, Ming-Yang); Huang, WC (Huang, Wei-Chih); Tsai, YLS (Tsai, Yue-Lin Sming); Yuan, Q (Yuan, Qiang)
JOURNAL OF COSMOLOGY AND ASTROPARTICLE PHYSICS
期: 11 文献号: 039
The potential antiproton excess in the AMS-02 data is of much interest and can probably come from dark matter annihilations. Based on the effective field theory approach, in this work we investigate the compatibility of the DM interpretation of the AMS-02 antiproton excess and the null results from direct detection experiments, LUX, PandaX-II, and XENON1T. We focus on dimension-five and -six operators with fermion DM. Only one of dimension-five and one of dimension-six operators can successfully account for the antiproton excess, while the rest either are excluded by direct detection or require very small cut-off scales which invalidate the effective field theory approach.

第 57 条，共 248 条

Revisit of cosmic ray antiprotons from dark matter annihilation with updated constraints on the background model from AMS-02 and collider data

Cui, MY (Cui, Ming-Yang); Pan, X (Pan, Xu); Yuan, Q (Yuan, Qiang); Fan, YZ (Fan, Yi-Zhong); Zong, HS (Zong, Hong-Shi)
JOURNAL OF COSMOLOGY AND ASTROPARTICLE PHYSICS
期: 6 文献号: 024
We study the cosmic ray antiprotons with updated constraints on the propagation, proton injection, and solar modulation parameters based on the newest AMS-02 data near the Earth and Voyager data in the local interstellar space, and on the cross section of antiproton production due to proton-proton collisions based on new collider data. We use a Bayesian approach to properly consider the uncertainties of the model predictions of both the background and the dark matter (DM) annihilation components of antiprotons. We find that including an extra component of antiprotons from the annihilation of DM particles into a pair of quarks can improve the fit to the AMS-02 antiproton data considerably. The favored mass of DM particles is about 60 similar to 100 GeV, and the annihilation cross section is just at the level of the thermal production of DM (<sigma upsilon > similar to O (10(-26)) cm(3) s(-1)).

第 58 条，共 248 条

A systematic Chandra study of Sgr A*: II. X-ray flare statistics

Yuan, Q (Yuan, Qiang); Wang, QD (Wang, Q. Daniel); Liu, SM (Liu, Siming); Wu, K (Wu, Kinwah)
MONTHLY NOTICES OF THE ROYAL ASTRONOMICAL SOCIETY
卷: 473 期: 1 页: 306-316
The routinely flaring events from Sgr A* trace dynamic, high-energy processes in the immediate vicinity of the supermassive black hole. We statistically study temporal and spectral properties, as well as fluence and duration distributions, of the flares detected by the Chandra X-ray Observatory from 1999 to 2012. The detection incompleteness and bias are carefully accounted for in determining these distributions. We find that the fluence distribution can be well characterized by a power law with a slope of 1.73(-0.19)(+0.20), while the durations (tau in seconds) by a lognormal function with a mean log(tau) = 3.39(-0.24)(+0.27) and an intrinsic dispersion sigma = 0.28(-0.06)(+0.08). No significant correlation between the fluence and duration is detected. The apparent positive correlation, as reported previously, is mainly due to the detection bias (i.e. weak flares can be detected only when their durations are short). These results indicate that the simple self-organized criticality model has difficulties in explaining these flares. We further find that bright flares usually have asymmetric light curves with no statistically evident difference/preference between the rising and decaying phases in terms of their spectral/timing properties. Our spectral analysis shows that although a power-law model with a photon index of 2.0 +/- 0.4 gives a satisfactory fit to the joint spectra of strong and weak flares, there is weak evidence for a softer spectrum of weaker flares. This work demonstrates the potential to use statistical properties of X-ray flares to probe their trigger and emission mechanisms, as well as the radiation propagation around the black hole.

第 59 条，共 248 条

Heart beats from the dark side

Chang, J (Chang, Jin)
卷: 2 期: 1 页: 99-99
NATURE ASTRONOMY
Baryonic matter (including the Sun, the Moon, the Earth, part of our Milky Way and so on) accounts for only ~5% of the energy density of the current Universe, while dark matter accounts for more than five times more. But dark matter is so difficult to detect that, until now, there is only macroscopic astronomical evidence indicative of its existence. In fact, we have yet to detect a single dark matter particle despite using equipment of the highest sensitivity currently available.
There are several options for detecting dark matter particles. One technique, called the indirect method, tries to find hints of dark matter particles by detecting high-energy cosmic rays in space with a large particle spectrometer. The mystery of dark matter could be unravelled using information from these high-energy cosmic rays, such as the excess of the positron fraction, which was observed by the PAMELA detector and confirmed by the Alpha Magnetic Spectrometer - 02 (AMS-02). But such an excess could be due to nearby pulsars and not dark matter.
DAMPE, nicknamed Wukong after the Monkey King in Chinese mythology, is a space-based telescope in a Sun-synchronous, 500 km orbit (Fig. 1). It was launched on 17 December 2015. This observatory indirectly detects dark matter particles by directly measuring high-energy cosmic rays in space. There have been several space-based projects before DAMPE, such as Fermi (a gamma ray telescope) and AMS-02 (a high-precision magnetic spectrometer). DAMPE has four sub-detectors: the PSD (plastic scintillator detector) to measure charge; the STK (silicon tracker) to measure particle trajectories; the BGO (bismuth germinate) calorimeter to measure particle energy and type; and the NUD (neutron detector) again to measure particle type. The key feature of DAMPE is the BGO calorimeter, which is a three-dimensional imaging calorimeter with a thickness of about 32 radiation lengths. This ensures that DAMPE has very good sensitivity (better energy resolution and higher electron/proton separation power) for high-energy e± and gamma-rays, opening an observing ‘window’ in the TeV energy range in space. The BGO is the biggest calorimeter in space at present. DAMPE’s main scientific objectives include: (1) understanding the mechanisms of particle acceleration operating in astrophysical sources, and the propagation of cosmic rays in the Milky Way; (2) probing the nature of dark matter; (3) studying the gamma-ray emission from Galactic and extragalactic sources.

第 60 条，共 248 条

Electron acceleration by turbulent plasmoid reconnection

Zhou, X (Zhou, X.); Buchner, J (Buechner, J.); Widmer, F (Widmer, F.); Munoz, PA (Munoz, P. A.)
PHYSICS OF PLASMAS
卷: 25 期: 4 文献号: 042904
In space and astrophysical plasmas, like in planetary magnetospheres, as that of Mercury, energetic electrons are often found near current sheets, which hint at electron acceleration by magnetic reconnection. Unfortunately, electron acceleration by reconnection is not well understood yet, in particular, acceleration by turbulent plasmoid reconnection. We have investigated electron acceleration by turbulent plasmoid reconnection, described by MHD simulations, via test particle calculations. In order to avoid resolving all relevant turbulence scales down to the dissipation scales, a mean-field turbulence model is used to describe the turbulence of sub-grid scales and their effects via a turbulent electromotive force (EMF). The mean-field model describes the turbulent EMF as a function of the mean values of current density, vorticity, magnetic field as well as of the energy,

cross-helicity, and residual helicity of the turbulence. We found that, mainly around X-points of turbulent reconnection, strongly enhanced localized EMFs most efficiently accelerated electrons and caused the formation of power-law spectra. Magnetic-field-aligned EMFs, caused by the turbulence, dominate the electron acceleration process. Scaling the acceleration processes to parameters of the Hermean magnetotail, electron energies up to 60 keV can be reached by turbulent plasmoid reconnection through the thermal plasma. Published by AIP Publishing.

第 61 条，共 248 条

Dark Matter Particle Explorer observations of high-energy cosmic ray electrons plus positrons and their physical implications

Yuan, Q (Yuan, Qiang); Feng, L (Feng, Lei)
SCIENCE CHINA-PHYSICS MECHANICS & ASTRONOMY
卷: 61 期: 10 文献号: UNSP 101002
The DArk Matter Particle Explorer (DAMPE) is a satellite-borne, high-energy particle and -ray detector, which is dedicated to indirectly detecting particle dark matter and studying high-energy astrophysics. The first results about precise measurement of the cosmic ray electron plus positron spectrum between 25 GeV and 4.6 TeV were published recently. The DAMPE spectrum reveals an interesting spectral softening arount 0:9 TeV and a tentative peak around 1:4 TeV. These results have inspired extensive discussion. The detector of DAMPE, the data analysis, and the first results are introduced. In particular, the physical interpretations of the DAMPE data are reviewed.

第 62 条，共 248 条

Interpretation of the DAMPE 1.4 TeV peak according to the decaying dark matter model

Pan, X (Pan, Xu); Zhang, C (Zhang, Cun); Feng, L (Feng, Lei)
SCIENCE CHINA-PHYSICS MECHANICS & ASTRONOMY
卷: 61 期: 10 文献号: UNSP 101006
Highly accurate measurements of cosmic ray electron flux by the dark matter particle explorer (DAMPE) ranging between 25 GeV and 4.6 TeV have recently been published. A sharp peak structure was found at 1.4 TeV. This unexpected peak structure can be reproduced by the annihilation/decay of a nearby dark matter (DM) halo. In this study, we adopt the decaying-DM model to interpret the 1.4 TeV peak. We found that the decay products of the local DM subhalo could contribute to the DMAPE peak with m (DM) = 3 TeV and tau 10(28) s. We also obtain constraints on DM lifetime and the distance of the local DM subhalo by comparison with DAMPE data.

第 63 条，共 248 条

Prototype design of electronics readout system for solar gamma-ray spectrometer's high energy deposited

Chen Wei; Guo Jianhua; Wang Shen
Nuclear Techniques
卷: 41 期: 2 页: 020402-1-020402-7
[Background] The large area solar gamma-ray spectrometer (LASGA) is a high-energy radiation detector that consists of anti-coincidence detectors and calorimeter. The calorimeter is composed of 5 orthogonal LaBr3 (lanthanum bromide) layers. Each layer includes fourteen 25 mm*25 mm*400 mm LaBr_3 crystals. To achieve large dynamic range, each LaBr_3 crystal matches with two independent readout elements with different gains. High gain readout uses a photomultiplier tube (PMT) while the low gain uses photodiode (PD). Since PD has no amplification capability for photoelectrons, the LASGA readout system requires a low-noise readout electronics system to achieve a high signal-to-noise ratio (SNR). [Purpose] This study aims to design an electronics prototype system with high dynamic range and low noise properties. [Methods] A 64-channel charge sensitive ASIC (VA140) produced by the IDEAS Inc. was used in front-end electronics board. And an Altera cyclone field-programmable gate array (FPGA) (EP3C25Q240C8) was employed to control the ASIC, analog to digital converter (ADC) and digital to analog converter (DAC) chips in data acquisition board. The digitalized detector signal was packaged in field-programmable gate array (FPGA) and sent to personal computer (PC) for processing. [Results] The performance of the electronics prototype was tested, while the minimum ionizing particles (MIPs) response of LaBr3 with cosmic ray muon was carried out as well. The test results showed that the noise level of the electronics system (@ 0 pF) and the detection system (connected with PD) at room temperature was about 600 e~- and 1 800 e~- respectively. And there was a good linearity in the range of 0-200 fC. The integral nonlinearity (INL) of 126 channels in the range of 0-180 fC was better than 3%. [Conclusion] Single bromide lanthanum unit can measure the energy deposited linearly up to 250 MeV. The dynamic range and SNR of the prototype system could fully meet the project's requirements.

第 64 条，共 248 条

Dark Matter Particle Explorer and Its First Results

Chang Jin
Chinese Journal of Space Science
卷: 38 期: 5 页: 610-614
The Dark Matter Particle Explorer (DAMPE) is China's first astronomical satellite dedicated to the indirect detection of dark matter particles and the study of high-energy astrophysics. It can measure high-energy electrons and gamma-rays up to 10 TeV with unprecedentedly high energy resolution and low background. Cosmic ray nuclei up to 100 TeV can also be measured. DAMPE was launched on December 17, 2015, and has been operating smoothly in space for more than two years since then. The first results about the precise measurements of the electron plus positron spectrum between 25 GeV and 4.6 TeV have been reported.

第 65 条，共 248 条

The Design and Realization of the Payload Integrated Test System for DAMPE

Xu Zunlei; Zhang Yongqiang; Zhang Zhe; Zang Jingjing; Zhang Yunlong; Guo Jianhua; Cai Mingsheng; Chang Jin
Acta Astronomica Sinica
卷: 59 期: 3 页: 25_1-25_11
The DArk Matter Particle Explorer (DAMPE) is a space-borne high-energy cosmic ray detector. The payload consists of five subsystems, including the Plastic Scintillator Detector (PSD), the Silicon-Tungsten tracKer converter detector(STK), the Bismuth germanate (BGO) calorimeter, the Neutron Detector (NUD), and the Data AcQuisition system (DAQ). The five subsystems work collaboratively to collect the information of cosmic rays. In order to systematically verify the performance of the payload before launch, we developed a set of integrated test system for the ground tests of the payload based on the LabWindows/CVI (C programming language Virtual Instrument) platform. This system realizes the integration and automation of the comprehensive ground tests of the payload, improves

the security, reliability, and efficiency of the ground tests, and guarantees the successful delivery of the payload.

第 66 条，共 248 条

空间间接探测暗物质粒子

Chang Jin
现代物理知识
DOI：10.13405/j.cnki.xdwz.2018.02.007
在过去的几十年间,人类对于整个宇宙的认识有了飞跃式的发展,取得了辉煌的成就。基于近年天文观测的结果,一个暗物质鳎暗能量鳎暴涨的宇宙学标准模型被建立起来。我们的宇宙组成,如图 1 所示:已知的基本粒子只占整个宇宙的 5%左右,而 27%左右是不发光的暗物质,68%左右是类似真空能的暗能量。寻找暗物质粒子,研究暗能量的本质等,结合微观世界和宇观世界,结合粒子物理和宇宙学的研究已成为 21 世纪物理学和天文学。

第 67 条，共 248 条

The X-ray binary system in the EP era

Gou Lijun; Dong Yanting; Wang Zhongxiang; Li Xiangdong; Liu Jifeng; Liu Bifang; Yuan Feng; Zhang Shu; Yan Shuping; Li Lixin; Yuan Yefei; Gu Weimin
Scientia Sinica Physica, Mechanica & Astronomica
卷: 48 期: 3 页: 039509-1-039509-7
Searching for X-ray binaries and establishing a large sample are the foundation of answering many scientific problems, such as, how many BH X-ray binaries are there within our Milky Way galaxy? Does there exist a real gap between the mass distribution of neutron stars and black holes? Is there any black hole system within globular clusters? The planned mission Einstein Probe (EP) has a much better sensitivity compared to the past missions, so it is expected to discover many new X-ray binary systems over its operating period, which will play a key role in helping solve the problems above then.

第 68 条，共 248 条

The second-closest gamma-ray burst: sub-luminous GRB 111005A with no supernova in a super-solar metallicity environment

Michalowski, MJ (Michalowski, Michal J.); Xu, D (Xu, Dong); Stevens, J (Stevens, Jamie); Levan, A (Levan, Andrew); Yang, J (Yang, Jun); Paragi, Z (Paragi, Zsolt); Kamble, A (Kamble, Atish); Tsai, AL (Tsai, An-Li); Dannerbauer, H (Dannerbauer, Helmut); van der Horst, AJ (van der Horst, Alexander J.); Shao, L (Shao, Lang); Crosby, D (Crosby, David); Gentile, G (Gentile, Gianfranco); Stanway, E (Stanway, Elizabeth); Wiersema, K (Wiersema, Klaas); Fynbo, JPU (Fynbo, Johan P. U.); Tanvir, NR (Tanvir, Nial R.); Kamphuis, P (Kamphuis, Peter); Garrett, M (Garrett, Michael); Bartczak, P (Bartczak, Przemyslaw)
ASTRONOMY & ASTROPHYSICS
卷: 616 文献号: A169
We report the detection of the radio afterglow of a long gamma-ray burst (GRB) 111005A at 5-345 GHz, including very long baseline interferometry observations with a positional error of 0.2 mas. The afterglow position is coincident with the disc of a galaxy ESO 58049 at z = 0.01326 (similar to 1 '' from its centre), which makes GRB 111005A the second-closest GRB known to date, after GRB 980425. The radio afterglow of GRB 111005A was an order of magnitude less luminous than those of local low-luminosity GRBs, and obviously less luminous than those of cosmological GRBs. The radio flux was approximately constant and then experienced an unusually rapid decay a month after the GRB explosion Similarly to only two other GRBs, we did not find the associated supernovae (SNe), despite deep near - and mid-infrared observations 1-9 days after the GRB explosion, reaching similar to 20 times fainter than other SNe associated with GRBs. Moreover, we measured a twice-solar metallicity for the GRB location. The low gamma-ray and radio luminosities, rapid decay, lack of a SN, and super-solar metallicity suggest that GRB 111005A represents a rare class of GRB that is different from typical core-collapse events. We modelled the spectral energy distribution of the GRB 111005A host finding that it is a moderately star-forming dwarf galaxy, similar to the host of GRB 980425. The existence of two local GRBs in such galaxies is still consistent with the hypothesis that the GRB rate is proportional to the cosmic star formation rate (SFR) density, but suggests that the GRB rate is biased towards low SFRs. Using the far-infrared detection of ESO 580-49, we conclude that the hosts of both GRBs 111005A and 980425 exhibit lower dust content than what would be expected from their stellar masses and optical colors.

第 69 条，共 248 条

A Comprehensive Analysis of Fermi Gamma-Ray Burst Data. IV. Spectral Lag and its Relation to E-p Evolution

Lu, RJ (Lu, Rui-Jing); Liang, YF (Liang, Yun-Feng); Lin, DB (Lin, Da-Bin); Lu, J (Lu, Jing); Wang, XG (Wang, Xiang-Gao); Lu, HJ (Lu, Hou-Jun); Liu, HB (Liu, Hong-Bang); Liang, EW (Liang, En-Wei); Zhang, B (Zhang, Bing)
ASTROPHYSICAL JOURNAL
卷: 865 期: 2 文献号: 153
The spectral evolution and spectral lag behavior of 92 bright pulses from 84 gamma-ray bursts observed by the Fermi Gamma-ray Burst Monitor (GBM) telescope are studied. These pulses can be classified into hard-to-soft pulses (H2S; 64/92), H2S-dominated-tracking pulses (21/92), and other tracking pulses (7/92). We focus on the relationship between spectral evolution and spectral lags of H2S and H2S-dominated-tracking pulses. The main trend of spectral evolution (lag behavior) is estimated with log E-p alpha k(E) log(t + t(0)) ((tau) over cap alpha k((tau) over cap) log E), where E-p is the peak photon energy in the radiation spectrum, t + t(0) is the observer time relative to the beginning of pulse - t(0), and (tau) over cap is the spectral lag of photons with energy E with respect to the energy band 8-25 keV For H2S and H2S-dominated-tracking pulses, a weak correlation between k((tau) over cap)/W and k(E) is found, where W is the pulse width. We also study the spectral lag behavior with peak time t(pE) of pulses for 30 well-shaped pulses and estimate the main trend of the spectral lag behavior with log t(pE) alpha k(tp) log E. It is found that k(tp) is correlated with k(E). We perform simulations under a phenomenological model of spectral evolution, and find that these correlations are reproduced. We then conclude that spectral lags are closely related to spectral evolution within the pulse. The most natural explanation of these observations is that the emission is from the electrons in the same fluid unit at an emission site moving away from the central engine, as expected in the models invoking magnetic dissipation in a moderately high-sigma outflow.

第 70 条，共 248 条

Understanding the spectral hardenings and radial distribution of Galactic cosmic rays and Fermi diffuse gamma rays with spatially-dependent propagation

Guo, YQ (Guo, Yi-Qing); Yuan, Q (Yuan, Qiang)
PHYSICAL REVIEW D
卷: 97 期: 6 文献号: 063008
Recent direct measurements of Galactic cosmic ray spectra by

balloon/space-borne detectors reveal spectral hardenings of all major nucleus species at rigidities of a few hundred GV. The all-sky diffuse gamma-ray emissions measured by the Fermi Large Area Telescope also show spatial variations of the intensities and spectral indices of cosmic rays. These new observations challenge the traditional simple acceleration and/or propagation scenario of Galactic cosmic rays. In this work, we propose a spatially dependent diffusion scenario to explain all these phenomena. The diffusion coefficient is assumed to be anticorrelated with the source distribution, which is a natural expectation from the charged particle transportation in a turbulent magnetic field. The spatially dependent diffusion model also gives a lower level of anisotropies of cosmic rays, which are consistent with observations by underground muons and air shower experiments. The spectral variations of cosmic rays across the Galaxy can be properly reproduced by this model.

第 71 条，共 248 条

Magnetic Reconnection at the Earliest Stage of Solar Flux Emergence

Tian, H (Tian, Hui); Zhu, XS (Zhu, Xiaoshuai); Peter, H (Peter, Hardi); Zhao, J (Zhao, Jie); Samanta, T (Samanta, Tanmoy); Chen, YJ (Chen, Yajie)
ASTROPHYSICAL JOURNAL
卷: 854 期: 2 文献号: 174
On 2016 September 20, the Interface Region Imaging Spectrograph observed an active region during its earliest emerging phase for almost 7 hr. The Helioseismic and Magnetic Imager on board the Solar Dynamics Observatory observed continuous emergence of small-scale magnetic bipoles with a rate of similar to 10(16) Mx s(-1). The emergence of magnetic fluxes and interactions between different polarities lead to the frequent occurrence of ultraviolet (UV) bursts, which exhibit as intense transient brightenings in the 1400 angstrom images. In the meantime, discrete small patches with the same magnetic polarity tend to move together and merge, leading to the enhancement of the magnetic fields and thus the formation of pores (small sunspots) at some locations. The spectra of these UV bursts are characterized by the superposition of several chromospheric absorption lines on the greatly broadened profiles of some emission lines formed at typical transition region temperatures, suggesting heating of the local materials to a few tens of thousands of kelvin in the lower atmosphere by magnetic reconnection. Some bursts reveal blue-and redshifts of similar to 100 km s(-1) at neighboring pixels, indicating the spatially resolved bidirectional reconnection outflows. Many such bursts appear to be associated with the cancellation of magnetic fluxes with a rate of the order of similar to 10(15) Mx s(-1). We also investigate the three-dimensional magnetic field topology through a magnetohydrostatic model and find that a small fraction of the bursts are associated with bald patches (magnetic dips). Finally, we find that almost all bursts are located in regions of large squashing factor at the height of similar to 1 Mm, reinforcing our conclusion that these bursts are produced through reconnection in the lower atmosphere.

第 72 条，共 248 条

Two Solar Tornadoes Observed with the Interface Region Imaging Spectrograph

Yang, ZH (Yang, Zihao); Tian, H (Tian, Hui); Peter, H (Peter, Hardi); Su, Y (Su, Yang); Samanta, T (Samanta, Tanmoy); Zhang, JW (Zhang, Jingwen); Chen, YJ (Chen, Yajie)
ASTROPHYSICAL JOURNAL
卷: 852 期: 2 文献号: 79
The barbs or legs of some prominences show an apparent motion of rotation, which are often termed solar tornadoes. It is under debate whether the apparent motion is a real rotating motion, or caused by oscillations or counter-streaming flows. We present analysis results from spectroscopic observations of two tornadoes by the Interface Region Imaging Spectrograph. Each tornado was observed for more than 2.5 hr. Doppler velocities are derived through a single Gaussian fit to the Mg II k 2796 angstrom and Si IV 1393 angstrom. line profiles. We find coherent and stable redshifts and blueshifts adjacent to each other across the tornado axes, which appears to favor the interpretation of these tornadoes as rotating cool plasmas with temperatures of 10(4) K-10(5) K. This interpretation is further supported by simultaneous observations of the Atmospheric Imaging Assembly on board the Solar Dynamics Observatory, which reveal periodic motions of dark structures in the tornadoes. Our results demonstrate that spectroscopic observations can provide key information to disentangle different physical processes in solar prominences.

第 73 条，共 248 条

Two-zone Diffusion of Electrons and Positrons from Geminga Explains the Positron Anomaly

Fang, K (Fang, Kun); Bi, XJ (Bi, Xiao-Jun); Yin, PF (Yin, Peng-Fei); Yuan, Q (Yuan, Qiang)
ASTROPHYSICAL JOURNAL
卷: 863 期: 1 文献号: 30
The recent HAWC observations of a very-high-energy 7-ray halo around Geminga and Monogem indicate a very slow diffusion of cosmic rays that results in a tiny contribution of positrons from these two pulsars to the local flux. This makes the cosmic positron excess anomaly observed by PAMELA and AMS-02 even more puzzling. However, from the boron-to-carbon ratio data one can infer that the average diffusion coefficient in the Galaxy should be much larger. In this work we propose a two-zone diffusion model in which the diffusion is slow only in a small region around the source, outside of which the propagation is as fast as usual. We find that this scenario can naturally explain the positron excess data with parameters even more reasonable than those in the conventional one-zone diffusion model. The reason is that during the lifetime of Geminga (similar to 300 kyr), the electrons/positrons have propagated too far away with a fast diffusion and led to a low local flux. The slow-diffusion region in the two-zone model helps to confine the electrons/positrons for a long time and lead to an enhancement of the local flux. So under the constraint of the HAWC observations, pulsars are still the probable origin of the cosmic-ray positron excess.

第 74 条，共 248 条

Two-neutron halo state of B-15 around 3.48 MeV by a three-body model

Bai, D (Bai, Dong); Ren, ZZ (Ren, Zhongzhou); Dong, TK (Dong, Tiekuang)
CHINESE PHYSICS C
卷: 42 期: 6 文献号: 064103
We investigate low-lying bound states of the neutron-rich nucleus B-15 by assuming it is a three-body system made of an inert core B-13 and two valence neutrons. The three-body wave functions are obtained using the Faddeev formalism. Special attention is paid to the excited state at 3.48(6) MeV observed in the (13)c(14c,N-12)B-15 reaction, whose properties are less clear theoretically. In our three-body model, besides the ground state 3/(2)2 a second 3/(2)2- state is discovered at around 3.61 MeV, which might be identified with the excited state observed at 3.48(6) MeV. We study this 3/(2)2- state in detail. It turns out to be a two-neutron halo

state with a large matter radius r(m)approximate to 4.770 fm.

第 75 条，共 248 条

Performance of a scintillation detector array operated with LHAASO-KM2A electronics

Wang, Z (Wang, Zhen); Guo, YQ (Guo, Yiqing); Cai, H (Cai, Hui); Chang, JF (Chang, Jinfan); Chen, TL (Chen, Tianlu); Danzengluobu (Danzengluobu); Feng, YL (Feng, Youliang); Gao, Q (Gao, Qi); Gou, QB (Gou, Quanbu); Guo, YY (Guo, Yingying); Hou, C (Hou, Chao); Hu, HB (Hu, Hongbo); Labaciren (Labaciren); Liu, C (Liu, Cheng); Li, HJ (Li, Haijin); Liu, J (Liu, Jia); Liu, MY (Liu, Maoyuan); Qiao, BQ (Qiao, Bingqiang); Qian, XL (Qian, Xiangli); Sheng, XD (Sheng, Xiangdong); Tian, Z (Tian, Zhen); Wang, Q (Wang, Qun); Xue, L (Xue, Liang); Yao, YH (Yao, Yuhua); Zhang, SR (Zhang, Shaoru); Zhang, XY (Zhang, Xueyao); Zhang, Y (Zhang, Yi)

EXPERIMENTAL ASTRONOMY

卷: 45 期: 3 页: 363-377

A scintillation detector array composed of 115 detectors and covering an area of about 20000 m(2) was installed at the end of 2016 at the Yangbajing international cosmic ray observatory and has been taking data since then. The array is equipped with electronics from Large High Altitude Air Shower Observatory Square Kilometer Complex Array (LHAASO-KM2A) and, in turn, currently serves as the largest debugging and testing platform for the LHAASO-KM2A. Furthermore, the array was used to study the performance of a wide field-of-view air Cherenkov telescope by providing accurate information on the shower core, direction and energy, etc. This work is mainly dealing with the scintillation detector array. The experimental setup and the offline calibration are described in detail. Then, a thorough comparison between the data and Monte Carlo (MC) simulations is presented and a good agreement is obtained. With the even-odd method, the resolutions of the shower direction and core are measured. Finally, successful observations of the expected Moon's and Sun's shadows of cosmic rays (CRs) verify the measured angular resolution.

第 76 条，共 248 条

Calibration and Status of the 3-D Imaging Calorimeter of DAMPE for Cosmic Ray Physics on Orbit

Wu, LB (Wu, Libo); Wen, SC (Wen, Sicheng); Liu, CM (Liu, Chengming); Dai, HT (Dai, Haoting); Wei, YF (Wei, Yifeng); Zhang, ZY (Zhang, Zhiyong); Wang, XL (Wang, Xiaolian); Xu, ZZ (Xu, Zizong); Feng, CQ (Feng, Changqing); Liu, SB (Liu, Shubin); An, Q (An, Qi); Zhang, YL (Zhang, Yunlong); Huang, GS (Huang, Guangshun); Wang, YP (Wang, Yuanpeng); Yue, C (Yue, Chuan); Zang, JJ (Zang, Jingjing); Guo, JH (Guo, Jianhua); Wu, J (Wu, Jian); Chang, J (Chang, Jin)

IEEE TRANSACTIONS ON NUCLEAR SCIENCE

卷: 65 期: 8 页: 2007-2012

The Dark Matter Particle Explorer developed in China was designed to search for evidence of dark matter particles by observing primary cosmic rays and gamma rays in the energy range from 5 GeV to 10 TeV. Since its launch in December 2015, a large quantity of data has been recorded. With the data set acquired during more than a year of operation in space, a precise time-dependent calibration for the energy measured by the bismuth germanate oxide (BGO) electromagnetic calorimeter (ECAL) has been developed. In this paper, the instrumentation and development of the BGO ECAL are briefly described. The calibration on orbit, including that of the pedestal, attenuation length, minimum ionizing particle peak, and dynode ratio, is discussed, and additional details about the calibration methods and performance in space are presented.

第 77 条，共 248 条

Internal alignment and position resolution of the silicon tracker of DAMPE determined with orbit data

Tykhonov, A (Tykhonov, A.); Ambrosi, G (Ambrosi, G.); Asfandiyarov, R (Asfandiyarov, R.); Azzarello, P (Azzarello, P.); Bernardini, P (Bernardini, P.); Bertucci, B (Bertucci, B.); Bolognini, A (Bolognini, A.); Cadoux, F (Cadoux, F.); D'Amone, A (D'Amone, A.); De Benedittis, A (De Benedittis, A.); De Mitri, I (De Mitri, I.); Di Santo, M (Di Santo, M.); Dong, YF (Dong, Y. F.); Duranti, M (Duranti, M.); D'Urso, D (D'Urso, D.); Fan, RR (Fan, R. R.); Fusco, P (Fusco, P.); Gallo, V (Gallo, V.); Gao, M (Gao, M.); Gargano, F (Gargano, F.); Garrappa, S (Garrappa, S.); Gong, K (Gong, K.); Ionica, M (Ionica, M.); La Marra, D (La Marra, D.); Lei, SJ (Lei, S. J.); Li, X (Li, X.); Loparco, F (Loparco, F.); Marsella, G (Marsella, G.); Mazziotta, MN (Mazziotta, M. N.); Peng, WX (Peng, W. X.); Qiao, R (Qiao, R.); Salinas, MM (Salinas, M. M.); Surdo, A (Surdo, A.); Vagelli, V (Vagelli, V.); Vitillo, S (Vitillo, S.); Wang, HY (Wang, H. Y.); Wang, JZ (Wang, J. Z.); Wang, ZM (Wang, Z. M.); Wu, D (Wu, D.); Wu, X (Wu, X.); Zhang, F (Zhang, F.); Zhang, JY (Zhang, J. Y.); Zhao, H (Zhao, H.); Zimmer, S (Zimmer, S.)

NUCLEAR INSTRUMENTS & METHODS IN PHYSICS RESEARCH SECTION A-ACCELERATORS SPECTROMETERS DETECTORS AND ASSOCIATED EQUIPMENT

卷: 893 页: 43-56

The DArk Matter Particle Explorer (DAMPE) is a space-borne particle detector designed to probe electrons and gamma-rays in the few GeV to 10 TeV energy range, as well as cosmic-ray proton and nuclei components between 10 GeV and 100 TeV. The silicon-tungsten tracker-converter is a crucial component of DAMPE. It allows the direction of incoming photons converting into electron-positron pairs to be estimated, and the trajectory and charge (Z) of cosmic-ray particles to be identified. It consists of 768 silicon micro-strip sensors assembled in 6 double layers with a total active area of 6.6 m(2). Silicon planes are interleaved with three layers of tungsten plates, resulting in about one radiation length of material in the tracker. Internal alignment parameters of the tracker have been determined on orbit, with non-showering protons and helium nuclei. We describe the alignment procedure and present the position resolution and alignment stability measurements.

第 78 条，共 248 条

Validation of Gean4 physics models for nuclear beams in extended media

Chen, JL (Chen, Junliang); Yun, SJ (Yun, Sujun); Dong, TK (Dong, Tiekuang); Ren, ZZ (Ren, Zhongzhou); Zhang, XP (Zhang, Xiaoping)

NUCLEAR INSTRUMENTS & METHODS IN PHYSICS RESEARCH SECTION B-BEAM INTERACTIONS WITH MATERIALS AND ATOMS

卷: 434 页: 113-119

The physical and biological processes induced by energetic heavy ions in extended media are of great importance for human space exploration and ion therapy. In this paper we check the validity of some nucleus-nucleus inelastic collision models in Geant4 for the transportation of heavy nuclei in materials. The depth-dose distributions of(12)C and(56) Fe beams in extended media and the yields of secondary fragments have been simulated by G4WilsonAbrasion model, G4BinaryLightIon model and G4QMD model. Then the propagation of heavy nuclei through materials used in space industry and the angular distributions of secondary neutrons are also simulated for further validation of the models. By comparing the simulated results with experimental data, it is found that the G4QMD model gives the best results. The implication for estimating the radiation environment on Mars

caused by GCRs is also discussed.

第 79 条，共 248 条

Dark Energy Survey year 1 results: Cosmological constraints from galaxy clustering and weak lensing

Abbott, TMC (Abbott, T. M. C.); Abdalla, FB (Abdalla, F. B.); Alarcon, A (Alarcon, A.); Aleksic, J (Aleksic, J.); Allam, S (Allam, S.); Allen, S (Allen, S.); Amara, A (Amara, A.); Annis, J (Annis, J.); Asorey, J (Asorey, J.); Avila, S (Avila, S.); Bacon, D (Bacon, D.); Balbinot, E (Balbinot, E.); Banerji, M (Banerji, M.); Banik, N (Banik, N.); Barkhouse, W (Barkhouse, W.); Baumer, M (Baumer, M.); Baxter, E (Baxter, E.); Bechtol, K (Bechtol, K.); Becker, MR (Becker, M. R.); Benoit-Levy, A (Benoit-Levy, A.); Benson, BA (Benson, B. A.); Bernstein, GM (Bernstein, G. M.); Bertin, E (Bertin, E.); Blazek, J (Blazek, J.); Bridle, SL (Bridle, S. L.); Brooks, D (Brooks, D.); Brout, D (Brout, D.); Buckley-Geer, E (Buckley-Geer, E.); Burke, DL (Burke, D. L.); Busha, MT (Busha, M. T.); Campos, A (Campos, A.); Capozzi, D (Capozzi, D.); Rosell, AC (Rosell, A. Carnero); Kind, MC (Kind, M. Carrasco); Carretero, J (Carretero, J.); Castander, FJ (Castander, F. J.); Cawthon, R (Cawthon, R.); Chang, C (Chang, C.); Chen, N (Chen, N.); Childress, M (Childress, M.); Choi, A (Choi, A.); Conselice, C (Conselice, C.); Crittenden, R (Crittenden, R.); Crocce, M (Crocce, M.); Cunha, CE (Cunha, C. E.); D'Andrea, CB (D'Andrea, C. B.); da Costa, LN (da Costa, L. N.); Das, R (Das, R.); Davis, TM (Davis, T. M.); Davis, C (Davis, C.); De Vicente, J (De Vicente, J.); Depoy, DL (DePoy, D. L.); DeRose, J (DeRose, J.); Desai, S (Desai, S.); Diehl, HT (Diehl, H. T.); Dietrich, JP (Dietrich, J. P.); Dodelson, S (Dodelson, S.); Doel, P (Doel, P.); Drlica-Wagner, A (Drlica-Wagner, A.); Eifler, TF (Eifler, T. F.); Elliott, AE (Elliott, A. E.); Elsner, F (Elsner, F.); Elvin-Poole, J (Elvin-Poole, J.); Estrada, J (Estrada, J.); Evrard, AE (Evrard, A. E.); Fang, Y (Fang, Y.); Fernandez, E (Fernandez, E.); Ferte, A (Ferte, A.); Finley, DA (Finley, D. A.); Flaugher, B (Flaugher, B.); Fosalba, P (Fosalba, P.); Friedrich, O (Friedrich, O.); Frieman, J (Frieman, J.); Garcia-Bellido, J (Garcia-Bellido, J.); Garcia-Fernandez, M (Garcia-Fernandez, M.); Gatti, M (Gatti, M.); Gaztanaga, E (Gaztanaga, E.); Gerdes, DW (Gerdes, D. W.); Giannantonio, T (Giannantonio, T.); Gill, MSS (Gill, M. S. S.); Glazebrook, K (Glazebrook, K.); Goldstein, DA (Goldstein, D. A.); Gruen, D (Gruen, D.); Gruendl, RA (Gruendl, R. A.); Gschwend, J (Gschwend, J.); Gutierrez, G (Gutierrez, G.); Hamilton, S (Hamilton, S.); Hartley, WG (Hartley, W. G.); Hinton, SR (Hinton, S. R.); Honscheid, K (Honscheid, K.); Hoyle, B (Hoyle, B.); Huterer, D (Huterer, D.); Jain, B (Jain, B.); James, DJ (James, D. J.); Jarvis, M (Jarvis, M.); Jeltema, T (Jeltema, T.); Johnson, MD (Johnson, M. D.); Johnson, MWG (Johnson, M. W. G.); Kacprzak, T (Kacprzak, T.); Kent, S (Kent, S.); Kim, AG (Kim, A. G.); King, A (King, A.); Kirk, D (Kirk, D.); Kokron, N (Kokron, N.); Kovacs, A (Kovacs, A.); Krause, E (Krause, E.); Krawiec, C (Krawiec, C.); Kremin, A (Kremin, A.); Kuehn, K (Kuehn, K.); Kuhlmann, S (Kuhlmann, S.); Kuropatkin, N (Kuropatkin, N.); Lacasa, F (Lacasa, F.); Lahav, O (Lahav, O.); Li, TS (Li, T. S.); Liddle, AR (Liddle, A. R.); Lidman, C (Lidman, C.); Lima, M (Lima, M.); Lin, H (Lin, H.); MacCrann, N (MacCrann, N.); Maia, MAG (Maia, M. A. G.); Makler, M (Makler, M.); Manera, M (Manera, M.); March, M (March, M.); Marshall, JL (Marshall, J. L.); Martini, P (Martini, P.); McMahon, RG (McMahon, R. G.); Melchior, P (Melchior, P.); Menanteau, F (Menanteau, F.); Miquel, R (Miquel, R.); Miranda, V (Miranda, V.); Mudd, D (Mudd, D.); Muir, J (Muir, J.); Moller, A (Moller, A.); Neilsen, E (Neilsen, E.); Nichol, RC (Nichol, R. C.); Nord, B (Nord, B.); Nugent, P (Nugent, P.); Ogando, RLC (Ogando, R. L. C.); Palmese, A (Palmese, A.); Peacock, J (Peacock, J.); Peiris, HV (Peiris, H. V.); Peoples, J (Peoples, J.); Percival, WJ (Percival, W. J.); Petravick, D (Petravick, D.); Plazas, AA (Plazas, A. A.); Porredon, A (Porredon, A.); Prat, J (Prat, J.); Pujol, A (Pujol, A.); Rau, MM (Rau, M. M.); Refregier, A (Refregier, A.); Ricker, PM (Ricker, P. M.); Roe, N (Roe, N.); Rollins, RP (Rollins, R. P.); Romer, AK (Romer, A. K.); Roodman, A (Roodman, A.); Rosenfeld, R (Rosenfeld, R.); Ross, AJ (Ross, A. J.); Rozo, E (Rozo, E.); Rykoff, ES (Rykoff, E. S.); Sako, M (Sako, M.); Salvador, AI (Salvador, A. I.); Samuroff, S (Samuroff, S.); Sanchez, C (Sanchez, C.); Sanchez, E (Sanchez, E.); Santiago, B (Santiago, B.); Scarpine, V (Scarpine, V.); Schindler, R (Schindler, R.); Scolnic, D (Scolnic, D.); Secco, LF (Secco, L. F.); Serrano, S (Serrano, S.); Sevilla-Noarbe, I (Sevilla-Noarbe, I.); Sheldon, E (Sheldon, E.); Smith, RC (Smith, R. C.); Smith, M (Smith, M.); Smith, J (Smith, J.); Soares-Santos, M (Soares-Santos, M.); Sobreira, F (Sobreira, F.); Suchyta, E (Suchyta, E.); Tarle, G (Tarle, G.); Thomas, D (Thomas, D.); Troxel, MA (Troxel, M. A.); Tucker, DL (Tucker, D. L.); Tucker, BE (Tucker, B. E.); Uddin, SA (Uddin, S. A.); Varga, TN (Varga, T. N.); Vielzeuf, P (Vielzeuf, P.); Vikram, V (Vikram, V.); Vivas, AK (Vivas, A. K.); Walker, AR (Walker, A. R.); Wang, M (Wang, M.); Wechsler, RH (Wechsler, R. H.); Weller, J (Weller, J.); Wester, W (Wester, W.); Wolf, RC (Wolf, R. C.); Yanny, B (Yanny, B.); Yuan, F (Yuan, F.); Zenteno, A (Zenteno, A.); Zhang, B (Zhang, B.); Zhang, Y (Zhang, Y.); Zuntz, J (Zuntz, J.)

PHYSICAL REVIEW D

卷: 98 期: 4 文献号: 043526

We present cosmological results from a combined analysis of galaxy clustering and weak gravitational lensing, using 1321 deg(2) of griz imaging data from the first year of the Dark Energy Survey (DES Y1). We combine three two-point functions: (i) the cosmic shear correlation function of 26 million source galaxies in four redshift bins, (ii) the galaxy angular autocorrelation function of 650,000 luminous red galaxies in five redshift bins, and (iii) the galaxy-shear cross-correlation of luminous red galaxy positions and source galaxy shears. To demonstrate the robustness of these results, we use independent pairs of galaxy shape, photometric-redshift estimation and validation, and likelihood analysis pipelines. To prevent confirmation bias, the bulk of the analysis was carried out while "blind" to the true results; we describe an extensive suite of systematics checks performed and passed during this blinded phase. The data are modeled in flat Lambda CDM and wCDM cosmologies, marginalizing over 20 nuisance parameters, varying 6 (for Lambda CDM) or 7 (for wCDM) cosmological parameters including the neutrino mass density and including the 457 x 457 element analytic covariance matrix. We find consistent cosmological results from these three two-point functions and from their combination obtain S-8 equivalent to sigma(8) (Omega(m)/0.3)(0.5) = 0.773(-0.020)(+0.026) and Omega(m) = 0.267(-0.017)(+0.030) for Lambda CDM; for wCDM, we find S-8 = 0.782(-0.024)(+0.036) , Omega(m) = 0.284(-0.030)(+0.033), and w = -0.82(-0.20)(+0.21) at 68% C.L. The precision of these DES Y1 constraints rivals that from the Planck cosmic microwave background measurements, allowing a comparison of structure in the very early and late Universe on equal terms. Although the DES Y1 best-fit values for S-8 and Omega(m) are lower than the central values from Planck for both Lambda CDM and wCDM, the Bayes factor indicates that the DES Y1 and Planck data sets are consistent with each other in the context of Lambda CDM. Combining DES Y1 with Planck, baryonic acoustic oscillation measurements from SDSS, 6dF, and BOSS and type Ia supernovae from the Joint Lightcurve Analysis data set, we derive very tight constraints on cosmological parameters: S-8 = 0.802 +/- 0.012 and Omega(m) = 0.298 +/- 0.007 in Lambda CDM and w = -1.00(-0.04)(+0.05) in wCDM. Upcoming Dark Energy Survey analyses will provide more stringent tests of the Lambda CDM model and extensions such as a time-varying equation of state of dark energy or modified gravity.

第 80 条，共 248 条

Dark Energy Survey year 1 results: Galaxy clustering for combined probes

Elvin-Poole, J (Elvin-Poole, J.); Crocce, M (Crocce, M.); Ross, AJ (Ross, A. J.); Giannantonio, T (Giannantonio, T.); Rozo, E (Rozo, E.); Rykoff, ES (Rykoff, E. S.); Avila, S (Avila, S.); Banik, N (Banik, N.); Blazek, J (Blazek, J.); Bridle, SL (Bridle, S. L.); Cawthon, R (Cawthon, R.); Drlica-Wagner, A (Drlica-Wagner, A.); Friedrich, O (Friedrich, O.); Kokron, N (Kokron, N.); Krause, E (Krause, E.); MacCrann, N (MacCrann, N.); Prat, J (Prat, J.); Sanchez, C (Sanchez, C.); Secco, LF (Secco, L. F.); Sevilla-Noarbe, I (Sevilla-Noarbe, I.); Troxel, MA (Troxel, M. A.); Abbott, TMC (Abbott, T. M. C.); Abdalla, FB (Abdalla, F. B.); Allam, S (Allam, S.); Annis, J (Annis, J.); Asorey, J (Asorey, J.); Bechtol, K (Bechtol, K.); Becker, MR (Becker, M. R.); Benoit-Levy, A (Benoit-Levy, A.); Bernstein, GM (Bernstein, G. M.); Bertin, E (Bertin, E.); Brooks, D (Brooks, D.); Buckley-Geer, E (Buckley-Geer, E.); Burke, DL (Burke, D. L.); Rosell, A (Carnero Rosell, A.); Carollo, D (Carollo, D.); Kind, MC (Kind, M. Carrasco); Carretero, J (Carretero, J.); Castander, FJ (Castander, F. J.); Cunha, CE (Cunha, C. E.); D'Andrea, CB (D'Andrea, C. B.); Costa, LN (da Costa, L. N.); Davis, TM (Davis, T. M.); Davis, C (Davis, C.); Desai, S (Desai, S.); Diehl, HT (Diehl, H. T.); Dietrich, JP (Dietrich, J. P.); Dodelson, S (Dodelson, S.); Doel, P (Doel, P.); Eifler, TF (Eifler, T. F.); Evrard, AE (Evrard, A. E.); Fernandez, E (Fernandez, E.); Flaugher, B (Flaugher, B.); Fosalba, P (Fosalba, P.); Frieman, J (Frieman, J.); Garcia-Bellido, J (Garcia-Bellido, J.); Gaztanaga, E (Gaztanaga, E.); Gerdes, DW (Gerdes, D. W.); Glazebrook, K (Glazebrook, K.); Gruen, D (Gruen, D.); Gruendl, RA (Gruendl, R. A.); Gschwend, J (Gschwend, J.); Gutierrez, G (Gutierrez, G.); Hartley, WG (Hartley, W. G.); Hinton, SR (Hinton, S. R.); Honscheid, K (Honscheid, K.); Hoormann, JK (Hoormann, J. K.); Jain, B (Jain, B.); James, DJ (James, D. J.); Jarvis, M (Jarvis, M.); Jeltema, T (Jeltema, T.); Johnson, MWG (Johnson, M. W. G.); Johnson, MD (Johnson, M. D.); King, A (King, A.); Kuehn, K (Kuehn, K.); Kuhlmann, S (Kuhlmann, S.); Kuropatkin, N (Kuropatkin, N.); Lahav, O (Lahav, O.); Lewis, G (Lewis, G.); Li, TS (Li, T. S.); Lidman, C (Lidman, C.); Lima, M (Lima, M.); Lin, H (Lin, H.); Macaulay, E (Macaulay, E.); March, M (March, M.); Marshall, JL (Marshall, J. L.); Martini, P (Martini, P.); Melchior, P (Melchior, P.); Menanteau, F (Menanteau, F.); Miquel, R (Miquel, R.); Mohr, JJ (Mohr, J. J.); Moller, A (Moller, A.); Nichol, RC (Nichol, R. C.); Nord, B (Nord, B.); O'Neill, CR (O'Neill, C. R.); Percival, WJ (Percival, W. J.); Petravick, D (Petravick, D.); Plazas, AA (Plazas, A. A.); Romer, AK (Romer, A. K.); Sako, M (Sako, M.); Sanchez, E (Sanchez, E.); Scarpine, V (Scarpine, V.); Schindler, R (Schindler, R.); Schubnell, M (Schubnell, M.); Sheldon, E (Sheldon, E.); Smith, M (Smith, M.); Smith, RC (Smith, R. C.); Soares-Santos, M (Soares-Santos, M.); Sobreira, F (Sobreira, F.); Sommer, NE (Sommer, N. E.); Suchyta, E (Suchyta, E.); Swanson, MEC (Swanson, M. E. C.); Tarle, G (Tarle, G.); Thomas, D (Thomas, D.); Tucker, BE (Tucker, B. E.); Tucker, DL (Tucker, D. L.); Uddin, SA (Uddin, S. A.); Vikram, V (Vikram, V.); Walker, AR (Walker, A. R.); Wechsler, RH (Wechsler, R. H.); Weller, J (Weller, J.); Wester, W (Wester, W.); Wolf, RC (Wolf, R. C.); Yuan, F (Yuan, F.); Zhang, B (Zhang, B.); Zuntz, J (Zuntz, J.)
PHYSICAL REVIEW D
卷: 98 期: 4 文献号: 042006
We measure the clustering of DES year 1 galaxies that are intended to be combined with weak lensing samples in order to produce precise cosmological constraints from the joint analysis of large-scale structure and lensing correlations. Two-point correlation functions are measured for a sample of 6.6 x 10(5) luminous red galaxies selected using the REDMAGIC algorithm over an area of 1321 square degrees, in the redshift range 0.15 < z < 0.9, split into five tomographic redshift bins. The sample has a mean redshift uncertainty of sigma(z)/(1 + z) = 0.017. We quantify and correct spurious correlations induced by spatially variable survey properties, testing their impact on the clustering measurements and covariance. We demonstrate the sample's robustness by testing for stellar contamination, for potential biases that could arise from the systematic correction, and for the consistency between the two-point auto-and cross-correlation functions. We show that the corrections we apply have a significant impact on the resultant measurement of cosmological parameters, but that the results are robust against arbitrary choices in the correction method. We find the linear galaxy bias in each redshift bin in a fiducial cosmology to be b(sigma(8)/0.81) vertical bar(z=0.24) =1.40 +/- 0.07, b(sigma(8)/0.81) vertical bar(z=0.38) = 1.60 +/- 0.05, (sigma(8)/0.81) vertical bar(z=0.53) = 1.60 +/- 0.04 for galaxies with luminosities L/L-* > 0.5, b(sigma(8)/0.8) vertical bar(z=0.68) = 1.93 +/- 0.04 for L/L-* > 1 and b(sigma(8)/0.81) vertical bar(z=0.83) = 1.98 +/- 0.07 for L/L-* > 1.5, broadly consistent with expectations for the redshift and luminosity dependence of the bias of red galaxies. We show these measurements to be consistent with the linear bias obtained from tangential shear measurements.

第 81 条，共 248 条

New bounds on axionlike particles from the Fermi Large Area Telescope observation of PKS 2155-304

Zhang, C (Zhang, Cun); Liang, YF (Liang, Yun-Feng); Li, S (Li, Shang); Liao, NH (Liao, Neng-Hui); Feng, L (Feng, Lei); Yuan, Q (Yuan, Qiang); Fan, YZ (Fan, Yi-Zhong); Ren, ZZ (Ren, Zhong-Zhou)
PHYSICAL REVIEW D
卷: 97 期: 6 文献号: 063009
The axionlike particle (ALP)-photon mixing in the magnetic field around gamma-ray sources or along the line of sight could induce oscillation between photons and ALPs, which then causes irregularities in the gamma-ray spectra. In this work we search for such spectral irregularities in the spectrum of PKS 2155 - 304 using 8.6 years of data from the Fermi Large Area Telescope (Fermi-LAT). No significant evidence for the presence of ALP-photon oscillation is obtained, and the parameter space of ALPs is constrained. The exclusion region sensitively depends on the poorly known magnetic field of the host galaxy cluster of PKS 2155 - 304. If the magnetic field is as high as similar to 10 mu G, the "holelike" parameter region allowed in Ref. [1] can be ruled out.

第 82 条，共 248 条

Operation of the astronomical monitoring stations at Mt. Wumingshan

Liu, Y (Liu, Yu); Li, XB (Li, Xiaobo); Zhang, XF (Zhang, Xuefei); Song, TF (Song, Tengfei); Wang, JX (Wang, Jingxing); Zhao, MY (Zhao, Mingyu); Xia, LD (Xia, Lidong); Song, QW (Song, Qiwu)
OBSERVATORY OPERATIONS: STRATEGIES, PROCESSES, AND SYSTEMS VII
卷: 10704 文献号: UNSP 1070422
The Wumingshan mountain (Mt. WMS), located in the Grand Shangri-La area of south-west China, has been selected as one of the most potential regions for hosting China's next-generation ground-based large telescopes. Firstly, Mt. WMS has ideal astronomical conditions for both day-time and night-time observations. Comprehensive analysis of remote and on-site long-term meteorological, geological and geographic data suggests that WMS satisfies the strict requirements for an excellent candidate site, through a series of key parameters including average seeing factor ro, sky brightness, clear-sky days, precipitable water vapor content (PWVC), refractive index structure constant, atmospheric coherence time, isoplanatic angle and meteorological information etc. Averagely, its daily seeing factor is over 10 cm and its night seeing factor is 0.9 arcsec on ground. The average

wind speed is less than 5 m/s. The average normalized PWVC at unit air mass is about 2.5 mm. The average yearly sunshine duration is generally more than 2500 hours. The amount of yearly clear sky days and nights are respectively 250 d and 270 d. The median night sky brightness level is 21.8 mag arcsec-2. The atmosphere cleanliness is also excellent. Secondly, Mt. WMS possesses the necessary conditions for the establishment of high altitude observatories. Its ridge is flat and spreads over 2 km2. The large relative elevation difference in the local terrain, plus the existence of population settlements at low altitude (2800 m) in the vicinity, substantially reduces the future cost for construction, settlement, and logistics. Its geological structure is stable, and there is virtually no record of geological disaster or inclement weather. The nearby counties have low population density (-5 km-2) and there have been extensive transportation networks. In October 2014, we initiated a long-term monitoring project in Mt. WMS. We have been collecting data from two monitoring sites for more than three years. Both sites are located about 47004800 m above the sea level. Our instruments mainly include the solar and stellar Differential Image Motion Monitors, the Sky Brightness Monitors, the PWVC monitors, the Atmospheric Temperature Fluctuation Monitors, the Multi-wavelength Solar Photometers and robot meterological stations, and so on. There have been a lot of activities within the ASO-G (i.e., CGST and large coronagraph) sites' study since our last reports. In this paper, we introduce the daily observation, transmission, storage and analysis of the harvested data, and the overall operation, management and technical support of the monitoring platforms.

会议名称: Conference on Observatory Operations - Strategies, Processes, and Systems VII
会议日期: JUN 11-15, 2018
会议地点: Austin, TX

第 83 条，共 248 条

An algorithm to resolve gamma-rays from charged cosmic rays with DAMPE

Xu, ZL (Xu, Zun-Lei); Duan, KK (Duan, Kai-Kai); Shen, ZQ (Shen, Zhao-Qiang); Lei, SJ (Lei, Shi-Jun); Dong, TK (Dong, Tie-Kuang); Gargano, F (Gargano, Fabio); Garrappa, S (Garrappa, Simone); Guo, DY (Guo, Dong-Ya); Jiang, W (Jiang, Wei); Li, X (Li, Xiang); Liang, YF (Liang, Yun-Feng); Mazziotta, MN (Mazziotta, Mario Nicola); Salinas, MFM (Salinas, Maria Fernanda Munoz); Su, M (Su, Meng); Vagelli, V (Vagelli, Valerio); Yuan, Q (Yuan, Qiang); Yue, C (Yue, Chuan); Zang, JJ (Zang, Jing-Jing); Zhang, YP (Zhang, Ya-Peng); Zhang, YL (Zhang, Yun-Long); Zimmer, S (Zimmer, Stephan)

RESEARCH IN ASTRONOMY AND ASTROPHYSICS
卷: 18 期: 3 文献号: 27

The DArk Matter Particle Explorer (DAMPE), also known as Wukong in China, which was launched on 2015 December 17, is a new high energy cosmic ray and gamma-ray satellite-borne observatory. One of the main scientific goals of DAMPE is to observe GeV-TeV high energy gamma-ray with accurate energy, angular and time resolution, to indirectly search for dark matter particles and for the study of high energy astrophysics. Due to the comparatively higher fluxes of charged cosmic rays with respect to gamma-ray, it is challenging to identify gamma-ray with sufficiently high efficiency, minimizing the amount of charged cosmic ray contamination. In this work we present a method to identify gamma-ray in DAMPE data based on Monte Carlo simulations, using the powerful electromagnetic/hadronic shower discrimination provided by the calorimeter and the veto detection of charged particles provided by the plastic scintillation detector. Monte Carlo simulations show that after this selection the number of electrons and protons that contaminate the selected gamma-ray events at similar to 10GeV amounts to less than 1% of the selected sample. Finally, we use flight data to verify the effectiveness of the method by highlighting known gamma-ray sources in the sky and by reconstructing preliminary light curves of the Geminga pulsar.

第 84 条，共 248 条

用于空间天文的硅微条探测器原型样机研制

韦家驹

DOI：10.11889/j.0253-3219.2018.hjs.41.120402

γ射线的天文观测是目前天文观测的前沿课题,通过观测高能γ射线的能谱和空间分布,可以研究宇宙中暗物质的分布及其物理特性。在众多γ射线探测器中,硅微条探测器具有很高的位置分辨率和能量分辨率,并且可以拼接组成大探测面,非常适合探测粒子的径迹和能量。为了解决硅微条探测器的关键技术,包括探测器微组装、前端读出电子学、数据采集电路,实验室自主研制了探测器样机并进行一系列测试。该样机的 384 个通道在 0～180f C 的输入动态范围内具有很好的线性(积分非线性小于 5%),同时具有很低的噪声(等效输入噪声电荷小于 0.16 fC)。样机的宇宙线能谱曲线可以清晰分辨出最小电离粒子的峰位约 2.8 fC,并且可以用朗道卷积高斯函数精确拟合。

第 85 条，共 248 条

Statistical Analysis on XMM-Newton X-Ray Flares of Mrk 421: Distributions of Peak Flux and Flaring Time Duration

Yan, DH (Yan, Dahai); Yang, SB (Yang, Shenbang); Zhang, PF (Zhang, Pengfei); Dai, BZ (Dai, Benzhong); Wang, JC (Wang, Jiancheng); Zhang, L (Zhang, Li)

ASTROPHYSICAL JOURNAL
卷: 864 期: 2 文献号: 164

The energy dissipation mechanism in blazar jet is unknown. Blazar flares could provide insights into this problem. Here we report statistical results of XMM-Newton observations of X-ray flares in Mrk 421. We analyze all public XMM-Newton X-ray observations for Mrk 421, and construct the light curves. Through fitting the light curves, we obtain the flare-profile parameters, such as peak flux (F-p) and flaring time duration (T-fl). It is found that the distributions of F-p and T-fl both obey a power-law form, with the same index of alpha(F) = alpha(T) approximate to 1. The statistical properties are consistent with the predictions for a self-organized criticality system with energy dissipation in one-dimensional space. This is similar to a solar flare, but with different space dimensions of the energy dissipation domain. This suggests that the X-ray flaers of Mrk 421 might be driven by a magnetic reconnection mechanism. Moreover, in the analysis, we find that variability on a timescale of similar to 1000 s appears frequently. This rapid variability indicates a magnetic field of >= 2.1 delta(-1/3)(D) G (delta(D) is the Doppler factor) in the emission region.

第 86 条，共 248 条

Testing Relativistic Boost as the Cause of Gamma-Ray Quasi-periodic Oscillation in a Blazar

Yan, DH (Yan, Dahai); Zhou, JN (Zhou, Jianeng); Zhang, PF (Zhang, Pengfei); Zhu, QQ (Zhu, Qianqian); Wang, JC (Wang, Jiancheng)

ASTROPHYSICAL JOURNAL
卷: 867 期: 1 文献号: 53
The mechanism for producing gamma-ray quasi-periodic oscillation (QPO) in blazars is unknown. One possibility is the geometric model, in which without the need for intrinsic quasi-periodic variation, the relativistic Doppler factor changes periodically, resulting in observed gamma-ray QPO. We propose a method to test this geometric model. We analyze the Fermi-LAT data of PG 1553+113 spanning from 2008 August until 2018 February. According to 29 four-month average spectral energy distributions in the energy range of 0.1-300 GeV, we split the Fermi-LAT energy range into three bands: 0.1-1 GeV, 1-10 GeV, and 10-300 GeV. The spectrum in each energy range can be successfully fitted by a power law. The light curves and photon indices in the three energy ranges are obtained. Then, light curves in three narrow energy ranges, i.e., 0.2-0.5 GeV, 2-5 GeV, and 20-40 GeV, are constructed, and the relative variability amplitudes in the three narrow energy ranges are calculated. A discrete-correlation analysis is performed for the light curves. Our results indicate that (i) the light curves in the different energy ranges follow the same pattern showed in the light curve above 0.1 GeV; (ii) the three groups of photon indices in the energy ranges of 0.1-1 GeV, 1-10 GeV, and 10-300 GeV keep nearly constant; and (iii) the ratio between relative variability amplitudes in different narrow energy ranges are equal (within their errors) to the prediction by the Doppler effect. Our results support the scenario of the relativistic boost producing the gamma-ray QPO for PG 1553+113.

第 87 条，共 248 条

A 34.5 day quasi-periodic oscillation in gamma-ray emission from the blazar PKS 2247-131

Zhou, JN (Zhou, Jianeng); Wang, ZX (Wang, Zhongxiang); Chen, L (Chen, Liang); Wiita, PJ (Wiita, Paul J.); Vadakkumthani, J (Vadakkumthani, Jithesh); Morrell, N (Morrell, Nidia); Zhang, PF (Zhang, Pengfei); Zhang, JJ (Zhang, Jujia)
NATURE COMMUNICATIONS
卷: 9 文献号: 4599
Since 2016 October, the active galaxy PKS 2247-131 has undergone a gamma-ray outburst, which we studied using data obtained with the Fermi Gamma-ray Space Telescope. The emission arises from a relativistic jet in PKS 2247-131, as an optical spectrum only shows a few weak absorption lines, typical of the BL Lacertae sub-class of the blazar class of active galactic nuclei. Here we report a similar or equal to 34.5 day quasi-periodic oscillation (QPO) in the emission after the initial flux peak of the outburst. Compared to one-year time-scale QPOs, previously identified in blazars in Fermi energies, PKS 2247-131 exhibits the first clear case of a relatively short, month-like oscillation. We show that this QPO can be explained in terms of a helical structure in the jet, where the viewing angle to the dominant emission region in the jet undergoes periodic changes. The time scale of the QPO suggests the presence of binary supermassive black holes in PKS 2247-131.

第 88 条，共 248 条

Detection of gamma-ray emission from the Coma cluster with Fermi Large Area Telescope and tentative evidence for an extended spatial structure

Xi, SQ (Xi, Shao-Qiang); Wang, XY (Wang, Xiang-Yu); Liang, YF (Liang, Yun-Feng); Peng, FK (Peng, Fang-Kun); Yang, RZ (Yang, Rui-Zi); Liu, RY (Liu, Ruo-Yu)
PHYSICAL REVIEW D
卷: 98 期: 6 文献号: 063006
Many galaxy clusters have giant halos of nonthermal radio emission, indicating the presence of relativistic electrons in the clusters. Relativistic protons may also be accelerated by merger and/or accretion shocks in galaxy clusters. These cosmic-ray (CR) electrons and/or protons are expected to produce gamma rays through inverse-Compton scatterings or inelastic pp collisions respectively. Despite of intense efforts in searching for high-energy gamma-ray emission from galaxy clusters, conclusive evidence is still missing so far. Here we report the discovery of >= 200 MeV gamma-ray emission from the Coma cluster direction with an unbinned likelihood analysis of the 9 years of Fermi-LAT Pass 8 data. The gamma-ray emission shows a spatial morphology roughly coincident with the giant radio halo, with an apparent excess at the southwest of the cluster. Using the test statistic analysis, we further find tentative evidence that the gammaray emission at the Coma center is spatially extended. The extended component has an integral energy flux of similar to 2 x 10(-12) erg cm(-2) S-1 in the energy range of 0.2-300 GeV and the spectrum is soft with a photon index of similar or equal to -2.7. Interpreting the gamma-ray emission as arising from CR proton interaction, we find that the volume-averaged value of the CR to thermal pressure ratio in the Coma cluster is about similar to 2%. Our results show that galaxy clusters are likely a new type of GeV gamma-ray sources, and they are probably also giant reservoirs of CR protons.

UV/X-ray Astronomy Research Group

第 89 条，共 248 条

Resonant Scattering Effect on the Soft X-Ray Line Emission from the Hot Interstellar Medium. I. Galactic Bulges

Chen, Y (Chen, Yang); Wang, QD (Wang, Q. Daniel); Zhang, GY (Zhang, Gao-Yuan); Zhang, SN (Zhang, Shuinai); Ji, L (Ji, Li)
ASTROPHYSICAL JOURNAL
卷: 861 期: 2 文献号: 138
Diffuse soft X-ray line emission is commonly used to trace the thermal and chemical properties of the hot interstellar medium, as well as its content, in nearby galaxies. Although resonant-line scattering complicates the interpretation of the emission, it also offers an opportunity to measure the kinematics of the medium. We have implemented a direct Monte Carlo simulation scheme that enables us to account for the resonant scattering (RS) effect in the medium, in principle, with arbitrary spatial, thermal, chemical, and kinematic distributions. Here we apply this scheme via dimensionless calculation to an isothermal, chemically uniform, and spherically symmetric medium with a radial density distribution characterized by a / beta-model. This application simultaneously accounts for both optical depth-dependent spatial distortion and intensity change of the resonant-line emission due to the scattering, consistent with previous calculations. We further apply the modeling scheme to the 0 VII and 0 VIII emission line complex observed in the XMM-Newton RGS spectrum of the M31 bulge. This modeling, although with various limitations due to its simplicity, shows that the RS could indeed account for much of the spatial distortion of the emission, as well as the relative intensities of the lines, especially the large forbidden-to-resonant-line ratio of the 0 VII Heck triplet. We estimate the isotropic turbulence Mach number of the medium in M31 as similar to 0.17 for the

first time and the line-emitting gas temperature as similar to 2.3 x 10(6)K. We conclude that the RS may in general play an important role in shaping the soft X-ray spectra of diffuse hot gas in normal galaxies.

第 90 条，共 248 条

Probing the dynamical state, baryon content, and multiphase nature of galaxy clusters with bright background QSOs

Ge, C (Ge, Chong); Wang, QD (Wang, Q. Daniel); Burchett, JN (Burchett, Joseph N.); Tripp, TM (Tripp, Todd M.); Sun, M (Sun, Ming); Li, ZY (Li, Zhiyuan); Gu, QS (Gu, Qiusheng); Ji, L (Ji, Li)
MONTHLY NOTICES OF THE ROYAL ASTRONOMICAL SOCIETY
卷: 481 期: 3 页: 4111-4122
We have initiated a programme to study the physical/dynamical state of gas in galaxy clusters and the impact of the cluster environment on gaseous haloes of individual galaxies using X-ray imaging and UV absorption line spectroscopy of background QSOs. Here, we report results from the analysis Chandra and XMM-Newton archival data of five galaxy clusters with such QSOs, one of which has an archival UV spectrum. We characterize the gravitational masses and dynamical states, as well as the hot intracluster medium (ICM) properties of these clusters. Most clusters are dynamically disturbed clusters based on the X-ray morphology parameters, the X-ray temperature profiles, the large offset between X-ray peak, and brightest cluster galaxy (BCG). The baryon contents in the hot ICM and stars of these clusters within r(500) are lower than the values expected from the gravitational masses, according to the standard cosmology. We also estimate column densities of the hot ICM along the sightlines towards the background QSOs as well as place upper limits on the warm-hot phase for the one sightline with existing UV observations. These column densities, compared with those of the warm and warm-hot ICM to be measured with UV absorption line spectroscopy, will enable us to probe the relationship among various gaseous phases and their connection to the heating/cooling and dynamical processes of the clusters. Furthermore, our analysis of the archival QSO spectrum probing one cluster underscores the need for high-quality, targeted UV observations to robustly constrain the 10(5-6) K gas phase.

第 91 条，共 248 条

Disc-corona interaction in the heartbeat state of GRS 1915+105

Yan, SP (Yan, Shu-Ping); Ji, L (Ji, Li); Liu, SM (Liu, Si-Ming); Mendez, M (Mendez, Mariano); Wang, N (Wang, Na); Li, XD (Li, Xiang-Dong); Qu, JL (Qu, Jin-Lu); Sun, W (Sun, Wei); Ge, MY (Ge, Ming-Yu); Liao, JY (Liao, Jin-Yuan); Niu, S (Niu, Shu); Ding, GQ (Ding, Guo-Qiang); Liu, QZ (Liu, Qing-Zhong)
MONTHLY NOTICES OF THE ROYAL ASTRONOMICAL SOCIETY
卷: 474 期: 1 页: 1214-1224
Timing analysis provides information about the dynamics of matter accreting on to neutron stars and black holes, and hence is crucial for studying the physics of the accretion flow around these objects. It is difficult, however, to associate the different variability components with each of the spectral components of the accretion flow. We apply several new methods to two Rossi X-ray Timing Explorer observations of the black hole binary GRS 1915+105 during its heartbeat state to explore the origin of the X-ray variability and the interactions of the accretion-flow components. We offer a promising window into the disc-corona interaction through analysing the formation regions of the disc aperiodic variabilities with different time-scales via comparing the corresponding transition energies of the amplitude-ratio spectra. In a previous paper, we analysed the Fourier power density as a function of energy and frequency to study the origin of the aperiodic variability, and combined that analysis with the phase lag as a function of frequency to derive a picture of the disc-corona interaction in this source. We here, for the first time, investigate the phase-lag as a function of energy and frequency, and display some interesting details of the disc-corona interaction. Besides, the results from the shape of amplitude-ratio spectrum and from several other aspects suggest that the quasi-periodic oscillation originates from the corona.

II. Antarctic Astronomy Radio Astronomy

Stellar Structure, Evolution and Pulsation

第 92 条，共 248 条

Turbulent convection and pulsation stability of stars - III. Non-adiabatic oscillations of red giants

D. R. Xiong, L. Deng, C. Zhang
MNRAS, 480, 2698-2703
We have computed linear non-adiabatic oscillations of luminous red giants using a non-local and anisotropic time-dependent theory of convection. The results show that low-order radial modes can be self-excited. Their excitation is the result of radiation and the coupling between convection and oscillations. Turbulent pressure has important effects on the excitation of oscillations in red variables.

Center for Antarctic Astronomy

第 93 条，共 248 条

Late-time Flattening of Type Ia Supernova Light Curves: Constraints from SN 2014J in M82

Yang, Y (Yang, Yi); Wang, LF (Wang, Lifan); Baade, D (Baade, Dietrich); Brown, PJ (Brown, Peter. J.); Cikota, A (Cikota, Aleksandar); Cracraft, M (Cracraft, Misty); Hoflich, PA (Hoflich, Peter A.); Maund, JR (Maund, Justyn R.); Patat, F (Patat, Ferdinando); Sparks, WB (Sparks, William B.); Spyromilio, J (Spyromilio, Jason); Stevance, HF (Stevance, Heloise F.); Wang, XF (Wang, Xiaofeng); Wheeler, JC (Wheeler, J. Craig)

ASTROPHYSICAL JOURNAL

卷: 852 期: 2 文献号: 89

The very nearby Type Ia supernova 2014J in M82 offers a rare opportunity to study the physics of thermonuclear supernovae at extremely late phases (greater than or similar to 800 days). Using the Hubble Space Telescope, we obtained 6 epochs of high-precision photometry for SN 2014J from 277 days to 1181 days past the B-band maximum light. The reprocessing of electrons and X-rays emitted by the radioactive decay chain Co-57 -> Fe-57 is needed to explain the significant flattening of both the F606W-band and the pseudo-bolometric light curves. The flattening confirms previous predictions that the late-time evolution of type Ia supernova luminosities requires additional energy input from the decay of Co-57. By assuming the F606W-band luminosity scales with the bolometric luminosity at similar to 500 days after the B-band maximum light, a mass ratio Ni-57/Ni-56 similar to 0.065(-0.005)(+0.004) is required. This mass ratio is roughly similar to 3 times the solar ratio and favors a progenitor white dwarf with a mass near the Chandrasekhar limit. A similar fit using the constructed pseudo-bolometric luminosity gives a mass ratio Ni-57/Ni-56 similar to 0.066(-0.009)(+0.008) . Astrometric tests based on the multi-epoch HST ACS/WFC images reveal no significant circumstellar light echoes in between 0.3 and 100 pc from the supernova.

第 94 条，共 248 条

Observations of Turbulent Magnetic Reconnection within a Solar Current Sheet

Cheng, X (Cheng, X.); Li, Y (Li, Y.); Wan, LF (Wan, L. F.); Ding, MD (Ding, M. D.); Chen, PF (Chen, P. F.); Zhang, J (Zhang, J.); Liu, JJ (Liu, J. J.)

ASTROPHYSICAL JOURNAL

卷: 866 期: 1 文献号: 64

Magnetic reconnection is a fundamental physical process in various astrophysical, space, and laboratory environments. Many pieces of evidence for magnetic reconnection have been uncovered. However, its specific processes that could be fragmented and turbulent have been short of direct observational evidence. Here, we present observations of a super-hot current sheet during the SOL2017-09-10T X8.2-class solar flare that display the fragmented and turbulent nature of magnetic reconnection. As bilateral plasmas converge toward the current sheet, significant plasma heating and nonthermal motions are detected therein. Two oppositely directed outflow jets are intermittently expelled out of the fragmenting current sheet, whose intensity shows a power-law distribution in the spatial frequency domain. The intensity and velocity of the sunward outflow jets also display a power-law distribution in the temporal frequency domain. The length-to-width ratio of current sheet is estimated to be larger than the theoretical threshold and thus ensures its occurrence. The observations therefore suggest that fragmented and turbulent magnetic reconnection occurs in the long stretching current sheet.

第 95 条，共 248 条

Optical Observations of the Young Type Ic Supernova SN 2014L in M99

Zhang, Jujia，Wang, Xiaofeng，Vinkó, József.

The Astrophysical Journal 863(1):109 •

We present optical spectroscopic and photometric observations of the nearby type Ic supernova (SN Ic) SN 2014L. This SN was discovered by the Tsinghua-NAOC Transient Survey (TNTS) in the nearby type-Sc spiral galaxy M99 (NGC 4254). Fitting to the early-time light curve indicates that SN 2014L was detected at only a few hours after the shock breakout, and it reached a peak brightness of

$M_{\rm V} = -17.73 \pm 0.28$ mag ($L= [2.06\pm 0.50] \times 10^{42}$ erg s^{-1}) approximately 13 days later. SN 2014L shows a close resemblance to SN 2007gr in the photometric evolution, while it shows stronger absorption features of intermediate-mass elements (especially \CaII) in the early-time spectra. Based on simple modeling of the observed light curves, we derived the mass of synthesized ^{56}Ni as $M_{\rm Ni} = 0.075 \pm 0.025 M_{\odot}$, and the mass and total energy of the ejecta as $M_{\rm ej} = 1.00 \pm 0.20 M_\odot$ and $E_{\rm ej}=1.45\pm0.25$ foe, respectively. Given these typical explosion parameters, the early detection, and the extensive observations, we suggest that SN 2014L could be a template sample for the investigation of SNe Ic.

DOI： 10.3847/1538-4357/aaceaf

第 96 条，共 248 条

Characterization of Type Ia Supernova Light Curves Using Principal Component Analysis of Sparse Functional Data

He, SY (He, Shiyuan); Wang, LF (Wang, Lifan); Huang, JHZ (Huang, Jianhua Z.)

ASTROPHYSICAL JOURNAL

卷: 857 期: 2 文献号: 110

With growing data from ongoing and future supernova surveys, it is possible to empirically quantify the shapes of SNIa light curves in more detail, and to quantitatively relate the shape parameters with the intrinsic properties of SNIa. Building such relationships is critical in controlling systematic errors associated with supernova cosmology. Based on a collection of well-observed SNIa samples accumulated in the past years, we construct an empirical SNIa light curve model using a statistical method called the functional principal component analysis (FPCA) for sparse and irregularly sampled functional data. Using this method, the entire light curve of an SNIa is represented by a linear combination of principal component functions, and the SNIa is represented by a few numbers called "principal component scores." These scores are used to establish relations between light curve shapes and physical quantities such as intrinsic color, interstellar dust reddening, spectral line strength, and spectral classes. These relations allow for descriptions of some critical physical quantities based purely on light curve shape parameters. Our study shows that some important spectral feature information is being encoded in the broad band light curves; for instance, we find that the light curve shapes are correlated with the velocity and velocity gradient of the Si II.6355 line. This is important for supernova surveys (e.g., LSST and WFIRST). Moreover, the FPCA light curve model is used to construct the entire light curve shape, which in turn is used in a functional linear form to adjust intrinsic luminosity when fitting distance models.

第 97 条，共 248 条

Mapping Circumstellar Matter with Polarized Light: The Case of Supernova 2014J in M82

Yang, Y (Yang, Yi); Wang, LF (Wang, Lifan); Baade, D (Baade, Dietrich); Brown, PJ (Brown, Peter. J.); Cikota, A (Cikota, Aleksandar); Cracraft, M (Cracraft, Misty); Hoflich, PA (Hoflich, Peter A.); Maund, JR (Maund, Justyn R.); Patat, F (Patat, Ferdinando); Sparks, WB (Sparks, William B.); Spyromilio, J (Spyromilio, Jason); Stevance, HF (Stevance, Heloise F.); Wang, XF (Wang, Xiaofeng); Wheeler, JC (Wheeler, J. Craig)

ASTROPHYSICAL JOURNAL

卷: 854 期: 1 文献号: 55

Optical polarimetry is an effective way of probing the environment of a supernova for dust. We acquired linear HST ACS/WFC polarimetry in bandsF475W, F606W, and F775W of the supernova (SN) 2014J in M82 at six epochs from similar to 277 days to similar to 1181 days after the B-band maximum. The polarization measured at day 277 shows conspicuous deviations from other epochs. These differences can be attributed to at least similar to 10(-6) M-circle dot of circumstellar dust located at a distance of similar to 5 x 10(17) cm from the SN. The scattering dust grains revealed by these observations seem to be aligned with the dust in the interstellar medium that is responsible for the large reddening toward the supernova. The presence of this circumstellar dust sets strong constraints on the progenitor system that led to the explosion of SN 2014J; however, it cannot discriminate between single-and double-degenerate models.

第 98 条，共 248 条

The Scattering of FRBs by the Intergalactic Medium: Variations, Strength, and Dependence on Dispersion Measures

Zhu, WS (Zhu, Weishan); Feng, LL (Feng, Long-Long); Zhang, FP (Zhang, Fupeng)

ASTROPHYSICAL JOURNAL

卷: 865 期: 2 文献号: 147

The scattering of fast radio bursts (FRBs) by the intergalactic medium (IGM) is explored using cosmological hydrodynamical simulations. We confirm that the scattering by the clumpy IGM has significant line-of-sight variations. We demonstrate that the scattering by the IGM in the voids and walls of the cosmic web is weak, but it can be significantly enhanced by the gas in clusters and filaments. The observed nonmonotonic dependence of the FRB widths on the dispersion measures (DM) cannot determine whether the IGM is an important scattering matter or not. The IGM may dominate the scattering of some FRBs, and the host galaxy dominates others. For the former case, the scattering should be primarily caused by the medium in clusters. A mock sample of 500 sources shows that tau(IGM) alpha DMIGM (1.6-2.1) at z < 1.5. Assuming that the turbulence follows Kolmogorov scaling, we find that an outer scale of L0 similar to 5 pc is required to make tau(IGM) 1-10 ms at nu = 1 GHz. The required L-0 similar to 5 pc can alleviate the tension in the timescales of turbulent heating and cooling but is still similar to 4 orders of magnitude lower than the presumed injection scale of turbulence in the IGM. The gap is expected to be effectively shortened if the simulation resolution is further increased. The mechanisms that may further reduce the gap are shortly discussed. If future observations can justify the role of the IGM in the broadening of FRBs, it can help to probe the gas in clusters and filaments.

第 99 条，共 248 条

A Large-scale Survey of CO and Its Isotopologues toward the Rosette Molecular Cloud

Li, C (Li, Chong); Wang, HC (Wang, Hongchi); Zhang, MM (Zhang, Miaomiao); Ma, YH (Ma, Yuehui); Fang, M (Fang, Min); Yang, J (Yang, Ji)

ASTROPHYSICAL JOURNAL SUPPLEMENT SERIES

卷: 238 期: 1 文献号: 10

Using the PMO-13.7 m millimeter telescope at Delingha in China, we have conducted a large-scale simultaneous survey of (CO)-C-12, (CO)-C-13, and (CO)-O-18 J = 1 - 0 emission toward the Rosette molecular cloud (RMC) region with a sky coverage of 3 degrees.5 x 2 degrees.5. The majority of the emission in the region comes from the RMC complex, with velocities lying in the range from -2 to 20.5 km s(-1). Beyond this velocity range, 73 molecular clumps are identified with kinematic distances from 2.4 to 11 kpc. Based on the spatial and velocity distribution, nine individual clouds, C1-C9, have been identified for the RMC complex. It appears that the C3 cloud is different from other clouds in the RMC complex in view of its characteristic velocity, excitation temperature, and velocity dispersion. Most of the young stellar clusters in the region are located in positions of both high column density and high excitation temperature. Seven new molecular filaments are discovered in the RMC complex. Evidence for cloud-cloud collision is found in the region of young stellar clusters REFL9 and PouF, showing that these young stellar clusters probably result from a cloud-cloud collision. The abundance ratios of (CO)-C-13 to (CO)-O-18 in the region have a mean value of 13.7, which is 2.5 times larger than the solar system value, showing that UV photons from the nearby OB clusters have a strong influence on the chemistry of clouds in the RMC complex.

第 100 条，共 248 条

Molecular Gas toward the Gemini OB1 Molecular Cloud Complex. II. CO Outflow Candidates with Possible WISE Associations

Li, YJ (Li, Yingjie); Li, FC (Li, Fa-Cheng); Xu, Y (Xu, Ye); Wang, C (Wang, Chen); Du, XY (Du, Xin-Yu); Yang, WJ (Yang, Wenjin); Yang, J (Yang, Ji)

ASTROPHYSICAL JOURNAL SUPPLEMENT SERIES

卷: 235 期: 1 文献号: 15

We present a large-scale survey of CO outflows in the Gem OB1 molecular cloud complex and its surroundings, using the Purple Mountain Observatory Delingha 13.7 m telescope. A total of 198 outflow candidates were identified over a large area (similar to 58.5 square degrees), of which 193 are newly detected. Approximately 68% (134/198) are associated with the Gem OB1 molecular cloud complex, including clouds GGMC 1, GGMC 2, BFS 52, GGMC 3, and GGMC 4. Other regions studied are: the Local arm (Local Lynds, West Front), Swallow, Horn, and Remote cloud. Outflow candidates in GGMC 1, BFS 52, and Swallow are mainly located at ring-like or filamentary structures. To avoid excessive uncertainty in distant regions (greater than or similar to 3.8 kpc), we only estimated the physical parameters for clouds in the Gem OB1 molecular cloud complex and in the Local arm. In those clouds, the total kinetic energy and the energy injection rate of the identified outflow candidates are less than or similar to 1% and less than or similar to 3% of the turbulent energy and the turbulent dissipation rate of each cloud, indicating that the identified outflow candidates cannot provide enough energy to balance turbulence of their host cloud at the scale of the entire cloud (several to dozens of parsecs). The gravitational binding energy of each cloud is greater than or similar to 135 times the total kinetic energy of the identified outflow candidates within the corresponding cloud, indicating that the identified outflow candidates cannot cause major disruptions to the integrity of their host cloud at the scale of the entire cloud.

第 101 条，共 248 条

Introduction of Chinese Antarctic Optical Telescopes

Li, ZY (Li, Zhengyang); Yuan, XY (Yuan, Xiangyan); Cui, XQ (Cui, Xiangqun); Wang, LF (Wang, Lifan); Shang, ZH (Shang, Zhaohui); Du, FJ (Du, Fujia); Gong, XF (Gong, Xuefei); Gu, BZ (Gu, Bozhong); Hu, Y (Hu, Yi); Jiang, P (Jiang, Peng); Li, XY (Li, Xiaoyan); Lu, HP (Lu, Haiping); Ma, B (Ma, Bin); Wei, FH (Wei, Fuhai); Wen, HK (Wen, Haikun); Xu, J (Xu, Jin); Yang, SH (Yang, Shihai); Zhou, HY (Zhou, Honyan)

GROUND-BASED AND AIRBORNE TELESCOPES VII

卷: 10700 文献号: 107001L

The site testing shows that Antarctic Dome A is one of the best site on earth for astronomical observations, for wavelength ranging from visible to infrared and sub-millimeter. Continuous observation for nearly four months in polar nights makes Dome A quite suitable for time domain astronomy. In the past decade CCAA already led a series of Antarctic astronomy activities and telescope projects which will be introduced in this paper. The first generation telescope is Chinese Small Telescope Array known as CSTAR, which was composed of four identical telescopes with 145mm entrance pupil, 20 square degrees FOV and different filters, all pointing to the celestial South Point, mainly used for variable stars detection and site testing. The telescope was deployed in Dome A in Jan. 2008, and followed by automatic observations for four consecutive winters. Three Antarctic Survey Telescopes (AST3) is the second generation telescope capable of pointing and tracking in very low temperature, with 500mm entrance pupil, 8.5 square degree FOV. AST3-1 and AST3-2 were respectively mounted on Dome A in Jan. 2012 and 2015, fully remotely controlled for supernovae survey and exoplanets searching. In Aug. 2017, AST3-2 successfully detected the optical counterpart of LIGO Source GW 170817. Now AST3-3 is under development for both optical and near infrared sky survey by matching different cameras. Based on the experience of the above smaller sized optical telescopes, the 2.5m Kunlun Dark Universe Survey Telescope (KDUST) was proposed for high resolution imaging over wide field of view. Currently the KDUST proposal was submitted to the government and waiting for project review.

会议名称: Conference on Ground-based and Airborne Telescopes VII

会议日期: JUN 10-15, 2018

会议地点: Austin, TX

第 102 条，共 248 条

Optical observations of the 2002cx-like supernova 2014ek and characterizations of SNe Iax

Li, LY (Li, Linyi); Wang, XF (Wang, Xiaofeng); Zhang, JJ (Zhang,

Jujia); Arcavi, I (Arcavi, Iair); Zhang, TM (Zhang, Tianmeng); Rui, LM (Rui, Liming); Hosseinzadeh, G (Hosseinzadeh, Griffin); Howell, DA (Howell, D. Andrew); McCully, C (McCully, Curtis); Zhang, KC (Zhang, Kaicheng); Valenti, S (Valenti, Stefano); Mo, J (Mo, Jun); Li, WX (Li, Wenxiong); Huang, F (Huang, Fang); Xiang, DF (Xiang, Danfeng); Wang, LF (Wang, Lifan); Zhou, X (Zhou, Xu)

MONTHLY NOTICES OF THE ROYAL ASTRONOMICAL SOCIETY

卷: 478 期: 4 页: 4575-4589

We present optical observations of supernova (SN) 2014ek, discovered during the Tsinghua University-National Astronomical Observatories, Chinese Academy of Sciences (NAOC) Transient Survey (TNTS), which shows properties that are consistent with those of SN2002cx-like events (dubbed as SNe Iax). The photometry indicates that it is underluminous compared with normal SNe Ia, with the absolute V-band peak magnitude being -17.66 +/- 0.20 mag. The spectra are characterized by highly ionized Fe III and intermediate-mass elements (IMEs). The expansion velocity of the ejecta is found to be similar to 5000 km s(-1) near the maximum light, only half of that measured for normal SNe Ia. The overall spectral evolution is quite similar to that of SN 2002cx and SN 2005hk, while the absorption features of the main IMEs seem to be relatively weaker. The Ni-56 mass synthesized in the explosion is estimated to be about 0.08M(circle dot) from the pseudo-bolometric light curve. Based on a large sample of SNe Iax, we examined the relations between peak luminosity, ejecta velocity, decline rate and peak V-R colour, but did not find noticeable correlations between these observables, in particular when a few extreme events like SN 2008ha are excluded from the analysis. For this sample, we also studied the birthplace environments and confirm that they still hold the trend of occurring preferentially in late-type spiral galaxies. Moreover, SNe Iax tend to occur in large star-forming regions of their host galaxies, more similar to SNe Ibc than SNe II, favouring the idea that their progenitors should be associated with very young stellar populations. Nevertheless, the progenitors of SNe Iax may have relatively lower metallicity, as suggested by the evidence that they prefer to explode in outer regions of host galaxies.

第 103 条，共 248 条

The first release of the AST3-1 Point Source Catalogue from Dome A, Antarctica

Ma, B (Ma, Bin); Shang, ZH (Shang, Zhaohui); Hu, Y (Hu, Yi); Hu, KL (Hu, Keliang); Liu, Q (Liu, Qiang); Ashley, MCB (Ashley, Michael C. B.); Cui, XQ (Cui, Xiangqun); Du, FJ (Du, Fujia); Fan, DW (Fan, Dongwei); Feng, LL (Feng, Longlong); Huang, F (Huang, Fang); Gu, BZ (Gu, Bozhong); He, BL (He, Boliang); Ji, T (Ji, Tuo); Li, XY (Li, Xiaoyan); Li, ZY (Li, Zhengyang); Liu, HG (Liu, Huigen); Tian, QG (Tian, Qiguo); Tao, C (Tao, Charling); Wang, DX (Wang, Daxing); Wang, LF (Wang, Lifan); Wang, SH (Wang, Songhu); Wang, XF (Wang, Xiaofeng); Wei, P (Wei, Peng); Wu, JH (Wu, Jianghua); Xu, LZ (Xu, Lingzhe); Yang, SH (Yang, Shihai); Yang, M (Yang, Ming); Yang, Y (Yang, Yi); Yu, C (Yu, Ce); Yuan, XY (Yuan, Xiangyan); Zhou, HY (Zhou, Hongyan); Zhang, H (Zhang, Hui); Zhang, XG (Zhang, Xueguang); Zhang, Y (Zhang, Yi); Zhao, C (Zhao, Cheng); Zhou, JL (Zhou, Jilin); Zhu, ZH (Zhu, Zong-Hong)

MONTHLY NOTICES OF THE ROYAL ASTRONOMICAL SOCIETY

卷: 479 期: 1 页: 111-120

The three Antarctic Survey Telescopes (AST3) aim to carry out time-domain imaging survey at Dome A, Antarctica, The first of the three telescopes (AST3-1) was successfully deployed in 2012 January. AST3-1 is a 500 mm aperture modified Schmidt telescope with a 680 mm diameter primary mirror. AST3-1 is equipped with a SDSS i filter and a 10k x 10k frame transfer CCD camera, reduced to 5k x 10k by electronic shuttering, resulting in a 4.3 deg(2) field of view. To verify the capability of AST3-1 for a variety of science goals, extensive commissioning was carried out between 2012 March and May. The commissioning included a survey covering 2000 deg(2) as well as the entire Large and Small Magellanic Clouds. Frequent repeated images were made of the centre of the Large Magellanic Cloud, a selected exoplanet transit field, and fields including some Wolf-Rayet stars. Here, we present the data reduction and photometric measurements of the point sources observed by AST3-1. We have achieved a survey depth of 19.3 mag in 60 s exposures with 5 mmag precision in the light curves of bright stars. The facility achieves sub-mmag photometric precision under stable survey conditions, approaching its photon noise limit, These results demonstrate that AST3-1 at Dome A is extraordinarily competitive in time-domain astronomy, including both quick searches for faint transients and the detection of tiny transit signals.

第 104 条，共 248 条

Dark Energy Survey Year 1 results: cross-correlation redshifts - methods and systematics characterization

Gatti, M (Gatti, M.); Vielzeuf, P (Vielzeuf, P.); Davis, C (Davis, C.); Cawthon, R (Cawthon, R.); Rau, MM (Rau, M. M.); DeRose, J (DeRose, J.); De Vicente, J (De Vicente, J.); Alarcon, A (Alarcon, A.); Rozo, E (Rozo, E.); Gaztanaga, E (Gaztanaga, E.); Hoyle, B (Hoyle, B.); Miquel, R (Miquel, R.); Bernstein, GM (Bernstein, G. M.); Bonnett, C (Bonnett, C.); Rosell, AC (Rosell, A. Carnero); Castander, FJ (Castander, F. J.); Chang, C (Chang, C.); da Costa, LN (da Costa, L. N.); Gruen, D (Gruen, D.); Gschwend, J (Gschwend, J.); Hartley, WG (Hartley, W. G.); Lin, H (Lin, H.); MacCrann, N (MacCrann, N.); Maia, MAG (Maia, M. A. G.); Ogando, RLC (Ogando, R. L. C.); Roodman, A (Roodman, A.); Sevilla-Noarbe, I (Sevilla-Noarbe, I.); Troxel, MA (Troxel, M. A.); Wechsler, RH (Wechsler, R. H.); Asorey, J (Asorey, J.); Davis, TM (Davis, T. M.); Glazebrook, K (Glazebrook, K.); Hinton, SR (Hinton, S. R.); Lewis, G (Lewis, G.); Lidman, C (Lidman, C.); Macaulay, E (Macaulay, E.); Moller, A (Moeller, A.); O'Neill, CR (O'Neill, C. R.); Sommer, NE (Sommer, N. E.); Uddin, SA (Uddin, S. A.); Yuan, F (Yuan, F.); Zhang, B (Zhang, B.); Abbott, TMC (Abbott, T. M. C.); Allam, S (Allam, S.); Annis, J (Annis, J.); Bechtol, K (Bechtol, K.); Brooks, D (Brooks, D.); Burke, DL (Burke, D. L.); Carollo, D (Carollo, D.); Kind, MC (Kind, M. Carrasco); Carretero, J (Carretero, J.); Cunha, CE (Cunha, C. E.); D'Andrea, CB (D'Andrea, C. B.); Depoy, DL (Depoy, D. L.); Desai, S (Desai, S.); Eifler, TF (Eifler, T. F.); Evrard, AE (Evrard, A. E.); Flaugher, B (Flaugher, B.); Fosalba, P (Fosalba, P.); Frieman, J (Frieman, J.); Garcia-Bellido, J (Garcia-Bellido, J.); Gerdes, DW (Gerdes, D. W.); Goldstein, DA (Goldstein, D. A.); Gruendl, RA (Gruendl, R. A.); Gutierrez, G (Gutierrez, G.); Honscheid, K (Honscheid, K.); Hoormann, JK (Hoormann, J. K.); Jain, B (Jain, B.); James, DJ (James, D. J.); Jarvis, M (Jarvis, M.); Jeltema, T (Jeltema, T.); Johnson, MWG (Johnson, M. W. G.); Johnson, MD (Johnson, M. D.); Krause, E (Krause, E.); Kuehn, K (Kuehn, K.); Kuhlmann, S (Kuhlmann, S.); Kuropatkin, N (Kuropatkin, N.); Li, TS (Li, T. S.); Lima, M (Lima, M.); Marshall, JL

(Marshall, J. L.); Melchior, P (Melchior, P.); Menanteau, F (Menanteau, F.); Nichol, RC (Nichol, R. C.); Nord, B (Nord, B.); Plazas, AA (Plazas, A. A.); Reil, K (Reil, K.); Rykoff, ES (Rykoff, E. S.); Sako, M (Sako, M.); Sanchez, E (Sanchez, E.); Scarpine, V (Scarpine, V.); Schubnell, M (Schubnell, M.); Sheldon, E (Sheldon, E.); Smith, M (Smith, M.); Smith, RC (Smith, R. C.); Soares-Santos, M (Soares-Santos, M.); Sobreira, F (Sobreira, F.); Suchyta, E (Suchyta, E.); Swanson, MEC (Swanson, M. E. C.); Tarle, G (Tarle, G.); Thomas, D (Thomas, D.); Tucker, BE (Tucker, B. E.); Tucker, DL (Tucker, D. L.); Vikram, V (Vikram, V.); Walker, AR (Walker, A. R.); Weller, J (Weller, J.); Wester, W (Wester, W.); Wolf, RC (Wolf, R. C.)

MONTHLY NOTICES OF THE ROYAL ASTRONOMICAL SOCIETY

卷: 477 期: 2 页: 1651-1669

We use numerical simulations to characterize the performance of a clustering-based method to calibrate photometric redshift biases. In particular, we cross-correlate the weak lensing source galaxies from the Dark Energy Survey Year 1 sample with redMaGiC galaxies (luminous red galaxies with secure photometric redshifts) to estimate the redshift distribution of the former sample. The recovered redshift distributions are used to calibrate the photometric redshift bias of standard photo-z methods applied to the same source galaxy sample. We apply the method to two photo-z codes run in our simulated data: Bayesian Photometric Redshift and Directional Neighbourhood Fitting. We characterize the systematic uncertainties of our calibration procedure, and find that these systematic uncertainties dominate our error budget. The dominant systematics are due to our assumption of unevolving bias and clustering across each redshift bin, and to differences between the shapes of the redshift distributions derived by clustering versus photo-zs. The systematic uncertainty in the mean redshift bias of the source galaxy sample is Delta z less than or similar to 0.02, though the precise value depends on the redshift bin under consideration. We discuss possible ways to mitigate the impact of our dominant systematics in future analyses.

第 105 条，共 248 条

Dark Energy Survey Year 1 Results: redshift distributions of the weak-lensing source galaxies

Hoyle, B (Hoyle, B.); Gruen, D (Gruen, D.); Bernstein, GM (Bernstein, G. M.); Rau, MM (Rau, M. M.); De Vicente, J (De Vicente, J.); Hartley, G (Hartley, G.); Gaztanaga, E (Gaztanaga, E.); DeRose, J (DeRose, J.); Troxel, MA (Troxel, M. A.); Davis, C (Davis, C.); Alarcon, A (Alarcon, A.); MacCrann, N (MacCrann, N.); Prat, J (Prat, J.); Sanchez, C (Sanchez, C.); Sheldon, E (Sheldon, E.); Wechsler, RH (Wechsler, R. H.); Asorey, J (Asorey, J.); Becker, MR (Becker, M. R.); Bonnett, C (Bonnett, C.); Rosell, AC (Rosell, A. Carnero); Carollo, D (Carollo, D.); Kind, MC (Kind, M. Carrasco); Castander, FJ (Castander, F. J.); Cawthon, R (Cawthon, R.); Chang, C (Chang, C.); Childress, M (Childress, M.); Davis, TM (Davis, T. M.); Drlica-Wagner, A (Drlica-Wagner, A.); Gatti, M (Gatti, M.); Glazebrook, K (Glazebrook, K.); Gschwend, J (Gschwend, J.); Hinton, SR (Hinton, S. R.); Hoormann, JK (Hoormann, J. K.); Kim, AG (Kim, A. G.); King, A (King, A.); Kuehn, K (Kuehn, K.); Lewis, G (Lewis, G.); Lidman, C (Lidman, C.); Lin, H (Lin, H.); Macaulay, E (Macaulay, E.); Maia, MAG (Maia, M. A. G.); Martini, P (Martini, P.); Mudd, D (Mudd, D.); Moller, A (Moller, A.); Nichol, RC (Nichol, R. C.); Ogando, RLC (Ogando, R. L. C.); Rollins, RP (Rollins, R. P.); Roodman, A (Roodman, A.); Ross, AJ (Ross, A. J.); Rozo, E (Rozo, E.); Rykoff, ES (Rykoff, E. S.); Samuroff, S (Samuroff, S.); Sevilla-Noarbe, I (Sevilla-Noarbe, I.); Sharp, R (Sharp, R.); Sommer, NE (Sommer, N. E.); Tucker, BE (Tucker, B. E.); Uddin, SA (Uddin, S. A.); Varga, TN (Varga, T. N.); Vielzeuf, P (Vielzeuf, P.); Yuan, F (Yuan, F.); Zhang, B (Zhang, B.); Abbott, TMC (Abbott, T. M. C.); Abdalla, FB (Abdalla, F. B.); Allam, S (Allam, S.); Annis, J (Annis, J.); Bechtol, K (Bechtol, K.); Benoit-Levy, A (Benoit-Levy, A.); Bertin, E (Bertin, E.); Brooks, D (Brooks, D.); Buckley-Geer, E (Buckley-Geer, E.); Burke, L (Burke, L.); Busha, MT (Busha, M. T.); Capozzi, D (Capozzi, D.); Carretero, J (Carretero, J.); Crocce, M (Crocce, M.); D'Andrea, CB (D'Andrea, C. B.); da Costa, LN (da Costa, L. N.); Depoy, DL (Depoy, D. L.); Desai, S (Desai, S.); Diehl, HT (Diehl, H. T.); Doel, P (Doel, P.); Eifler, TF (Eifler, T. F.); Estrada, J (Estrada, J.); Evrard, AE (Evrard, A. E.); Fernandez, E (Fernandez, E.); Flaugher, B (Flaugher, B.); Fosalba, P (Fosalba, P.); Frieman, J (Frieman, J.); Garcia-Bellido, J (Garcia-Bellido, J.); Gerdes, DW (Gerdes, D. W.); Giannantonio, T (Giannantonio, T.); Goldstein, DA (Goldstein, D. A.); Gruendl, RA (Gruendl, R. A.); Gutierrez, G (Gutierrez, G.); Honscheid, K (Honscheid, K.); James, DJ (James, D. J.); Jarvis, M (Jarvis, M.); Jeltema, T (Jeltema, T.); Johnson, MWG (Johnson, M. W. G.); Johnson, MD (Johnson, M. D.); Kirk, D (Kirk, D.); Krause, E (Krause, E.); Kuhlmann, S (Kuhlmann, S.); Kuropatkin, N (Kuropatkin, N.); Lahav, O (Lahav, O.); Li, TS (Li, T. S.); Lima, M (Lima, M.); March, M (March, M.); Marshall, L (Marshall, L.); Melchior, P (Melchior, P.); Menanteau, F (Menanteau, F.); Miquel, R (Miquel, R.); Nord, B (Nord, B.); O'Neill, CR (O'Neill, C. R.); Plazas, AA (Plazas, A. A.); Romer, AK (Romer, A. K.); Sako, M (Sako, M.); Sanchez, E (Sanchez, E.); Santiago, B (Santiago, B.); Scarpine, V (Scarpine, V.); Schindler, R (Schindler, R.); Schubnell, M (Schubnell, M.); Smith, M (Smith, M.); Smith, RC (Smith, R. C.); Soares-Santos, M (Soares-Santos, M.); Sobreira, F (Sobreira, F.); Suchyta, E (Suchyta, E.); Swanson, MEC (Swanson, M. E. C.); Tarle, G (Tarle, G.); Thomas, D (Thomas, D.); Tucker, DL (Tucker, D. L.); Vikram, V (Vikram, V.); Walker, AR (Walker, A. R.); Weller, J (Weller, J.); Wester, W (Wester, W.); Wolf, RC (Wolf, R. C.); Yanny, B (Yanny, B.); Zuntz, J (Zuntz, J.)

MONTHLY NOTICES OF THE ROYAL ASTRONOMICAL SOCIETY

卷: 478 期: 1 页: 592-610

We describe the derivation and validation of redshift distribution estimates and their uncertainties for the populations of galaxies used as weak-lensing sources in the Dark Energy Survey (DES) Year 1 cosmological analyses. The Bayesian Photometric Redshift (BPZ) code is used to assign galaxies to four redshift bins between z approximate to 0.2 and approximate to 1.3, and to produce initial estimates of the lensing-weighted redshift distributions n(PZ)(i)(z) proportional to d(n)(i)/dz for members of bin i. Accurate determination of cosmological parameters depends critically on knowledge of n(i), but is insensitive to bin assignments or redshift errors for individual galaxies. The cosmological analyses allow for shifts n(i)(z) = n(PZ)(i)(z - Delta z(i)) to correct the mean redshift of n(i)(z) for biases in n(PZ)(i). The Delta z(i) are constrained by comparison of independently estimated 30-band photometric redshifts of galaxies in the Cosmic Evolution Survey (COSMOS) field to BPZ estimates made from the DES griz fluxes, for a sample matched in fluxes, pre-seeing size, and lensing weight to the DES weak-lensing sources. In companion papers, the Delta z(i) of the three lowest redshift bins are further constrained by the angular clustering of the source galaxies around red galaxies with secure photometric redshifts at 0.15 < z < 0.9. This

paper details the BPZ and COSMOS procedures, and demonstrates that the cosmological inference is insensitive to details of the n(i)(z) beyond the choice of Delta z(i). The clustering and COSMOS validation methods produce consistent estimates of Delta z(i) in the bins where both can be applied, with combined uncertainties of sigma(i)(Delta z) = 0.015, 0.013, 0.011, and 0.022 in the four bins. Repeating the photo-z procedure instead using the Directional Neighbourhood Fitting algorithm, or using the n(i)(z) estimated from the matched sample in COSMOS, yields no discernible difference in cosmological inferences.

第 106 条，共 248 条

Rapidly evolving transients in the Dark Energy Survey

Pursiainen, M (Pursiainen, M.); Childress, M (Childress, M.); Smith, M (Smith, M.); Prajs, S (Prajs, S.); Sullivan, M (Sullivan, M.); Davis, TM (Davis, T. M.); Foley, RJ (Foley, R. J.); Asorey, J (Asorey, J.); Calcino, J (Calcino, J.); Carollo, D (Carollo, D.); Curtin, C (Curtin, C.); D'Andrea, CB (D'Andrea, C. B.); Glazebrook, K (Glazebrook, K.); Gutierrez, C (Gutierrez, C.); Hinton, SR (Hinton, S. R.); Hoormann, JK (Hoormann, J. K.); Inserra, C (Inserra, C.); Kessler, R (Kessler, R.); King, A (King, A.); Kuehn, K (Kuehn, K.); Lewis, GF (Lewis, G. F.); Lidman, C (Lidman, C.); Macaulay, E (Macaulay, E.); Moller, A (Moller, A.); Nichol, RC (Nichol, R. C.); Sako, M (Sako, M.); Sommer, NE (Sommer, N. E.); Swann, E (Swann, E.); Tucker, BE (Tucker, B. E.); Uddin, SA (Uddin, S. A.); Wiseman, P (Wiseman, P.); Zhang, B (Zhang, B.); Abbott, TMC (Abbott, T. M. C.); Abdalla, FB (Abdalla, F. B.); Allam, S (Allam, S.); Annis, J (Annis, J.); Avila, S (Avila, S.); Brooks, D (Brooks, D.); Buckley-Geer, E (Buckley-Geer, E.); Burke, DL (Burke, D. L.); Rosell, AC (Rosell, A. Carnero); Kind, MC (Kind, M. Carrasco); Carretero, J (Carretero, J.); Castander, FJ (Castander, F. J.); Cunha, CE (Cunha, C. E.); Davis, C (Davis, C.); Vicente, J (De Vicente, J.); Diehl, HT (Diehl, H. T.); Doel, P (Doel, P.); Eifler, TF (Eifler, T. F.); Flaugher, B (Flaugher, B.); Fosalba, P (Fosalba, P.); Frieman, J (Frieman, J.); Garcia-Bellido, J (Garcia-Bellido, J.); Gruen, D (Gruen, D.); Gruendl, RA (Gruendl, R. A.); Gutierrez, G (Gutierrez, G.); Hartley, WG (Hartley, W. G.); Hollowood, DL (Hollowood, D. L.); Honscheid, K (Honscheid, K.); James, DJ (James, D. J.); Jeltema, T (Jeltema, T.); Kuropatkin, N (Kuropatkin, N.); Li, TS (Li, T. S.); Lima, M (Lima, M.); Maia, MAG (Maia, M. A. G.); Martini, P (Martini, P.); Menanteau, F (Menanteau, F.); Ogando, RLC (Ogando, R. L. C.); Plazas, AA (Plazas, A. A.); Roodman, A (Roodman, A.); Sanchez, E (Sanchez, E.); Scarpine, V (Scarpine, V.); Schindler, R (Schindler, R.); Smith, RC (Smith, R. C.); Soares-Santos, M (Soares-Santos, M.); Sobreira, F (Sobreira, F.); Suchyta, E (Suchyta, E.); Swanson, MEC (Swanson, M. E. C.); Tarle, G (Tarle, G.); Tucker, DL (Tucker, D. L.); Walker, AR (Walker, A. R.)

MONTHLY NOTICES OF THE ROYAL ASTRONOMICAL SOCIETY

卷: 481 期: 1 页: 894-917

We present the results of a search for rapidly evolving transients in the Dark Energy Survey Supernova Programme. These events are characterized by fast light-curve evolution (rise to peak in less than or similar to 10 d and exponential decline in less than or similar to 30 d after peak). We discovered 72 events, including 37 transients with a spectroscopic redshift from host galaxy spectral features. The 37 events increase the total number of rapid optical transients by more than a factor of two. They are found at a wide range of redshifts (0.05 < z < 1.56) and peak brightnesses (-15.75 > M-g > -22.25). The multiband photometry is well fit by a blackbody up to few weeks after peak. The events appear to be hot (T approximate to 10 000-30 000 K) and large (R approximate to 10(14) -2 x 10(15) cm) at peak, and generally expand and cool in time, though some events show evidence for a receding photosphere with roughly constant temperature. Spectra taken around peak are dominated by a blue featureless continuum consistent with hot, optically thick ejecta. We compare our events with a previously suggested physical scenario involving shock breakout in an optically thick wind surrounding a core-collapse supernova, we conclude that current models for such a scenario might need an additional power source to describe the exponential decline. We find that these transients tend to favour star-forming host galaxies, which could be consistent with a core-collapse origin. However, more detailed modelling of the light curves is necessary to determine their physical origin.

Galaxy Cosmology and Dark Energy

第 107 条，共 248 条

The build up of the correlation between halo spin and the large-scale structure

Wang, P (Wang, Peng); Kang, X (Kang, Xi)

MONTHLY NOTICES OF THE ROYAL ASTRONOMICAL SOCIETY

卷: 473 期: 2 页: 1562-1569

Both simulations and observations have confirmed that the spin of haloes/galaxies is correlated with the large-scale structure (LSS) with a mass dependence such that the spin of low-mass haloes/galaxies tend to be parallel with the LSS, while that of massive haloes/galaxies tend to be perpendicular with the LSS. It is still unclear how this mass dependence is built up over time. We use N-body simulations to trace the evolution of the halo spin-LSS correlation and find that at early times the spin of all halo progenitors is parallel with the LSS. As time goes on, mass collapsing around massive halo is more isotropic, especially the recent mass accretion along the slowest collapsing direction is significant and it brings the halo spin to be perpendicular with the LSS. Adopting the fractional anisotropy (FA) parameter to describe the degree of anisotropy of the large-scale environment, we find that the spin-LSS correlation is a strong function of the environment such that a higher FA (more anisotropic environment) leads to an aligned signal, and a lower anisotropy leads to a misaligned signal. In general, our results show that the spin-LSS correlation is a combined consequence of mass flow and halo growth within the cosmic web. Our predicted environmental dependence between spin and large-scale structure can be further tested using galaxy surveys.

第 108 条，共 248 条

An Accurate Centroiding Algorithm for PSF Reconstruction

Lu, TH (Lu, Tianhuan); Luo, WT (Luo, Wentao); Zhang, J (Zhang, Jun); Zhang, JJ (Zhang, Jiajun); Li, HK (Li, Hekun); Dong, FY (Dong, Fuyu); Li, YK (Li, Yingke); Liu, DZ (Liu, Dezi); Fu, LP (Fu, Liping); Li, GL (Li, Guoliang); Fan, ZH (Fan, Zuhui)

ASTRONOMICAL JOURNAL

卷: 156 期: 1 文献号: 14

In this work, we present a novel centroiding method based on Fourier space Phase Fitting (FPF) for Point Spread Function (PSF) reconstruction. We generate two sets of simulations to test our method. The first set is generated by GalSim with an elliptical Moffat profile and strong anisotropy that shifts the center of the PSF. The second set of simulations is drawn from CFHT i band stellar imaging data. We find non-negligible anisotropy from CFHT stellar images, which leads to similar to 0.08 scatter in units of pixels using a polynomial fitting method (Vakili & Hogg). When we apply the FPF method to estimate the centroid in real space, the scatter reduces to similar to 0.04 in S/N = 200 CFHT-like sample. In low signal-to-noise ratio (S/N; 50 and 100) CFHT-like samples, the background noise dominates the shifting of the centroid; therefore, the scatter estimated from different methods is similar. We compare polynomial fitting and FPF using GalSim simulation with optical anisotropy. We find that in all S/N (50, 100, and 200) samples, FPF performs better than polynomial fitting by a factor of similar to 3. In general, we suggest that in real observations there exists anisotropy that shifts the centroid, and thus, the FPF method provides a better way to accurately locate it.

第 109 条，共 248 条

An Investigation of Intracluster Light Evolution Using Cosmological Hydrodynamical Simulations

Tang, L (Tang, Lin); Lin, WP (Lin, Weipeng); Cui, WG (Cui, Weiguang); Kang, X (Kang, Xi); Wang, Y (Wang, Yang); Contini, E (Contini, E.); Yu, Y (Yu, Yu)

ASTROPHYSICAL JOURNAL
卷: 859 期: 2 文献号: 85

Intracluster light (ICL) in observations is usually identified through the surface brightness limit (SBL) method. In this paper, for the first time we produce mock images of galaxy groups and clusters, using a cosmological hydrodynamical simulation to investigate the ICL fraction and focus on its dependence on observational parameters, e.g., the SBL, the effects of cosmological redshift-dimming, point-spread function (PSF), and CCD pixel size. Detailed analyses suggest that the width of the PSF has a significant effect on the measured ICL fraction, while the relatively small pixel size shows almost no influence. It is found that the measured ICL fraction depends strongly on the SBL. At a fixed SBL and redshift, the measured ICL fraction decreases with increasing halo mass, while with a much fainter SBL, it does not depend on halo mass at low redshifts. In our work, the measured ICL fraction shows a clear dependence on the cosmological redshift-dimming effect. It is found that there is more mass locked in the ICL component than light, suggesting that the use of a constant mass-to-light ratio at high surface brightness levels will lead to an underestimate of ICL mass. Furthermore, it is found that the radial profile of ICL shows a characteristic radius that is almost independent of halo mass. The current measurement of ICL from observations has a large dispersion due to different methods, and we emphasize the importance of using the same definition when observational results are compared with theoretical predictions.

第 110 条，共 248 条

StarGO: A New Method to Identify the Galactic Origins of Halo Stars

Yuan, Z (Yuan, Zhen); Chang, J (Chang, Jiang); Banerjee, P (Banerjee, Projjwal); Han, JX (Han, Jiaxin); Kang, X (Kang, Xi); Smith, MC (Smith, M. C.)

ASTROPHYSICAL JOURNAL
卷: 863 期: 1 文献号: 26

We develop a new method, Stars' Galactic Origin (StarGO), to identify the galactic origins of halo stars using their kinematics. Our method is based on a self-organizing map (SOM), which is one of the most popular unsupervised learning algorithms. STARGO combines SOM with a novel adaptive group identification algorithm with essentially no free parameters. To evaluate our model, we build a synthetic stellar halo from mergers of nine satellites in the Milky Way. We construct the mock catalog by extracting a heliocentric volume of 10 kpc from our simulations and assigning expected observational uncertainties corresponding to bright stars from Gaia DR2 and LAMOST DR5. We compare the results from STARGO against those from a friends-of-friends-based method in the space of orbital energy and angular momentum. We show that STARGO is able to systematically identify more satellites and achieve higher number fraction of identified stars for most of the satellites within the extracted heliocentric volume. When applied to data from Gaia DR2, STARGO will enable us to reveal the origins of the inner stellar halo in unprecedented detail.

第 111 条，共 248 条

Prediction of Supernova Rates in Known Galaxy-Galaxy Strong-lens Systems

Shu, YP (Shu, Yiping); Bolton, AS (Bolton, Adam S.); Mao, SD (Mao, Shude); Kang, X (Kang, Xi); Li, GL (Li, Guoliang); Soraisam, M (Soraisam, Monika)

ASTROPHYSICAL JOURNAL
卷: 864 期: 1 文献号: 91

We propose a new strategy of finding strongly lensed supernovae (SNe) by monitoring known galaxy-scale strong-lens systems. Strongly lensed SNe are potentially powerful tools for the study of cosmology, galaxy evolution, and stellar populations, but they are extremely rare. By targeting known strongly lensed star-forming galaxies, our strategy significantly boosts the detection efficiency for lensed SNe compared to a blind search. As a reference sample, we compile the 128 galaxy-galaxy strong-lens systems from the Sloan Lens ACS Survey (SLACS), the SLACS for the Masses Survey, and the Baryon Oscillation Spectroscopic Survey Emission-Line Lens Survey. Within this sample, we estimate the rates of strongly lensed Type Ia SN (SNIa) and core-collapse SN (CCSN) to be 1.23 +/- 0.12 and 10.4 +/- 1.1 events per year, respectively. The lensed SN images are expected to be widely separated with a median separation of 2 arcsec. Assuming a conservative fiducial lensing magnification factor of 5 for the most highly magnified SN image, we forecast that a monitoring program with a single-visit depth of 24.7 mag (5 sigma point source, r band) and a cadence of 5 days can detect 0.49 strongly lensed SNIa event and 2.1 strongly lensed CCSN events per year within this sample. Our proposed targeted-search strategy is particularly useful for prompt and efficient identifications and follow-up observations of strongly lensed SN candidates. It also allows telescopes with small fields of view and limited time to efficiently discover strongly lensed SNe with a pencil-beam scanning strategy.

第 112 条，共 248 条

ELUCID. V. Lighting Dark Matter Halos with Galaxies

Yang, XH (Yang, Xiaohu); Zhang, YC (Zhang, Youcai); Wang, HY (Wang, Huiyuan); Liu, CZ (Liu, Chengze); Lu, TH (Lu, Tianhuan); Li, SJ (Li, Shijie); Shi, F (Shi, Feng); Jing, YP (Jing, Y. P.); Mo, HJ (Mo, H. J.); van den Bosch, FC (van den Bosch, Frank C.); Kang, X (Kang, Xi); Cui, WG (Cui, Weiguang); Guo, H (Guo, Hong); Li, GL (Li, Guoliang); Lim, SH (Lim, S. H.); Lu, Y (Lu, Yi); Luo, WT (Luo, Wentao); Wei, CL (Wei, Chengliang); Yang, L (Yang, Lei)

ASTROPHYSICAL JOURNAL

卷: 860 期: 1 文献号: 30

In a recent study, using the distribution of galaxies in the north galactic pole of the SDSS DR7 region enclosed in a 500 h(-1) Mpc box, we carried out our ELUCID simulation (ELUCID III). Here, we light the dark matter halos and subhalos in the reconstructed region in the simulation with galaxies in the SDSS observations using a novel neighborhood abundance matching method. Before we make use of the galaxy-subhalo connections established in the ELUCID simulation to evaluate galaxy formation models, we set out to explore the reliability of such a link. For this purpose, we focus on the following few aspects of galaxies: (1) the central-subhalo luminosity and mass relations, (2) the satellite fraction of galaxies, (3) the conditional luminosity function (CLF) and conditional stellar mass function (CSMF) of galaxies, and (4) the cross-correlation functions between galaxies and dark matter particles, most of which are measured separately for all, red, and blue galaxy populations. We find that our neighborhood abundance matching method accurately reproduces the central-subhalo relations, satellite fraction, and the CLFs, CSMFs, and biases of galaxies. These features ensure that galaxy-subhalo connections thus established will be very useful in constraining galaxy formation processes. We provide some suggestions for the three levels of using the galaxy-subhalo pairs for galaxy formation constraints. The galaxy-subhalo links and the subhalo merger trees in the SDSS DR7 region extracted from our ELUCID simulation are available upon request.

第 113 条，共 248 条

Galaxy-Galaxy Weak-lensing Measurements from SDSS. II. Host Halo Properties of Galaxy Groups

Luo, WT (Luo, Wentao); Yang, XH (Yang, Xiaohu); Lu, TH (Lu, Tianhuan); Shi, F (Shi, Feng); Zhang, J (Zhang, Jun); Mo, HJ (Mo, H. J.); Shu, CG (Shu, Chenggang); Fu, LP (Fu, Liping); Radovich, M (Radovich, Mario); Zhang, JJ (Zhang, Jiajun); Li, N (Li, Nan); Sunayama, T (Sunayama, Tomomi); Wang, L (Wang, Lei)

ASTROPHYSICAL JOURNAL

卷: 862 期: 1 文献号: 4

In this second paper in a series studying galaxy-galaxy lensing signals using Sloan Digital Sky Survey Data Release 7 (SDSS DR7), we present our measurement and modeling of the lensing signals around groups of galaxies. We divide the groups into four halo mass bins and measure the signals around four different halo-center tracers: brightest central galaxies (BCGs), luminosity-weighted centers, number-weighted centers, and X-ray peak positions. For groups cross-identified in both X-ray and SDSS DR7, we further split the groups into low and high X-ray emission subsamples, both of which are assigned to two halo-center tracers, BCGs and X-ray peak positions. The galaxy-galaxy lensing signals show that BCGs, among the four candidates, are the best halo-center tracers. We model the lensing signals using a combination of four contributions: the off-center NFW host halo profile, subhalo contribution, stellar contribution, and projected two-halo term. We sample the posterior of five parameters, i.e., the halo mass, concentration, off-centering distance, subhalo mass, and fraction of subhalos, via a Monte Carlo Markov Chain (MCMC)package using the galaxy-galaxy lensing signals. After taking into account the sampling effects (e.g., Eddington bias), we found that the best-fit halo masses obtained from lensing signals are quite consistent with those obtained in the group catalog based on an abundance matching method, except in the lowest mass bin.

第 114 条，共 248 条

Removing the Impact of Correlated PSF Uncertainties in Weak Lensing

Lu, TH (Lu, Tianhuan); Zhang, J (Zhang, Jun); Dong, FY (Dong, Fuyu); Li, YK (Li, Yingke); Liu, DZ (Liu, Dezi); Fu, LP (Fu, Liping); Li, GL (Li, Guoliang); Fan, ZH (Fan, Zuhui)

ASTROPHYSICAL JOURNAL

卷: 858 期: 2 文献号: 122

Accurate reconstruction of the spatial distributions of the point-spread function (PSF) is crucial for high precision cosmic shear measurements. Nevertheless, current methods are not good at recovering the PSF fluctuations of high spatial frequencies. In general, the residual PSF fluctuations are spatially correlated, and therefore can significantly contaminate the correlation functions of the weak lensing signals. We propose a method to correct for this contamination statistically, without any assumptions on the PSF and galaxy morphologies or their spatial distribution. We demonstrate our idea with the data from the W2 field of CFHTLenS.

第 115 条，共 248 条

An Investigation of the Interstellar Environment of Supernova Remnant CTB87

Liu, QC (Liu, Qian-Cheng); Chen, Y (Chen, Yang); Chen, BQ (Chen, Bing-Qiu); Zhou, P (Zhou, Ping); Wang, XT (Wang, Xiao-Tao); Su, Y (Su, Yang)

ASTROPHYSICAL JOURNAL

卷: 859 期: 2 文献号: 173

We present a new millimeter CO-line observation toward supernova remnant (SNR) CTB 87, which was regarded purely as a pulsar wind nebula (PWN), and an optical investigation of a coincident surrounding superbubble. The CO observation shows that the SNR delineated by the radio emission is projectively covered by a molecular cloud (MC) complex at VLSR = -60 to -54 km s(-1). Both the symmetric axis of the radio emission and the trailing X-ray PWN appear projectively to be along a gap between two molecular gas patches at -58 to -57 km s(-1). Asymmetric broad profiles of (CO)-C-12 lines peaked at -58 km s(-1) are found at the eastern and southwestern edges of the radio emission. This represents a kinematic signature consistent with an SNR-MC interaction. We also find that a superbubble, similar to 37' in radius, appears to surround the SNR from H I 21 cm (V-LSR similar to-61 to -68 km s(-1)), WISE mid-IR, and optical extinction data. We build a multi-band photometric stellar

sample of stars within the superbubble region and find 82 OB star candidates. The likely peak distance in the stars' distribution seems consistent with the distance previously suggested for CTB 87. We suggest the arc-like radio emission is mainly a relic of the part of the blast wave that propagates into the MC complex and is now in a radiative stage while the other part of the blast wave has been expanding into the low-density region in the superbubble. This scenario naturally explains the lack of X-ray emission related to the ejecta and blast wave. The SNR-MC interaction also favors a hadronic contribution to the.-ray emission from the CTB 87 region.

第 116 条，共 248 条

Dynamic Equilibrium Sets of the Atomic Content of Galaxies across Cosmic Time

Wang, L (Wang, Liang); Obreschkow, D (Obreschkow, Danail); Lagos, CDP (Lagos, Claudia D. P.); Sweet, SM (Sweet, Sarah M.); Fisher, DB (Fisher, Deanne B.); Glazebrook, K (Glazebrook, Karl); Maccio, AV (Maccio, Andrea V.); Dutton, AA (Dutton, Aaron A.); Kang, X (Kang, Xi)
ASTROPHYSICAL JOURNAL
卷: 868 期: 2 文献号: 93
We analyze 88 independent, high-resolution, cosmological zoomed-in simulations of disk galaxies in the NIHAO simulations suite to explore the connection between the atomic gas fraction and angular momentum (AM) of baryons throughout cosmic time. The study is motivated by the analytical model of Obreschkow et al., which predicts a relation between the atomic gas fraction f(atm) and the integrated atomic stability parameter q = j sigma/(GM), where M and j are the mass and specific AM of the galaxy (stars+cold gas) and sigma is the velocity dispersion of the atomic gas. We show that the simulated galaxies follow this relation from their formation (z similar or equal to 4) to the present within similar to 0.5 dex. To explain this behavior, we explore the evolution of the local Toomre stability and find that 90%-100% of the atomic gas in all simulated galaxies is stable at any time. In other words, throughout the entire epoch of peak star formation until today, the timescale for accretion is longer than the timescale to reach equilibrium, thus resulting in a quasi-static equilibrium of atomic gas at any time. Hence, the evolution of f(atm) depends on the complex hierarchical growth history primarily via the evolution of q. An exception is galaxies subject to strong environmental effects.

第 117 条，共 248 条

The Discrepancy between Einstein Mass and Dynamical Mass for SIS and Power-law Mass Models

Li, R (Li, Rui); Wang, JC (Wang, Jiancheng); Shu, YP (Shu, Yiping); Xu, ZY (Xu, Zhaoyi)
ASTROPHYSICAL JOURNAL
卷: 855 期: 1 文献号: 64
We investigate the discrepancy between the two-dimensional projected lensing mass and the dynamical mass for an ensemble of 97 strong gravitational lensing systems discovered by the Sloan Lens ACS Survey, the BOSS Emission-Line Lens Survey (BELLS), and the BELLS for GALaxy-Ly alpha EmitteR sYstems Survey. We fit the lensing data to obtain the Einstein mass and use the velocity dispersion of the lensing galaxies provided by the Sloan Digital Sky Survey to get the projected dynamical mass within the Einstein radius by assuming the power-law mass approximation. The discrepancy is found to be obvious and quantified by Bayesian analysis. For the singular isothermal sphere mass model, we obtain that the Einstein mass is 20.7% more than the dynamical mass, and the discrepancy increases with the redshift of the lensing galaxies. For the more general power-law mass model, the discrepancy still exists within a 1 sigma credible region. We suspect the main reason for this discrepancy is mass contamination, including all invisible masses along the line of sight. In addition, the measurement errors and the approximation of the mass models could also contribute to the discrepancy.

第 118 条，共 248 条

The Spin Alignment of Galaxies with the Large-scale Tidal Field in Hydrodynamic Simulations

Wang, P (Wang, Peng); Guo, Q (Guo, Quan); Kang, X (Kang, Xi); Libeskind, NI (Libeskind, Noam, I)
ASTROPHYSICAL JOURNAL
卷: 866 期: 2 文献号: 138
The correlation between the spins of dark matter halos and the large-scale structure (LSS) has been studied in great detail over a large redshift range, while investigations of galaxies are still incomplete. Motivated by this point, we use the state-of-the-art hydrodynamic simulation, Illustris-1, to investigate mainly the spin-LSS correlation of galaxies at a redshift of z = 0. We mainly find that the spins of low-mass, blue, oblate galaxies are preferentially aligned with the slowest collapsing direction (e(3)) of the large-scale tidal field, while massive, red, prolate galaxy spins tend to be perpendicular to e(3). The transition from a parallel to a perpendicular trend occurs at similar to 10(9.4) h(-1) M-circle dot in the stellar mass, similar to 0.62 in the g-r color, and similar to 0.4 in triaxiality. The transition stellar mass decreases with increasing redshifts. The alignment was found to be primarily correlated with the galaxy stellar mass. Our results are consistent with previous studies both in N-body simulations and observations. Our study also fills the vacancy in the study of the galaxy spin-LSS correlation at z = 0 using hydrodynamical simulations and also provides important insight to understand the formation and evolution of galaxy angular momentum.

第 119 条，共 248 条

SDSS J0909+4449: A large-separation strongly lensed quasar at z similar to 2.8 with three images

Shu, YP (Shu, Yiping); Marques-Chaves, R (Marques-Chaves, Rui); Evans, NW (Evans, N. Wyn); Perez-Fournon, I (Perez-Fournon, Ismael)
MONTHLY NOTICES OF THE ROYAL ASTRONOMICAL SOCIETY
卷: 481 期: 1 页: L136-L140
We report the discovery of SDSS J0909+4449, an exceptional system consisting of a quasar at z = 2.788 strongly lensed by a group of galaxies at z similar to 0.9 into three images separated by up to 14 arcsec based on archival data collected by the Sloan Digital Sky Survey, extended Baryon Oscillation Spectroscopic Survey, Beijing-Arizona Sky Survey, the Mayall z-band Legacy Survey, and the Gemini Telescope. We discuss two hypotheses on the nature of SDSS J0909+4449, i.e. a rare triply imaged quasar in the naked cusp configuration and a typical quadruply imaged quasar with the fourth image undetected in this data. We find that simple lens models can provide excellent fits to the observed image positions and the non-detection under either hypothesis. Deeper imaging data, spectroscopic

observations, and follow-up light-curve measurements will be helpful in determining which hypothesis is correct and provide better constraints on the lens mass distribution. Nevertheless, given its unusually large image separations, SDSS J0909+4449 will be a unique probe for the mass structure and the underlying cooling and stellar feedback processes on group or cluster scales.

第 120 条，共 248 条

Strong-lensing measurement of the total-mass-density profile out to three effective radii for z similar to 0.5 early-type galaxies

Li, R (Li, Rui); Shu, YP (Shu, Yiping); Wang, JC (Wang, Jiancheng)
MONTHLY NOTICES OF THE ROYAL ASTRONOMICAL SOCIETY
卷: 480 期: 1 页: 431-438
We measure the total-mass-density profiles out to three effective radii for a sample of 63 z similar to 0.5, massive early-type galaxies (ETGs) acting as strong gravitational lenses through a joint analysis of lensing and stellar dynamics. The compilation is selected from three galaxy-scale strong-lens samples, namely the Baryon Oscillation Spectroscopic Survey (BOSS) Emission-Line Lens Survey (BELLS), the BELLS for GALaxy-Ly alpha EmitteR sYstems Survey (BELLS GALLERY), and the Strong Lensing Legacy Survey (SL2S). Utilizing the wide source-redshift coverage (0.8-3.5) provided by these three samples, we build a statistically significant ensemble of massive ETGs for which robust mass measurements can be achieved within a broad range of Einstein radii up to three effective radii. Characterizing the three-dimensional total-mass-density distribution by a power-law profile as rho proportional to r(-gamma), we find that the average logarithmic density slope for the entire sample is <gamma > = 2.000(-0.032)(+0.033) (68 per cent CL) with an intrinsic scatter of delta = 0.180(-0.028)(+0.032). Further parametrizing gamma as a function of redshift z and the ratio of Einstein radius to effective radius R-ein/R-eff, we find that the average density distributions of these massive ETGs become steeper at later cosmic times and at larger radii, with magnitudes d <gamma >/dz = -0.309(-0.160)(+0.166) and d <gamma >/d log(10)(R-ein/R-eff) = 0.194(-0.083)(+0.092).

第 121 条，共 248 条

The correspondence between convergence peaks from weak lensing and massive dark matter haloes

Wei, CL (Wei, Chengliang); Li, GL (Li, Guoliang); Kang, X (Kang, Xi); Liu, XK (Liu, Xiangkun); Fan, ZH (Fan, Zuhui); Yuan, S (Yuan, Shuo); Pan, CZ (Pan, Chuzhong)
MONTHLY NOTICES OF THE ROYAL ASTRONOMICAL SOCIETY
卷: 478 期: 3 页: 2987-2998
The convergence peaks, constructed from galaxy shape measurement in weak lensing, are a powerful probe of cosmology as the peaks can be connected with the underlined dark matter haloes. However, the capability of convergence peak statistic is affected by the noise in galaxy shape measurement, signal-to-noise ratio (SNR), as well as the contribution from the projected mass distribution from the large-scale structures along the line of sight (LOS). In this paper, we use the ray-tracing simulation on a curved sky to investigate the correspondence between the convergence peak and the dark matter haloes at the LOS. We find that, in case of no noise and for source galaxies at z(s) = 1, more than 65 per cent peaks with SNR >= 3 (SNR) are related to more than one massive haloes with mass larger than 10(13)M(circle dot). Those massive haloes contribute 87.2 per cent to high peaks (SNR >= 5) and the remaining contributions are from the large-scale structures. On the other hand, the peak distribution is skewed by the noise in galaxy shape measurement, especially for lower SNR peaks. In the noisy field where the shape noise is modelled as a Gaussian distribution, about 60 per cent high peaks (SNR >= 5) are true peaks and the fraction decreases to 20 per cent for lower peaks (3 <= SNR < 5). Furthermore, we find that high peaks (SNR >= 5) are dominated by very massive haloes larger than 10(14) M-circle dot.

第 122 条，共 248 条

The different growth pathways of brightest cluster galaxies and intracluster light

Contini, E (Contini, E.); Yi, SK (Yi, S. K.); Kang, X (Kang, X.)
MONTHLY NOTICES OF THE ROYAL ASTRONOMICAL SOCIETY
卷: 479 期: 1 页: 932-944
We study the growth pathways of brightest central galaxies (BCGs) and intracluster light (ICE) by means of a semi-analytic model. We assume that ICL forms by stellar stripping of satellite galaxies and violent processes during mergers, and implement two independent models: One considers both mergers and stellar stripping (named STANDARD model), and the other considers only mergers (named MERGERS model). We find that BCGs and ICL form, grow, and overall evolve at different times and with different time-scales, but they show a clear coevolution after redshift z similar to 0.7-0.8. Around 90 per cent of the ICE from stellar stripping is built up in the innermost 150 kpc from the halo centre and the dominant contribution comes from disc-like galaxies (B/T < 0.4) through a large number of small/intermediate stripping events (M-strip/M-sat < 0.3). The fractions of stellar mass in BCGs and in the ICL over the total stellar mass within the virial radius of the halo evolve differently with time. At high redshift, the BCG accounts for the bulk of the mass, but its contribution gradually decreases with time and stays constant after z similar to 0.4-0.5. The ICL, instead, grows very fast and its contribution keeps increasing down to the present time. The STANDARD and MERGERS models make very similar predictions in most of the cases, but predict different amounts of ICL associated with galaxies within the virial radius of the group/cluster other than the BCG, at z = 0. We then suggest that this quantity is a valid observable that can shed light on the relative importance of mergers and stellar stripping for the formation of ICL.

第 123 条，共 248 条

The large-scale environment from cosmological simulations I. The baryonic cosmic web (vol 473, pg 68, 2018)

Cui, WG (Cui, Weiguang); Knebe, A (Knebe, Alexander); Yepes, G (Yepes, Gustavo); Yang, XH (Yang, Xiaohu); Borgani, S (Borgani, Stefano); Kang, X (Kang, Xi); Power, C (Power, Chris); Staveley-Smith, L (Staveley-Smith, Lister)
MONTHLY NOTICES OF THE ROYAL ASTRONOMICAL SOCIETY
卷: 474 期: 3 页: 4130-4132
DOI: 10.1093/mnras/stx2949
出版年: MAR 2018
在 BIOSIS Citation Index 中的被引频次: 0

第 124 条，共 248 条

A high dust emissivity index β for a CO-faint galaxy in a filamentary Lyα nebula at z = 3.1

Yuta Kato, Yuichi Matsuda, Daisuke Iono, Bunyo Hatsukade, Hideki Umehata, Kotaro Kohno, David M Alexander, Yiping Ao, Scott C Chapman, Matthew Hayes
the Astronomical Society of Japan,
Volume 70, Issue 5, October 2018, L6,
We present CO J = 4–3 line and 3 mm dust continuum observations of a 100 kpc-scale filamentary Lyα nebula (SSA22 LAB18) at z = 3.1 using the Atacama Large Millimeter/submillimeter Array (ALMA). We detected the CO J = 4–3 line at a systemic zCO = 3.093 ± 0.001 at 11 σ from one of the ALMA continuum sources associated with the Lyα filament. We estimated the CO J = 4–3 luminosity of L ′ CO(4−3)=(2.3±0.2)×109LCO(4−3) ′ =(2.3±0.2)×109K km s−1 pc2 for this CO source, which is one order of magnitude smaller than those of typical z > 1 dusty star-forming galaxies (DSFGs) of similar far-infrared luminosity LIR ∼ 1012 L⊙. We derived a molecular gas mass of Mgas=(4.4+0.9−0.6)×109M ⊙ Mgas=(4.4−0.6+0.9)×109M ⊙ and a star-formation rate of SFR =270 ± 160 M⊙ yr−1. We also estimated a gas depletion time of τdep = 17 ± 10 Myr, which is shorter than those of typical DSFGs. It is suggested that this source is in the transition phase from DSFG to a gas-poor, early-type galaxy. From ALMA to Herschel multi-band dust continuum observations, we measured a dust emissivity index β = 2.3 ± 0.2, which is similar to those of local gas-poor, early-type galaxies. From recent laboratory experiments, the specific chemical compositions needed to reproduce such a high β for interstellar dust at the submillimeter wavelengths. ALMA CO and multi-band dust continuum observations can constrain the evolutionary stage of high-redshift galaxies through τdep and β, and thus we can investigate the chemical composition of dust even in the early Universe.

第 125 条，共 248 条

The magnification invariant of circularly-symmetric lens models

Wei, CL (Wei, Cheng-Liang); Chu, Z (Chu, Zhe); Shu, YP (Shu, Yi-Ping)
RESEARCH IN ASTRONOMY AND ASTROPHYSICS
卷: 18 期: 7 文献号: 80
In the context of strong gravitational lensing, the magnification of an image is crucially important for constraining various lens models. For several commonly used quadruple lens models, the magnification invariants, defined as the sum of the signed magnifications of images, have been analytically derived when the image multiplicity is a maximum. In this paper, we further study the magnification of several disk lens models, including (a) exponential disk lens, (b) Gaussian disk lens, (c) modified Hubble profile lens, and another two of the popular three-dimensional symmetrical lens models, (d) NFW lens and (e) Einasto lens. We find that magnification invariant exists for each lens model. Moreover, our results show that magnification invariants can be significantly changed by the characteristic surface mass density kappa(c).

第 126 条，共 248 条

Alignment between Satellite and Central Galaxies in the SDSS DR7: Dependence on Large-scale Environment

Wang, P (Wang, Peng); Luo, Y (Luo, Yu); Kang, X (Kang, Xi); Libeskind, NI (Libeskind, Noam I.); Wang, L (Wang, Lei); Zhang, YC (Zhang, Youcai); Tempel, E (Tempel, Elmo); Guo, Q (Guo, Quan)
ASTROPHYSICAL JOURNAL
卷: 859 期: 2 文献号: 115
The alignment between satellites and central galaxies has been studied in detail both in observational and theoretical works. The widely accepted fact is that satellites preferentially reside along the major axis of their central galaxy. However, the origin and large-scale environmental dependence of this alignment are still unknown. In an attempt to determine these variables, we use data constructed from Sloan Digital Sky Survey DR7 to investigate the large-scale environmental dependence of this alignment with emphasis on examining the alignment's dependence on the color of the central galaxy. We find a very strong large-scale environmental dependence of the satellite-central alignment (SCA) in groups with blue centrals. Satellites of blue centrals in knots are preferentially located perpendicular to the major axes of the centrals, and the alignment angle decreases with environment, namely, when going from knots to voids. The alignment angle strongly depends on the (0.1)(g - r) color of centrals. We suggest that the SCA is the result of a competition between satellite accretion within large-scale structure (LSS) and galaxy evolution inside host halos. For groups containing red central galaxies, the SCA is mainly determined by the evolution effect, while for blue central dominated groups, the effect of the LSS plays a more important role, especially in knots. Our results provide an explanation for how the SCA forms within different large-scale environments. The perpendicular case in groups and knots with blue centrals may also provide insight into understanding similar polar arrangements, such as the formation of the Milky Way and Centaurus A's satellite system.

第 127 条，共 248 条

Full-sky Ray-tracing Simulation of Weak Lensing Using ELUCID Simulations: Exploring Galaxy Intrinsic Alignment and Cosmic Shear Correlations

Wei, CL (Wei, Chengliang); Li, GL (Li, Guoliang); Kang, X (Kang, Xi); Luo, Y (Luo, Yu); Xia, QL (Xia, Qianli); Wang, P (Wang, Peng); Yang, XH (Yang, Xiaohu); Wang, HY (Wang, Huiyuan); Jing, YP (Jing, Yipeng); Mo, HJ (Mo, Houjun); Lin, WP (Lin, Weipeng); Wang, Y (Wang, Yang); Li, SJ (Li, Shijie); Lu, Y (Lu, Yi); Zhang, YC (Zhang, Youcai); Lim, SH (Lim, S. H.); Tweed, D (Tweed, Dylan); Cui, WG (Cui, Weiguang)
ASTROPHYSICAL JOURNAL
卷: 853 期: 1 文献号: 25
The intrinsic alignment of galaxies is an important systematic effect in weak-lensing surveys, which can affect the derived cosmological parameters. One direct way to distinguish different alignment models and quantify their effects on the measurement is to produce mock weak-lensing surveys. In this work, we use the full-sky ray-tracing technique to produce mock images of galaxies from the ELUCID N-body simulation run with WMAP9 cosmology. In our model, we assume that the shape of the central elliptical galaxy follows that of the dark matter halo, and that of the spiral galaxy follows the halo spin. Using the mock galaxy images, a combination of galaxy intrinsic shape and the gravitational shear, we compare the predicted tomographic shear correlations to the results of the Kilo-Degree Survey (KiDS) and Deep Lens Survey (DLS). We find that our predictions stay between the KiDS and DLS results. We rule out a model

in which the satellite galaxies are radially aligned with the center galaxy; otherwise, the shear correlations on small scales are too high. Most importantly, we find that although the intrinsic alignment of spiral galaxies is very weak, they induce a positive correlation between the gravitational shear signal and the intrinsic galaxy orientation (GI). This is because the spiral galaxy is tangentially aligned with the nearby large-scale overdensity, contrary to the radial alignment of the elliptical galaxy. Our results explain the origin of the detected positive GI term in the weak-lensing surveys. We conclude that in future analyses, the GI model must include the dependence on galaxy types in more detail.

第 128 条，共 248 条

Statistical Test of Distance-Duality Relation with Type Ia Supernovae and Baryon Acoustic Oscillations

Ma, C (Ma, Cong); Corasaniti, PS (Corasaniti, Pier-Stefano)
ASTROPHYSICAL JOURNAL
卷: 861 期: 2 文献号: 124
We test the distance-duality relation eta equivalent to d(L) [(1 + z)(2)d(A)] = 1 between cosmological luminosity distance (d(L)) from the JLA SNe Ia compilation and angular-diameter distance (d(A)) based on Baryon Oscillation Spectroscopic Survey (BOSS) and WiggleZ baryon acoustic oscillation measurements. The d(L) measurements are matched to d(A) redshift by a statistically consistent compression procedure. With Monte Carlo methods, nontrivial and correlated distributions of. can be explored in a straightforward manner without resorting to a particular evolution template eta(z). Assuming independent constraints on cosmological parameters that are necessary to obtain d(L) and d(A) values, we find 9% constraints consistent with eta = 1 from the analysis of SNIa + BOSS and an 18% bound results from SNIa + WiggleZ. These results are contrary to previous claims that eta < 1 has been found close to or above the 1 sigma level. We discuss the effect of different cosmological parameter inputs and the use of the apparent deviation from distance-duality as a proxy of systematic effects on cosmic distance measurements. The results suggest possible systematic overestimation of SNIa luminosity distances compared with d(A) data when a Planck Lambda CDM cosmological parameter inference is used to enhance the precision. If interpreted as an extinction correction due to a gray dust component, the effect is broadly consistent with independent observational constraints.

第 129 条，共 248 条

ELUCID. IV. Galaxy Quenching and its Relation to Halo Mass, Environment, and Assembly Bias

Wang, HY (Wang, Huiyuan); Mo, HJ (Mo, H. J.); Chen, SH (Chen, Sihan); Yang, Y (Yang, Yang); Yang, XH (Yang, Xiaohu); Wang, E (van den Bosch, Frank C.); van den Bosch, FC (Jing, Yipeng); Jing, YP (Kang, Xi); Kang, X (Lin, Weipeng); Lin, WP (Lim, S. H.); Lim, SH (Huang, Shuiyao); Huang, SY (Lu, Yi); Lu, Y (Li, Shijie); Li, SJ (Cui, Weiguang); Cui, WG (Zhang, Youcai); Zhang, YC (Tweed, Dylan); Tweed, D (Wei, Chengliang); Wei, CL (Li, Guoliang); Li, GL (Shi, Feng); Shi, F (Wang, Enci)
ASTROPHYSICAL JOURNAL
卷: 852 期: 1 文献号: 31
We examine the quenched fraction of central and satellite galaxies as a function of galaxy stellar mass, halo mass, and the matter density of their large-scale environment. Matter densities are inferred from our ELUCID simulation, a constrained simulation of the local universe sampled by SDSS, while halo masses and central/satellite classification are taken from the galaxy group catalog of Yang et al. The quenched fraction for the total population increases systematically with the three quantities. We find that the"environmental quenching efficiency," which quantifies the quenched fraction as a function of halo mass, is independent of stellar mass. And this independence is the origin of the stellar mass independence of density-based quenching efficiency found in previous studies. Considering centrals and satellites separately, we find that the two populations follow similar correlations of quenching efficiency with halo mass and stellar mass, suggesting that they have experienced similar quenching processes in their host halo. We demonstrate that satellite quenching alone cannot account for the environmental quenching efficiency of the total galaxy population, and that the difference between the two populations found previously arises mainly from the fact that centrals and satellites of the same stellar mass reside, on average, in halos of different mass. After removing these effects of halo mass and stellar mass, there remains a weak, but significant, residual dependence on environmental density, which is eliminated when halo assembly bias is taken into account. Our results therefore indicate that halo mass is the prime environmental parameter that regulates the quenching of both centrals and satellites.

第 130 条，共 248 条

The BOSS Emission-line Lens Survey. V. Morphology and Substructure of Lensed Ly alpha Emitters at Redshift Z approximate to 2.5 in the BELLS GALLERY

Cornachione, MA (Cornachione, Matthew A.); Bolton, AS (Bolton, Adam S.); Shu, YP (Shu, Yiping); Zheng, Z (Zheng, Zheng); Montero-Dorta, AD (Montero-Dorta, Antonio D.); Brownstein, JR (Brownstein, Joel R.); Oguri, M (Oguri, Masamune); Kochanek, CS (Kochanek, Christopher S.); Mao, SD (Mao, Shude); Perez-Fournon, I (Perez-Fournon, Ismael); Marques-Chaves, R (Marques-Chaves, Rui); Menard, B (Menard, Brice)
ASTROPHYSICAL JOURNAL
卷: 853 期: 2 文献号: 148
We present a morphological study of the 17 lensed Ly alpha emitter (LAE) galaxies of the Baryon Oscillation Spectroscopic Survey Emission-Line Lens Survey (BELLS) for the GALaxy-Ly alpha EmitteR sYstems (BELLS GALLERY) sample. This analysis combines the magnification effect of strong galaxy-galaxy lensing with the high resolution of the Hubble Space Telescope to achieve a physical resolution of similar to 80 pc for this 2 < z < 3 LAE sample, allowing a detailed characterization of the LAE rest-frame ultraviolet continuum surface brightness profiles and substructure. We use lens-model reconstructions of the LAEs to identify and model individual clumps, which we subsequently use to constrain the parameters of a generative statistical model of the LAE population. Since the BELLS GALLERY sample is selected primarily on the basis of Ly alpha emission, the LAEs that we study here are likely to be directly comparable to those selected in wide-field, narrowband LAE surveys, in contrast with the lensed LAEs identified in cluster-lensing fields. We find an LAE clumpiness fraction of approximately

88%, which is significantly higher than that found in previous (non-lensing) studies. We find a well-resolved characteristic clump half-light radii of similar to 350 pc, a scale comparable to the largest H II regions seen in the local universe. This statistical characterization of LAE surface-brightness profiles will be incorporated into future lensing analyses using the BELLS GALLERY sample to constrain the incidence of dark-matter substructure in the foreground lensing galaxies.

第 131 条，共 248 条

The Strong Gravitationally Lensed Herschel Galaxy HLock01: Optical Spectroscopy Reveals a Close Galaxy Merger with Evidence of Inflowing Gas

Marques-Chaves, R (Marques-Chaves, Rui); Perez-Fournon, I (Perez-Fournon, Ismael); Gavazzi, R (Gavazzi, Raphael); Martinez-Navajas, PI (Martinez-Navajas, Paloma I.); Riechers, D (Riechers, Dominik); Rigopoulou, D (Rigopoulou, Dimitra); Cabrera-Lavers, A (Cabrera-Lavers, Antonio); Clements, DL (Clements, David L.); Cooray, A (Cooray, Asantha); Farrah, D (Farrah, Duncan); Ivison, RJ (Ivison, Rob J.); Jimenez-Angel, CE (Jimenez-Angel, Camilo E.); Nayyeri, H (Nayyeri, Hooshang); Oliver, S (Oliver, Seb); Omont, A (Omont, Alain); Scott, D (Scott, Douglas); Shu, YP (Shu, Yiping); Wardlow, J (Wardlow, Julie)

ASTROPHYSICAL JOURNAL

卷: 854 期: 2 文献号: 151

The submillimeter galaxy (SMG) HERMES J105751.1+ 573027 (hereafter HLock01) at z = 2.9574 +/- 0.0001 is one of the brightest gravitationally lensed sources discovered in the Herschel Multi-tiered Extragalactic Survey. Apart from the high flux densities in the far-infrared, it is also extremely bright in the rest-frame ultraviolet (UV), with a total apparent magnitude m(UV) similar or equal to 19.7 mag. We report here deep spectroscopic observations with the Gran Telescopio Canarias of the optically bright lensed images of HLock01. Our results suggest that HLock01 is a merger system composed of the Herschel-selected SMG and an optically bright Lyman break-like galaxy (LBG), separated by only 3.3 kpc in projection. While the SMG appears very massive. (M-* similar or equal to 5 x 10(11) M-circle dot), with a highly extinguished stellar component (A(V) similar or equal to 4.3), the LBG is a young, lower-mass (M-* similar or equal to 1 x 10(10) M-circle dot), but still luminous (10 x L-UV*) satellite galaxy. Detailed analysis of the high signal-to-noise ratio (S/N) rest-frame UV spectrum of the LBG shows complex kinematics of the gas, exhibiting both blueshifted and redshifted absorption components. While the blueshifted component is associated with strong galactic outflows from the massive stars in the LBG, as is common in most star-forming galaxies, the redshifted component may be associated with gas inflow seen along a favorable sightline to the LBG. We also find evidence of an extended gas reservoir around HLock01 at an impact parameter of 110 kpc, through the detection of C II lambda lambda 1334 absorption in the red wing of a bright Ly alpha emitter at z similar or equal to 3.327. The data presented here highlight the power of gravitational lensing in high S/N studies to probe deeply into the physics of high-z star-forming galaxies.

Star Formation in Galaxies

第 132 条，共 248 条

A Survey of Atomic Carbon [C i] in High-redshift Main-sequence Galaxies

Valentino, Francesco，Magdis, Georgios E.，Daddi, Emanuele

10.3847/1538-4357/aaeb88

The Astrophysical Journal

We present the first results of an ALMA survey of the lower fine structure line of atomic carbon [C I]$(^3P_1\,-\,^{3}P_0)$ in far infrared-selected galaxies on the main sequence at $z\sim1.2$ in the COSMOS field. We compare our sample with a comprehensive compilation of data available in the literature for local and high-redshift starbursting systems and quasars. We show that the [C I]($^3P_1$\rightarrow$$^3P_0$) luminosity correlates on global scales with the infrared luminosity $L_{\rm IR}$ similarly to low-J CO transitions. We report a systematic variation of $L'_{\rm [C\,I]^3P_1\,-\,^3P_0}$/$L_{\rm IR}$ as a function of the galaxy type, with the ratio being larger for main-sequence galaxies than for starbursts and sub-millimeter galaxies at fixed $L_{\rm IR}$. The $L'_{\rm [C\,I]^3P_1\,-\,^3P_0}$/$L'_{\rm CO(2-1)}$ and $M_{\rm{[C I]}}$/$M_{\rm dust}$ mass ratios are similar for main-sequence galaxies and for local and high-redshift starbursts within a 0.2 dex intrinsic scatter, suggesting that [C I] is a good tracer of molecular gas mass as CO and dust.

第 133 条，共 248 条

Herschel Spectroscopy of the Taffy Galaxies (UGC 12914/12915=VV 254): Enhanced [C II] Emission in the Collisionally Formed Bridge

Peterson, BW (Peterson, B. W.); Appleton, PN (Appleton, P. N.); Bitsakis, T (Bitsakis, T.); Guillard, P (Guillard, P.); Alatalo, K (Alatalo, K.); Boulanger, F (Boulanger, F.); Cluver, M (Cluver, M.); Duc, PA (Duc, P. -A.); Falgarone, E (Falgarone, E.); Gallagher, S (Gallagher, S.); Gao, Y (Gao, Y.); Helou, G (Helou, G.); Jarrett, TH (Jarrett, T. H.); Joshi, B (Joshi, B.); Lisenfeld, U (Lisenfeld, U.); Lu, N (Lu, N.); Ogle, P (Ogle, P.); des Forets, GP (des Forets, G. Pineau); van der Werf, P (van der Werf, P.); Xu, CK (Xu, C. K.)

ASTROPHYSICAL JOURNAL

卷: 855 期: 2 文献号: 141

Using the PACS and SPIRE spectrometers on board Herschel, we obtained observations of the Taffy galaxies (UGC 12914/12915) and bridge. The Taffy system is believed to be the result of a face-on collision between two gas-rich galaxies, in which the stellar disks passed through each other, but the gas was dispersed into a massive H I and molecular bridge between them. Emission is detected and mapped in both galaxies and the bridge in the [C II] 157.7 mu m and [O I]63.2 mu m fine-structure lines. Additionally, SPIRE FTS spectroscopy detects the [C I] P-3(2) -> P-3(1)(809.3 GHz) and [C I] P-3(1) -> P-3(0)(492.2 GHz) neutral carbon lines, and weakly detects high-J CO transitions in the bridge. These results indicate that the bridge is composed of a warm multi-phase medium consistent with shock and turbulent heating. Despite low star formation rates in the bridge, the [C II] emission appears to be enhanced, reaching [C II]/FIR ratios of 3.3% in parts of the bridge. Both the [C II] and [O I] lines show broad intrinsic multi-component profiles, similar

to those seen in previous CO (1-0) and H I observations. The [C II] emission shares similar line profiles with both the double-peaked H I profiles and shares a high-velocity component with single-peaked CO profiles in the bridge, suggesting that the [C II] emission originates in both the neutral and molecular phases. We show that it is feasible that a combination of turbulently heated H-2 and high column-density H I, resulting from the galaxy collision, is responsible for the enhanced [C II] emission.

第 134 条，共 248 条

CO (7-6), [C I] 370 mu m, and [N II] 205 mu m Line Emission of the QSO BRI1335-0417 at Redshift 4.407

Lu, NY (Lu, Nanyao); Cao, TW (Cao, Tianwen); Diaz-Santos, T (Diaz-Santos, Tanio); Zhao, YH (Zhao, Yinghe); Privon, GC (Privon, George C.); Cheng, C (Cheng, Cheng); Gao, Y (Gao, Yu); Xu, CK (Xu, C. Kevin); Charmandaris, V (Charmandaris, Vassilis); Rigopoulou, D (Rigopoulou, Dimitra); van der Werf, PP (van der Werf, Paul P.); Huang, JS (Huang, Jiasheng); Wang, Z (Wang, Zhong); Evans, AS (Evans, Aaron S.); Sanders, DB (Sanders, David B.)

ASTROPHYSICAL JOURNAL

卷: 864 期: 1 文献号: 38

We present the results from our Atacama Large Millimeter/submillimeter Array (ALMA) imaging observations of the CO(7-6), [C I] 370 mu m (hereafter [C I]), and [N II] 205 mu m (hereafter [N II]) lines and their underlying continuum emission of BRI 1335-0417, an infrared bright quasar at z = 4.407. At the achieved resolutions of similar to 1.'' 1 to 1.'' 2 (or 7.5-8.2 kpc), the continuum at 205 and 372 mu m (rest frame), the CO(7-6), and the [C I] emissions are at best barely resolved whereas the [N II] emission is well resolved with a beam-deconvolved major axis of 1.'' 3 (+/- 0.'' 3) or 9(+/- 2) kpc. As a warm dense gas tracer, the CO(7-6) emission shows a more compact spatial distribution and a significantly higher peak velocity dispersion than the other two lines that probe lower density gas, a picture favoring a merger-triggered star formation (SF) scenario over an orderly rotating SF disk. The CO(7 -6) data also indicate a possible QSO-driven gas outflow that reaches a maximum line-of-sight velocity of 500-600 km s(-1). The far-infrared (FIR) dust temperature (T-dust) of 41.5 K from a graybody fit to the continuum agrees well with the average T-dust inferred from various line luminosity ratios. The resulting LCO(7-6)/L-FIR luminosity ratio is consistent with that of local luminous infrared galaxies powered predominantly by SF. The LCO(7-6)-inferred SF rate is 5.1(+/- 1.5) x 10(3) M-circle dot yr(-1). The system has an effective star-forming region of 1.7(-0.8)(+1.7) kpc in diameter and a molecular gas reservoir of similar to 5 x 10(11) M-circle dot.

第 135 条，共 248 条

The MALATANG Survey: The L-GAS-L-IR Correlation on Sub-kiloparsec Scale in Six Nearby Star-forming Galaxies as Traced by HCN J=4 -> 3 and HCO+ J=4 -> 3

Tan, QH (Tan, Qing-Hua); Gao, Y (Gao, Yu); Zhang, ZY (Zhang, Zhi-Yu); Greve, TR (Greve, Thomas R.); Jiang, XJ (Jiang, Xue-Jian); Wilson, CD (Wilson, Christine D.); Yang, CT (Yang, Chen-Tao); Bemis, A (Bemis, Ashley); Chung, A (Chung, Aeree); Matsushita, S (Matsushita, Satoki); Shi, Y (Shi, Yong); Ao, YP (Ao, Yi-Ping); Brinks, E (Brinks, Elias); Currie, MJ (Currie, Malcolm J.); Davis, TA (Davis, Timothy A.); Grijs, R (de Grijs, Richard); Ho, LC (Ho, Luis C.); Imanishi, M (Imanishi, Masatoshi); Kohno, K (Kohno, Kotaro); Lee, B (Lee, Bumhyun); Parsons, H (Parsons, Harriet); Rawlings, MG (Rawlings, Mark G.); Rigopoulou, D (Rigopoulou, Dimitra); Rosolowsky, E (Rosolowsky, Erik); Bulger, J (Bulger, Joanna); Chen, H (Chen, Hao); Chapman, SC (Chapman, Scott C.); Eden, D (Eden, David); Gear, WK (Gear, Walter K.); Gu, QS (Gu, Qiu-Sheng); He, JH (He, Jin-Hua); Jiao, Q (Jiao, Qian); Liu, DZ (Liu, Dai-Zhong); Liu, LJ (Liu, Li-Jie); Li, XH (Li, Xiao-Hu); Michalowski, MJ (Michalowski, Michal J.); Nguyen-Luong, (Quang Nguyen-Luong); Qiu, JJ (Qiu, Jian-Jie); Smith, MWL (Smith, Matthew W. L.); Violino, G (Violino, Giulio); Wang, JF (Wang, Jian-Fa); Wang, JF (Wang, Jun-Feng); Wang, JZ (Wang, Jun-Zhi); Yeh, S (Yeh, Sherry); Zhao, YH (Zhao, Ying-He); Zhu, M (Zhu, Ming)

ASTROPHYSICAL JOURNAL

卷: 860 期: 2 文献号: 165

We present HCN J = 4 -> 3 and HCO+ J = 4 -> 3 maps of six nearby star-forming galaxies, NGC 253, NGC 1068, IC 342, M82, M83, and NGC 6946, obtained with the James Clerk Maxwell Telescope as part of the MALATANG survey. All galaxies were mapped in the central 2' x 2' region at 14 '' (FWHM) resolution (corresponding to linear scales of similar to 0.2-1.0 kpc). The L-IR-L'(dense) relation, where the dense gas is traced by the HCN J = 4 -> 3 and the HCO+ J = 4 -> 3 emission, measured in our sample of spatially resolved galaxies is found to follow the linear correlation established globally in galaxies within the scatter. We find that the luminosity ratio, L-IR/L'(dense), shows systematic variations with L-IR within individual spatially resolved galaxies, whereas the galaxy-integrated ratios vary little. A rising trend is also found between L-IR/L'(dense) ratio and the warm-dust temperature gauged by the 70 mu m/100 mu m flux ratio. We find that the luminosity ratios of IR/HCN (4-3) and IR/HCO+ (4-3), which can be taken as a proxy for the star formation efficiency (SFE) in the dense molecular gas (SFEdense), appear to be nearly independent of the dense gas fraction (f(dense)) for our sample of galaxies. The SFE of the total molecular gas (SFEmol) is found to increase substantially with f(dense) when combining our data with those on local (ultra) luminous infrared galaxies and high-z quasars. The mean L'(HCN(4-3))/L'(HCO+(4-3)) line ratio measured for the six targeted galaxies is 0.9 +/- 0.6. No significant correlation is found for the L'(HCN(4-3)) L'(HCO+(4-3)) ratio with the star formation rate as traced by L-IR, nor with the warm-dust temperature, for the different populations of galaxies.

第 136 条，共 248 条

Far-infrared Herschel SPIRE spectroscopy of lensed starbursts reveals physical conditions of ionized gas

Zhang, ZY (Zhang, Zhi-Yu); Ivison, RJ (Ivison, R. J.); George, RD (George, R. D.); Zhao, YH (Zhao, Yinghe); Dunne, L (Dunne, L.); Herrera-Camus, R (Herrera-Camus, R.); Lewis, AJR (Lewis, A. J. R.); Liu, DZ (Liu, Daizhong); Naylor, D (Naylor, D.); Oteo, I (Oteo, Ivan); Riechers, DA (Riechers, D. A.); Smail, I (Smail, Ian); Yang, CT (Yang, Chentao); Eales, S (Eales, Stephen); Hopwood, R (Hopwood, Ros); Maddox, S (Maddox, Steve); Omont, A (Omont, Alain); van der Werf, P (van der Werf, Paul)

MONTHLY NOTICES OF THE ROYAL ASTRONOMICAL SOCIETY

卷: 481 期: 1 页: 59-97

The most intensively star-forming galaxies are extremely luminous at far-infrared (FIR) wavelengths, highly obscured at optical and ultraviolet wavelengths, and lie at z >= 1-3. We present a programme of FIR spectroscopic observations with

the SPIRE FTS, as well as photometric observations with PACS, both on board Herschel, towards a sample of 45 gravitationally lensed, dusty starbursts across z similar to 1-3.6. In total, we detected 27 individual lines down to 3 sigma, including nine [C II] 158 mu m lines with confirmed spectroscopic redshifts, five possible [C II] lines consistent with their FIR photometric redshifts, and in some individual sources a few [OIII] 88 mu m, [O III] 52 mu m, [O I] 145 mu m, [O I] 63 mu m, [N II] 122 mu m and OH 119 mu m (in absorption) lines. To derive the typical physical properties of the gas in the sample, we stack all spectra weighted by their intrinsic luminosity and by their 500 mu m flux densities, with the spectra scaled to a common redshift. In the stacked spectra, we detect emission lines of [CII] 158 mu m, [N II] 122 mu m, [O III] 88 mu m, [O III] 52 mu m, [O I] 63 mu m and the absorption doublet of OH at 119 mu m, at high fidelity. We find that the average electron densities traced by the [NII] and [O III] lines are higher than the average values in local star-forming galaxies and ULIRGs, using the same tracers. From the [NII]/[C II] and [O I]/[C II] ratios, we find that the [CII] emission is likely dominated by the photodominated regions (PDR), instead of by ionized gas or large-scale shocks.

第 137 条，共 248 条

Super-deblended Dust Emission in Galaxies. I. The GOODS-North Catalog and the Cosmic Star Formation Rate Density out to Redshift 6

Liu, Daizhong，Daddi, Emanuele，Dickinson, Mark
The Astrophysical Journal 853(2)
We present a new technique to measure multi-wavelength "Super-deblended" photometry from highly confused images, which we apply to Herschel and ground-based far-infrared (FIR) and (sub-)millimeter (mm) data in the northern field of the Great Observatories Origins Deep Survey (GOODS). There are two key novelties. First, starting with a large database of deep Spitzer 24{\mu}m and VLA 20cm detections that are used to define prior positions for fitting the FIR/submm data, we perform an active selection of useful priors independently at each frequency band, moving from less to more confused bands. Exploiting knowledge of redshift and all available photometry, we identify hopelessly faint priors that we remove from the fitting pool. This approach significantly reduces blending degeneracies and allows reliable photometry to be obtained for galaxies in FIR+mm bands. Second, we obtain well-behaved, nearly Gaussian flux density uncertainties, individually tailored to all fitted priors in each band. This is done by exploiting extensive simulations that allow us to calibrate.

第 138 条，共 248 条

Super-deblended Dust Emission in Galaxies. II. Far-IR to (Sub)millimeter Photometry and High-redshift Galaxy Candidates in the Full COSMOS Field

Jin Shuowen， Daddi Emanuele， Liu Daizhong
The Astrophysical Journal
We present a "super-deblended" far-infrared to (sub)millimeter photometric catalog in the Cosmic Evolution Survey (COSMOS), prepared with the method recently developed by Liu et al. 2018, with key adaptations. We obtain point spread function (PSF) fitting photometry at fixed prior positions including 88,008 galaxies detected in either VLA 1.4~GHz, 3~GHz and/or MIPS 24~$μ$m images. By adding a specifically carved mass-selected sample (with an evolving stellar mass limit), a highly complete prior sample of 194,428 galaxies is achieved for deblending FIR/(sub)mm images. We performed ``active' removal of non relevant priors at FIR/(sub)mm bands using spectral energy distribution (SED) fitting and redshift information. In order to cope with the shallower COSMOS data we subtract from the maps the flux of faint non-fitted priors and explicitly account for the uncertainty of this step. The resulting photometry (including data from Spitzer, Herschel, SCUBA2, AzTEC, MAMBO and NSF's Karl G. Jansky Very Large Array at 3~GHz and 1.4~GHz) displays well behaved.

第 139 条，共 248 条

The Effect of Galaxy Interactions on Molecular Gas Properties

Pan, HA (Pan, Hsi-An); Lin, L (Lin, Lihwai); Hsieh, BC (Hsieh, Bau-Ching); Xiao, T (Xiao, Ting); Gao, Y (Gao, Yang); Ellison, SL (Ellison, Sara L.); Scudder, JM (Scudder, Jillian M.); Barrera-Ballesteros, J (Barrera-Ballesteros, Jorge); Yuan, FT (Yuan, Fangting); Saintonge, A (Saintonge, Amelie); Wilsons, CD (Wilsons, Christine D.); Hwang, HS (Hwang, Ho Seong); De Looze, I (De Looze, Ilse); Gao, Y (Gao, Yu); Ho, LC (Ho, Luis C.); Brinks, E (Brinks, Elias); Mok, A (Mok, Angus); Brown, T (Brown, Toby); Davis, TA (Davis, Timothy A.); Williams, TG (Williams, Thomas G.); Chung, A (Chung, Aeree); Parsons, H (Parsons, Harriet); Bureau, M (Bureau, Martin); Sargent, MT (Sargent, Mark T.); Chung, EJ (Chung, Eun Jung); Kim, E (Kim, Eunbin); Liu, T (Liu, Tie); Michalowski, MJ (Michalowski, Michal J.); Tosaki, T (Tosaki, Tomoka)
ASTROPHYSICAL JOURNAL
卷: 868 期: 2 文献号: 132
Galaxy interactions are often accompanied by an enhanced star formation rate (SFR). Since molecular gas is essential for star formation, it is vital to establish whether and by how much galaxy interactions affect the molecular gas properties. We investigate the effect of interactions on global molecular gas properties by studying a sample of 58 galaxies in pairs and 154 control galaxies. Molecular gas properties are determined from observations with the JCMT, PMO, and CSO telescopes and supplemented with data from the xCOLD GASS and JINGLE surveys at¹²CO(1-0) and ¹²CO(2-1). The SFR, gas mass (M<INF>H2</INF>), and gas fraction (f<INF>gas</INF>) are all enhanced in galaxies in pairs by similar to 2.5 times compared to the controls matched in redshift, mass, and effective radius, while the enhancement of star formation efficiency (SFE equivalent to SFR/M<INF>H2</INF>) is less than a factor of 2. We also find that the enhancements in SFR, M<INF>H<INF>2</INF></INF> and f<INF>gas</INF>, increase with decreasing pair separation and are larger in systems with smaller stellar mass ratio. Conversely, the SFE is only enhanced in close pairs (separation <20 kpc) and equal-mass systems; therefore, most galaxies in pairs lie in the same parameter space on the SFR-M<INF>H</INF><INF>2</INF> plane as controls. This is the first time that the dependence of molecular gas properties on merger configurations is probed statistically with a relatively large sample and a carefully selected control sample for individual galaxies. We conclude that galaxy

interactions do modify the molecular gas properties, although the strength of the effect is dependent on merger configuration.

第 140 条，共 248 条

The Herschel Bright Sources (HerBS): sample definition and SCUBA-2 observations

Bakx, TJLC (Bakx, Tom J. L. C.); Eales, SA (Eales, S. A.); Negrello, M (Negrello, M.); Smith, MWL (Smith, M. W. L.); Valiante, E (Valiante, E.); Holland, WS (Holland, W. S.); Baes, M (Baes, M.); Bourne, N (Bourne, N.); Clements, DL (Clements, D. L.); Dannerbauer, H (Dannerbauer, H.); De Zotti, G (De Zotti, G.); Dunne, L (Dunne, L.); Dye, S (Dye, S.); Furlanetto, C (Furlanetto, C.); Ivison, RJ (Ivison, R. J.); Maddox, S (Maddox, S.); Marchetti, L (Marchetti, L.); Michalowski, MJ (Michalowski, M. J.); Omont, A (Omont, A.); Oteo, I (Oteo, I.); Wardlow, JL (Wardlow, J. L.); van der Werf, P (van der Werf, P.); Yang, C (Yang, C.)

MONTHLY NOTICES OF THE ROYAL ASTRONOMICAL SOCIETY
卷: 473 期: 2 页: 1751-1773

We present the Herschel Bright Sources (HerBS) sample, a sample of bright, high-redshift Herschel sources detected in the 616.4 deg(2) Herschel Astrophysical Terahertz Large Area Survey. The HerBS sample contains 209 galaxies, selected with a 500 mu m flux density greater than 80 mJy and an estimated redshift greater than 2. The sample consists of a combination of hyperluminous infrared galaxies and lensed ultraluminous infrared galaxies during the epoch of peak cosmic star formation. In this paper, we present Submillimetre CommonUser Bolometer Array 2 (SCUBA-2) observations at 850 mu m of 189 galaxies of the HerBS sample, 152 of these sources were detected. We fit a spectral template to the HerschelSpectral and Photometric Imaging Receiver (SPIRE) and 850 mu m SCUBA-2 flux densities of 22 sources with spectroscopically determined redshifts, using a two- component modified blackbody spectrum as a template. We find a cold- and hot- dust temperature of 21.29(-1.66)(+1.35) and 45.80(-3.48)(+2.88) K, a cold-to-hot dust mass ratio of 26.62(-6.74)(+5.61) and a beta of 1.83(-0.28)(+0.14) . The poor quality of the fit suggests that the sample of galaxies is too diverse to be explained by our simple model. Comparison of our sample to a galaxy evolution model indicates that the fraction of lenses are high. Out of the 152 SCUBA-2 detected galaxies, the model predicts 128.4 +/- 2.1 of those galaxies to be lensed (84.5 per cent). The SPIRE 500 mu m flux suggests that out of all 209 HerBS sources, we expect 158.1 +/- 1.7 lensed sources, giving a total lensing fraction of 76 per cent.

第 141 条，共 248 条

VALES - IV. Exploring the transition of star formation efficiencies between normal and starburst galaxies using APEX/SEPIA Band-5 and ALMA at low redshift

Cheng, C (Cheng, C.); Ibar, E (Ibar, E.); Hughes, TM (Hughes, T. M.); Villanueva, V (Villanueva, V.); Leiton, R (Leiton, R.); Orellana, G (Orellana, G.); Arancibia, AM (Munoz Arancibia, A.); Lu, N (Lu, N.); Xu, CK (Xu, C. K.); Willmer, CNA (Willmer, C. N. A.); Huang, J (Huang, J.); Cao, T (Cao, T.); Yang, C (Yang, C.); Xue, YQ (Xue, Y. Q.); Torstensson, K (Torstensson, K.)

MONTHLY NOTICES OF THE ROYAL ASTRONOMICAL SOCIETY
卷: 475 期: 1 页: 248-256

In this work, we present new the Swedish-ESO PI receiver for the Atacama Pathfinder Experiment APEX/SEPIA Band-5 observations targeting the CO (J = 2-1) emission line of 24 Herschel-detected galaxies at z = 0.1-0.2. Combining this sample with our recent new Valparafso ALMA Line Emission Survey (VALES), we investigate the star formation efficiencies [SFEs = star formation rate (SFR)/M-H2] of galaxies at low redshift. We find the SFE of our sample bridges the gap between normal star-forming galaxies and Ultra-Luminous Infrared Galaxies (ULIRGs), which are thought to be triggered by different star formation modes. Considering the SFE' as the SFR and the L'(CO) ratio, our data show a continuous and smooth increment as a function of infrared luminosity (or star formation rate) with a scatter about 0.5 dex, instead of a steep jump with a bimodal behaviour. This result is due to the use of a sample with a much larger range of sSFR/sSFR(ms) using LIRGs, with luminosities covering the range between normal and ULIRGs. We conclude that the main parameters controlling the scatter of the SFE in star-forming galaxies are the systematic uncertainty of the alpha(CO) conversion factor, the gas fraction, and physical size.

第 142 条，共 248 条

JINGLE, a JCMT legacy survey of dust and gas for galaxy evolution studies - I. Survey overview and first results

Saintonge, Amelie1; Wilson, Christine D.2; Xiao, Ting3,4; Lin, Lihwai5; Hwang, Ho Seong6; Tosaki, Tomoka7;Bureau, Martin8; Cigan, Phillip J.9; Clark, Christopher J. R.9; Clements, David L.10; De Looze, Ilse1,11;Dharmawardena, Thavisha5,12; Gao, Yang4; Gear, Walter K.9; Greenslade, Joshua10; Lamperti, Isabella1; Lee, Jong Chul13; Li, Cheng14; Michalowski, Michal J.15,16; Mok, Angus2; Pan, Hsi-An5; Sansom, Anne E.17; Sargent, Mark18; Smith, Matthew W. L.9; Williams, Thomas9; Yang, Chentao19,20; Zhu, Ming30; Accurso, Gioacchino1;Barmby, Pauline21; Brinks, Elias22; Bourne, Nathan1,15; Brown, Toby2; Chung, Aeree23; Chung, Eun Jung13;Cibinel, Anna18; Coppin, Kristen22; Davies, Jonathan9; Davis, Timothy A.9; Eales, Steve9; Fanciullo, Lapo5; Fang, Taotao24; Gao, Yu19,20; Glass, David H. W.17; Gomez, Haley L.9; Greve, Thomas1; He JH(何金华)25,26,27 ; Ho, Luis C.28,29; Huang, Feng24; Jeong, Hyunjin13; Jiang, Xuejian19,20; Jiao, Qian30; Kemper, Francisca5; Kim, Ji Hoon31; Kim, Minjin13; Kim, Taehyun13; Ko, Jongwan13; Kong, Xu32; Lacaille, Kevin2; Lacey, Cedric G.33; Lee, Bumhyun23; Lee, Joon Hyeop13; Lee, Wing-Kit5,34; Masters, Karen35,36; Oh, Se-Heon13; Papadopoulos, Padelis9; Park, Changbom6; Park, Sung-Joon13; Parsons, Harriet44; Rowlands, Kate37; Scicluna, Peter5; Scudder, Jillian M.18,38; Sethuram, Ramya4; Serjeant, Stephen39; Shao, Yali28; Sheen, Yun-Kyeong13; Shi, Yong40,41; Shim, Hyunjin42; Smith, Connor M. A.9; Spekkens, Kristine43; Tsai, An-Li12; Verma, Aprajita8; Urquhart, Sheona39;Violino, Giulio22; Viti, Serena1; Wake, David43; Wang, Junfeng24; Wouterloot, Jan44; Yang, Yujin13; Yim, Kijeong13; Yuan, Fangting4; Zheng, Zheng1,3

MONTHLY NOTICES OF THE ROYAL ASTRONOMICAL SOCIETY

JINGLE is a new JCMT legacy survey designed to systematically study the cold interstellar medium of galaxies in the local Universe. As part of the survey we perform 850 mu m continuum measurements with SCUBA-2 for a representative sample of 193 Herschel-selected galaxies withM(*) > 10(9) M-circle dot, as well as integrated CO(2-1) line fluxes with RxA3m for a subset of 90 of these galaxies. The sample is selected from fields covered by the

Herschel-ATLAS survey that are also targeted by the MaNGA optical integral-field spectroscopic survey. The new JCMT observations combined with the multiwavelength ancillary data will allow for the robust characterization of the properties of dust in the nearby Universe, and the benchmarking of scaling relations between dust, gas, and global galaxy properties. In this paper we give an overview of the survey objectives and details about the sample selection and JCMT observations, present a consistent 30-band UV-to-FIR photometric catalogue with derived properties, and introduce the JINGLE Main Data Release. Science highlights include the non-linearity of the relation between 850 mu m luminosity and CO line luminosity (log LCO(2-1) = 1.372 logL(850)-1.376), and the serendipitous discovery of candidate z > 6 galaxies.

Molecular Clouds and Star Formation

第 143 条，共 248 条

The Serpens filament at the onset of slightly supercritical collapse

Gong, Y (Gong, Y.); Li, GX (Li, G. X.); Mao, RQ (Mao, R. Q.); Henkel, C (Henkel, C.); Menten, KM (Menten, K. M.); Fang, M (Fang, M.); Wang, M (Wang, M.); Sun, JX (Sun, J. X.)
ASTRONOMY & ASTROPHYSICS
卷: 620 文献号: A62
The Serpens filament, as one of the nearest infrared dark clouds, is regarded as a pristine filament at a very early evolutionary stage of star formation. In order to study its molecular content and dynamical state, we mapped this filament in seven species: (CO)-O-18, HCO+, HNC, HCN, N2H+, CS, and CH3OH. Among them, HCO+, HNC, HCN, and CS show self-absorption, while (CO)-O-18 is most sensitive to the filamentary structure. A kinematic analysis demonstrates that this filament forms a velocity-coherent (trans) sonic structure, a large part of which is one of the most quiescent regions in the Serpens cloud. Widespread (CO)-O-18 depletion is found throughout the Serpens filament. Based on the Herschel dust-derived H-2 column density map, the line mass of the filament is 36-41 M-circle dot pc(-1), and its full width at half maximum is 0.17 +/- 0.01 pc, while its length is approximate to 1.6 pc. The inner radial column density profile of this filament can be well fitted with a Plummer profile with an exponent of 2.2 +/- 0.1, a scale radius of 0.018 +/- 0.003 pc, and a central density of (4.0 +/- 0.8) x 10(4) cm(-3). The Serpens filament appears to be slightly supercritical. The widespread blue-skewed HNC and CS line profiles and HCN hyperfine line anomalies across this filament indicate radial infall in parts of the Serpens filament. (CO)-O-18 velocity gradients also indicate accretion flows along the filament. The velocity and density structures suggest that such accretion flows are likely due to a longitudinal collapse parallel to the filament's long axis. Both the radial infall rate (similar to 72 M-circle dot Myr(-1), inferred from HNC and CS blue-skewed profiles) and the longitudinal accretion rate (similar to 10 M-circle dot Myr(-1), inferred from (CO)-O-18 velocity gradients) along the Serpens filament are lower than all previously reported values in other filaments. This indicates that the Serpens filament lies at an early evolutionary stage when collapse has just begun, or that thermal and nonthermal support are effective in providing support against gravity.

第 144 条，共 248 条

Magnetic Fields toward Ophiuchus-B Derived from SCUBA-2 Polarization Measurements

Soam, A (Soam, Archana); Pattle, K (Pattle, Kate); Ward-Thompson, D (Ward-Thompson, Derek); Lee, CW (Lee, Chang Won); Sadavoy, S (Sadavoy, Sarah); Koch, PM (Koch, Patrick M.); Kim, G (Kim, Gwanjeong); Kwon, J (Kwon, Jungmi); Kwon, W (Kwon, Woojin); Arzoumanian, D (Arzoumanian, Doris); Berry, D (Berry, David); Hoang, T (Hoang, Thiem); Tamura, M (Tamura, Motohide); Lee, SS (Lee, Sang-Sung); Liu, T (Liu, Tie); Kim, KT (Kim, Kee-Tae); Johnstone, D (Johnstone, Doug); Nakamura, F (Nakamura, Fumitaka); Lyo, AR (Lyo, A-Ran); Onaka, T (Onaka, Takashi); Kim, J (Kim, Jongsoo); Furuya, RS (Furuya, Ray S.); Hasegawa, T (Hasegawa, Tetsuo); Lai, SP (Lai, Shih-Ping); Bastien, P (Bastien, Pierre); Chung, EJ (Chung, Eun Jung); Kim, S (Kim, Shinyoung); Parsons, H (Parsons, Harriet); Rawlings, MG (Rawlings, Mark G.); Mairs, S (Mairs, Steve); Graves, SF (Graves, Sarah F.); Robitaille, JF (Robitaille, Jean-Franois); Liu, HL (Liu, Hong-Li); Whitworth, AP (Whitworth, Anthony P.); Eswaraiah, C (Eswaraiah, Chakali); Rao, R (Rao, Ramprasad); Yoo, H (Yoo, Hyunju); Houde, M (Houde, Martin); Kang, JH (Kang, Ji-hyun); Doi, Y (Doi, Yasuo); Choi, M (Choi, Minho); Kang, M (Kang, Miju); Coude, S (Coude, Simon); Li, HB (Li, Hua-bai); Matsumura, M (Matsumura, Masafumi); Matthews, BC (Matthews, Brenda C.); Pon, A (Pon, Andy); Di Francesco, J (Di Francesco, James); Hayashi, SS (Hayashi, Saeko S.); Kawabata, KS (Kawabata, Koji S.); Inutsuka, SI (Inutsuka, Shu-ichiro); Qiu, K (Qiu, Keping); Franzmann, E (Franzmann, Erica); Friberg, P (Friberg, Per); Greaves, JS (Greaves, Jane S.); Kirk, JM (Kirk, Jason M.); Li, D (Li, Di); Shinnaga, H (Shinnaga, Hiroko); van Loo, S (van Loo, Sven); Aso, Y (Aso, Yusuke); Byun, DY (Byun, Do-Young); Chen, HR (Chen, Huei-Ru); Chen, MCY (Chen, Mike C. -Y.); Chen, WP (Chen, Wen Ping); Ching, TC (Ching, Tao-Chung); Cho, J (Cho, Jungyeon); Chrysostomou, A (Chrysostomou, Antonio); Drabek-Maunder, E (Drabek-Maunder, Emily); Eyres, SPS (Eyres, Stewart P. S.); Fiege, J (Fiege, Jason); Friesen, RK (Friesen, Rachel K.); Fuller, G (Fuller, Gary); Gledhill, T (Gledhill, Tim); Griffin, MJ (Griffin, Matt J.); Gu, QL (Gu, Qilao); Hatchell, J (Hatchell, Jennifer); Holland, W (Holland, Wayne); Inoue, T (Inoue, Tsuyoshi); Iwasaki, K (Iwasaki, Kazunari); Jeong, IG (Jeong, Il-Gyo); Kang, SJ (Kang, Sung-ju); Kemper, F (Kemper, Francisca); Kim, KH (Kim, Kyoung Hee); Kim, MR (Kim, Mi-Ryang); Lacaille, KM (Lacaille, Kevin M.); Lee, JE (Lee, Jeong-Eun); Li, DL (Li, Dalei); Liu, JH (Liu, Junhao); Liu, SY (Liu, Sheng-Yuan); Moriarty-Schieven, GH (Moriarty-Schieven, Gerald H.); Nakanishi, H (Nakanishi, Hiroyuki); Ohashi, N (Ohashi, Nagayoshi); Peretto, N (Peretto, Nicolas); Pyo, TS (Pyo, Tae-Soo); Qian, L (Qian, Lei); Retter, B (Retter, Brendan); Richer, J (Richer, John); Rigby, A (Rigby, Andrew); Savini, G (Savini, Giorgio); Scaife, AMM (Scaife, Anna M. M.); Tang, YW (Tang, Ya-Wen); Tomisaka, K (Tomisaka, Kohji); Wang, HC (Wang, Hongchi); Wang, JW (Wang, Jia-Wei); Yen, HW (Yen, Hsi-Wei); Yuan, JH (Yuan, Jinghua); Zhang, CP (Zhang, Chuan-Peng); Zhang, GY (Zhang, Guoyin); Zhou, JJ (Zhou, Jianjun); Zhu, L (Zhu, Lei); Andre, P (Andre, Philippe); Dowell, D (Dowell, Darren); Falle, S (Falle, Sam); Tsukamoto, Y (Tsukamoto, Yusuke); Kanamori, Y (Kanamori, Yoshihiro); Kataoka, A (Kataoka, Akimasa); Kobayashi, MIN (Kobayashi, Masato I. N.); Nagata, T (Nagata, Tetsuya); Saito, H (Saito,

Hiro); Seta, M (Seta, Masumichi); Hwang, J (Hwang, Jihye); Han, I (Han, Ilseung); Lee, H (Lee, Hyeseung); Zenko, T (Zenko, Tetsuya)
ASTROPHYSICAL JOURNAL
卷: 861 期: 1 文献号: 65
We present the results of dust emission polarization measurements of Ophiuchus-B (Oph-B) carried out using the Submillimetre Common-User Bolometer Array 2 (SCUBA-2) camera with its associated polarimeter (POL-2) on the James Clerk Maxwell Telescope in Hawaii. This work is part of the B-fields in Star-forming Region Observations survey initiated to understand the role of magnetic fields in star formation for nearby star-forming molecular clouds. We present a first look at the geometry and strength of magnetic fields in Oph-B. The field geometry is traced over similar to 0.2 pc, with clear detection of both of the sub-clumps of Oph-B. The field pattern appears significantly disordered in sub-clump Oph-B1. The field geometry in Oph-B2 is more ordered, with a tendency to be along the major axis of the clump, parallel to the filamentary structure within which it lies. The degree of polarization decreases systematically toward the dense core material in the two sub-clumps. The field lines in the lower density material along the periphery are smoothly joined to the large-scale magnetic fields probed by NIR polarization observations. We estimated a magnetic field strength of 630 +/- 410 mu G in the Oph-B2 sub-clump using a Davis-Chandrasekhar-Fermi analysis. With this magnetic field strength, we find a mass-to-flux ratio lambda = 1.6 +/- 1.1, which suggests that the Oph-B2 clump is slightly magnetically supercritical.

第 145 条，共 248 条

Molecular line emission in NGC 4945, imaged with ALMA

Henkel, C (Henkel, C.); Muehle, S (Muehle, S.); Bendo, G (Bendo, G.); Jozsa, GIG (Jozsa, G. I. G.); Gong, Y (Gong, Y.); Viti, S (Viti, S.); Aalto, S (Aalto, S.); Combes, F (Combes, F.); Garcia-Burillo, S (Garcia-Burillo, S.); Hunt, LK (Hunt, L. K.); Mangum, J (Mangum, J.); Martin, S (Martin, S.); Muller, S (Muller, S.); Ott, J (Ott, J.); Werf, PD (van der Werf, P.); Malawi, AA (Malawi, A. A.); Ismail, H (Ismail, H.); Alkhuja, E (Alkhuja, E.); Asiri, HM (Asiri, H. M.); Aladro, R (Aladro, R.); Alves, F (Alves, F.); Ao, Y (Ao, Y.); Baan, WA (Baan, W. A.); Costagliola, F (Costagliola, F.); Fuller, G (Fuller, G.); Greene, J (Greene, J.); Impellizzeri, CMV (Impellizzeri, C. M. V.); Kamali, F (Kamali, F.); Klessen, RS (Klessen, R. S.); Mauersberger, R (Mauersberger, R.); Tang, XD (Tang, X. D.); Tristram, K (Tristram, K.); Wang, M (Wang, M.); Zhang, JS (Zhang, J. S.)
ASTRONOMY & ASTROPHYSICS
卷: 615 文献号: A155
NGC 4945 is one of the nearest (D approximate to 3.8 Mpc; 1" approximate to 19 pc) starburst galaxies. To investigate the structure, dynamics, and composition of the dense nuclear gas of this galaxy, ALMA band 3 (lambda approximate to 3-4mm) observations were carried out with approximate to 2" resolution. Three HCN and two HCO+ isotopologues, CS, C3H2, SiO, HCO, and CH3C2H were measured. Spectral line imaging demonstrates the presence of a rotating nuclear disk of projected size 10" x 2" reaching out to a galactocentric radius of r 100 pc with position angle PA = 45 degrees +/- 2 degrees, inclination i = 75 degrees +/- 2 degrees and an unresolved bright central core of less than or similar to 2" size The continuum source, representing mostly free free radiation from star forming regions, is more compact than the nuclear disk by a linear factor of two but shows the same position angle and is centered 0".39 +/- 0".14 northeast of the nuclear accretion disk defined by H2O maser emission. Near the systemic velocity but outside the nuclear disk, both HCN J = 1 -> 0 and CS J = 2 -> 1 delineate molecular arms of length greater than or similar to 15" (greater than or similar to 285 pc) on opposite sides of the dynamical center. These are connected by a (deprojected) approximate to 0.6 kpc sized molecular bridge, likely a dense gaseous bar seen almost ends -on, shifting gas from the front and back side into the nuclear disk. Modeling this nuclear disk located farther inside (r less than or similar to 100 pc) with tilted rings provides a good fit by inferring a coplanar outflow reaching a characteristic deprojected velocity of approximate to 50 km s(-1). All our molecular lines, with the notable exception of CH3C2H, show significant absorption near the systemic velocity (approximate to 571 km s(-1)), within the range approximate to 500-660 km s(-1). Apparently, only molecular transitions with low critical H-2 density (n(crit) less than or similar to 10(4) cm(-3)) do not show absorption. The velocity field of the nuclear disk, derived from CH3C2H, provides evidence for rigid rotation in the inner few arcseconds and a dynamical mass of M-tot = (2.1 +/- 0.2) x 10(8) M-circle dot inside a galactocentric radius of 2".45 (approximate to 45 pc), with a significantly flattened rotation curve farther out. Velocity integrated line intensity maps with most pronounced absorption show molecular peak positions up to approximate to 1".5 (approximate to 30 pc) southwest of the continuum peak, presumably due to absorption, which appears to be most severe slightly northeast of the nuclear maser disk. A nitrogen isotope ratio of N-14/N-15 approximate to 200-450 is estimated. This range of values is much higher then previously reported on a tentative basis. Therefore, because N-15 is less abundant than expected, the question for strong N-15 enrichment by massive star ejecta in starbursts still remains to be settled.

第 146 条，共 248 条

ALMA 26 Arcmin(2) Survey of GOODS-S at One Millimeter (ASAGAO): Average Morphology of High-z Dusty Star-forming Galaxies in an Exponential Disk (n similar or equal to 1)

Fujimoto, S (Fujimoto, Seiji); Ouchi, M (Ouchi, Masami); Kohno, K (Kohno, Kotaro); Yamaguchi, Y (Yamaguchi, Yuki); Hatsukade, B (Hatsukade, Bunyo); Ueda, Y (Ueda, Yoshihiro); Shibuya, T (Shibuya, Takatoshi); Inoue, S (Inoue, Shigeki); Oogi, T (Oogi, Taira); Toft, S (Toft, Sune); Gomez-Guijarro, C (Gomez-Guijarro, Carlos); Wang, T (Wang, Tao); Espada, D (Espada, Daniel); Nagao, T (Nagao, Tohru); Tanaka, I (Tanaka, Ichi); Ao, YP (Ao, Yiping); Umehata, H (Umehata, Hideki); Taniguchi, Y (Taniguchi, Yoshiaki); Nakanishi, K (Nakanishi, Kouichiro); Rujopakarn, W (Rujopakarn, Wiphu); Ivison, RJ (Ivison, R. J.); Wang, WH (Wang, Wei-hao); Lee, MM (Lee, Minju M.); Tadaki, K (Tadaki, Ken-ichi); Tamura, Y (Tamura, Yoichi); Dunlop, JS (Dunlop, J. S.)
ASTROPHYSICAL JOURNAL
卷: 861 期: 1 文献号: 7
We present morphological properties of dusty star-forming galaxies at z = 1-3 determined with the high-resolution (FWHM similar to 0.'' 19) Atacama Large Milllimeter/submillimeter Array (ALMA) 1 mm map of our ASAGAO survey covering a 26 arcmin(2) area in GOODS-S. In conjunction with the ALMA archival data, our sample consists of 45 ALMA sources with infrared luminosity (L-IR) range of similar to 10(11) - 10(13) L circle dot. To obtain an

average rest-frame far-infrared (FIR) profile, we perform individual measurements and careful stacking of the ALMA sources using the uv-visibility method that includes positional-uncertainty and smoothing-effect evaluations through Monte Carlo simulations. We find that our sample has an average FIR-wavelength Sersic index and effective radius of n(FIR) = 1.2 +/- 0.2 and R-e,R- FIR = 1.0-1.3 kpc, respectively, additionally with a point-source component at the center, indicative of the existence of active galactic nuclei. The average FIR profile agrees with a morphology of an exponential disk clearly distinguished from a de Vaucouleurs spheroidal profile (Sersic index of 4). We also examine the rest-frame optical Sersic index n(opt) and effective radius R-e,R-opt with deep Hubble Space Telescope (HST) images. Interestingly, we obtain n(opt) = 0.9 +/- 0.3 (similar or equal to n(FIR)) and R-e,R-opt = 3.2 +/- 0.6 kpc (> R-e,R-FIR), suggesting that the dusty disk-like structure is embedded within a larger stellar disk. The rest-frame UV and FIR data of HST and ALMA provide us with a radial profile of the total star formation rate (SFR), where the infrared SFR dominates over the UV SFR at the center. Under the assumption of a constant SFR, a compact stellar distribution in z similar to 1-2 compact quiescent galaxies (cQGs) is well reproduced, while a spheroidal stellar morphology of cQGs (n(opt) = 4) is not, suggestive of other important mechanism(s) such as dynamical dissipation.

第 147 条，共 248 条

Kinetic temperature of massive star-forming molecular clumps measured with formaldehyde III. The Orion molecular cloud 1

Tang, XD (Tang, X. D.); Henkel, C (Henkel, C.); Menten, KM (Menten, K. M.); Wyrowski, F (Wyrowski, F.); Brinkmann, N (Brinkmann, N.); Zheng, XW (Zheng, X. W.); Gong, Y (Gong, Y.); Lin, YX (Lin, Y. X.); Esimbek, J (Esimbek, J.); Zhou, JJ (Zhou, J. J.); Yuan, Y (Yuan, Y.); Li, DL (Li, D. L.); He, YX (He, Y. X.)

ASTRONOMY & ASTROPHYSICS

卷: 609 文献号: A16

We mapped the kinetic temperature structure of the Orion molecular cloud 1 (OMC-1) with para-H2CO(J(KaKc) = 3(03)-2(02), 3(22)- 2(21), and 3(21)-2(20)) using the APEX 12m telescope. This is compared with the temperatures derived from the ratio of the NH3 (2, 2)/(1, 1) inversion lines and the dust emission. Using the RADEX non-LTE model, we derive the gas kinetic temperature modeling the measured averaged line ratios of para-H(2)CO3(22)-2(21)/3(03)-2(02) and 3(21)-2(20)/3(03)-2(02). The gas kinetic temperatures derived from the para-H(2)COline ratios are warm, ranging from 30 to > 200K with an average of 62 +/- 2K at a spatial density of 105 cm(-3). These temperatures are higher than those obtained from NH3 (2, 2) /(1, 1) and CH3CCH(6-5) in the OMC-1 region. The gas kinetic temperatures derived from para-H2CO agree with those obtained from warm dust components measured in the mid infrared (MIR), which indicates that the para-H2CO(3-2) ratios trace dense and warm gas. The cold dust components measured in the far infrared (FIR) are consistent with those measured with NH3 (2, 2) /(1, 1) and the CH3CCH(6-5) line series. With dust at MIR wavelengths and para-H2CO(3-2) on one side, and dust at FIR wavelengths, NH3 (2, 2) /(1, 1), and CH3CCH(6-5) on the other, dust and gas temperatures appear to be equivalent in the dense gas (n(H-2) greater than or similar to 104 cm 3) of the OMC-1 region, but provide a bimodal distribution, one more directly related to star formation than the other. The non-thermal velocity dispersions of para-H2CO are positively correlated with the gas kinetic temperatures in regions of strong non-thermal motion (Mach number > greater than or similar to 2 : 5) of the OMC-1, implying that the higher temperature traced by para-H2CO is related to turbulence on a similar to 0.06 pc scale. Combining the temperature measurements with para-H2CO and NH3 (2, 2) /(1, 1) line ratios, we find direct evidence for the dense gas along the northern part of the OMC-1 10 km s(-1) filament heated by radiation from the central Orion nebula.

第 148 条，共 248 条

A First Look at BISTRO Observations of the rho Oph-A core

Kwon, J (Kwon, Jungmi); Doi, Y (Doi, Yasuo); Tamura, M (Tamura, Motohide); Matsumura, M (Matsumura, Masafumi); Pattle, K (Pattle, Kate); Berry, D (Berry, David); Sadavoy, S (Sadavoy, Sarah); Matthews, BC (Matthews, Brenda C.); Ward-Thompson, D (Ward-Thompson, Derek); Hasegawa, T (Hasegawa, Tetsuo); Furuya, RS (Furuya, Ray S.); Pon, A (Pon, Andy); Di Francesco, J (Di Francesco, James); Arzoumanian, D (Arzoumanian, Doris); Hayashi, SS (Hayashi, Saeko S.); Kawabata, KS (Kawabata, Koji S.); Onaka, T (Onaka, Takashi); Choi, M (Choi, Minho); Kang, M (Kang, Miju); Hoang, T (Hoang, Thiem); Lee, CW (Lee, Chang Won); Lee, SS (Lee, Sang-Sung); Liu, HL (Liu, Hong-Li); Liu, T (Liu, Tie); Inutsuka, S (Inutsuka, Shu-ichiro); Eswaraiah, C (Eswaraiah, Chakali); Bastien, P (Bastien, Pierre); Kwon, W (Kwon, Woojin); Lai, SP (Lai, Shih-Ping); Qiu, KP (Qiu, Keping); Coude, S (Coude, Simon); Franzmann, E (Franzmann, Erica); Friberg, P (Friberg, Per); Graves, SF (Graves, Sarah F.); Greaves, JS (Greaves, Jane S.); Houde, M (Houde, Martin); Johnstone, D (Johnstone, Doug); Kirk, JM (Kirk, Jason M.); Koch, PM (Koch, Patrick M.); Di Li, D (Li, Di); Parsons, H (Parsons, Harriet); Rao, R (Rao, Ramprasad); Rawlings, MG (Rawlings, Mark G.); Shinnaga, H (Shinnaga, Hiroko); van Loo, S (van Loo, Sven); Aso, Y (Aso, Yusuke); Byun, DY (Byun, Do-Young); Chen, HR (Chen, Huei-Ru); Chen, MCY (Chen, Mike C. -Y.); Chen, WP (Chen, Wen Ping); Ching, TC (Ching, Tao-Chung); Cho, J (Cho, Jungyeon); Chrysostomou, A (Chrysostomou, Antonio); Chung, EJ (Chung, Eun Jung); Drabek-Maunder, E (Drabek-Maunder, Emily); Eyres, SPS (Eyres, Stewart P. S.); Fiege, J (Fiege, Jason); Friesen, RK (Friesen, Rachel K.); Fuller, G (Fuller, Gary); Gledhill, T (Gledhill, Tim); Griffin, MJ (Griffin, Matt J.); Gu, Q (Gu, Qilao); Hatchell, J (Hatchell, Jennifer); Holland, W (Holland, Wayne); Inoue, T (Inoue, Tsuyoshi); Iwasaki, K (Iwasaki, Kazunari); Jeong, IG (Jeong, Il-Gyo); Kang, JH (Kang, Ji-hyun); Kang, SJ (Kang, Sung-ju); Kemper, F (Kemper, Francisca); Kim, G (Kim, Gwanjeong); Kim, J (Kim, Jongsoo); Kim, KT (Kim, Kee-Tae); Kim, KH (Kim, Kyoung Hee); Kim, MR (Kim, Mi-Ryang); Kim, S (Kim, Shinyoung); Lacaille, KM (Lacaille, Kevin M.); Lee, JE (Lee, Jeong-Eun); Li, DL (Li, Dalei); Li, HB (Li, Hua-bai); Liu, JH (Liu, Junhao); Liu, SY (Liu, Sheng-Yuan); Lyo, AR (Lyo, A-Ran); Mairs, S (Mairs, Steve); Moriarty-Schieven, GH (Moriarty-Schieven, Gerald H.); Nakamura, F (Nakamura, Fumitaka); Nakanishi, H (Nakanishi, Hiroyuki); Ohashi, N (Ohashi, Nagayoshi); Peretto, N (Peretto, Nicolas); Pyo, TS (Pyo, Tae-Soo); Qian, L (Qian, Lei); Retter, B (Retter, Brendan); Richer, J (Richer, John); Rigby, A (Rigby, Andrew); Robitaille, JF (Robitaille, Jean-Franois); Savini, G (Savini, Giorgio); Scaife, AMM (Scaife, Anna M. M.); Soam, A (Soam, Archana); Tang, YW (Tang, Ya-Wen); Tomisaka, K (Tomisaka, Kohji); Wang, HC (Wang, Hongchi); Wang, JW (Wang, Jia-Wei); Whitworth, AP (Whitworth, Anthony P.); Yen, HW (Yen, Hsi-Wei); Yoo, H (Yoo, Hyunju); Yuan, JH (Yuan,

Jinghua); Zhang, CP (Zhang, Chuan-Peng); Zhang, GY (Zhang, Guoyin); Zhou, JJ (Zhou, Jianjun); Zhu, L (Zhu, Lei); Andre, P (Andre, Philippe); Dowell, CD (Dowell, C. Darren); Falle, S (Falle, Sam); Tsukamoto, Y (Tsukamoto, Yusuke); Nakagawa, T (Nakagawa, Takao); Kanamori, Y (Kanamori, Yoshihiro); Kataoka, A (Kataoka, Akimasa); Kobayashi, MIN (Kobayashi, Masato I. N.); Nagata, T (Nagata, Tetsuya); Saito, H (Saito, Hiro); Seta, M (Seta, Masumichi); Zenko, T (Zenko, Tetsuya)
ASTROPHYSICAL JOURNAL
卷: 859 期: 1 文献号: 4
We present 850 mu m imaging polarimetry data of the rho Oph-A core taken with the Submillimeter Common-User Bolometer Array-2 (SCUBA-2) and its polarimeter (POL-2) as part of our ongoing survey project, B-fields In STar forming RegiOns (BISTRO). The polarization vectors are used to identify the orientation of the magnetic field projected on the plane of the sky at a resolution of 0.01 pc. We identify 10 subregions with distinct polarization fractions and angles in the 0.2 pc rho Oph-A core; some of them can be part of a coherent magnetic field structure in the rho Oph region. The results are consistent with previous observations of the brightest regions of rho Oph-A, where the degrees of polarization are at a level of a few percent, but our data reveal for the first time the magnetic field structures in the fainter regions surrounding the core where the degree of polarization is much higher (>5%). A comparison with previous near-infrared polarimetric data shows that there are several magnetic field components that are consistent at near-infrared and submillimeter wavelengths. Using the Davis-Chandrasekhar-Fermi method, we also derive magnetic field strengths in several subcore regions, which range from approximately 0.2 to 5 mG. We also find a correlation between the magnetic field orientations projected on the sky and the core centroid velocity components.

第 149 条，共 248 条

The Arizona Radio Observatory CO Mapping Survey of Galactic Molecular Clouds. VI. The Cep OB3 Cloud (Cepheus B and C) in CO J=2-1, (CO)-C-13 J=2-1, and CO J=3-2

Bieging, JH (Bieging, John H.); Patel, S (Patel, Saahil); Hofmann, R (Hofmann, Ryan); Peters, WL (Peters, William L.); Kainulainen, J (Kainulainen, Jouni); Zhang, MM (Zhang, Miaomiao); Stutz, AM (Stutz, Amelia M.)
ASTROPHYSICAL JOURNAL SUPPLEMENT SERIES
卷: 238 期: 2 文献号: 20
We present (1) new fully sampled maps of CO and (CO)-C-13 J = 2-1 emission and CO J = 3-2 emission toward the molecular clouds Cep B and C, associated with the Cep OB3 association; (2) a map of extinction, A(V), derived from IR colors of background stars; and (3) the distribution of young stellar objects (YSOs) over the same field as the molecular maps. An LTE analysis of the CO and (CO)-C-13. maps yields the distribution of molecular column densities and temperatures. Substantial variations are evident across the clouds; smaller subregions show correlations between molecular properties and dust extinction, consistent with a picture of outer photodissociation regions with a layer of CO-dark molecular gas, a CO self-shielded interior, and an inner cold dense region where CO is largely depleted onto grains. Comparing the distribution of YSOs with molecular gas surface density shows a power-law relation very similar in slope to that for the giant molecular cloud associated with the H II region Sh2-235 from a previous paper in this series that employed the same methodology. We note the presence of several compact, isolated CO emission sources in the J = 3-2 maps. The gas temperature and (CO)-C-13. velocity dispersion yield a map of the sonic Mach number, which varies across the cloud but always exceeds unity, confirming the pervasiveness of supersonic turbulence over length scales greater than or similar to 0.1 pc (the map resolution). We also compute a J = 2-1 CO X-factor that varies with position but is, on average, within. 20% of the Galactic average derived from CO J = 1-0 observations.

Galaxy formation and wide Field Sky Survey

第 150 条，共 248 条

A Machine-learning Method for Identifying Multiwavelength Counterparts of Submillimeter Galaxies: Training and Testing Using AS2UDS and ALESS

An, FX (An, Fang Xia); Stach, SM (Stach, S. M.); Smail, I (Smail, Ian); Swinbank, AM (Swinbank, A. M.); Almaini, O (Almaini, O.); Simpson, C (Simpson, C.); Hartley, W (Hartley, W.); Maltby, DT (Maltby, D. T.); Ivison, RJ (Ivison, R. J.); Arumugam, V (Arumugam, V.); Wardlow, JL (Wardlow, J. L.); Cooke, EA (Cooke, E. A.); Gullberg, B (Gullberg, B.); Thomson, AP (Thomson, A. P.); Chen, CC (Chen, Chian-Chou); Simpson, JM (Simpson, J. M.); Geach, JE (Geach, J. E.); Scott, D (Scott, D.); Dunlop, JS (Dunlop, J. S.); Farrah, D (Farrah, D.); van der Werf, P (van der Werf, P.); Blain, AW (Blain, A. W.); Conselice, C (Conselice, C.); Michalowski, M (Michalowski, M.); Chapman, SC (Chapman, S. C.); Coppin, KEK (Coppin, K. E. K.)
ASTROPHYSICAL JOURNAL
卷: 862 期: 2 文献号: 101
We describe the application of supervised machine-learning algorithms to identify the likely multiwavelength counterparts to submillimeter sources detected in panoramic, single-dish submillimeter surveys. As a training set, we employ a sample of 695 (S-870 mu m greater than or similar to 1 mJy) submillimeter galaxies (SMGs) with precise identifications from the ALMA follow-up of the SCUBA-2 Cosmology Legacy Survey's UKIDSS-UDS field (AS2UDS). We show that radio emission, near-/mid-infrared colors, photometric redshift, and absolute H-band magnitude are effective predictors that can distinguish SMGs from submillimeter-faint field galaxies. Our combined radio + machinelearning method is able to successfully recover similar to 85% of ALMA-identified SMGs that are detected in at least three bands from the ultraviolet to radio. We confirm the robustness of our method by dividing our training set into independent subsets and using these for training and testing, respectively, as well as applying our method to an independent sample of similar to 100 ALMA-identified SMGs from the ALMA/LABOCA ECDF-South Survey (ALESS). To further test our methodology, we stack the 870 mu m ALMA maps at the positions of those K-band galaxies that are classified as SMG counterparts by the machine learning but do not have a >4.3 sigma ALMA detection. The median peak flux density of these galaxies is

S-870 mu m, = (0.61 +/- 0.03) mJy, demonstrating that our method can recover faint and/or diffuse SMGs even when they are below the detection threshold of our ALMA observations. In future, we will apply this method to samples drawn from panoramic single-dish submillimeter surveys that currently lack interferometric follow-up observations to address science questions that can only be tackled with large statistical samples of SMGs.

第 151 条，共 248 条

大视场巡天望远镜探测器响应与滤光片优化分析

师冬冬郑宪忠赵海斌娄铮王海仁钱元刘伟姚大志

天文学报

DOI：10.15940/j.cnki.0001-5245.2018.03.001

大视场巡天望远镜(Wide Field Survey Telescope,WFST)是采用主焦式光学设计、2.5 m 口径、具备强大巡天能力的望远镜,可以开展大规模图像巡天,用于刻画银河系和近邻宇宙的组成和结构、普查太阳系天体和外部构成、开展时域天文监测等科学研究工作.结合大视场巡天望远镜光学系统的透过率、西藏阿里站址的大气透过率和冒纳凯阿台址的天光发射谱,比较不同电荷耦合器件(Charge Coupled Device,CCD)量子响应曲线、读出噪声和不同曝光时间情况下,不同类型天体在 u、g、r、i、z 和 w 波段的能谱响应,分析各个波段测光信噪比,优化确定 CCD 响应曲线和用于太阳系天体巡天的白光滤光片(w)设计.分析结果显示:蓝敏 CCD 对探测超新星等高能爆发暂现源有优势,但在 r、i、z 波段效率降低,从而降低这些波段的巡天探测灵敏度.光学宽带 CCD 响应曲线兼顾蓝端和红端能谱响应,在相同观测时间内,可以实现比蓝敏 CCD 更高的巡天灵敏度.采用宽带 CCD 响应曲线,结合估算的 WFST 系统光学成像效率及站址的天光和消光,计算给出了巡天观测对太阳系天体(G2V 恒星光谱)、椭圆星系(E)、漩涡星系(Sbc/Scd)、不规则星系(Im)、类星体、I 型和 II 型超新星的探测灵敏度.通过调节 w 波段的带宽和中心波长,可以实现对不同类型天体的能谱响应信噪比最大化.综合比较,确定 w 滤光片的优化设计波长范围为 367－795 nm.最后,计算给出了各波段长期巡天图像数据叠加的探测灵敏度随曝光时间的变化曲线

第 152 条，共 248 条

High-Speed Device-Independent Quantum Random Number Generation without a Detection Loophole

Liu, Y (Liu, Yang); Yuan, X (Yuan, Xiao); Li, MH (Li, Ming-Han); Zhang, WJ (Zhang, Weijun); Zhao, Q (Zhao, Qi); Zhong, JQ (Zhong, Jiaqiang); Cao, Y (Cao, Yuan); Li, YH (Li, Yu-Huai); Chen, LK (Chen, Luo-Kan); Li, H (Li, Hao); Peng, TY (Peng, Tianyi); Chen, YA (Chen, Yu-Ao); Peng, CZ (Peng, Cheng-Zhi); Shi, SC (Shi, Sheng-Cai); Wang, Z (Wang, Zhen); You, LX (You, Lixing); Ma, XF (Ma, Xiongfeng); Fan, JY (Fan, Jingyun); Zhang, Q (Zhang, Qiang); Pan, JW (Pan, Jian-Wei)

PHYSICAL REVIEW LETTERS

卷: 120 期: 1 文献号: 010503

Quantum mechanics provides the means of generating genuine randomness that is impossible with deterministic classical processes. Remarkably, the unpredictability of randomness can be certified in a manner that is independent of implementation devices. Here, we present an experimental study of device-independent quantum random number generation based on a detection-loophole-free Bell test with entangled photons. In the randomness analysis, without the independent identical distribution assumption, we consider the worst case scenario that the adversary launches the most powerful attacks against the quantum adversary. After considering statistical fluctuations and applying an 80 Gb x 45.6 Mb Toeplitz matrix hashing, we achieve a final random bit rate of 114 bits/s, with a failure probability less than 10(-5). This marks a critical step towards realistic applications in cryptography and fundamental physics tests.

第 153 条，共 248 条

Upgrading SCUBA-2 with a newly designed thermal filter stack

Cookson, JL (Cookson, Jamie L.); Bintley, D (Bintley, Dan); Li, SL (Li, Shaoliang); Ade, PAR (Ade, Peter A. R.); Sudiwala, R (Sudiwala, Rashmikant); Tucker, C (Tucker, Carole)

MILLIMETER, SUBMILLIMETER, AND FAR-INFRARED DETECTORS AND INSTRUMENTATION FOR ASTRONOMY IX

卷: 10708 文献号: 1070839

SCUBA-2 is a world leading wide field submillimeter camera on the JCMT with two, large format background limited TES arrays, which are used to image simultaneously in the 450 mu m and 850um atmospheric windows. SCUBA-2 has been producing excellent science for over 6 years however, as we reported previously, excess in-band power loading of the arrays is a concern. One possibility that we considered was that the currently installed hot-pressed filters at the 4K stage were being warmed significantly above 4K by incoming infrared radiation. In an attempt to reduce the power loading we cryogenically tested a new 60K filter stack that incorporated a redesigned thermal blocking filter. A direct comparison was then made to the performance of the existing 60K filter stack installed in SCUBA-2. We saw a tremendous improvement in the infrared rejection with the new design and proceeded to install the new filter stack into SCUBA-2.

In this paper, we describe the testing and installation of the new and improved design of thermal blocking filter into the instrument and report the resulting performance change based on data from the first 12 months of science operation with the new filters. We also present the combined filter bandpass profiles as measured in-situ with FTS-2.

会议名称: Conference on Millimeter, Submillimeter, and Far-Infrared Detectors and Instrumentation for Astronomy IX

会议日期: JUN 12-15, 2018

会议地点: Austin, TX

High – energy time-domain astronomy

第 154 条，共 248 条

Improved selection criteria for H II regions, based on IRAS sources

Yan, QZ (Yan, Qing-Zeng); Xu, Y (Xu, Ye); Walsh, AJ (Walsh, A. J.); Macquart, JP (Macquart, J. P.); MacLeod, GC (MacLeod, G. C.); Zhang, B (Zhang, Bo); Hancock, PJ (Hancock, P. J.); Chen, X (Chen, Xi); Tang, ZH (Tang, Zheng-Hong)

MONTHLY NOTICES OF THE ROYAL ASTRONOMICAL SOCIETY
卷: 476 期: 3 页: 3981-3990
We present new criteria for selecting HII regions from the Infrared Astronomical Satellite (IRAS) Point Source Catalogue (PSC), based on an HII region catalogue derived manually from the all-sky Wide-field Infrared Survey Explorer (WISE). The criteria are used to augment the number of HII region candidates in theMilkyWay. The criteria are defined by the linear decision boundary of two samples: IRAS point sources associated with known HII regions, which serve as the HII region sample, and IRAS point sources at high Galactic latitudes, which serve as the non-H II region sample. Amachine learning classifier, specifically a support vector machine, is used to determine the decision boundary. We investigate all combinations of four IRAS bands and suggest that the optimal criterion is log (F-60/F-12) >= (-0.19 x log (F-100/F-25) + 1.52), with detections at 60 and 100 mu m. This selects 3041 HII region candidates from the IRAS PSC. We find that IRAS HII region candidates show evidence of evolution on the two-colour diagram. Merging the WISE HII catalogue with IRAS HII region candidates, we estimate a lower limit of approximately 10 200 for the number of HII regions in the Milky Way.

第 155 条，共 248 条

ALMA twenty-six arcmin2 survey of GOODS-S at one millimeter (ASAGAO): Source catalog and number counts

Hatsukade, Bunyo，Kohno, Kotaro，Yamaguchi, Yuki.
Publications of the Astronomical Society of Japan
10.1093/pasj/psy104
We present the survey design, data reduction, construction of images, and source catalog of the Atacama Large Millimeter/submillimeter Array (ALMA) twenty-six arcmin^2 survey of GOODS-S at one-millimeter (ASAGAO). ASAGAO is a deep (1sigma ~ 61 uJy/beam for a 250 klambda-tapered map with a synthesized beam size of 0.51" x 0.45") and wide area (26 arcmin^2) survey on a contiguous field at 1.2 mm. By combining with ALMA archival data in the GOODS-South field, we obtained a deeper map in the same region (1sigma ~ 30 uJy/beam for a deep region with a 250 klambda-taper, and a synthesized beam size of 0.59" x 0.53"), providing the largest sample of sources (25 sources at >=5.0sigma, 45 sources at >=4.5sigma) among ALMA blank-field surveys to date. The number counts shows that 52(+11 -8)% of the extragalactic background light at 1.2 mm is resolved into discrete sources at S1.2m > 135 uJy. We create infrared (IR) luminosity functions (LFs) in the redshift range of z = 1-3 from the ASAGAO sources with KS-band counterparts.

第 156 条，共 248 条

The first CCD photometric study of the open cluster NGC 744

Wang, K (Wang, Kun); Deng, LC (Deng, Li-Cai); Luo, ZQ (Luo, Zhi-Quan); Yan, ZZ (Yan, Zheng-Zhou); Liu, QL (Liu, Qi-Li); Sun, JJ (Sun, Jin-Jiang); Zhou, Q (Zhou, Qiang)
RESEARCH IN ASTRONOMY AND ASTROPHYSICS
卷: 18 期: 11 文献号: 139
We present the first CCD photometric observations of open cluster NGC 744, as part of the 50BiN Open Cluster Survey. The color-magnitude diagrams of this cluster were derived from absolute BV RI photometry on a good photometric night. A brief isochrone fitting gives a distance modulus of (m- M)(v) = 11.58 +/- 0.2 and a reddening of E(B-V) = 0.35 +/- 0.05 with an age of log t = 8.30 +/- 0.05. By carefully examining the RV time-series data, we discovered four new variable stars in a 20' x 20' field around the cluster. We classified them as three eclipsing binary stars and one delta Scuti pulsating star, mainly based on the light-curve shape, the detected periods and the positions on the color-magnitude diagrams.

Gas distribution and Properties of the Milky Way

第 157 条，共 248 条

Performance of a 1.4 THz Twin-Slot Superconductivity Hot Electron Bolometer Mixer

Daowei Wang K.M. Zhou Yuan Ren
DOI: 10.1109/ICMMT.2018.8563642
Conference: 2018 International Conference on Microwave and Millimeter Wave Technology (ICMMT)
In this paper, the direct detection behaviors of a superconducting hot electron bolometer integrated with a log spiral antenna are investigated by using Fourier Transform Spectrometer (FTS). We find the response of the bolometer to a modulated signal can be detected by a lock-in amplifier not only from the DC bias current, but also from the output noise power at the IF port of the HEB.

第 158 条，共 248 条

Sparse Millimeter-Wave InSAR Imaging Approach Based on MC

Yilong Zhang，Yuehua Li，Jianfei Chen
IEEE Geoscience and Remote Sensing Letters
High-resolution millimetre wave images of contiguous targets often suffer from the influence of sidelobe artefacts, partial correlation between targets and so on. Owing to the characteristics of near-field synthetic aperture imaging radiometers [such as the changing point spread function (PSF) and slender sideline], the existing CLEAN algorithms are unsuitable for near-field synthetic aperture.

Millimeter & Sub-Millimeter Wave Laboratory

第 159 条，共 248 条

Terahertz Superconducting Radiometric Spectrometer in Tibet for Atmospheric Science

S. Li, Q. J. Yao, D. Liu, W. Y. Duan, K. Zhang, J. D. Jin, Z. H. Lin, F. Wu, J. P. Yang and W. Miao,
Terahertz superconducting radiometric spectrometer (TSRS), as one of seven instruments of the atmospheric profiling synthetic observation system (APSOS) project, was completed in the middle
J. Infrared, Millimeter, Terahertz Waves, pp. 1-12, 2018.

第 160 条，共 248 条

Sparse Millimeter-Wave InSAR Imaging Approach Based on MC

Y. L. Zhang, Y. H. Li, J. F. Chen, S. Shahir and S. Safavi-Naeini,
High-resolution millimetre wave images of contiguous targets often suffer from the influence of sidelobe artefacts, partial correlation between targets and so on. Owing to the characteristics of near-field synthetic aperture imaging radiometers [such as the changing point spread function (PSF) and slender sideline], the existing CLEAN algorithms are unsuitable for near-field synthetic aperture
IEEE Geosci. Rem. Sens. Lett., vol. 15, pp. 714-718, 2018.

第 161 条，共 248 条

Verification of the transparency of polystyrene multi-layer insulation using terahertz time domain spectroscopy

B. W. Fan, Q. Shi and S. C. Shi,
The effects of layer thickness on the compatibility between polycarbonate (PC) and polystyrene (PS) and physical properties of PC/PS multilayered film via nanolayer coextrusion are studied. The morphology of multilayered structure is observed using a scanning electron microscope. This multilayered structure may have a negative impact on the transparency, but it can improve the water resistance and heat resistance of film. To characterize the compatibility between PC and PS, differential scanning calorimetry is used to measure the glass transition temperature. The compatibility is found to be improved with the decrease of layer thickness. Therefore, the viscosity of multilayered film is also reduced with the decrease of layer thickness. In addition, the multilayered structure can improve the tensile strength with the increase of layer numbers. Because of the complete and continuous layer structure of PC, the PC/PS multilayered film can retain its mechanical strength at the temperature above Tg of PS.

in The 9th International Symposium on Ultrafast Phenomena and Terahertz Waves (ISUPTW 2018), 2018, p. WI15.

第 162 条，共 248 条

Terahertz Atmospheric Transmission Measured at Ali with a Fourier Transform Spectrometer

W. Miao, Z. H. Lin, S. Li, M. Yao, B. W. Fan, Y. Geng, S. L. Li, Q. J. Yao and S. C. Shi,
The terahertz (THz) and FIR band is a frequency regime to be fully explored in astronomy. However, water vapor renders the terrestrial atmosphere opaque to this band over nearly all of the Earth's surface. Dome A in Antarctic – the site for China's Antarctic Observatory, with an altitude of 4093 m and temperature below -80 Celsius degree in winter, may offer the best possible access for ground-based astronomical observations in the THz and FIR band. We recently carried out measurements of atmospheric radiation from Dome A spanning the entire water vapor pure rotation band from 20 μm to 350 μm wavelength by an unmanned Fourier transform spectrometer (FTS). Our measurements expose atmospheric windows having significant transmission throughout this band. This talk will firstly introduce our FTS measurement results from Dome A, and then the latest development of superconducting mixers and detectors for the DATE5 telescope proposed to build at China's Antarctic Observatory.
in Fourier Transform Spectroscopy, 2018, p. FT3B. 3.

第 163 条，共 248 条

A Fully Integrated Heterodyne Receiver Based on a Hot Electron Bolometer Mixer and a Quantum Cascade Laser

W. Miao, H. Gao, Z. Lou, J. Hu, W. Zhang, Y. Ren, K. M. Zhou, S. C. Shi, H. Li, J. C. Cao and D. Yan,
We report on a very compact heterodyne receiver by integrating a superconducting NbN hot electron bolometer (HEB) mixer and a semi-insulating surface-plasmon quantum cascade laser (QCL) operating at 2.5 THz as local oscillator in a single block. To ensure effective pumping of the HEB mixer, the QCL's beam is collimated with a parabolic mirror that is integrated in the block too. After the collimation, the beam coupling efficiency between the HEB mixer and the QCL reaches approximately 0.9 and the superconducting HEB mixer can be easily pumped by the QCL. We then measured the receiver noise temperature of the integrated HEB/QCL receiver with a vacuum experimental setup. The lowest uncorrected receiver noise temperature is found to be about 750 K at 2.5 THz.

presented at the 29th IEEE International Symposium on Space THz Technology (ISSTT2018), Pasadena, 2018.

第 164 条，共 248 条

Characterization of a graphene-based terahertz hot-electron bolometer

H. Gao, W. Miao, Z. Wang, W. Zhang, Y. Geng, S. C. Shi, C. Yu, Z. He, Q. Liu and F. Z H,

In this paper, we present the development of a graphene-based hot electron bolometer with Johnson noise readout. The bolometer is a graphene microbridge connected to a log spiral antenna

in Infrared, Millimeter-Wave, and Terahertz Technologies V, 2018, p. 108260X.

第 165 条，共 248 条

High Sensitivity Terahertz Detection Module

K. Zhang, S. C. Shi, Q. J. Yao, J. Li, W. Zhang, Z. H. Lin, Z. Lou, W. Miao, D. Liu and R. Q. Mao,
High Sensitivity Terahertz Detection Module (HSTDM) is one of the backend modules planned for the Chinese Space Station Telescope. The HSTDM is a 0.41~0.51THz high sensitivity, high frequency resolution niobium nitride (NbN) SIS (Superconductor-Insulator-Superconductor) receiver system operating in a temperature range of 10K. The HSTDM will be used to achieve dual science tasks on terahertz astronomical and atmospheric observations from

space, while demonstrating the high-energy-gap NbN superconducting mixer technology and terahertz signal source technology in space. In this paper, the HSTDM project and system are presented.
in 2018 International Conference on Microwave and Millimeter Wave Technology (ICMMT), 2018, pp. 1-3.

第 166 条，共 248 条

Characterization of NB and TiN superconducting CPW lines with thru-line calibration method

W. T. Lv, J. Hu, J. P. Yang, Z. Wang and S. C. Shi,
A superconducting sampling measurement system is a highly useful tool for analyzing ultrahigh speed electrical signals in cryogenic environments, due to a time resolution at ps levels with low current levels of /spl mu/A. The digitizing sampling system is composed of a Josephson sampling circuit, digital delay line, feedback signal detection circuit and a computer. The Josephson sampling circuit is designed for ETL's Nb-AlO/sub x/-Nb junction technology. A TDR measurement method using a CPW flip-chip bonding technique is proposed. The theoretical spatial resolution is estimated to reach around a hundred /spl mu/m.
in Infrared, Millimeter-Wave, and Terahertz Technologies V, 2018, p. 108260S.

第 167 条，共 248 条

The influence of Nb and Ti interface on DC characteristics of superconducting titanium transition edge sensors

Y. Geng, W. Zhang, Z. Wang, J. Q. Zhong, W. Miao, Q. J. Yao and S. C. Shi,
TESs are attractive in quantum optics and quantum information experiments owing to high efficiency and photon number resolving capability. We present the DC characteristics of TESs with different overlapping area between Ti microbridge and Nb leads.

in The 9th International Symposium on Ultrafast Phenomena and Terahertz Waves (ISUPTW 2018), 2018, p. ThB4.

第 168 条，共 248 条

Dependence of Noise Temperature of Superconducting HEB Mixers on Frequency and Bath Temperature

K. M. Zhou, D. W. Wang, W. Miao, W. Zhang and S. C. Shi,
Abstract In this paper, the noise temperature and IF bandwidth of a 1.4 THz twin-slot antenna coupled NbN superconducting HEB mixer are thoroughly investigated. The RF noise and conversion gain of the HEB mixer have been measured and analyzed. An anti-reflection coating has been applied on the elliptical lens to reduce the RF noise, the measured lowest noise temperature (450 K) achieves state-of-the-art sensitivity at 1.3 THz. The measured IF noise bandwidth is about 3 GHz, which is sufficiently large for some astronomical applications.
in 2018 International Conference on Microwave and Millimeter Wave Technology (ICMMT), 2018, pp. 1-3.

第 169 条，共 248 条

Performance of a 1.4 THz Twin-Slot Superconductivity Hot Electron Bolometer Mixer

D. W. Wang, K. M. Zhou, Y. Ren, W. Miao, W. Zhang and S. C. Shi,

In order to improve the response performance of mid-infrared detectors, we designed and fabricated a superconducting hot electron bolometer mixer (HEBM) with a mid-infrared twin slot antenna. The design frequency was 61.3 THz, and the HEBs were formed as a superconducting strip with Au antennas and electrodes. Here, the superconductivity of the Nb/NbN layer under the Au electrodes was suppressed by a Ni (1.8 nm) thin film. For evaluating the mid-infrared HEBM properties, measurement setup without beam splitter was constructed. In this setup, local oscillator power was applied directly to the HEBM, and we confirmed that the critical current of the HEB can be reduced to be almost zero by the LO irradiation. The HEBM responses with clear polarization dependencies were also observed.

in 2018 International Conference on Microwave and Millimeter Wave Technology (ICMMT), 2018, pp. 1-3.

第 170 条，共 248 条

Near-field measurements of the terahertz superconducting spectrometer for atmospheric observation

Jie Hu, Sheng Li , Chuan Su
The optical verification of a terahertz superconducting spectrometer (TSR) featured withsuperconducting-insulator-superconducting (SIS) receivers developed at Purple Mountain Observatory (PMO) foratmospheric profiling synthetic observation system project (APSOS) has been presented. Near-fields of TSR at 230GHz and 280 GHz have been measured and far-fields are derived. The misalignment of the optics at 280 GHz is analysed in detail by physical optics (PO)

Telescope Technology Laboratory

第 171 条，共 248 条

Analysis of a discrete-layout bimorph disk elements piezoelectric deformable mirror

Wang, HR (Wang, Hairen); Chen, ZG (Chen, Ziguang); Yang, SF (Yang, Shengfeng); Hu, L (Hu, Lin); Hu, M (Hu, Ming)
JOURNAL OF ASTRONOMICAL TELESCOPES INSTRUMENTS AND SYSTEMS
卷: 4 期: 2 文献号: 029001
We introduce a discrete-layout bimorph disk elements piezoelectric deformable mirror (DBDEPDM), driven by the circular flexural-mode piezoelectric actuators. We formulated an electromechanical model for analyzing the performance of the new deformable mirror. As a numerical example, a 21-actuators DBDEPDM with an aperture of 165 mm was modeled. The presented results demonstrate that the DBDEPDM has a stroke larger than 10 mu m and the resonance frequency is 4.456 kHz. Compared with the

conventional piezoelectric deformable mirrors, the DBDEPDM has a larger stroke, higher resonance frequency, and provides higher spatial resolution due to the circular shape of its actuators. Moreover, numerical simulations of influence functions on the model are provided. (C) 2018 Society of Photo-Optical Instrumentation Engineers (SPIE)

第 172 条，共 248 条

Research on the optimization of a bimorph piezoelectric deformable mirror based on zeroth-order method

Hairen Wang，Lin Hu

DOI： 10.1117/12.2231590

The deformable mirror adjusts the mirror surface shape to compensate the wavefront error in the adaptive optics system. Recently, the adaptive optics has been widely used in many applications, such as astronomical telescopes, high power laser systems, etc. These applications require large diameter deformable mirrors with large stroke, high speed and low cost. Thus, the bimorph piezoelectric deformable mirror, which is a good match for the applications, has attracted more and more attentions. In this paper, we use zeroth-order optimization method to optimize the physical parameters of a bimorph piezoelectric deformable mirror that consists of a metal reflective layer deposited on the top of a slim piezoelectric ceramic surface layer. The electrodes are deposited on the bottom of the piezoelectric ceramic layer. The physical parameters to be optimized include the optimal thickness ratio between the piezoelectric layer and reflective layer, inter-electrode distance, and so on. A few reasonable designs are obtained by a comparative study presented for three geometries of electrodes

第 173 条，共 248 条

南极 5 m 太赫兹望远镜指向与调焦校准精度分析

康浩然左营喜娄铮何茜茹

天文学报

指向校准与副面调焦是天线测量的重要组成部分,对射电望远镜实际的观测性能有重要影响.根据南极 5 m 太赫兹望远镜(DATE5)指向精度和离焦增益损失的指标要求,计算得到了指向校准与副面调焦观测过程中对信噪比的要求,并以此为依据选取了若干可行的候选校准源,包括太阳系行星和超致密电离氢区.分析了大气吸收和校准源角直径对测量精度的影响.仿真分析结果表明:望远镜在南极工作时,这些校准源在一定的高度角范围内可以提供足够强的流量密度,用来验证预先建立的太赫兹和光学望远镜两光轴指向偏差模型以及副面调焦模型.

第 174 条，共 248 条

Zhou Tao; Ye Zhoujun; Shi Yaohui; Liang Yanmin; Hao Xufeng; Qian Yuan

Thermal distortion for honeycomb sandwich construction rigid reflector of satellite antenna

Acta Materiae Compositae Sinica
卷: 35 期: 8 页: 2065-2073

To explore the main self-structure factors affecting the thermal distortion of rigid antenna reflector in orbit,a spaceborne honeycomb sandwich structure model with a diameter of 1.2mwas analyzed.Firstly,by altering the skin material,the thickness of adhesive,the property include stiffness and coefficient of thermal expansion (CTE)of honeycomb,a finite element simulation software was used to calculate the root mean square(RMS)of the thermal deformation of the reflector when the ambient temperature changes from 20℃to-80℃.Furthermore,the causes of each factor were analyzed.Secondly,two typical honeycomb sandwich structure reflectors of M55Jand T300skin materials were prepared by autoclave molding process so as to validate simulation results.The results indicate that the thermal deformation of the M55J skin material reflector is smaller than that of the T300.In addition, there is a linear relationship between the thermal distortion and the thickness of the adhesive,the thinner the later, the smaller the former.When the thickness of the adhesive layer is constant,the thermal deformation of the honeycomb is the dominant factor.The effect of the skin stiffness on the thermal deformation of honeycomb is obvious as the increasment of the stiffness value is 2times.Moreover,when the normal CTE of honeycomb is changed by 11 times,the relative increment of thermal deformation is more than 80%.The thermal distortions of the two typical reflectors were measured as the environment temperature changed from 20℃to-80℃.The difference of the thermal distortion between simulation and testing is 15.7%and 15.2%,respectively,which proves the simulation results are reliable.By optimizing the corresponding parameters can provide reference for the design of spaceborne antenna reflector.

第 175 条，共 248 条

Development of a compact readout system for optical CCD in Higashi-Hiroshima Observatory

Liu, W (Liu, Wei); Sako, S (Sako, Shigeyuki); Kawabata, K (Kawabata, Koji); Shi, SC (Shi, Sheng-Cai); Yoshida, M (Yoshida, Michitoshi); Utsumi, Y (Utsumi, Yousuke)

HIGH ENERGY, OPTICAL, AND INFRARED DETECTORS FOR ASTRONOMY VIII
卷: 10709 文献号: 107091X

We developed a new CCD readout system for the Kanata 1.5m telescope in Higashi-Hiroshima Astronomical Observatory, Hiroshima University, Japan, based on the system originally developed by the Kiso Array Controller (KAC) project. In this development we aim at reducing the size and the cost of the system. The system consists of CCD drive circuit, three-order low-pass filters, differential input A/D converter, FPGA, LVDC board, and can be operated by Linux host. We report the current design and performances of this system, and the future work as well. This readout system will be easily applicable to many other astronomical instruments.

会议名称: Conference on High Energy, Optical, and Infrared Detectors for Astronomy VIII
会议日期: JUN 10-13, 2018

第 176 条，共 248 条

A comparative study of the thermal performance of primary mirror at the four typical sites

Wang, HR (Wang, Hairen); Cheng, JQ (Cheng, Jingquan); Lou, Z (Lou, Zheng); Liang, M (Liang, Ming); Zheng, XZ (Zheng, Xianzhong); Zuo, YX (Zuo, Yingxi); Yang, J (Yang, Ji)

OPTIK
卷: 174 页: 727-738
We propose a heat dissipation model to assess whether the material and thickness of the primary mirror of a telescope design exceed the upper constraint of the requirement in terms of the four typical sites: Dome A of Antarctica, Ali of Tibet, Mauna Kea of Hawaii and Chajnantor of Chile. It accounts for thermal conduction, heat convection, and radiation heat transfer whose effective sky temperature depends on the ambient air temperature, vapor pressure, and relative humidity. In addition, the values of the heat convection coefficient, sharply decreasing due to the low atmospheric pressure, are considered. We apply the model to analyze the thermal performance of a 2.5 m primary mirror of a wide field survey telescope (WFST). Under the conditions of the four typical sites in the world, a comparative study of WFST for two thicknesses of the primary mirror is presented via steady thermal analysis and transient thermal analysis using the proposed model. The results reveal that all RMS errors on the mirror surface of primary mirrors are smaller than 5 nm, which fulfill the performance requirements of WFST, and demonstrate that the proposed model is useful for evaluating the heat dissipation of the primary mirror on those sites.

第 177 条，共 248 条

The TOP-SCOPE Survey of Planck Galactic Cold Clumps: Survey Overview and Results of an Exemplar Source, PGCC G26.53+0.17

Liu, T (Liu, Tie); Kim, KT (Kim, Kee-Tae); Juvela, M (Juvela, Mika); Wang, K (Wang, Ke); Tatematsu, K (Tatematsu, Ken'ichi); Di Francesco, J (Di Francesco, James); Liu, SY (Liu, Sheng-Yuan); Wu, YF (Wu, Yuefang); Thompson, M (Thompson, Mark); Fuller, G (Fuller, Gary); Eden, D (Eden, David); Li, D (Li, Di); Ristorcelli, I (Ristorcelli, I.); Kang, SJ (Kang, Sung-ju); Lin, YX (Lin, Yuxin); Johnstone, D (Johnstone, D.); He, JH (He, J. H.); Koch, PM (Koch, P. M.); Sanhueza, P (Sanhueza, Patricio); Qin, SL (Qin, Sheng-Li); Zhang, Q (Zhang, Q.); Hirano, N (Hirano, N.); Goldsmith, PF (Goldsmith, Paul F.); Evans, NJ (Evans, Neal J., II); White, GJ (White, Glenn J.); Choi, M (Choi, Minho); Lee, CW (Lee, Chang Won); Toth, LV (Toth, L. V.); Mairs, S (Mairs, Steve); Yi, HW (Yi, H. -W.); Tang, MY (Tang, Mengyao); Soam, A (Soam, Archana); Peretto, N (Peretto, N.); Samal, MR (Samal, Manash R.); Fich, M (Fich, Michel); Parsons, H (Parsons, Harriet); Yuan, JH (Yuan, Jinghua); Zhang, CP (Zhang, Chuan-Peng); Malinen, J (Malinen, Johanna); Bendo, GJ (Bendo, George J.); Rivera-Ingraham, A (Rivera-Ingraham, A.); Liu, HL (Liu, Hong-Li); Wouterloot, J (Wouterloot, Jan); Li, PS (Li, Pak Shing); Qian, L (Qian, Lei); Rawlings, J (Rawlings, Jonathan); Rawlings, MG (Rawlings, Mark G.); Feng, SY (Feng, Siyi); Aikawa, Y (Aikawa, Yuri); Akhter, S (Akhter, S.); Alina, D (Alina, Dana); Bell, G (Bell, Graham); Bernard, JP (Bernard, J. -P.); Blain, A (Blain, Andrew); Bogner, R (Bogner, Rebeka); Bronfman, L (Bronfman, L.); Byun, DY (Byun, D. -Y.); Chapman, S (Chapman, Scott); Chen, HR (Chen, Huei-Ru); Chen, M (Chen, M.); Chen, WP (Chen, Wen-Ping); Chen, X (Chen, X.); Chen, XP (Chen, Xuepeng); Chrysostomou, A (Chrysostomou, A.); Cosentino, G (Cosentino, Giuliana); Cunningham, MR (Cunningham, M. R.); Demyk, K (Demyk, K.); Drabek-Maunder, E (Drabek-Maunder, Emily); Doi, Y (Doi, Yasuo); Eswaraiah, C (Eswaraiah, C.); Falgarone, E (Falgarone, Edith); Feher, O (Feher, O.); Fraser, H (Fraser, Helen); Friberg, P (Friberg, Per); Garay, G (Garay, G.); Ge, JX (Ge, J. X.); Gear, WK (Gear, W. K.); Greaves, J (Greaves, Jane); Guan, X (Guan, X.); Harvey-Smith, L (Harvey-Smith, Lisa); Hasegawa, T (Hasegawa, Tetsuo); Hatchell, J (Hatchell, J.); He, YX (He, Yuxin); Henkel, C (Henkel, C.); Hirota, T (Hirota, T.); Holland, W (Holland, W.); Hughes, A (Hughes, A.); Jarken, E (Jarken, E.); Ji, TG (Ji, Tae-Geun); Jimenez-Serra, I (Jimenez-Serra, Izaskun); Kang, MJ (Kang, Miju); Kawabata, KS (Kawabata, Koji S.); Kim, G (Kim, Gwanjeong); Kim, J (Kim, Jungha); Kim, J (Kim, Jongsoo); Kim, S (Kim, Shinyoung); Koo, BC (Koo, B. -C.); Kwon, W (Kwon, Woojin); Kuan, YJ (Kuan, Yi-Jehng); Lacaille, KM (Lacaille, K. M.); Lai, SP (Lai, Shih-Ping); Lee, CF (Lee, C. F.); Lee, JE (Lee, J. -E.); Lee, YU (Lee, Y. -U.); Li, DL (Li, Dalei); Li, HB (Li, Hua-Bai); Lo, N (Lo, N.); Lopez, JAP (Lopez, John A. P.); Lu, X (Lu, Xing); Lyo, AR (Lyo, A-Ran); Mardones, D (Mardones, D.); Marston, A (Marston, A.); McGehee, P (McGehee, P.); Meng, F (Meng, F.); Montier, L (Montier, L.); Montillaud, J (Montillaud, Julien); Moore, T (Moore, T.); Morata, O (Morata, O.); Moriarty-Schieven, GH (Moriarty-Schieven, Gerald H.); Ohashi, S (Ohashi, S.); Pak, S (Pak, Soojong); Park, G (Park, Geumsook); Paladini, R (Paladini, R.); Pattle, KM (Pattle, Kate M.); Pech, G (Pech, Gerardo); Pelkonen, VM (Pelkonen, V. -M.); Qiu, K (Qiu, K.); Ren, ZY (Ren, Zhi-Yuan); Richer, J (Richer, John); Saito, M (Saito, M.); Sakai, T (Sakai, Takeshi); Shang, H (Shang, H.); Shinnaga, H (Shinnaga, Hiroko); Stamatellos, D (Stamatellos, Dimitris); Tang, YW (Tang, Y. -W.); Traficante, A (Traficante, Alessio); Vastel, C (Vastel, Charlotte); Viti, S (Viti, S.); Walsh, A (Walsh, Andrew); Wang, BR (Wang, Bingru); Wang, HC (Wang, Hongchi); Wang, JZ (Wang, Junzhi); Ward-Thompson, D (Ward-Thompson, D.); Whitworth, A (Whitworth, Anthony); Xu, Y (Xu, Ye); Yang, J (Yang, J.); Yang, YL (Yang, Yao-Lun); Yuan, LX (Yuan, Lixia); Zavagno, A (Zavagno, A.); Zhang, GY (Zhang, Guoyin); Zhang, HW (Zhang, H. -W.); Zhou, CL (Zhou, Chenlin); Zhou, JJ (Zhou, Jianjun); Zhu, L (Zhu, Lei); Zuo, P (Zuo, Pei); Zhang, C (Zhang, Chao)
ASTROPHYSICAL JOURNAL SUPPLEMENT SERIES
卷: 234 期: 2 文献号: 28
The low dust temperatures (< 14 K) of Planck Galactic cold clumps (PGCCs) make them ideal targets to probe the initial conditions and very early phase of star formation. "TOP-SCOPE" is a joint survey program targeting similar to 2000 PGCCs in J = 1-0 transitions of CO isotopologues and similar to 1000 PGCCs in 850 mu m continuum emission. The objective of the "TOP-SCOPE" survey and the joint surveys (SMT 10 m, KVN 21 m, and NRO 45 m) is to statistically study the initial conditions occurring during star formation and the evolution of molecular clouds, across a wide range of environments. The observations, data analysis, and example science cases for these surveys are introduced with an exemplar source, PGCC G26.53+0.17 (G26), which is a filamentary infrared dark cloud (IRDC). The total mass, length, and mean line mass (M/L) of the G26 filament are similar to 6200 M-circle dot, similar to 12 pc, and similar to 500 M-circle dot pc(-1), respectively. Ten massive clumps, including eight starless ones, are found along the filament. The most massive clump as a whole may still be in global collapse, while its denser part seems to be undergoing expansion owing to outflow feedback. The fragmentation in the G26 filament from cloud scale to clump scale is in agreement with gravitational fragmentation of an isothermal, nonmagnetized, and turbulent supported cylinder. A bimodal behavior in dust emissivity spectral index (beta) distribution is found in G26, suggesting grain growth along the filament. The G26 filament may be formed owing to large-scale compression flows evidenced by the temperature and velocity gradients across its natal cloud.

Delingha millimeter wave Observation Station

第 178 条，共 248 条

A comparison of the local spiral structure from Gaia DR2 and VLBI maser parallaxes

Xu, Y (Xu, Y.); Bian, SB (Bian, S. B.); Reid, MJ (Reid, M. J.); Li, JJ (Li, J. J.); Zhang, B (Zhang, B.); Yan, QZ (Yan, Q. Z.); Dame, TM (Dame, T. M.); Menten, KM (Menten, K. M.); He, ZH (He, Z. H.); Liao, SL (Liao, S. L.); Tang, ZH (Tang, Z. H.)
ASTRONOMY & ASTROPHYSICS
卷: 616 文献号: L15
Context. The Gaia mission has released the second data set (Gaia DR2), which contains parallaxes and proper motions for a large number of massive, young stars.
Aims. We investigate the spiral structure in the solar neighborhood revealed by Gaia DR2 and compare it with that depicted by VLBI maser parallaxes.
Methods. We examined three samples with different constraints on parallax uncertainty and distance errors and stellar spectral types: (1) all OB stars with parallax errors of less than 10%; (2) only O-type stars with 0.1 mas errors imposed and with parallax distance errors of less than 0.2 kpc; and (3) only O-type stars with 0.05 mas errors imposed and with parallax distance errors of less than 0.3 kpc.
Results. In spite of the significant distance uncertainties for stars in DR2 beyond 1.4 kpc, the spiral structure in the solar neighborhood demonstrated by Gaia agrees well with that illustrated by VLBI maser results. The O-type stars available from DR2 extend the spiral arm models determined from VLBI maser parallaxes into the fourth Galactic quadrant, and suggest the existence of a new spur between the Local and Sagittarius arms.

第 179 条，共 248 条

德令哈 13.7m 望远镜谱线 OTF 观测系统

孙继先 逯登荣 杨戟 苏扬 张少博 周鑫 林镇辉
天文学报
紫金山天文台研制的毫米波段多波束超导成像频谱接收机(简称超导成像频谱仪)于 2010 年底安装到 13.7 m 望远镜上.为发挥超导成像频谱仪的观测能力,紫金山天文台研发了基于多波束接收机的快速高效巡天的 OTF(On-The-Fly)观测方法,在国际上首次提出并运用了"隔行扫描"的 OTF 扫描方法,对该方法进行了系统的测试和验证,并做了观测参数的优化.研发了"OTF 观测星表生成器"软件,该软件提供参考点查找、观测时间估算、rms(root mean square)估算、最佳观测时段选择等功能.研发了 OTF 数据预处理软件,该软件具有坏数据剔除、数据修正功能,并能够结合 GILDS 软件完成数据网格化(Gridding)处理.通过实际观测测试,观测结果与美国五大学射电天文台(Five College Radio Astronomy Observatory,FCRAO)观测相符.该系统 2011 年用于 13.7 m 望远镜谱线成图观测,在银河画卷项目观测和其他课题成图观测中得到广泛的应用,取得了很好的观测结果,验证了该系统的有效性.

第 180 条，共 248 条

Gas kinematics and star formation in the filamentary molecular cloud G47.06+0.26

Xu, JL (Xu, Jin-Long); Xu, Y (Xu, Ye); Zhang, CP (Zhang, Chuan-Peng); Liu, XL (Liu, Xiao-Lan); Yu, NP (Yu, Naiping); Ning, CC (Ning, Chang-Chun); Ju, BG (Ju, Bing-Gang)
ASTRONOMY & ASTROPHYSICS
卷: 609 文献号: A43
Aims. We performed a multi-wavelength study toward the filamentary cloud G47.06 + 0.26 to investigate the gas kinematics and star formation.
Methods. We present the (CO)-C-12 (J = 1-0), (CO)-C-13 (J = 1-0) and (CO)-O-18 (J = 1-0) observations of G47.06 + 0.26 obtained with the Purple Mountain Observation (PMO) 13.7 m radio telescope to investigate the detailed kinematics of the filament. Radio continuum and infrared archival data were obtained from the NRAO VLA Sky Survey (NVSS), the APEX Telescope Large Area Survey of the Galaxy (ATLASGAL), the Galactic Legacy Infrared Mid-Plane Survey Extraordinaire (GLIMPSE) survey, and the Multi-band Imaging Photometer Survey of the Galaxy (MIPSGAL). To trace massive clumps and extract young stellar objects in G47.06 + 0.26, we used the BGPS catalog v2.0 and the GLIMPSE I catalog, respectively.
Results. The (CO)-C-12 (J = 1-0) and (CO)-C-13 (J = 1-0) emission of G47.06 + 0.26 appear to show a filamentary structure. The filament extends about 45' (58.1 pc) along the east-west direction. The mean width is about 6.8 pc, as traced by the (CO)-C-13 (J = 1 0) emission. G47.06 + 0.26 has a linear mass density of similar to 361.5 M-circle dot pc(-1). The external pressure (due to neighboring bubbles and HII regions) may help preventing the filament from dispersing under the effects of turbulence. From the velocity-field map, we discern a velocity gradient perpendicular to G47.06 + 0.26. From the Bolocam Galactic Plane Survey (BGPS) catalog, we found nine BGPS sources in G47.06 + 0.26, that appear to these sources have sufficient mass to form massive stars. We obtained that the clump formation efficiency (CFE) is similar to 18% in the filament. Four infrared bubbles were found to be located in, and adjacent to, G47.06 + 0.26. Particularly, infrared bubble N98 shows a cometary structure. CO molecular gas adjacent to N98 also shows a very intense emission. HII regions associated with infrared bubbles can inject the energy to surrounding gas. We calculated the kinetic energy, ionization energy, and thermal energy of two HII regions in G47.06 + 0.26. From the GLIMPSE I catalog, we selected some Class I sources with an age of similar to 10(5) yr, which are clustered along the filament. The feedback from the HII regions may cause the formation of a new generation of stars in filament G47.06 + 0.26.

第 181 条，共 248 条

The spiral structure of the Milky Way

Xu, Y (Xu, Ye); Hou, LG (Hou, Li-Gang); Wu, YW (Wu, Yuan-Wei)
RESEARCH IN ASTRONOMY AND ASTROPHYSICS
卷: 18 期: 12 文献号: 146
The morphology and kinematics of the spiral structure of the Milky Way are long-standing problems in astrophysics. In this review we firstly summarize variousmethodswith

different tracers used to solve this puzzle. The astrometry of Galactic sources is gradually alleviating this difficult situation caused mainly by large distance uncertainties, as we can currently obtain accurate parallaxes (a few mu as) and proper motions (approximate to 1 kms(-1)) by using Very Long Baseline Interferometry (VLBI). On the other hand, the Gaia mission is providing the largest, uniform sample of parallaxes for O-type stars in the entire Milky Way. Based upon the VLBI maser and Gaia O-star parallax measurements, nearby spiral structures of the Perseus, Local, Sagittarius and Scutum Arms are determined in unprecedented detail. Meanwhile, we estimate fundamental Galactic parameters of the distance to the Galactic center, R-0, to be 8.35 +/- 0.18 kpc, and circular rotation speed at the Sun, theta(0), to be 240 +/- 10 kms(-1). We found kinematic differences between O stars and interstellar masers: the O stars, on average, rotate faster, > 8 kms(-1) than maser-traced high-mass star forming regions.

第 182 条，共 248 条

A 95 GHz methanol emission survey toward eight small supernova remnants

Ying-Jie LiYe XuXi ChenDeng-Rong LuYan SunXin-Yu DuZhi-Qiang Shen

Research in Astronomy and Astrophysics

We report on a 95 GHz（80-71A+） methanol（CH3OH） emission survey with the Purple Mountain Observatory Delingha 13.7 m telescope. Eight supernova remnants（SNRs） with angular size<10′ were observed, but emission was only detected in three SNRs near the Galactic center（Sgr A East,G 0.1－0.1 and G 359.92－0.09）. CH3OH emission mainly surrounds the SNRs and can be decomposed into nine spatial peaks with the velocity range of eight peaks being（-30, 70） km s-1, and the other is（70, 120） km s-1. They are probably excited by interaction with these SNRs and adjacent molecular gas in the central molecular zone （CMZ）, although star formation may play an important role in exciting CH3OH emission in some regions of CMZ. We infer that tidal action is unlikely to be an excitation source for CH3OH emission.

第 183 条，共 248 条

A challenge to identify an optical counterpart of the gravitational wave event GW151226 with Hyper Suprime-Cam(dagger)

Utsumi, Y (Utsumi, Yousuke); Tominaga, N (Tominaga, Nozomu); Tanaka, M (Tanaka, Masaomi); Morokuma, T (Morokuma, Tomoki); Yoshida, M (Yoshida, Michitoshi); Asakura, Y (Asakura, Yuichiro); Finet, F (Finet, Francois); Furusawa, H (Furusawa, Hisanori); Kawabata, KS (Kawabata, Koji S.); Liu, W (Liu, Wei); Matsubayashi, K (Matsubayashi, Kazuya); Moritani, Y (Moritani, Yuki); Motohara, K (Motohara, Kentaro); Nakata, F (Nakata, Fumiaki); Ohta, K (Ohta, Kouji); Terai, T (Terai, Tsuyoshi); Uemura, M (Uemura, Makoto); Yasuda, N (Yasuda, Naoki)

PUBLICATIONS OF THE ASTRONOMICAL SOCIETY OF JAPAN

卷: 70 期: 1 文献号: 1

We present the results of detailed analysis of an optical imaging survey conducted using the Subaru/Hyper Suprime-Cam (HSC) that aimed to identify an optical counterpart to the gravitational wave event GW151226. In half a night, the i- and z-band imaging survey by HSC covered 63.5 deg(2) of the error region, which contains about 7% of the LIGO localization probability, and the same field was observed in three different epochs. The detectable magnitude of the candidates in a differenced image is evaluated as i similar to 23.2 mag for the requirement of at least two 5 sigma detections, and 1744 candidates are discovered. Assuming a kilonova as an optical counterpart, we compare the optical properties of the candidates with model predictions. A red and rapidly declining light curve condition enables the discrimination of a kilonova from other transients, and a small number of candidates satisfy this condition. The presence of stellar-like counterparts in the reference frame suggests that the surviving candidates are likely to be flare stars. The fact that most of those candidates are in the galactic plane, vertical bar b vertical bar< 5 degrees, supports this interpretation. We also check whether the candidates are associated with the nearby GLADE galaxies, which reduces the number of contaminants even with a looser color cut. When a better probability map (with localization accuracy of similar to 50 deg(2)) is available, kilonova searches of up to approximately 200Mpc will become feasible by conducting immediate follow-up observations with an interval of 3-6 d.

III. Applied Celestial Mechanics and Space Object & Debris Research

Center for Space Object and Debris Research

第 184 条，共 248 条

An estimation of Envisat's rotational state accounting for the precession of its rotational axis caused by gravity-gradient torque

Lin, HY (Lin, Hou-Yuan); Zhao, CY (Zhao, Chang-Yin)
ADVANCES IN SPACE RESEARCH
卷: 61 期: 1 页: 182-188
The rotational state of Envisat is re-estimated using the specular glint times in optical observation data obtained from 2013 to 2015. The model is simplified to a uniaxial symmetric model with the first order variation of its angular momentum subject to a gravity gradient torque causing precession around the normal of the orbital plane. The sense of Envisat's rotation can be derived from observational data, and is found to be opposite to the sense of its orbital motion. The rotational period is estimated to be (120.674 +/- 0.068) exp ((4.5095 +/- 0.0096) x 10(-4).t, where t is measured in days from the beginning of 2013. The standard deviation is 0.760 s, making this the best fit obtained for Envisat in the literature to date. The results demonstrate that the angle between the angular momentum vector and the negative normal of the orbital plane librates around a mean value of 8.53 +/- 0.42 degrees with an amplitude from about 0.7 degrees (in 2013) to 0.5 degrees (in 2015), with the libration period equal to the precession period of the angtilar momentum, from about 4.8 days (in 2013) to 3.4 days (in 2015). The ratio of the minimum to maximum principal moments of inertia is estimated to be 0.0818 +/- 0.0011, and the initial longitude of the angular momentum in the orbital coordinate system is 40.5 degrees +/- 9.3 degrees. The direction of the rotation axis derived from our results at September 23, 2013, UTC 20:57 is similar to the results obtained from satellite laser ranging data but about 20 closer to the negative normal of the orbital plane. (C) 2017 COSPAR. Published by Elsevier Ltd. All rights reserved.

第 185 条，共 248 条

On the lunar node resonance of the orbital plane evolution of the Earth's satellite orbits

Zhu, TL (Zhu, Ting-Lei)
ADVANCES IN SPACE RESEARCH
卷: 61 期: 11 页: 2761-2776
This paper aims to investigate the effects of lunar node resonance on the circular medium Earth orbits (MEO). The dynamical model is established in classical Hamiltonian systems with the application of Lie transform to remove the non-resonant terms. Resonant condition, stability and phase structures are studied. The lunar node resonance occurs when the secular changing rates of the orbital node (with respect to the equator) and the lunar node (with respect to the ecliptic) form a simple integer ratio. The resonant conditions are satisfied for both inclined and equatorial orbits. The orbital plane would have long period (with typical timescales of several centuries) fluctuation due to the resonance. (C) 2018 COSPAR. Published by Elsevier Ltd. All rights reserved.

第 186 条，共 248 条

Deep Learning for Mid-term Forecast of Daily Index of Solar 10.6 cm Radio Flux

Xin Wang
DOI： 10.1007/978-981-10-4837-1_8
For mid-term forecast of the daily index of solar 10.7 cm radio flux with deep learning method,a neural network based on classical multi-layer perception model is proposed.The network contains only one hidden layer with 90 neutrons,and an autoregressive model of time series is implemented non-parametrically.In the forecast,historical daily indices as well as historical forecast error are considered.The model gives forecast of next 27 days with values of past 27 days.The network is trained and validated with historical data over 50 years,and the result clearly shows that the mean relative error is significantly reduced compared to the traditional methods.Unlike most of previous studies,in which the parameters of the model need to be rolling-updated,the parameters are fixed after the training with this model.The proposed model greatly simplifies daily operation of forecast and is extremely advantageous to the promotion in other applications.

第 187 条，共 248 条

卷帘快门 sCMOS 相机对空间碎片观测的影响研究

张晓祥 赵金宇 贾建禄 吴庆林 鹿瑶 高若城
光学与测量工程
同每个像素曝光开始及结束时间相同的传统科学级 CCD 相机相比,近年来出现的卷帘快门(rolling shutter)sCMOS 相机工作时每个像素的曝光开始及结束时间不同,曝光时间相同,因此需要评估 sCMOS 相机像素之间曝光开始及结束时间不同对空间碎片测量精度的影响。首先测试了卷帘快门 sCMOS 相机的工作时序和最大延迟时间,并得出曝光不同步的改正公式,再以激光卫星为目标,测试了两种典型观测模式下空间碎片的天文定位精度,并对应用曝光不同步改正前后结果进行对比。测试结果表明 sCMOS 相机卷帘快门的工作时序与理论一致,边缘曝光延迟最大 10ms;实测表明恒星位置内符合精度优于 2arcsec,目标天文定位精度优于 3arcsec。sCMOS 相机能够用于空间碎片观测,能够实现较高的位置测量精度。

第 188 条，共 248 条

高能光纤激光器光束合成技术

程雪王建立刘昌华
红外与激光工程
高能光纤激光器光束合成技术是近年来高能激光器尤其是定向能源应用中的研究热点,可突破单根单模光纤激光

的输出功率限制,为高功率高光束质量的激光武器应用奠定了理论基础。介绍了光纤激光非相干合成和相干合成的国内外研究现状,给出了非相干合成技术中光束重叠和光谱合成的基本合成原理,重点介绍了国内外多家研究机构光谱合成近年来所达到的技术水平;介绍了国内外相干合成技术的最新研究进展,对相干合成等效大口径激光阵列输出中几种不同的透射式相干合成阵列输出和反射式相干合成阵列输出的关键合成装置,以及相干合成单一孔径输出中的核心光学元件进行详细分析。最后简要对比了高能光纤激光器光束相干合成技术和非相干合成技术的优缺点和应用范围。

第 189 条，共 248 条

云量分割在空间目标观测中的研究

王恩旺 王恩达 樊亮 旃进伟 黄学海
计算机科学
空间碎片观测过程中,云层干扰是光学望远镜观测的一个瓶颈。提出一种新的云量计算方法,把云量仪检测到的云层分布图像分成 24 个区块,分别对每个区块的像素值进行统计,如果统计结果大于一个给定的阈值 T,则表示该区块的云比较多;如果小于阈值 T,则表示该区块内没有云层覆盖,可以将望远镜引导到该区块的对应位置。研究表明,该方法简单易行,具有较高的使用价值,可以实现对望远镜的自动引导,提高望远镜的观测效率。

第 190 条，共 248 条

双行根数编目体系轨道误差研究

许晓丽 熊永清
天文学报
大量空间目标的真实轨道无法精确知道,目前只能通过跟踪观测的数据进行定轨来得到估计轨道,而估计的轨道就会有误差.双行根数(TLE)是广泛使用的一种特殊编目轨道根数,其配套的轨道模型为 Simplified General Perturbations 4(SGP4)/Simplified Deep-space Perturbations 4(SDP4)模型.编目轨道的精度主要依赖于相应的观测模型和动力学模型,这些模型一般都不会非常准确,往往会有误差,有些误差可能直接导致编目定轨结果在局部为有偏估计.通过理论研究和仿真模拟,分析了动力学模型中地球非球形引力位田谐摄动项对编目轨道精度的影响,发现 TLE 编目轨道中存在随时间周期变化的系统差,该系统误差甚至可以达到千米量级.几何构型较好的测站分布在一定程度上可以削弱编目定轨中产生的系统误差,由于力学模型的限制,无法彻底消除.

第 191 条，共 248 条

云南天文台月球激光测距研究与试验

李语强伏红林李荣旺汤儒峰李祝莲翟东升张海涛皮晓宇叶贤基熊耀恒
中国激光
为了实现嫦娥四号中继星的激光测距,需要开展月球激光测距(LLR)进行技术验证。中国科学院云南天文台基于 1.2m 的望远镜研制了共光路 LLR 系统,在攻克了多项技术难题后,于 2018 年 1 月 22 日成功探测到 Apollo 15 月面反射器的回波信号,实现了 LLR。多次重复实验结果表明,该 LLR 系统具备极弱激光信号探测能力,系统测量精度达到米级。

第 192 条，共 248 条

Retrieval of atmospheric mass densities in lower thermosphere below 200 km from precise orbit of re-entry object CZ-3B R/B by analytical and numerical methods

Zhang, MJ (Zhang, Ming-Jiang); Wang, HB (Wang, Hong-Bo); Zhao, CY (Zhao, Chang-Yin); Xiong, JN (Xiong, Jian-Ning); Wei, D (Wei, Dong); Zhang, W (Zhang, Wei); Yu, SX (Yu, Sheng-Xian)
ASTROPHYSICS AND SPACE SCIENCE
卷: 363 期: 8 文献号: 175
Taking the re-entry object CZ-3B R/B (COSPAR identifier 2012-018D, NORAD catalog number 38253) as an example, retrieval of atmospheric mass densities in lower thermosphere below 200 km from its rebuilt precise orbit is studied in this paper. Two methodologies, i.e. analytical and numerical methods, are adopted in the retrieval. Basic principles of these two methodologies are briefly introduced. Based on the short-arc sparse observational data accumulated in the high accuracy re-entry prediction, orbit determinations of re-entry object CZ-3B R/B are performed sectionally, and then its precise orbit is rebuilt. According to the orbit theory, the variation of orbital semi-major axis of re-entry object CZ-3B R/B induced by atmospheric drag perturbation only is derived from the rebuilt precise orbit. In the derivation of secular change of the orbital semi-major axis of re-entry object CZ-3B R/B induced by atmospheric drag perturbation only, the time-span is set as one minute tentatively. And then retrieval results of atmospheric mass densities in lower thermosphere below 200 km by analytical and numerical methods are presented, as well as their bias deviations from the calculated results of the NRLMSISE-00 empirical model of the atmosphere. Setting bias deviation bands, the corresponding 'confidence coefficients' of the retrieved atmospheric mass densities with respect to the model values are given. Average bias deviations of the retrieved atmospheric mass densities by analytical and numerical methods from the model values are also calculated respectively. On the whole, the retrieved atmospheric mass densities by numerical method approach to the model values more closely; the differences between the retrieved results and the model values are relatively smaller at the peaks of atmospheric mass densities than the other places.

第 193 条，共 248 条

Beam combining of high energy fibre lasers

Cheng Xue; Wang Jianli; Liu Changhua
Infrared and Laser engineering
卷: 47 期: 1 页: 0103011-1-0103011-11
Beam combining of high energy fibre lasers is the research hotspot especially for the directed energy application in recent years, which can overcome the output power lever limits of one single-mode fibre laser, and establish the theoretical foundation for the application of laser weapons with high power and perfect beam quality. Research status of fibre laser incoherent combining and coherent combining were presented. In the section of incoherent combining, the combining principle and combining level of beam overlap and spectral beam combining were introduced. In the section of coherent combining, the key combining apparatus of transmission-type and reflection-type equivalent large aperture laser array output and optical element of single aperture output were analyzed in detail. The advantages and disadvantages and range of application of high power fibre laser beam coherent combining and incoherent combining were compared briefly.

第 194 条，共 248 条

Orbit error characteristic and distribution of TLE using CHAMP orbit data

Xu, XL (Xu, Xiao-li); Xiong, YQ (Xiong, Yong-qing)
ASTROPHYSICS AND SPACE SCIENCE
卷: 363 期: 2 文献号: 31
Space object orbital covariance data is required for collision risk assessments, but publicly accessible two line element (TLE) data does not provide orbital error information. This paper compared historical TLE data and GPS precision ephemerides of CHAMP to assess TLE orbit accuracy from 2002 to 2008, inclusive. TLE error spatial variations with longitude and latitude were calculated to analyze error characteristics and distribution. The results indicate that TLE orbit data are systematically biased from the limited SGP4 model. The biases can reach the level of kilometers, and the sign and magnitude are correlate significantly with longitude.

Satellite Precise Orbit Determination and Application

第 195 条，共 248 条

Influence of Ice Nuclei Parameterization Schemes on the Hail Process

Liu, XL (Liu, Xiaoli); Fu, Y (Fu, Ye); Cao, ZB (Cao, Zhibin); Jin, SL (Jin, Shuanglong)
ADVANCES IN METEOROLOGY
文献号: 4204137
Ice nuclei are very important factors as they significantly affect the development and evolvement of convective clouds such as hail clouds. In this study, numerical simulations of hail processes in the Zhejiang Province were conducted using a mesoscale numerical model (WRF v3.4). The effects of six ice nuclei parameterization schemes on the macroscopic and microscopic structures of hail clouds were compared. The effect of the ice nuclei concentration on ground hailfall is stronger than that on ground rainfall. There were significant spatiotemporal, intensity, and distribution differences in hailfall. Changes in the ice nuclei concentration caused different changes in hydrometeors and directly affected the ice crystals, and, hence, the spatiotemporal distribution of other hydrometeors and the thermodynamic structure of clouds. An increased ice nuclei concentration raises the initial concentration of ice crystals with higher mixing ratio. In the developing and early maturation stages of hail cloud, a larger number of ice crystals competed for water vapor with increasing ice nuclei concentration. This effect prevents ice crystals from maturing into snow particles and inhibits the formation and growth of hail embryos. During later maturation stages, updraft in the cloud intensified and more supercooled water was transported above the 0 degrees C level, benefitting the production and growth of hail particles. An increased ice nuclei concentration therefore favors the formation of hail.

第 196 条，共 248 条

Numerical Study of a Southwest Vortex Rainstorm Process Influenced by the Eastward Movement of Tibetan Plateau Vortex

Xiaoli Liu Zhibin Cao
Advances in Meteorology
A number of studies revealed the possible eastward movement of the Tibetan Plateau low-pressure system in summer and indicated the enhancement effect of this process on the southwest vortex in the Sichuan Basin, which can induce strong convective precipitation and flood events in China. In this study, a numerical simulation of a southwest vortex rainstorm process was performed. The results show that the low-pressure system originated from the Tibetan Plateau affects the southwest vortex mainly at the middle level, causing the strength increase of southwest vortex (SWV), and acts as a connection between the positive vorticity centers at the upper and lower layers. For the microscopic cloud structure, the vertical updraft of the cloud cluster embedded in the SWV increases as the low-pressure system from the plateau arrives at the Sichuan Basin. Vapor and liquid cloud water at the lower level are transported upward, based on which the ice cloud at the upper level and the warm cloud at the lower level are joined to create favorable conditions for the growth of ice crystals. As the ice crystals grow up, snow and graupel particles form, which substantially elevates the precipitation. This effect leads to the rapid development of SWV rainstorm clouds and the occurrence of precipitation. In addition to the effect of the plateau vortex, the subsequent merging of the convective clouds is another important factor for heavy rainfall because it also leads to development of convective clouds, causing heavy rainfall.

IV. Planetary Sciences and Deep Space Exploration

Near Earth Object Survey and Solar System Bodies

第 197 条，共 248 条

The GTC exoplanet transit spectroscopy survey IX. Detection of haze, Na, K, and Li in the super-Neptune WASP-127b

Chen, G (Chen, G.); Palle, E (Palle, E.); Welbanks, L (Welbanks, L.); Prieto-Arranz, J (Prieto-Arranz, J.); Madhusudhan, N (Madhusudhan, N.); Gandhi, S (Gandhi, S.); Casasayas-Barris, N (Casasayas-Barris, N.); Murgas, F (Murgas, F.); Nortmann, L (Nortmann, L.); Crouzet, N (Crouzet, N.); Parviainen, H (Parviainen, H.); Gandolfi, D (Gandolfi, D.)

ASTRONOMY & ASTROPHYSICS

卷: 616 文献号: A145

Exoplanets with relatively clear atmospheres are prime targets for detailed studies of chemical compositions and abundances in their atmospheres. Alkali metals have long been suggested to exhibit broad wings due to pressure broadening, but most of the alkali detections only show very narrow absorption cores, probably because of the presence of clouds. We report the strong detection of the pressure-broadened spectral profiles of Na, K, and Li absorption in the atmosphere of the super-Neptune WASP-127b, at 4.1 sigma, 5.0 sigma, and 3.4 sigma, respectively. We performed a spectral retrieval modeling on the high-quality optical transmission spectrum newly acquired with the 10.4m Gran Telescopio Canarias (GTC), in combination with the re-analyzed optical transmission spectrum obtained with the 2.5 m Nordic Optical Telescope (NOT). By assuming a patchy cloudy model, we retrieved the abundances of Na, K, and Li, which are super-solar at 3.7 sigma for K and 5.1 sigma for Li (and only 1.8 sigma for Na). We constrained the presence of haze coverage to be around 52%. We also found a hint of water absorption, but cannot constrain it with the global retrieval owing to larger uncertainties in the probed wavelengths. WASP-127b will be extremely valuable for atmospheric characterization in the era of James Webb Space Telescope.

第 198 条，共 248 条

基于 Fermi-LAT 数据的暗物质湮灭线谱搜寻及悟空号的伽马射线分析软件开发

梁云峰

天文学报

在现代的天体物理观测中,有许多天文现象包括星系旋转曲线、星系团的质量测量、宇宙微波背景辐射的角功率谱等,难以用现有模型进行解释.它们跨越多个尺度—小至星系尺度,大至整个宇宙尺度,需要在模型中额外引入一定的质量才能令观测现象得到很好的解释,而提供这些质量的"物质"却难以用通常的电磁波或中微子手段探测到.这部分物质被称为"暗物质".根据现有的观测结果,它们应具有正常的引力相互作用,没有强相互作用和电磁相互作用,寿命很长(显著长于宇宙的寿命).

第 199 条，共 248 条

Na I and H alpha absorption features in the atmosphere of MASCARA-2b/KELT-20b

Casasayas-Barris, N (Casasayas-Barris, N.); Palle, E (Palle, E.); Yan, F (Yan, F.); Chen, G (Chen, G.); Albrecht, S (Albrecht, S.); Nortmann, L (Nortmann, L.); Van Eylen, V (Van Eylen, V.); Snellen, I (Snellen, I.); Talens, GJJ (Talens, G. J. J.); Hernandez, JIG (Gonzalez Hernandez, J. I.); Rebolo, R (Rebolo, R.); Otten, GPPL (Otten, G. P. P. L.)

ASTRONOMY & ASTROPHYSICS

卷: 616 文献号: A151

We used the HARPS-North high resolution spectrograph (R = 115 000) at Telescopio Nazionale Galileo (TNG) to observe one transit of the highly irradiated planet MASCARA-2b/KELT-20b. Using only one transit observation, we are able to clearly resolve the spectral features of the atomic sodium (Na I) doublet and the H alpha line in its atmosphere, which are corroborated with the transmission calculated from their respective transmission light curves (TLC). In particular, we resolve two spectral features centered on the Na I doublet position with an averaged absorption depth of 0.17 +/- 0.03% for a 0.75 angstrom bandwidth with line contrasts of 0.44 +/- 0.11% (D-2) and 0.37 +/- 0.08% (D-1). The Na I TLC have also been computed, showing a large Rossiter-McLaughlin (RM) effect, which has a 0.20 +/- 0.05% Na I transit absorption for a 0.75 angstrom passband that is consistent with the absorption depth value measured from the final transmission spectrum. We observe a second feature centered on the H alpha line with 0.6 +/- 0.1% contrast and an absorption depth of 0.59 +/- 0.08% for a 0.75 angstrom passband that has consistent absorptions in its TLC, which corresponds to an effective radius of R-lambda/R-P = 1.20 +/- 0.04. While the signal-to-noise ratio (S/N) of the final transmission spectrum is not sufficient to adjust different temperature profiles to the lines, we find that higher temperatures than the equilibrium (T-eq = 2260 +/- 50K) are needed to explain the lines contrast. Particularly, we find that the Na I lines core require a temperature of T = 4210 +/- 180K and that H alpha requires a temperature of T = 4330 +/- 520 K. MASCARA-2b, like other planets orbiting A-type stars, receives a large amount of UV energy from its host star. This energy excites the atomic hydrogen and produces H alpha absorption, leading to the expansion and abrasion of the atmosphere. The study of other Balmer lines in the transmission spectrum would allow the determination of the atmospheric temperature profile and the calculation of the lifetime of the atmosphere with escape rate measurements. In the case of MASCARA-2b, residual features are observed in the H beta and H gamma lines, but they are not statistically significant. More transit

observations are needed to confirm our findings in Na I and H alpha and to build up enough S/N to explore the presence of H beta and H gamma planetary absorptions.

第 200 条，共 248 条

The GTC exoplanet transit spectroscopy survey VIII. Flat transmission spectrum for the warm gas giant WASP-80b

Parviainen, H (Parviainen, H.); Palle, E (Palle, E.); Chen, G (Chen, G.); Nortmann, L (Nortmann, L.); Murgas, F (Murgas, F.); Nowak, G (Nowak, G.); Aigrain, S (Aigrain, S.); Booth, A (Booth, A.); Abazorius, M (Abazorius, M.); Iro, N (Iro, N.)

ASTRONOMY & ASTROPHYSICS

卷: 609 文献号: A33

Aims. We set out to study the atmosphere of WASP-80b, a warm inflated gas giant with an equilibrium temperature of similar to 800 K, using ground-based transmission spectroscopy covering the spectral range from 520 to 910 nm. The observations allow us to probe the existence and abundance of K and Na in WASP-80b's atmosphere, existence of high-altitude clouds, and Rayleigh-scattering in the blue end of the spectrum.

Methods. We observed two spectroscopic time series of WASP-80b transits with the OSIRIS spectrograph installed in the Gran Telescopio Canarias (GTC), and use the observations to estimate the planet's transmission spectrum between 520 nm and 910 nm in 20 nm-wide passbands, and around the K I and Na I resonance doublets in 6 nm-wide passbands. We jointly model three previously published broadband datasets consisting of 27 light curves, prior to a transmission spectroscopy analysis in order to obtain improved estimates of the planet's orbital parameters, average radius ratio, and stellar density. The parameter posteriors from the broadband analysis are used to set informative priors on the transmission spectroscopy analysis. The final transmission spectroscopy analyses are carried out jointly for the two nights using a divide-by-white approach to remove the common-mode systematics, and Gaussian processes to model the residual wavelength-dependent systematics.

Results. We recover a flat transmission spectrum with no evidence of Rayleigh scattering or K I or Na I absorption, and obtain an improved system characterisation as a by-product of the broadband- and GTC-dataset modelling. The transmission spectra estimated separately from the two observing runs are consistent with each other, as are the transmission spectra estimated using either a parametric or nonparametric systematics model. The flat transmission spectrum favours an atmosphere model with high-altitude clouds over cloud-free models with stellar or sub-stellar metallicities.

Conclusions. Our results disagree with the recently published discovery of strong K I absorption in WASP-80b's atmosphere based on ground-based transmission spectroscopy with FORS2 at VLT.

第 201 条，共 248 条

Detection of He I λ10830 Å absorption on HD 189733 b with CARMENES high-resolution transmission spectroscopy

Caballero, J.A. y Sanz Forcada, J. y Cortés Contreras, Miriam y Montes Gutiérrez, David

We present three transit observations of HD 189733 b obtained with the high-resolution spectrograph CARMENES at Calar Alto. A strong absorption signal is detected in the near-infrared He I triplet at 10830 Å in all three transits. During mid-transit, the mean absorption level is 0.88 ± 0.04% measured in a ±10 km s^(−1) range at a net blueshift of −3.5 ± 0.4 km s s^(−1) (10829.84–10830.57 Å). The absorption signal exhibits radial velocities of +6.5 ± 3.1 km s s^(−1) and −12.6 ± 1.0 km s s^(−1) during ingress and egress, respectively; all radial velocities are measured in the planetary rest frame. We show that stellar activity related pseudo-signals interfere with the planetary atmospheric absorption signal. They could contribute as much as 80% of the observed signal and might also affect the observed radial velocity signature, but pseudo-signals are very unlikely to explain the entire signal. The observed line ratio between the two unresolved and the third line of the He I triplet is 2.8 ± 0.2, which strongly deviates from the value expected for an optically thin atmospheres. When interpreted in terms of absorption in the planetary atmosphere, this favors a compact helium atmosphere with an extent of only 0.2 planetary radii and a substantial column density on the order of 4 × 10^(12) cm s^(−2) . The observed radial velocities can be understood either in terms of atmospheric circulation with equatorial superrotation or as a sign of an asymmetric atmospheric component of evaporating material. We detect no clear signature of ongoing evaporation, like pre- or post-transit absorption, which could indicate material beyond the planetary Roche lobe, or radial velocities in excess of the escape velocity. These findings do not contradict planetary evaporation, but only show that the detected helium absorption in HD 189733 b does not trace the atmospheric layers that show pronounced escape signatures.

第 202 条，共 248 条

Tilting Styx and Nix but not Uranus with a Spin-Precession-Mean-motion resonance

Quillen, AC (Quillen, Alice C.); Chen, YY (Chen, Yuan-Yuan); Noyelles, B (Noyelles, Benoit); Loane, S (Loane, Santiago)

CELESTIAL MECHANICS & DYNAMICAL ASTRONOMY

卷: 130 期: 2 文献号: UNSP 11

A Hamiltonian model is constructed for the spin axis of a planet perturbed by a nearby planet with both planets in orbit about a star. We expand the planet-planet gravitational potential perturbation to first order in orbital inclinations and eccentricities, finding terms describing spin resonances involving the spin precession rate and the two planetary mean motions. Convergent planetary migration allows the spinning planet to be captured into spin resonance. With initial obliquity near zero, the spin resonance can lift the planet's obliquity to near 90. or 180. depending upon whether the spin resonance is first or zeroth order in inclination. Past capture of Uranus into such a spin resonance could give an alternative non-collisional scenario accounting for Uranus's high obliquity. However,

we find that the time spent in spin resonance must be so long that this scenario cannot be responsible for Uranus's high obliquity. Our model can be used to study spin resonance in satellite systems. Our Hamiltonian model explains how Styx and Nix can be tilted to high obliquity via outward migration of Charon, a phenomenon previously seen in numerical simulations.

第 203 条，共 248 条

Transiting Exoplanet Monitoring Project (TEMP). IV. Refined System Parameters, Transit Timing Variations, and Orbital Stability of the Transiting Planetary System HAT-P-25

Wang, XY (Wang, Xian-Yu); Wang, SH (Wang, Songhu); Hinse, TC (Hinse, Tobias C.); Li, K (Li, Kai); Wang, YH (Wang, Yong-Hao); Laughlin, G (Laughlin, Gregory); Liu, HG (Liu, Hui-Gen); Zhang, H (Zhang, Hui); Wu, ZY (Wu, Zhen-Yu); Zhou, X (Zhou, Xu); Zhou, JL (Zhou, Ji-Lin); Hu, SM (Hu, Shao-Ming); Wu, DH (Wu, Dong-Hong); Peng, XY (Peng, Xi-Yan); Chen, YY (Chen, Yuan-Yuan)

PUBLICATIONS OF THE ASTRONOMICAL SOCIETY OF THE PACIFIC

卷: 130 期: 988 文献号: 064401

We present eight new light curves of the transiting extra-solar planet HAT-P-25b obtained from 2013 to 2016 with three telescopes at two observatories. We use the new light curves, along with recent literature material, to estimate the physical and orbital parameters of the transiting planet. Specifically, we determine the mid-transit times (T-C) and update the linear ephemeris, T-C[0] = 2456418.80996 +/- 0.00025 [BJD(TDB)] and P = 3.65281572 +/- 0.00000095 days. We carry out a search for transit timing variations (TTVs), and find no significant TTV signal at the Delta T = 80 s-level, placing a limit on the possible strength of planet-planet interactions (TTVG). In the course of our analysis, we calculate the upper mass-limits of the potential nearby perturbers. Near the 1:2, 2:1, and 3:1 resonances with HAT-P-25b, perturbers with masses greater than 0.5, 0.3, and 0.5 M-circle plus respectively, can be excluded. Furthermore, based on the analysis of TTVs caused by light travel time effect (LTTE) we also eliminate the possibility that a long-period perturber exists with M-p > 3000 M-J within a = 11.2 au of the parent star.

Ephemerial Astronomy and Astronomical Reference System

第 204 条，共 248 条

Probing f(T) gravity with gravitational time advancement

Deng, XM (Deng, Xue-Mei)
CLASSICAL AND QUANTUM GRAVITY
卷: 35 期: 17 文献号: 175013
The effects of a quadratic f(T) gravity on astronomical observations and solar system experiments were recently considered in previous works. Its deviation from Einstein's general relativity is characterized by a model parameter a and the cosmological constant A whose constraints were respectively found as vertical bar alpha vertical bar <= 2.3 x 10 m(2) and vertical bar Lambda vertical bar <= 1.8 x 10(-43) m(-2) in the solar system. In this paper, a new test of the f(T) gravity by measuring the gravitational time advancement is presented and studied. The gravitational time advancement arises in a two-way light propagation between an observer and a distant spacecraft, where the light traveling time is recorded by the observer's proper time. It is found that (1) relying on their signs, alpha and Lambda can make the gravitational time advancement smaller or larger than the one of general relativity; (2) the configuration of the inferior conjunction between the observer and the spacecraft is more suitable for detecting the advancement, because its effect is almost 3.5 times larger than the one in the superior conjunction; (3) the time advancement could be effectively complementary to Shapiro time delay for gravitational experiments in practice; and (4) the implement of planetary laser ranging and optical clocks in the future will provide much more insight into the f(T) gravity.

第 205 条，共 248 条

Solar system and binary pulsars tests of the minimal momentum uncertainty principle

Xue-Mei Deng
DOI： 10.1209/0295-5075/120/60004
The light time equation and frequency shift are worked out in the framework of a second parametrized post-Newtonian (2PPN) formalism in the Solar System barycentric reference system (SSBRS) developed in a recently published paper. Effects of each body's oblateness, spin and translational motion are taken into account for the light propagation. It is found that, at the second post-Newtonian

第 206 条，共 248 条

The nearby triple star HIP 101955

Fang, X (Fang, Xia)
ASTROMETRY AND ASTROPHYSICS IN THE GAIA SKY
卷: 12 期: S330 页: 356-357
The nearby triple star HIP 101955 with strongly inclined orbit still remains. Thus the long-term dynamical stability deserves to be discussed based on the new dynamical state parameters (component masses and kinematic parameters) derived from fitting the accurate three-body model to the radial velocity, the Hipparcos Intermediate Astrometric Data (HIAD), and the accumulated speckle and visual data. It is found that the three-body system remains integrated and most likely undergoes Kozai cycles. With the already accumulated high-precision data, the three-body effects cannot always be neglected in the determination of the dynamical state. And it is expected that this will be the general case under the available Gaia data.
会议名称: 330th Symposium of the International-Astronomical-Union (IAU)
会议日期: APR 24-28, 2017
会议地点: Nice, FRANCE

第 207 条，共 248 条

Effects of a brane world on gravitational time advancement

Deng, XM (Deng, Xue-Mei)
MODERN PHYSICS LETTERS A
卷: 33 期: 19 文献号: 1850110
Solar System tests of a brane world, which is called DMPR model, were studied in recent works. The correction of DMPR model to the general relativity (GR) in the four-dimensional curved spacetime can be parametrized by a "tidal charge" parameter Q. The parameter Q in this model was obtained and improved as vertical bar Q vertical bar less than or similar to 6.7 m(2) by the Earth-Mercury ranging. A new test of the DMPR model based on gravitational time advancement is proposed and investigated in this work. The advancement is a gravitational consequence on round-trip proper time duration of a photon. For ranging a distant spacecraft, it is shown that (1) the "tidal charge" parameter can make the advancement larger or smaller than the one of GR, depending on the sign of Q; (2) the superior conjunction (SC) and the inferior conjunction (IC) are all suitable for detecting the advancement; (3) the advancement can be complementary to the classical test of Shapiro time delay for detecting the brane world; and (4) the implementation of optical clocks and planetary laser ranging will provide more insights on the brane world model in the future.

第 208 条，共 248 条

双星观测量计算方法的改进及应用

陈健 夏芳 傅燕宁
天文学报
双星轨道拟合是基本天文研究领域的重要内容,其给出的动力学质量、轨道参数具有重要的应用价值.前者是恒星系统动力学研究和恒星物理演化研究必不可少的参量,后者则对提高亮星星表参考架的参考星数密度具有重要意义.但是,该项研究此前普遍采用了一些近似,如切平面的变化与空间的透视效应均被忽略.对上百个含亮子星的双星系统而言,这些近似引起观测量计算的偏差已经超过了当前的观测误差(1 mas).我们以牛顿二体模型为基础,用严格的立体几何关系改进了观测量的计算方法,通过仿真和观测数据验证了方法改进的有效性.拟合的结果表明,模型参数的拟合值和子星的观测量预报均有显著的改进.因此,对于双星,尤其是太阳系邻近的远距双星,改进观测量计算方法是必须的。

第 209 条，共 248 条

Testing Photons Coupled to Weyl Tensor with Gravitational Time Advancement

Li, G (Li, Gang); Deng, XM (Deng, Xue-Mei)
COMMUNICATIONS IN THEORETICAL PHYSICS
卷: 70 期: 6 页: 721-727
Classical Solar System tests of photons coupled to Weyl tensor with two polarizations were studied in a recent work. A coupling strength parameter a in this model was firstly obtained as |alpha| less than or similar to 4 x 10(11) m(2) by using available datasets in the Solar System. In this paper, a new test called by gravitational time advancement is proposed and investigated to test such the coupling. This new test, which is quite different from Shapiro time delay, depends strongly on round-trip proper time span (not coordinate time one) of flight of radio pulses between an observer on the Earth and a distant spacecraft. For ranging a spacecraft getting far away from the Sun, two special cases (the superior/inferior conjunctions) are used to analyse the observability in the advancement contributed by the Weyl coupling. We found that the situation of the inferior conjunction is more suitable for detecting the advancement caused by such the Weyl coupling. In either case, two kinds of polarizations make the advancement in the model smaller or larger than the one of general relativity. Although the observability in the advancement could be out of the reach of already existing technology, the implement of planetary laser ranging and optical clocks might provide us more insights on such the Weyl coupling in the near future.

The Sun and Solar System Plasmas

第 210 条，共 248 条

Excitation of Ion Cyclotron Waves by Ion and Electron Beams in Compensated-current System

Xiang, L (Xiang, L.); Wu, DJ (Wu, D. J.); Chen, L (Chen, L.)
ASTROPHYSICAL JOURNAL
卷: 857 期: 2 文献号: 108
Ion cyclotron waves (ICWs) can play important roles in the energization of plasma particles. Charged particle beams are ubiquitous in space, and astrophysical plasmas and can effectively lead to the generation of ICWs. Based on linear kinetic theory, we consider the excitation of ICWs by ion and electron beams in a compensated-current system. We also investigate the competition between reactive and kinetic instabilities. The results show that ion and electron beams both are capable of generating ICWs. For ICWs driven by ion beams, there is a critical beam velocity, v(bi)(c), and critical wavenumber, k(z)(c), for a fixed beam density; the reactive instability dominates the growth of ICWs when the ion-beam velocity v(bi) > v(bi)(c) and the wavenumber k(z) < k(z)(c), and the maximal growth rate is reached at k(z) similar or equal to 2k(z)(c)/3 for a given v(bi) > v(bi)(c). For the slow ion beams with v(bi) < v(bi)(c), the kinetic instability can provide important growth rates of ICWs. On the other hand, ICWs driven by electron beams are excited only by the reactive instability, but require a critical velocity, v(be)(c) >> v(A) (the Alfven velocity). In addition, the comparison between the approximate analytical results based on the kinetic theory and the exact numerical calculation based on the fluid model demonstrates that the reactive instabilities can well agree quantitatively with the numerical results by the fluid model. Finally, some possible applications of the present results to ICWs observed in the solar wind are briefly discussed.

第 211 条，共 248 条

Modulation of Ion and Electron Pitch Angle in the Presence of Large-amplitude, Low-frequency, Left-hand Circularly Polarized Electromagnetic Waves Observed by MMS

Zhao, JS (Zhao, J. S.); Wang, TY (Wang, T. Y.); Dunlop, MW (Dunlop, M. W.); He, JS (He, J. S.); Dong, XC (Dong, X. C.); Wu, DJ (Wu, D. J.); Khotyaintsev, YV (Khotyaintsev, Yu. V.); Ergun, RE (Ergun, R. E.); Russell, CT (Russell, C. T.); Giles, BL (Giles, B. L.); Torbert, RB (Torbert, R. B.); Burch, JL (Burch, J. L.)
ASTROPHYSICAL JOURNAL
卷: 867 期: 1 文献号: 58
Most studies on low-frequency electromagnetic cyclotron

waves have assumed a small wave amplitude, which ensures the reasonable application of linear and quasi-linear theories. However, the topic of large-amplitude electromagnetic cyclotron waves has not received much attention. Using Magnetospheric Multiscale measurements, this study observes low-frequency, left-hand circularly polarized electromagnetic waves with magnetic fluctuation similar to 1-2 nT in the dusk flank side of the Earth's magnetosheath. Considering the ambient magnetic field similar to 15 nT therein, the relative wave amplitude is of the order of 0.1. These large magnetic field fluctuations result in a periodic variation of the ion pitch angle. The electron pitch angle exhibits a localized distribution feature with a timescale approximating the wave period. Moreover, some electrons are trapped at a pitch angle similar to 90 degrees, and the trapping is more remarkable as strong waves arise. These two features of the electron pitch angle distribution imply that the trapping of electrons (partly) results from large-amplitude electromagnetic cyclotron fluctuations. Our results illustrate the important role of large-amplitude electromagnetic cyclotron waves on the dynamics of charged particles.

第 212 条，共 248 条

Nonlinear Decay of Alfven Waves Driven by Interplaying Two- and Three-dimensional Nonlinear Interactions

Zhao, JS (Zhao, J. S.); Voitenko, Y (Voitenko, Y.); De Keyser, J (De Keyser, J.); Wu, DJ (Wu, D. J.)
ASTROPHYSICAL JOURNAL
卷: 857 期: 1 文献号: 42
We study the decay of Alfven waves in the solar wind, accounting for the joint operation of two-dimensional (2D) scalar and three-dimensional (3D) vector nonlinear interactions between Alfven and slow waves. These interactions have previously been studied separately in long-and short-wavelength limits where they lead to 2D scalar and 3D vector decays, correspondingly. The joined action of the scalar and vector interactions shifts the transition between 2D and 3D decays to significantly smaller wavenumbers than was predicted by Zhao et al. who compared separate scalar and vector decays. In application to the broadband Alfven waves in the solar wind, this means that the vector nonlinear coupling dominates in the extended wavenumber range 5 x 10(-4) less than or similar to rho(i)k(0 perpendicular to) less than or similar to 1, where the decay is essentially 3D and nonlocal, generating product Alfven and slow waves around the ion gyroscale. Here.i is the ion gyroradius, and k(0 perpendicular to) is the pump Alfven wavenumber. It appears that, except for the smallest wavenumbers at and below rho(i)k(0 perpendicular to) similar to 10(-4) in Channel I, the nonlinear decay of magnetohydrodynamic Alfven waves propagating from the Sun is nonlocal and cannot generate counter-propagating Alfven waves with similar scales needed for the turbulent cascade. Evaluation of the nonlinear frequency shift shows that product Alfven waves can still be approximately described as normal Alfvenic eigenmodes. On the contrary, nonlinearly driven slow waves deviate considerably from normal modes and are therefore difficult to identify on the basis of their phase velocities and/or polarization.

第 213 条，共 248 条

Two- and Three-dimensional Nonlinear Instabilities of Whistler Waves

Zhao, JS (Zhao, Jinsong); Sun, HY (Sun, Heyu); Yu, MY (Yu, Mingyoung)
ASTROPHYSICAL JOURNAL
卷: 866 期: 2 文献号: 127
Recently, two-dimensional (2D) nonlinear instabilities of whistler waves from resonant wave-wave interaction have gained much attention in numerical simulations as well as observations in space plasmas. In this paper, both 2D and three-dimensional (3D) nonlinear instabilities of whistler waves are investigated using electron magnetohydrodynamics (EMHD). It is found that decay instabilities can excite waves with a broadband wavenumber spectrum, including highly oblique propagating whistler waves. Whistler waves with lambda(e)k = 1 would excite counter-propagating whistler waves, and the wave with lambda(e)k not equal 1 can produce both co- and counter-propagating whistler waves, where lambda(e) is the electron inertial length and k is the wavenumber. Moreover, it is shown that 3D instabilities have similar nonlinear growth rate distributions as in 2D decay for the azimuthal wavelength much larger than lambda(e). These results suggest that nonlinear wave-wave interaction can play an important role in the scattering of whistler waves in the solar wind and the Earth's magnetosphere, and are also helpful for understanding nonlinear wave-wave interaction in the formation and development of EMHD turbulence.

第 214 条，共 248 条

Nature of Magnetic Holes above Ion Scales: A Mixture of Stable Slow Magnetosonic and Unstable Mirror Modes in a Double-polytropic Scenario?

Zhang, L (Zhang, Lei); He, JS (He, Jiansen); Zhao, JS (Zhao, Jinsong); Yao, S (Yao, Shuo); Feng, XS (Feng, Xueshang)
ASTROPHYSICAL JOURNAL
卷: 864 期: 1 文献号: 35
Magnetic holes are common features with a prominent dip of magnetic field strength in space plasma turbulence. As to their nature, there exists a dispute of explanations among discontinuities, magnetic reconnection, solitons, kinetic-scale electron vortexes, slow waves, and mirror-mode instability. As magnetic holes are often accompanied by thermal anisotropy, at magnetohydrodynamic scales double-polytropic equations can serve as an appropriate description. The reason for the long-lasting dispute lies in the fact that both mirror-mode structures and oblique slow-mode waves are characterized with anticorrelation between plasma density (or temperature) and magnetic field strength, which, as often used in preceding works, is also the characteristic feature of magnetic holes. Therefore, to finally and unambiguously diagnose the nature of magnetic holes above ion scales, we propose to resort to other features, among which nu(parallel to) and its phase relation with vertical bar B vertical bar and n behave differently between mirrormode structures and slow-mode waves. Herewith we establish a model with superposition of both slow and mirror modes to reproduce the observed types of behaviors (n, nu(parallel to), vertical bar B vertical bar, T-parallel to, T-perpendicular to). This model inspires new understanding of the nature of magnetic holes: the magnetic hole in reality is not solely contributed by only one mode, but a mixture of the two modes with an adjustable amplitude ratio.

第 215 条，共 248 条

Observations of Whistler Waves Correlated with Electron-scale Coherent Structures in the Magnetosheath Turbulent Plasma

Huang, SY (Huang, S. Y.); Sahraoui, F (Sahraoui, F.); Yuan, ZG (Yuan, Z. G.); Le Contel, O (Le Contel, O.); Breuillard, H (Breuillard, H.); He, JS (He, J. S.); Zhao, JS (Zhao, J. S.); Fu, HS (Fu, H. S.); Zhou, M (Zhou, M.); Deng, XH (Deng, X. H.); Wang, XY (Wang, X. Y.); Du, JW (Du, J. W.); Yu, XD (Yu, X. D.); Wang, DD (Wang, D. D.); Pollock, CJ (Pollock, C. J.); Torbert, RB (Torbert, R. B.); Burch, JL (Burch, J. L.)
ASTROPHYSICAL JOURNAL
卷: 861 期: 1 文献号: 29
A new type of electron-scale coherent structure, referred to as electron vortex magnetic holes, was identified recently in the Earth's magnetosheath turbulent plasma. These electron-scale magnetic holes are characterized by magnetic field strength depression, electron density enhancement, temperature and temperature anisotropy increase (a significant increase in perpendicular temperature and a decrease in parallel temperature), and an electron vortex formed by the trapped electrons. The strong increase of electron temperature indicates that these magnetic holes have a strong connection with the energization of electrons. Here, using high time resolution in situ measurements from the MMS mission, it is further shown that electron-scale whistler waves coexist with electron-scale magnetic holes. These whistler waves were found not propagating from remote regions, but generated locally due to electron temperature anisotropy (Te-perpendicular to/Te-parallel to) inside the magnetic holes. This study provides new insights into the electron-scale plasma dynamics in turbulent plasmas.

第 216 条，共 248 条

Two-dimensional Hybrid Simulations of Filamentary Structures and Kinetic Slow Waves Downstream of a Quasi-parallel Shock

Hao, YF (Hao, Yufei); Lu, QM (Lu, Quanming); Gao, XL (Gao, Xinliang); Wang, HY (Wang, Huanyu); Wu, DJ (Wu, Dejin); Wang, S (Wang, Shui)
ASTROPHYSICAL JOURNAL
卷: 861 期: 1 文献号: 57
In this paper, with two-dimensional hybrid simulations, we study the generation mechanism of filamentary structures downstream of a quasi-parallel shock. The results show that in the downstream both the amplitude of magnetic field and number density exhibit obvious filamentary structures, and the magnetic field and number density are anticorrelated. Detailed analyses find that these downstream compressive waves propagate almost perpendicular to the magnetic field, and the dominant wave number is around the inverse of the ion kinetic scale. Their parallel and perpendicular components roughly satisfy delta B-parallel to/delta B-perpendicular to = root 1+1/rho(2)(i)k(perpendicular to)(2) (where delta B-parallel to and delta B-perpendicular to represent the parallel and in-plane perpendicular components of magnetic field, k(perpendicular to) is the wave number in the perpendicular direction, and rho(i) in the ion gyroradius), and their Alfven ratio also roughly agrees with the analytical relation R-Ai = (1 + 2 rho(2)k(perpendicular to)(2))/beta (where R-Ai and beta indicate the Alfven ratio and plasma beta, respectively), while the corresponding cross helicity and compressibility show good agreement with previous theoretical calculations. All of these properties are consistent with those of kinetic slow waves (KSWs). Therefore, we conclude that the filamentary structures downstream of a quasi-parallel shock are produced by the excitation of KSWs.

第 217 条，共 248 条

Polarization properties of low frequency electromagnetic cyclotron waves associated with magnetic clouds

Zhao, GQ (Zhao, G. Q.); Feng, HQ (Feng, H. Q.); Wu, DJ (Wu, D. J.); Huang, J (Huang, J.)
ASTROPHYSICS AND SPACE SCIENCE
卷: 363 期: 3 文献号: 49
Recent studies have revealed that there are a large number of low frequency electromagnetic cyclotron waves (ECWs) occurring in and around magnetic clouds (MCs) that are common magnetic structures in interplanetary space. Using magnetic field data from the STEREO spacecraft, this paper investigates polarization properties of ECWs associated with 120 MCs. Results show that the ECWs are highly transverse, strongly polarized waves with large ellipticities. Specifically, almost all of the waves take place with the ratios of transverse power to total power higher than 0.94, polarization degrees greater than 0.85, and ellipticities larger than 0.5. The mean values of these quantities can be up to 0.99, 0.96, 0.85, respectively. In particular, there is a tendency of ellipticities decreasing with respect to the wave normal angles for ECWs with left handed polarization. The decreasing tendency is consistent with the recent theory and simulation results.

第 218 条，共 248 条

Statistical Study of Low-Frequency Electromagnetic Cyclotron Waves in the Solar Wind at 1 AU

Zhao, GQ (Zhao, G. Q.); Feng, HQ (Feng, H. Q.); Wu, DJ (Wu, D. J.); Liu, Q (Liu, Q.); Zhao, Y (Zhao, Y.); Zhao, A (Zhao, A.); Huang, J (Huang, J.)
JOURNAL OF GEOPHYSICAL RESEARCH-SPACE PHYSICS
卷: 123 期: 3 页: 1715-1730
Electromagnetic cyclotron waves (ECWs) near the proton cyclotron frequency are common wave activities in the solar wind and have attracted much attention in recent years. This paper investigates 82,809 ECWs based on magnetic field data from the Solar Terrestrial Relations Observatory-A mission between 2007 and 2013. Results show that ECWs may last for just a few seconds or incessantly for several tens of minutes. The time fraction of ECW storms among all solar wind is about 0.9%; the storms are obtained with the duration threshold of 10 min, amplitude criterion of 0.032 nT, and time separation limit of 3 min for combination of intermittent ECWs. Most of ECWs have their amplitudes less than 1 nT, while some ECWs have large amplitudes comparable to the ambient magnetic field. The distributions of the durations and amplitudes of these ECWs are characterized by power law spectra, respectively, with spectrum indexes around 4. Statistically, there seems to be a tendency that ECWs with a longer duration will have a larger amplitude. Observed ECW properties are time dependent, and the median frequency of left-hand ECWs can be lower than that of right-hand ECWs in some months in the spacecraft frame. The percentage of left-hand ECWs varies in a large range with respect to months; it is much low (26%) in a month, though it frequently exceeds 50% in other months. Characteristics of ECWs with concurrent

polarizations are also researched. The present study should be of importance for a more complete picture of ECWs in the solar wind.

第 219 条，共 248 条

The Influence of IMF B-y on the Bow Shock: Observation Result

Wang, M (Wang, M.); Lu, JY (Lu, J. Y.); Kabin, K (Kabin, K.); Yuan, HZ (Yuan, H. Z.); Liu, ZQ (Liu, Z. -Q.); Zhao, JS (Zhao, J. S.); Li, G (Li, G.)
JOURNAL OF GEOPHYSICAL RESEARCH-SPACE PHYSICS
卷: 123 期: 3 页: 1915-1926
In this study we use the bow shock crossings contained in the Space Physics Data Facility database, collected by four spacecraft (IMP 8, Geotail, Magion-4, and Cluster1) to analyze the effect of the interplanetary magnetic field (IMF) B-y component on the bow shock position and shape. Although the IMF B-z component is usually considered much more geoeffective than B-y, we find that the dayside bow shock is more responsive to the eastward component of the IMF than the north-south one. We believe that the explanation lies in the changes that the B-z component induces on the magnetopause location and shape, which largely compensate the corresponding changes in the dayside bow shock location. In the tail, we find that the bow shock cross section is elongated roughly in the direction perpendicular to the IMF direction, which agrees with earlier modeling studies.

第 220 条，共 248 条

Ion-Scale Kinetic Alfven Turbulence: MMS Measurements of the Alfven Ratio in the Magnetosheath

Roberts, OW (Roberts, O. W.); Toledo-Redondo, S (Toledo-Redondo, S.); Perrone, D (Perrone, D.); Zhao, J (Zhao, J.); Narita, Y (Narita, Y.); Gershman, D (Gershman, D.); Nakamura, R (Nakamura, R.); Lavraud, B (Lavraud, B.); Escoubet, CP (Escoubet, C. P.); Giles, B (Giles, B.); Dorelli, J (Dorelli, J.); Pollock, C (Pollock, C.); Burch, J (Burch, J.)
GEOPHYSICAL RESEARCH LETTERS
卷: 45 期: 16 页: 7974-7984
Turbulence in the Earth's magnetosheath at ion kinetic scales is investigated with the magnetospheric multiscale spacecraft. Several possibilities in the wave paradigm have been invoked to explain plasma turbulence at ion kinetic scales such as kinetic Alfven, slow, or magnetosonic waves. To differentiate between these different plasma waves is a challenging task, especially since some waves, in particular, kinetic slow waves and kinetic Alfven waves, share some properties making the possibility to distinguishing between them very difficult. Using the excellent time resolution data set provided from both the fluxgate magnetometer and the Fast Plasma Instrument, the ratio of trace velocity fluctuations to the magnetic fluctuations (in Alfven units), which is termed the Alfven ratio, can be calculated down to ion kinetic scales. Comparison of the measured Alfven ratio is performed with respect to the expectation from two-fluid magnetohydrodynamic theory for the kinetic slow wave and kinetic Alfven wave. Moreover, the plasma data also allow normalized fluctuation amplitudes of density and magnetic field to be compared differentiating between magnetosonic-like and kinetic Alfven-like turbulence. Using these two different ratios, we can rule out that the fluctuations at ion scales are dominated by magnetosonic-like fluctuations or kinetic slow-like fluctuations and show that they are consistent with kinetic Alfven-like fluctuations. This suggests that in the wave paradigm, heating in the direction of the parallel magnetic field is predominantly by the Landau damping of the kinetic Alfven wave.

第 221 条，共 248 条

Observation of Oblique Lower Band Chorus Generated by Nonlinear Three-Wave Interaction

Teng, S (Teng, S.); Zhao, J (Zhao, J.); Tao, X (Tao, X.); Wang, S (Wang, S.); Reeves, GD (Reeves, G. D.) GEOPHYSICAL RESEARCH LETTERS
卷: 45 期: 13 页: 6343-6352
Oblique whistler mode waves have been suggested to play an important role in radiation belt electron dynamics. Recently, X. Fu et al. (2017,) proposed that highly oblique lower band whistler waves could be generated by nonlinear three-wave resonance. Here we present the first observational evidence of such process, using Van Allen Probes data, where an oblique lower band chorus wave is generated by two quasi-parallel waves through nonlinear three-wave interaction. The wave resonance condition is satisfied even in the presence of frequency chirping of one of the pump waves. Different from the simulation results of X. Fu et al. (2017), simultaneous particle data do not show a plateau in the electron distribution, which could be due to the very weak intensity of the generated waves. These results should help to better understand the generation of oblique waves in the inner magnetosphere and their relative roles in energetic electron dynamics.
Plain Language Summary Oblique lower band whistler mode waves play an important role in the energetic electron dynamics in the magnetosphere. Recent research has also tried to understand how these highly oblique waves are generated. This paper presents the observations which directly confirm a recently proposed generation mechanism of oblique waves via nonlinear wave-wave interaction. In this theory, an oblique whistler wave, called the daughter wave, can obtain energy from the coupling with two parent whistler waves. Our observation shows that the generated oblique whistler waves also exhibit frequency chirping, caused by the frequency chirping of one of the parent waves. However, the observed waves are too weak to effectively scatter or energize electrons. Our study should be useful to further understand how the oblique waves are excited and their effects on energetic electron dynamics in the inner magnetosphere.

Near Earth Object Telescope

第 222 条，共 248 条

Transiting Exoplanet Monitoring Project (TEMP). I. Refined System Parameters and Transit Timing Variations of HAT-P-29b

Wang, SH (Wang, Songhu); Wang, XY (Wang, Xian-Yu); Wang, YH (Wang, Yong-Hao); Liu, HG (Liu, Hui-Gen); Hinse, TC

(Hinse, Tobias C.); Eastman, J (Eastman, Jason); Bayliss, D (Bayliss, Daniel); Hori, Y (Hori, Yasunori); Hu, SM (Hu, Shao-Ming); Li, K (Li, Kai); Liu, JZ (Liu, Jinzhong); Narita, N (Narita, Norio); Peng, XY (Peng, Xiyan); Wittenmyer, RA (Wittenmyer, R. A.); Wu, ZY (Wu, Zhen-Yu); Zhang, H (Zhang, Hui); Zhang, XJ (Zhang, Xiaojia); Zhao, HB (Zhao, Haibin); Zhou, JL (Zhou, Ji-Lin); Zhou, G (Zhou, George); Zhou, X (Zhou, Xu); Laughlin, G (Laughlin, Gregory)
ASTRONOMICAL JOURNAL
卷: 156 期: 4 文献号: 181
We report the photometry of six transits of the hot Jupiter HAT-P-29b obtained from 2013 October to 2015 January. We analyze the new light curves, in combination with the published photometric, Doppler velocimetric, and spectroscopic measurements, finding an updated orbital ephemeris for the HAT-P-29 system, T-C[0] = 2456170.5494(15)[BJD(TDB)] and P = 5.723390(13) days. This result is 17.63 s (4.0 sigma) longer than the previously published value, amounting to errors exceeding 2.5 hr at the time of writing (on UTC 2018 June 1). The measured transit mid-times for HAT-P-29b show no compelling evidence of timing anomalies from a linear model, which rules out the presence of perturbers with masses greater than 0.6, 0.7, 0.5, and 0.4M(circle plus) near the 1:2, 2:3, 3:2, and 2:1 resonances with HAT-P-29b, respectively.

第 223 条，共 248 条

A Pilot Study of Asteroid Spin Rate Using the CNEOST at Xu-Yi Observatory

Yeh, TS (Yeh, Ting-Shuo); Chang, CK (Chang, Chan-Kao); Li, B (Li, Bin); Lin, HW (Lin, Hsing-Wen); Zhao, HB (Zhao, Hai-Bin); Ji, JH (Ji, Jian-Hui); Ip, WH (Ip, Wing-Huen)
SERENDIPITIES IN THE SOLAR SYSTEM AND BEYOND
卷: 513 页: 303-306
Several important physical properties of asteroid can be derived from light curve, such as rotation sense (e.g. rotation period and spin pole orientation), general shape (e.g., axis ratio estimated form light curve amplitude and shape model from light curve inversion), interior structure (i.e., the 2.2 hr spin-rate limit of rubble-pile asteroids) and taxonomic type (e.g., phase-curve relation). Moreover, the statistics on asteroid spin rate and pole orientation are also important to understand how rotational status was affected by various mechanisms (e.g., mutual collision, tidal force and the YORP effect). To have a comprehensive study on the aforementioned questions, it relies on a large sample of asteroid rotation. Therefore, we initiated our cross-strait bilateral cooperation with the Purple Mountain Observatory (PMO) to collect asteroid light curves using the CNEOST (Chinese Near-Earth Object Survey Telescope) at XuYi station. A pilot survey of-40 square degrees using 8-min cadence had been carried out during February 27-March 2 2017. 1650 light curves were collected, from which 79 highly reliable rotation periods were derived. In order to collect more samples, we will continue to carry out more high-cadence observations in next two years.
会议名称: Symposium Celebrating Prof. Wing-Huen Ip's 70th Birthday - Serendipities in the Solar System and Beyond

第 224 条，共 248 条

Transiting Exoplanet Monitoring Project (TEMP). III. On the Relocation of the Kepler-9 b Transit

Wang, SH (Wang, Songhu); Wu, DH (Wu, Dong-Hong); Addison, BC (Addison, Brett C.); Laughlin, G (Laughlin, Gregory); Liu, HG (Liu, Hui-Gen); Wang, YH (Wang, Yong-Hao); Yang, TZ (Yang, Taozhi); Yang, M (Yang, Ming); Yisikandeer, A (Yisikandeer, Abudusaimaitijiang); Hong, RQ (Hong, Renquan); Li, B (Li, Bin); Liu, JZ (Liu, Jinzhong); Zhao, HB (Zhao, Haibin); Wu, ZY (Wu, Zhen-Yu); Hu, SM (Hu, Shao-Ming); Zhou, X (Zhou, Xu); Zhou, JL (Zhou, Ji-Lin); Zhang, H (Zhang, Hui); Zheng, J (Zheng, Jie); Wang, W (Wang, Wei); Fan, Z (Fan, Zhou); Niu, HB (Niu, Hubiao); Chen, YY (Chen, Yuan-Yuan); Lu, H (Lu, Hao); Peng, XY (Peng, Xiyan); Li, K (Li, Kai); Guo, DF (Guo, Di-Fu)
ASTRONOMICAL JOURNAL
卷: 155 期: 2 文献号: 73
The Kepler-9 system harbors three known transiting planets. The system holds significant interest for several reasons. First, the outer two planets exhibit a period ratio that is close to a 2: 1 orbital commensurability, with attendant dynamical consequences. Second, both planets lie in the planetary mass "desert" that is generally associated with the rapid gas agglomeration phase of the core accretion process. Third, there exist attractive prospects for accurately measuring both the sky-projected stellar spin-orbit angles as well as the mutual orbital inclination between the planets in the system. Following the original Kepler detection announcement in 2010, the initially reported orbital ephemerides for Kepler-9. b and c have degraded significantly, due to the limited time base-line of observations on which the discovery of the system rested. Here, we report new ground-based photometric observations and extensive dynamical modeling of the system. These efforts allow us to photometrically recover the transit of Kepler-9. b and thereby greatly improve the predictions for upcoming transit mid-times. Accurate ephemerides of this system are important in order to confidently schedule follow-up observations of this system, for both in-transit Doppler measurements as well as for atmospheric transmission spectra taken during transit.

第 225 条，共 248 条

New open cluster candidates discovered in the XSTPS-GAC survey

Guo, JC (Guo, Jin-Cheng); Zhang, HW (Zhang, Hua-Wei); Zhang, HH (Zhang, Hui-Hua); Liu, XW (Liu, Xiao-Wei); Yuan, HB (Yuan, Hai-Bo); Huang, Y (Huang, Yang); Wang, S (Wang, Song); Chen, L (Chen, Li); Zhao, HB (Zhao, Hai-Bin); Liu, JF (Liu, Ji-Feng); Chen, BQ (Chen, Bing-Qiu); Xiang, MS (Xiang, Mao-Sheng); Tian, ZJ (Tian, Zhi-Jia); Huo, ZY (Huo, Zhi-Ying); Wang, C (Wang, Chun)
RESEARCH IN ASTRONOMY AND ASTROPHYSICS
卷: 18 期: 3 文献号: 32
The Xuyi Schmidt Telescope Photometric Survey of the Galactic Anti-center (XSTPS-GAC) is a photometric sky survey that covers nearly 6000 deg(2) towards the Galactic Anti-center (GAC) in the g, r, i bands. Half of its survey field is located on the Galactic Anti-center disk, which makes XSTPS-GAC highly suitable to search for new open clusters in the GAC region. In this paper, we report new open cluster candidates discovered in this survey, as well as properties of these open cluster candidates, such as age, distance and reddening, derived by isochrone fitting in the color-magnitude diagram (CMD). These open cluster candidates are stellar density peaks detected in the star density maps by applying the method from Koposov et al. Each candidate is inspected in terms of its true color image composed from three XSTPS-GAC band images. Then its CMD is checked, in order to identify whether the central

region stars have a clear isochrone-like trend differing from background stars. The parameters derived from isochrone fitting for these candidates are mainly based on three band photometry of XSTPS-GAC. Moreover, when these new candidates are able to be seen clearly in 2MASS data, their parameters are also derived based on the 2MASS (J - H, J) CMD. There are a total of 320 known open clusters rediscovered and 24 new open cluster candidates discovered in this work. Furthermore, the parameters of these new candidates, as well as another 11 previously known open clusters, are properly determined for the first time.

第 226 条，共 248 条

Fundamentals of the orbit and response for TianQin

Hu, XC (Hu, Xin-Chun); Li, XH (Li, Xiao-Hong); Wang, Y (Wang, Yan); Feng, WF (Feng, Wen-Fan); Zhou, MY (Zhou, Ming-Yue); Hu, YM (Hu, Yi-Ming); Hu, SC (Hu, Shou-Cun); Mei, JW (Mei, Jian-Wei); Shao, CG (Shao, Cheng-Gang)
CLASSICAL AND QUANTUM GRAVITY
卷: 35 期: 9 文献号: 095008
TianQin is a space-based laser interferometric gravitational wave detector aimed at detecting gravitational waves at low frequencies (0.1 mHz-1 Hz). It is formed by three identical drag-free spacecrafts in an equilateral triangular constellation orbiting around the Earth. The distance between each pair of spacecrafts is approximately 1.7 x 10(5) km. The spacecrafts are interconnected by infrared laser beams forming up to three Michelson-type interferometers. The detailed mission design and the study of science objectives for the TianQin project depend crucially on the orbit and the response of the detector. In this paper, we provide the analytic expressions for the coordinates of the orbit for each spacecraft in the heliocentric-ecliptic coordinate system to the leading orders. This enables a sufficiently accurate study of science objectives and data analysis, and serves as a first step to further orbit design and optimization. We calculate the response of a single Michelson detector to plane gravitational waves in arbitrary waveform which is valid in the full range of the sensitive frequencies. It is then used to generate the more realistic sensitivity curve of TianQin. We apply this model on a reference white-dwarf binary as a proof of principle.

第 227 条，共 248 条

Limits on radio emission from meteors using the MWA

Zhang, X (Zhang, X.); Hancock, P (Hancock, P.); Devillepoix, HAR (Devillepoix, H. A. R.); Wayth, RB (Wayth, R. B.); Beardsley, A (Beardsley, A.); Crosse, B (Crosse, B.); Emrich, D (Emrich, D.); Franzen, TMO (Franzen, T. M. O.); Gaensler, BM (Gaensler, B. M.); Horsley, L (Horsley, L.); Johnston-Hollitt, M (Johnston-Hollitt, M.); Kaplan, DL (Kaplan, D. L.); Kenney, D (Kenney, D.); Morales, MF (Morales, M. F.); Pallot, D (Pallot, D.); Steele, K (Steele, K.); Tingay, SJ (Tingay, S. J.); Trott, CM (Trott, C. M.); Walker, M (Walker, M.); Williams, A (Williams, A.); Wu, C (Wu, C.); Ji, JH (Ji, Jianghui); Ma, YH (Ma, Yuehua)
MONTHLY NOTICES OF THE ROYAL ASTRONOMICAL SOCIETY
卷: 477 期: 4 页: 5167-5176
Recently, low-frequency, broad-band radio emission has been observed accompanying bright meteors by the Long Wavelength Array (LWA). The broad-band spectra between 20 and 60MHz were captured for several events, while the spectral index (dependence of flux density on frequency, with S-nu proportional to nu(alpha)) was estimated to be -4 +/- 1 during the peak of meteor afterglows. Here we present a survey of meteor emission and other transient events using the Murchison Wide Field Array (MWA) at 72-103 MHz. In our 322 h survey, down to a 5 sigma detection threshold of 3.5 Jy beam(-1), no transient candidates were identified as intrinsic emission from meteors. We derived an upper limit of -3.7 (95 per cent confidence limit) on the spectral index in our frequency range. We also report detections of other transient events, such as reflected FM broadcast signals from small satellites, conclusively demonstrating the ability of the MWA to detect and track space debris on scales as small as 0.1 m in low Earth orbits.

第 228 条，共 248 条

Dynamical properties and acceleration of hierarchical dust in the vicinity of comet 67P/Churyumov-Gerasimenko

Skorov, Y (Skorov, Yu.); Reshetnyk, V (Reshetnyk, V.); Rezac, L (Rezac, L.); Zhao, Y (Zhao, Y.); Marschall, R (Marschall, R.); Blum, J (Blum, J.); Hartogh, P (Hartogh, P.)
MONTHLY NOTICES OF THE ROYAL ASTRONOMICAL SOCIETY
卷: 477 期: 4 页: 4896-4907
A significant fraction of cometary dust grains leaving the nucleus surface are extremely porous and fluffy particles as revealed by recent observation from the Rosetta mission. In this paper our aim is to investigate the dynamics of such grains when subjected to a gas flow, representing the cometary outgassing. We perform numerical experiments to quantify how the internal porous texture is reflected in quantities such as effective cross-section, gas drag coefficient, and light scattering efficiency. We also derive particle speeds for the different types of aggregates as a function of radial distance and compare them to the observations by the GIADA instrument. Using our original method for constructing hierarchical aggregates we increase the level of aggregation to reach particle sizes up to few millimeters, consistent with the observations. In addition, a non-constant gas velocity is now considered in the framework of free molecular as well as fully collisional flow models, and radiation pressure calculations use the effective medium theory appropriate for such particles. These improvements lead us to conclude that dynamical models should account for accelerating gas flow, which leads to a smaller terminal speed of fluffy dust grains. Secondly, solar radiation pressure calculated based on the Mie theory approximation can lead to orders of magnitude error for the very porous particles, instead the effective medium theory should be used. Finally, although numerical simulations can reproduce the GIADA measurements of dust speeds, we cannot conclude that there exists a preferred model of porous particles build as a ballistic cluster aggregate.

Laboratory for Planetary Science and Deep Space Exploration

第 229 条，共 248 条

Compositional Imprints in Density-Distance-Time: A Rocky Composition for Close-in Low-mass Exoplanets from the Location of the Valley of Evaporation

Jin, S (Jin, Sheng); Mordasini, C (Mordasini, Christoph)
ASTROPHYSICAL JOURNAL
卷: 853 期: 2 文献号: 163
We use an end-to-end model of planet formation, thermodynamic evolution, and atmospheric escape to investigate how the statistical imprints of evaporation depend on the bulk composition of planetary cores (rocky versus icy). We find that the population-wide imprints like the location of the "evaporation valley" in the distance-radius plane and the corresponding bimodal radius distribution clearly differ depending on the bulk composition of the cores. Comparison with the observed position of the valley suggests that close-in low-mass Kepler planets have a predominantly Earth-like rocky composition. Combined with the excess of period ratios outside of MMR, this suggests that low-mass Kepler planets formed inside of the water iceline but were still undergoing orbital migration. The core radius becomes visible for planets losing all primordial H/He. For planets in this " triangle of evaporation" in the distance-radius plane, the degeneracy in composition is reduced. In the observed planetary mass-mean density diagram, we identify a trend to more volatile-rich compositions with an increasing radius (R/R-circle plus less than or similar to 1.6 rocky; 1.6-3.0 ices, and/or H/He; greater than or similar to 3: H/He). The mass-density diagram contains important information about formation and evolution. Its characteristic broken V-shape reveals the transitions from solid planets to low-mass core-dominated planets with H/He and finally to gas-dominated giants. Evaporation causes the density and orbital distance to be anticorrelated for low-mass planets in contrast to giants, where closer-in planets are less dense, likely due to inflation. The temporal evolution of the statistical properties reported here will be of interest for the PLATO 2.0 mission, which will observe the temporal dimension.

第 230 条，共 248 条

Study on Rotational Parameters for Asteroid 4179 Toutatis from Chang'e-2's Close Flyby

Zhao, YH (Zhao, Yuhui); Ji, JH (Ji, Jianghui)
SERENDIPITIES IN THE SOLAR SYSTEM AND BEYOND
卷: 513 页: 111-114
This paper shows a review of the determination of rotational parameters of Toutatis based on the observational results from Chang'e-2's close flyby in Dec 2012. We use the 3-D shape model derived from ground-based radar observations to determine the 3-1-3 Euler angles at the flyby epoch, which are evaluated to be -20.1 degrees +/- 1, 27.6 degrees +/- 1 degrees and 42.2 degrees +/- 1 degrees. Spin and precession periods are evaluated to be 5.38 +/-. 0.03 days and 7.40 +/- 0.03 days, respectively. The large value of tumbling angle (angle between angular momentum axis and spin axis) caused the significant amplitude of Toutatis' tumbling attitude observed from Earth.
会议名称: Symposium Celebrating Prof. Wing-Huen Ip's 70th Birthday - Serendipities in the Solar System and Beyond
会议日期: JUL 10-13, 2017

第 231 条，共 248 条

云南保山地块香山组和丁家寨组沉积序列与碳同位素研究

罗亮王冬兵尹福光廖世勇任飞宁括步唐渊
沉积学报
通过对保山地块北部西邑地区下石炭统香山组和下二叠统丁家寨组详细的野外剖面实测与钻孔编录,并结合层序地层学、沉积相以及碳氧同位素分析结果认为,下石炭统香山组自下向上可分为三个岩性段,分别对应台前斜坡下部、台前斜坡上部、碳酸盐岩台地三种沉积环境。下二叠统丁家寨组为滨岸冰水沉积,下部为冰碛含砾钙质杂砂岩,发育落石构造。下石炭统香山组 δ13CPDB 值自下而上逐渐升高,环境可能较稳定,有机质埋藏增加。综合前人古地磁、生物区系对比、大地构造学等研究成果认为早石炭世保山地块较稳定,仍属冈瓦纳大陆北缘。丁家寨组冰碛含砾钙质杂砂岩结束后 δ13CPDB 值出现强烈负偏,与研究区冰期结束、早二叠世初次温度上升、大量玄武岩喷发等时限高度一致,共同说明了保山地块在早二叠世开始从冈瓦纳大陆北缘裂解出来,并开始向北漂移。该项研究的开展为探讨 Submasu 地块晚古生代的古海洋、古地理和气候演化具有重要意义,为全球同时期碳氧同位素数据库提供了新资料。

第 232 条，共 248 条

基于二叉树的太阳系小天体数值历表建立方法

胡寿村 季江徽
天文学报
在小天体深空探测任务中,经常需要调用力模型较完备的精确小天体数值历表,然而由于部分小天体可能有较大的轨道偏心率以及存在近距离飞越大行星的可能,导致传统的等区间分段切比雪夫多项式插值方法不适用于构建这些小天体的数值历表.在传统方法基础上采用结合误差自适应的二分法对原始轨道进行分段,并采用二叉树结构来组织所有的分段区间,能解决历表读取中的系数反查问题.以大偏心率近地小行星 4179 Toutatis 和 3200 Phaethon、大偏心率彗星 2P/Encke 以及将近距离飞越地球的 99942 Apophis 小行星为例,通过数值仿真证实了该算法的有效性.由于该方法没有对小天体的轨道性质做任何要求,因此能够作为构建太阳系小天体数值历表的通用方法,可应用于大量目标小天体的精确轨道设计中

第 233 条，共 248 条

基于调频广播信号的空间碎片探测方法

张翔 HANCOCK PaulWAYTH Randall 季江徽马月华
天文学报
空间碎片对人造卫星和飞船的威胁日益增长.为了保持一个安全的空间环境,需要寻找成本低而又准确的空间天体探测和追踪方法.前些年,使用射电望远镜作为被动雷达,探测空间碎片反射的调频广播信号的可能性已经被讨论过,并且月球和国际空间站反射的信号已经被默奇森大视场射电阵(MWA)探测到.介绍 MWA 探测到的卫星反射广播信号事件,论证 MWA 有能力探测 600 km 高度处 0.1 m 量级大小的空间碎片,位置误差在 10 km 左右.
空间碎片对人造卫星和飞船的威胁日益增长.为了保持一个安全的空间环境,需要寻找成本低而又准确的空间天体探测和追踪方法.前些年,使用射电望远镜作为被动雷达,探测空间碎片反射的调频广播信号的可能性已经被讨论过,并且月球和国际空间站反射的信号已经被默奇森大视场射电阵(MWA)探测到.介绍 MWA 探测到的卫星反射广播信号事件,论证 MWA 有能力探测 600 km 高度处 0.1 m 量级大小的空间碎片,位置误差在 10 km 左右.。

第 234 条，共 248 条

小行星热物理及 Yarkovsky 效应和 YORP 效应的研究进展

姜浩轩 季江徽

小行星热物理的研究是近年来小行星研究中一个前沿方向。简单阐述了在小行星热物理这一研究领域中常用的热物理模型,利用这些热物理模型并结合空间或地面红外望远镜的观测数据,可获得小行星的一些热物理参数,如热惯量、几何反照率、有效直径、表面粗糙度、表面温度等。介绍了小行星的形状模型及红外观测,还介绍了利用这些模型得到的部分小行星热物理参数。通过这些热物理参数,可进一步研究小行星的 Yarkovsky 效应和 YORP 效应等,甚至可为人造航天器着陆小行星表面及小行星采样返回任务提供相关科学信息。

第 235 条，共 248 条

New Constraints on Turbulence and Embedded Planet Mass in the HD 163296 Disk from Planet-Disk Hydrodynamic Simulations

Liu, SF (Liu, Shang-Fei); Jin, S (Jin, Sheng); Li, ST (Li, Shengtai); Isella, A (Isella, Andrea); Li, H (Li, Hui)

ASTROPHYSICAL JOURNAL

卷: 857 期: 2 文献号: 87

Recent Atacama Large Millimeter and Submillimeter Array (ALMA) observations of the protoplanetary disk around the Herbig Ae star HD 163296 revealed three depleted dust gaps at 60, 100, and 160 au in the 1.3 mm continuum as well as CO depletion in the middle and outer dust gaps. However, no CO depletion was found in the inner dust gap. To examine the planet-disk interaction model, we present results of 2D two fluid (gas + dust) hydrodynamic simulations coupled with 3D radiative transfer simulations. To fit the high gas-to-dust ratio of the first gap, we find that the Shakura-Sunyaev viscosity parameter alpha must be very small (less than or similar to 10(-4)) in the inner disk. On the other hand, a relatively large alpha (similar to 7.5 x 10(-3)) is required to reproduce the dust surface density in the outer disk. We interpret the variation of alpha as an indicator of the transition from an inner dead zone to the outer magnetorotational instability (MRI) active zone. Within similar to 100 au, the HD 163296 disk's ionization level is low, and non-ideal magnetohydrodynamic effects could suppress the MRI, so the disk can be largely laminar The disk's ionization level gradually increases toward larger radii, and the outermost disk (r > 300 au) becomes turbulent due to MRI. Under this condition, we find that the observed dust continuum and CO gas line emissions can be reasonably fit by three half-Jovian-mass planets (0.46, 0.46, and 0.58 M-J) at 59, 105, and 160 au, respectively.

第 236 条，共 248 条

Formation of S-type planets in close binaries: scattering-induced tidal capture of circumbinary planets

Gong, YX (Gong, Yan-Xiang); Ji, JH (Ji, Jianghui)

MONTHLY NOTICES OF THE ROYAL ASTRONOMICAL SOCIETY

卷: 478 期: 4 页: 4565-4574

Although several S-type and P-type planets in binary systems were discovered in past years, S-type planets have not yet been found in close binaries with an orbital separation not more than 5 au. Recent studies suggest that S-type planets in close binaries may be detected through high-accuracy observations. However, nowadays planet formation theories imply that it is difficult for S-type planets in close binaries systems to form in situ. In this work, we extensively perform numerical simulations to explore scenarios of planet-planet scattering among circumbinary planets and subsequent tidal capture in various binary configurations, to examine whether the mechanism can play a part in producing such kind of planets. Our results show that this mechanism is robust. The maximum capture probability is similar to 10 per cent, which can be comparable to the tidal capture probability of hot Jupiters in single star systems. The capture probability is related to binary configurations, where a smaller eccentricity or a low mass ratio of the binary will lead to a larger probability of capture, and vice versa. Furthermore, we find that S-type planets with retrograde orbits can be naturally produced via capture process. These planets on retrograde orbits can help us distinguish in situ formation and post-capture origin for S-type planet in close binaries systems. The forthcoming missions (PLATO) will provide the opportunity and feasibility to detect such planets. Our work provides several suggestions for selecting target binaries in search for S-type planets in the near future.

第 237 条，共 248 条

The formation mechanism of 4179 Toutatis' elongated bilobed structure in a close Earth encounter scenario

Hu, SC (Hu, Shoucun); Ji, JH (Ji, Jianghui); Richardson, DC (Richardson, Derek C.); Zhao, YH (Zhao, Yuhui); Zhang, Y (Zhang, Yun)

MONTHLY NOTICES OF THE ROYAL ASTRONOMICAL SOCIETY

卷: 478 期: 1 页: 501-515

The optical images of near-Earth asteroid 4179 Toutatis acquired by Chang'e-2 spacecraft show that Toutatis has an elongated contact binary configuration, with the contact point located along the long axis. We speculate that such configuration may have resulted from a low-speed impact between two components. In this work, we performed a series of numerical simulations and compared the results with the optical images, to examine the mechanism and better understand the formation of Toutatis. Herein, we propose a scenario that an assumed separated binary precursor could undergo a close encounter with Earth, leading to an impact between the primary and secondary, and the elongation is caused by Earth's tide. The precursor is assumed to be a doubly synchronous binary with a semimajor axis of 4R(p) (radius of primary) and the two components are represented as spherical cohesionless self-gravitating granular aggregates. The mutual orbits are simulated in a Monte Carlo routine to provide appropriate parameters for our N-body simulations of impact and tidal distortion. We employ the PK DG RAV package with a soft-sphere discrete element method to explore the entire scenarios. The results show that contact binary configurations are natural outcomes under this scenario, whereas the shape of the primary is almost not affected by the impact of the secondary. However, our simulations further provide an elongated contact binary configuration best matching to the shape of Toutatis at an approaching distance r(p) = 1.4-1.5 R-e (Earth radius), indicative of a likely formation scenario for configurations of Toutatis-like elongated contact binaries.

Laboratory for Astrochemistry and Planetary Sciences

第 238 条，共 248 条

Dating phosphates of the strongly shocked Suizhou chondrite

Li, SL (Li, Shaolin); Hsu, WB (Hsu, Weibiao)

AMERICAN MINERALOGIST

卷: 103 期: 11 页: 1789-1799

Impacts on undifferentiated asteroidal bodies provide invaluable information for understanding the solar system evolution. Nevertheless, dating early and small-scale impact events is technically challenging. Uranium-lead (U-Pb) systematics of U-bearing phases within shock-induced melt veins (SMVs) of chondrites may be significantly disturbed by localized heating, thus providing opportunities to date these impact events. As one of the major U hosts in chondrites, apatite in the Suizhou (L6) chondrite has been compositionally and structurally modified to varying degrees by shock metamorphism. Apatite grains in the host remained largely intact during the impact and have recorded the initial thermal cooling time (similar to 4550 Ma) on their parent body. Apatite grains in regions less than 100 mu m bordering the SMVs or in relatively "cold" regions within the SMVs were partly decomposed to tuite, driven by the localized transient heating within the SMVs. Their U-Pb systematics were disrupted to varying extents. Apatite in regions close to the center of the SMVs has been completely transformed to tuite, which yields an age of 4481 +/- 30 Ma (2 sigma), providing an upper limit to the impact event. This study clearly demonstrates that by integrating in situ U-Pb isotope analysis with detailed microstructural and compositional analysis of phosphates, it is possible to deduce the timing of early and small-scale celestial impact events, and hence create a more comprehensive understanding of the impact history of the solar system.

第 239 条，共 248 条

Multiple impact events on the L-chondritic parent body: Insights from SIMS U-Pb dating of Ca-phosphates in the NWA 7251 L-melt breccia

Li, Y (Li, Ye); Hsu, WB (Hsu, Weibiao)

METEORITICS & PLANETARY SCIENCE

卷: 53 期: 5 页: 1081-1095

Here we report in situ secondary ionization mass spectrometry Ca-phosphate U-Pb ages for an L-impact melt breccia (NWA 7251), which are integrated with petrological and mineral chemical studies of this meteorite. NWA 7251 is a heavily shocked rock that is composed mainly of the chondrite host, impact melt portion, and melt veins (crosscutting and pervasive type). The host is an L4 chondrite that has been shocked to S4. The impact melt portion has a fine-grained igneous texture, and is composed mainly of olivine, low-Ca pyroxene, high-Ca pyroxene, and albitic glass. The impact melt was generated at pressure of >30-35 GPa and temperature of >1300-1500 degrees C during an impact event. The Ca-phosphate grains in the host were affected by a shock heating event. Most of the Ca-phosphate grains in the melt were neocrystallized, but relatively large grains enclosed by or adjacent to metal veins or melt globules are likely inherited. The U-Pb isotopic systematics of Ca-phosphates in NWA 7251 yield an upper intercept age of 4457 +/- 56 Ma and a lower intercept age of 574 +/- 82 Ma on the normal U-Pb concordia diagram. The age of 4457 +/- 56 Ma is interpreted to be related to an early shocking event rather than the thermal metamorphism of the parent body. The impact melt and veins in NWA 7251 were generated at 574 +/- 82 Ma, resulting from disruption of the L chondrite parent body.

第 240 条，共 248 条

The nature of the L chondrite parent body's disruption as deduced from high-pressure phases in the Sixiangkou L6 chondrite

Li, SL (Li, Shaolin); Hsu, WB (Hsu, Weibiao)

METEORITICS & PLANETARY SCIENCE

卷: 53 期: 10 页: 2107-2121

The disruption of the L chondrite parent body (LCPB) at similar to 470Ma is currently the best-documented catastrophic celestial impact event, based on the large number of L chondritic materials associated with this event. Uranium-lead (U-Pb) dating of apatite and its high-pressure decomposition product, tuite, in the Sixiangkou L6 chondrite provides a temporal link to this event. The U-Pb system of phosphates adjacent to shock melt veins was altered to varying degrees and the discordance of the U-Pb system correlates closely with the extent of apatite decomposition. This suggests that the U-Pb system of apatite could be substantially disturbed by high-temperature pulse during shock compression from natural impacts, at least on the scale of mineral grains. Although many L chondrites can be temporally related to the catastrophic LCPB impact event, the shock conditions experienced by each individual meteorite vary. This could be due to the different geologic settings of these meteorites on their parent body. The shock pressure and duration derived from most meteorites may only reflect local shock features rather than the impact conditions, although they could provide lower limits to the impact conditions. The Sixiangkou shock duration (similar to 4s), estimated from high-pressure transformation kinetics, provides a lower limit to the high-pressure pulse of the LCPB disruption impact. Combined with available literature data of L chondrites associated with this impact event, our results suggest that the LCPB suffered a catastrophic collision with a large projectile (with a diameter of at least 18-22km) at a low impact velocity (5-6kms(-1)). This is consistent with astronomical estimates based on the dynamical evolution of L chondritic asteroids.

第 241 条，共 248 条

Petrogenesis of ore-bearing porphyry in non-subduction setting: a case study of the Eocene potassic intrusions in the western Yangtze Block

Liu, Z (Liu, Zheng); Liao, SY (Liao, Shi-Yong); Zhou, Q (Zhou, Qing); Zhang, X (Zhang, Xin)

MINERALOGY AND PETROLOGY

卷: 112 期: 6 页: 801-817

In the western Yangtze Block, abundant Eocene (similar to 38-34 Ma) potassic adakite-like intrusions and associated porphyry copper deposits are exposed in non-subduction setting, including Machangjing, Beiya, Binchuan, Habo and Tongchang intrusions. All these ore-bearing porphyries share many geochemical characteristics of adakite such as depletion in heavy rare earth elements (HREEs), enrichment in Sr and Ba, absence of negative Eu anomalies, high SiO2, Al2O3, Sr/Y, La/Yb and low Y, Yb contents. They also exhibit affinities of potassic rocks, e.g., alkali-rich, high K2O/Na2O ratios and enrichment in light rare earth elements (LREEs) and large ion lithophile elements (LILEs). Their Sr-Nd isotopic ratios are similar to coeval shoshonitic lamprophyres. Geochemical data indicate that they were probably produced by partial melting of newly underplated potassic rocks sourced from a modified and enriched lithospheric mantle. These underplated rocks have elevated oxygen fugacity, water and copper contents, with high metallogenic potential. We propose that all the studied potassic rocks were emplaced in a post-collisional setting, associated with the local removal of lithospheric mantle.

Planetary Spectroscopy Group

第 242 条，共 248 条

The Absolute Reflectance and New Calibration Site of the Moon

Wu, YZ (Wu, Yunzhao); Wang, ZC (Wang, Zhenchao); Cai, W (Cai, Wei); Lu, Y (Lu, Yu)

ASTRONOMICAL JOURNAL

卷: 155 期: 5 文献号: 213

How bright the Moon is forms a simple but fundamental and important question. Although numerous efforts have been made to answer this question such as use of sophisticated electro-optical measurements and suggestions for calibration sites, the answer is still debated. An in situ measurement with a calibration panel on the surface of the Moon is crucial for obtaining the accurate absolute reflectance and resolving the debate. China's Chang'E-3 (CE-3) "Yutu" rover accomplished this type of measurement using the Visible-Near Infrared Spectrometer (VNIS). The measurements of the VNIS, which were at large emission and phase angles, complement existing measurements for the range of photometric geometry. The in situ reflectance shows that the CE-3 landing site is very dark with an average reflectance of 3.86% in the visible bands. The results are compared with recent mission instruments: the Lunar Reconnaissance Orbiter Camera (LROC) Wide Angle Camera (WAC), the Spectral Profiler (SP) on board the SELENE, the Moon Mineralogy Mapper (M-3) on board the Chandrayaan-1, and the Chang'E-1 Interference Imaging Spectrometer (IIM). The differences in the measurements of these instruments are very large and indicate inherent differences in their absolute calibration. The M-3 and IIM measurements are smaller than LROC WAC and SP, and the VNIS measurement falls between these two pairs. When using the Moon as a radiance source for the on-orbit calibration of spacecraft instruments, one should be cautious about the data. We propose that the CE-3 landing site, a young and homogeneous surface, should serve as the new calibration site.

第 243 条，共 248 条

风暴洋晚期玄武岩厚度及规模研究

胡晓依 陈媛 张迅与 李少林 夏学齐 吴昀昭

天文学报

风暴洋是月球最大的月海,分布着大面积的晚期(爱拉托逊纪)玄武岩,是研究月球晚期岩浆活动的良好场所.了解月球晚期玄武岩的厚度、体积乃至喷发通量对于了解风暴洋乃至月球晚期的热演化具有重要意义.爱拉托逊纪玄武岩富橄榄石和钛铁矿,其下伏的雨海纪玄武岩富辉石,这两类玄武岩的光谱特征差异十分明显,极易通过高光谱数据进行地层识别.基于月球矿物制图仪(Moon Mineralogy Mapper,M3)数据判断撞击坑是否穿透上覆地层,利用撞击坑挖掘法研究风暴洋爱拉托逊纪玄武岩的厚度,并绘制风暴洋地区晚期玄武岩的高分辨率厚度分布图.结果表明:风暴洋爱拉托逊纪玄武岩的平均厚度约为(24±2)–(88±2)m,最大厚度出现在阿利斯塔克坑(Aristarchus)西部,大多超过 60 m,最小厚度值分布于研究区最南部,厚度约为 28–31 m.嫦娥五号预定着陆区(吕姆克山,Mons Rumker)附近的厚度约为 31–38 m.马里厄斯坑(Marius)以东的区域厚度约为 35–45 m,远小于 Weider 等人所估测的 100–300 m.风暴洋地区暴露的爱拉托逊纪玄武岩总体积约为 1.39×10~4km3,仅占风暴洋地区玄武岩总体积的 1.6%,表明爱拉托逊纪玄武岩浆活动较之雨海纪已极大减弱。

第 244 条，共 248 条

月球澄海玄武岩矿物成分研究

蔡伟 李少林 卢瑜 吴昀昭

天文学报

月球玄武岩的矿物组成反映了源区的化学成分和岩浆的结晶环境.了解月海玄武岩的矿物组成对研究月球岩浆演化具有重要意义.选择澄海为研究区,综合利用光谱、地形、元素等多源遥感数据将澄海划分为 55 个地质单元.基于月球矿物制图仪(Moon Mineralogy Mapper, M~3)数据,提取 84 条新鲜撞击坑光谱曲线,计算吸收中心波长、波段面积比等光谱参数.通过分析光谱吸收特征,获得澄海玄武岩镁铁质矿物的空间变化特征.研究结果表明,澄海玄武岩镁铁质矿物主要为高钙单斜辉石.澄海中部和南部地质单元具有较低的橄榄石/辉石比,东部和西部地质单元具有较高的橄榄石/辉石比.从东、西部到中部区域,橄榄石/辉石比例逐渐降低

第 245 条，共 248 条

Mineralogy of Mare Frigoris

Zhang Xiaomeng; Zhang Xunyu; Chen Yuan; Cai Wei; Lu Yu; Wu Yunzhao

Earth Science Frontiers

卷: 25 期: 1 页: 314-324

Mineral composition of mare basalt reflects chemical composition of magma source together with physical and

chemical environments of the rock's formation, which is significant for both researches of origin and evolution of the Moon and exploitation and utilization of lunar resource.In this study, an elongated mare was chosen as our research area, and Moon Mineralogy Mapper (M~3) hyperspectral data was applied to mineral spatial distribution.Mare Frigoris was mapped and characterized into 25 basalt units based on multi-source remote sensing data including spectrum, terrain and elements abundance.We extracted 169 spectra curves of fresh craters from M~3 hyperspectral image.Spectral parameters such as absorption center and absorption band area ratio were obtained through data processing.Mafic mineral variation of Mare Frigoris basalt was acquired by analyzing reflectance spectra's absorption features.Basalt units in eastern Frigoris are older, with mafic mineral dominated by clinopyroxene containing lower CaO compared to returned lunar samples, which is similar to older basalt units in Mare Serenitatis and Mare Imbrium.Basalt units of western Frigoris and Sinus Roris are younger and rich in olivine.And the late stage basalts in Oceanus Procellarum and Mare Imbrium show the same feature too.These wide-spread olivine-rich basalts suggest the uniqueness in the global evolution of the moon.Geographically speaking, Frigoris is an individual mare, but its source region may have connections with mares around in consideration of mineral differences between western and eastern Frigoris as well as mineral similarities with mares at the same location.

第 246 条，共 248 条

Geology, tectonism and composition of the northwest Imbrium region

Wu, YZ (Wu, Yunzhao); Li, L (Li, Lin); Luo, XX (Luo, Xiaoxing); Lu, Y (Lu, Yu); Chen, Y (Chen, Yuan); Pieters, CM (Pieters, Cade M.); Basilevsky, AT (Basilevsky, Alexander T.); Head, JW (Head, James W.)

ICARUS

卷: 303 页: 67-90

The objective of this study is to explore the regional geology of the northwest Imbrium region in which the Chang'E-3 (CE-3) landing site is located. CE-3 successfully landed on December 14, 2013 on the un-sampled Eratosthenian basalts whose study is important for understanding the evolution of the Moon. New geologic and structural maps of the research area were produced through the integrated analysis of diverse datasets. The highlands surrounding Imbrium differ from typical Farside Highlands Terrain (FHT). The Iridum highland region (as well as the surrounding Imbrium region) exhibits elevated concentrations of Fe, and abundant local exposures of low-Ca pyroxene and olivine bearing lithologies. In this study these highlands are named as mafic highlands (MH). Our dating results using crater size-frequency distributions (CSFDs) show that the Iridum basin (hosting Sinus Iridum) was formed-3.8 Ga, shortly following the Imbrium basin formation and before the last large multiringed basin, Orientale. The Eratosthenian period of lunar basalt eruptions, which lasted longer than other stratigraphic units, is suggested to divide into the Lower Eratosthenian mare (LEm) and Upper Eratosthenian mare (UEm) units. This subdivision is based on whether lava fronts can be clearly seen or not and the age separating the units is 2.35 Ga. The mafic mineralogy of the mare basalts in Imbrium is characterized by abundant olivine in the Eratosthenian-aged basalts and average pyroxene compositions near pigeonite to sub-calcic augite in the Imbrian and Em1 units. The thickness of individual lava for UEm units is 8-11 m, indicative of high effusion rates. The thickness of the Em3 unit ranges from similar to 17 m to similar to 45 m with lesser thickness to the west and greater thickness in the interior and to the east. The estimated volume and average flux of the Eratosthenian-aged basalts are greater than previously thought. The presence of these youngest basalts in the Procellarum-KREEP terrain (PKT) is hypothesized to be a causal relationship, with the PKT terrain reducing the thickness of the lithosphere and permitting preferential dike emplacement and extrusion there. We speculate that high-Ti and olivine-rich composition in late stage basalts may be consistent with low Si and high Ti and low degrees of partial melting. Large numbers of sinuous rilles and small ridges are identified and mapped. Many young ridges were found inside Imbrium, suggesting a very extended period (at least as young as the last 50 Ma) of the Moon's tectonic activity. The distinct compositions of both highlands and mare basalts and extended tectonism emphasize how the Imbrium basin is an important area for understanding the Moon.

第 247 条，共 248 条

Spectroscopic observations of the Moon at the lunar surface

Wu, YZ (Wu, Yunzhao); Hapke, B (Hapke, Bruce)

EARTH AND PLANETARY SCIENCE LETTERS

卷: 484 页: 145-153

The Moon's reflectance spectrum records many of its important properties. However, prior to Chang'E-3 (CE-3), no spectra had previously been measured on the lunar surface. Here we show the in situ reflectance spectra of the Moon acquired on the lunar surface by the Visible-Near Infrared Spectrometer (VNIS) onboard the CE-3 rover. The VNIS detected thermal radiation from the lunar regolith, though with much shorter wavelength range than typical thermal radiometer. The measured temperatures are higher than expected from theoretical model, indicating low thermal inertia of the lunar soil and the effects of grain facet on soil temperature in submillimeter scale. The in situ spectra also reveal that 1) brightness changes visible from orbit are related to the reduction in maturity due to the removal of the fine and weathered particles by the lander's rocket exhaust, not the smoothing of the surface and 2) the spectra of the uppermost soil detected by remote sensing exhibit substantial differences with that immediately beneath, which has important implications for the remote compositional analysis. The reflectance spectra measured by VNIS not only reveal the thermal, compositional, and space-weathering properties of the Moon but also provide a means for the calibration of optical instruments that view the surface remotely.

第 248 条，共 248 条

The Thickness and Volume of Young Basalts Within Mare Imbrium

Chen, Y (Chen, Yuan); Li, CL (Li, Chunlai); Ren, X (Ren, Xin); Liu, JJ (Liu, Jianjun); Wu, YZ (Wu, Yunzhao); Lu, Y (Lu, Yu); Cai,

W (Cai, Wei); Zhang, XY (Zhang, Xunyu)

JOURNAL OF GEOPHYSICAL RESEARCH-PLANETS

卷: 123 期: 2 页: 630-645

Basaltic volcanism is one of the most important geologic processes of the Moon. Research on the thickness and volume of late-stage basalts of Mare Imbrium helps better understand the source of lunar volcanism and eruption styles. Based on whether apparent flow fronts exist or not, the late-stage basalts within Mare Imbrium were divided into two groups, namely, Upper Eratosthenian basalts (UEm) and Lower Eratosthenian basalts (LEm). Employing the topographic profile analysis method for UEm and the crater excavation technique for LEm, we studied the thickness and distribution of Eratosthenian basalts in Mare Imbrium. For the UEm units, their thicknesses were estimated to be similar to 16-34 (2)m with several layers of individual lava (similar to 8-13m) inside. The estimated thickness of LEm units was similar to 14-45(1)m, with a trend of reducing thickness from north to south. The measured thickness of late-stage basalts around the Chang'E-3 landing site (similar to 371m) was quite close to the results acquired by the lunar penetrating radar carried on board the Yutu Rover (similar to 35m). The total volume of the late-stage basalts in Mare Imbrium was calculated to be similar to 8,671 (320)km(3), which is 4 times lower than that of Schaber's estimation (similar to 4x10(4)km(3)). Our results indicate that the actual volume is much lower than previous estimates of the final stage of the late basaltic eruption of Mare Imbrium. Together, the area flux and transport distance of the lava flows gradually decreased with time. These results suggest that late-stage volcanic evolution of the Moon might be revised.

Plain Language Summary The late stage younger than 3.1Ga volcanism of the Moon deposited large areas of basalts in Mare Imbrium and Oceanus Procellarum. These basalts have different colors (dark and blue) compared to old basalts sampled by Apollo and Luna missions. In order to understand how these young basalts erupted in Mare Imbrium, we estimated their thickness and volume using multiple data. Using detailed visible and near-infrared spectral data in combination with topographic information, we estimated the height of lava flows and the thickness of late-stage rocks excavated by impact craters. Our results indicate that these young basalts have a thickness of tens of meters and a total volume of similar to 8,671 (+/- 320)km(3). Both values are smaller than those of previous estimates, suggesting a smaller volcanic activity than previously thought. These results indicate that the magmatic activity gradually weakened in this region.

紫台历年发表论文情况

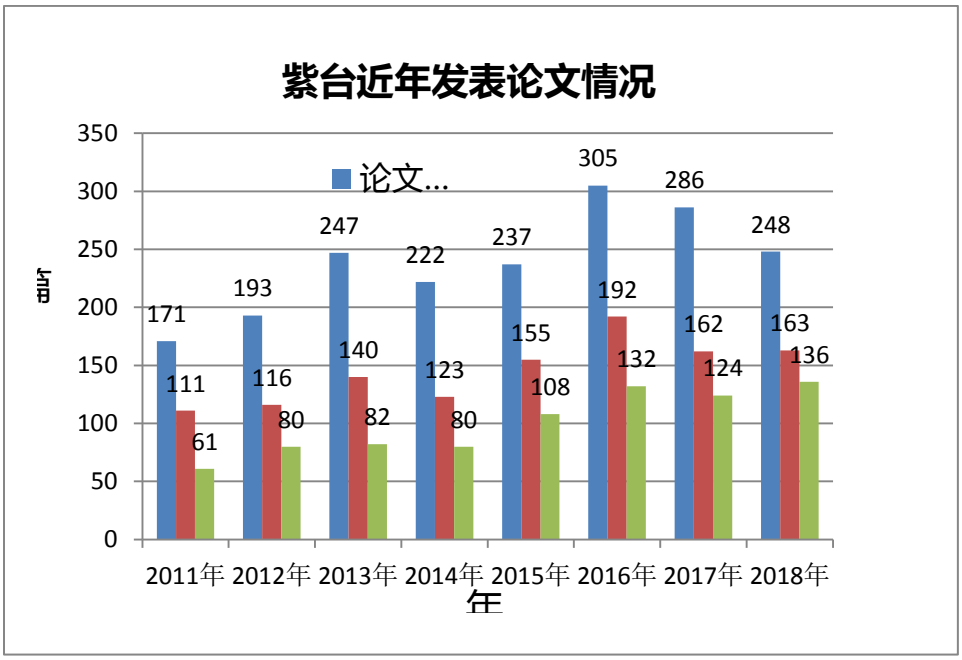

学术报告

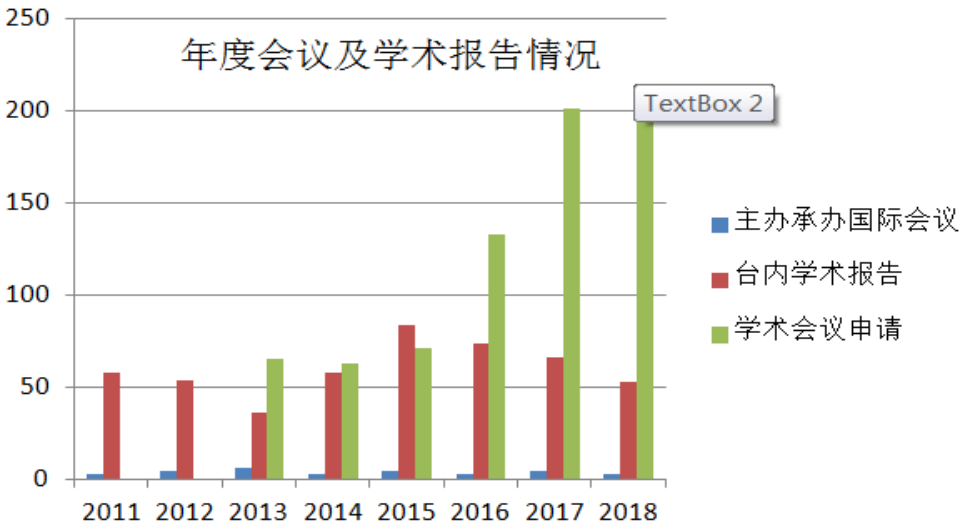

专利

2018 年专利申请统计					
序号	**申请号/专利号**	**发明名称**	**申请人**	**专利类型**	**状态**
1	2018101200766	利用磁控溅射法在硅衬底上制备氮化钛超导薄膜的方法	中国科学院紫金山天文台	发明	申请
2	201810261153X	一种无人值守柴油发电机组远程定量更换润滑油系统	中国科学院紫金山天文台	发明	申请
3	201810465855X	一种大视场巡天望远镜主焦光学系统	中国科学院紫金山天文台	发明	申请
4	2018105881988	一种大视场巡天望远镜的卡氏光学系统	中国科学院紫金山天文台	发明	申请
5	2018105881969	一种大视场巡天望远镜的三镜光学系统	中国科学院紫金山天文台	发明	申请
6	2018105932299	基于编码孔径的高灵敏度太赫兹超导光谱成像系统及系统成像方法	中国科学院紫金山天文台	发明	申请
7	2018108313962	一种远程事件同步设备	中国科学院紫金山天文台	发明	申请
8	2018108837173	一种分体式 KIDs 探测器样品封装装置	中国科学院紫金山天文台	发明	申请
9	2018108837737	一种具有 45°相移的集总元件功分器	中国科学院紫金山天文台	发明	申请
10	2018111056371	基于超导热电子探测器相干和非相干探测系统和探测方法	中国科学院紫金山天文台	发明	申请
11	2018111056579	太赫兹波段大规模阵列石墨烯探测器的多路读出系统	中国科学院紫金山天文台	发明	申请
12	2018111206665	一种大视场远紫外光谱成像仪	中国科学院紫金山天文台	发明	申请
13	201811147866X	基于有源正交混频器的 KIDs 探测器噪声测试电路及测试方法	中国科学院紫金山天文台	发明	申请
14	2018111486971	鉴频式 KIDs 探测器相位噪声测量电路系统及测量方法	中国科学院紫金山天文台	发明	申请
15	2018112870757	一种基于天文望远镜主动光学系统的复合因子优化方法	中国科学院紫金山天文台	发明	申请
16	2018113008264	大视场巡天望远镜主动光学系统实现方法	中国科学院紫金山天文台	发明	申请
17	2018115183060	自适应光学变形镜弹性模态像差表征方法	中国科学院紫金山天文台	发明	申请
18	2018112955172	低温 3GHz-9GHz 宽温区超宽带微波隔离器及应用	中国科学院紫金山天文台	发明	申请
19	2017113807050	一种基于数字摄影测量技术的高精度转动测量方法	中国科学院紫金山天文台	发明	授权

20	2016101320909	太赫兹外差阵列接收机偏置复用装置	中国科学院紫金山天文台	发明	授权
21	2015106016065	天文光学望远镜主镜侧支撑的一种 H-β复合优化法	中国科学院紫金山天文台	发明	授权
22	2016101545917	基于卡尔曼滤波的 KID 阵列探测器 S21 基线校准方法	中国科学院紫金山天文台	发明	授权
23	2015106007189	天文光学望远镜主镜轴支撑的一种变网格复合优化法	中国科学院紫金山天文台	发明	授权
24	2016105783793	一种利用环形器校准矢量场测量中移动电缆相位变化的装置及方法	中国科学院紫金山天文台	发明	授权
25	201510664582.8	低温 C 波段宽温区宽带微波隔离器及应用	中国科学院紫金山天文台	发明	授权

2018 年度发表科研论文、专著、专利一览表

团组与学科片	论文总数	第一单位论文	SCI 论文	第一单位 SCI 论文	第一单位 EI 论文	国际合作	著作	专利申请	专利授权	软件登记
宇宙伽马暴、中子星及相关物理研究团组	2	0	2	0	0	2	0	0	0	0
太阳高能及相关物理过程研究团组	10	4	10	4	0	9	0	0	0	0
太阳活动的多波段观测研究团组	12	6	12	6	0	10	0	0	0	0
宇宙高能粒子的加速和辐射研究团组	3	3	1	1	0	1	1	0	0	0
暗物质间接探测的相关物理研究团组	25	14	23	12	0	21	0	0	0	0
暗物质和空间天文实验室	32	15	24	9	0	22	0	0	0	0
紫外及 X 射线天文研究	3	2	3	2	0	3	0	0	0	0
暗物质和空间天文研究部　　合计	87	44	75	34	0	68	0	0	0	0
恒星结构、演化和脉动研究团组	4	4	2	2	0	3	0	0	0	0
南极天文中心	11	3	11	3	0	11	0	1	0	0
星系宇宙学和暗能量研究团组	23	7	22	6	0	21	0	0	0	0
星系中的恒星形成研究团组	5	1	5	1	0	5	0	0	0	0
分子云与恒星形成研究团组	6	2	6	2	0	6	0	0	0	0
星系形成与大视场巡天研究团组	9	2	8	1	0	8	0	0	0	0
高能时域天文研究团组	24	15	19	11	0	20	0	0	0	0
银河系气体分布与性质研究团组	1	1	1	1	0	1	0	0	0	0
毫米波和亚毫米波技术实验室	20	14	13	9	4	20	0	8	3	3
天文望远镜技术实验室	2	1	1	1	0	2	0	7	3	2
德令哈毫米波观测基地	3	2	2	1	0	2	0	0	0	0
南极天文和射电天文研究部　　合计	108	52	90	38	4	99	0	16	6	5
空间目标与碎片观测研究中心	10	9	3	3	1	3	0	1	0	2
卫星精密定轨及应用研究团组	2	0	2	0	0	2	0	0	0	0
应用天体力学和空间目标与碎片研究部　　合计	12	9	5	3	1	5	0	1	0	2
近地天体探测和太阳系天体研究团组	4	2	3	1	0	3	0	0	0	0
历算和天文参考系研究团组	6	6	5	5	0	1	0	0	0	0
太阳和太阳系等离子体研究团组	10	4	10	4	0	10	0	0	0	0
近地天体望远镜团组	4	0	4	0	0	4	0	0	0	0
行星科学与深空探测实验室	9	8	5	4	0	4	0	0	0	0
天体化学和行星科学实验室	4	3	4	3	0	1	0	0	0	0
盱眙天文观测站	0	0	0	0	0	0	0	0	0	0
行星光谱学研究团组	5	4	3	2	0	3	0	0	0	0
行星科学和深空探测研究部　　合计	42	27	34	19	0	26	0	0	0	0

其他	48	6	45	12	0	46	0	0	0	0
其他 **合计**	48	6	45	12	0	46	0	0	0	0
合计	297	138	249	106	5	244	0	17	6	7

国际合作与台内学术报告统计

团组与学科片	出访人次	占比	来访人次	占比	台内学术报告	占比	PMO Colloquium	占比
暗物质和空间天文								
暗物质和空间天文实验室	37	19%	0	0%		0%		
暗物质间接探测的相关物理研究	9	5%	1	1%	2	4%		
太阳高能及相关物理过程研究	8	4%	8	5%	2	4%	1	7%
太阳活动的多波段观测研究	8	4%	5	3%	2	4%		
宇宙高能粒子的加速和辐射研究	4	2%	6	4%	2	4%	1	7%
紫外及 X 射线天文研究	**4**	**2%**	**37**	**25%**	**2**	**4%**	**2**	**14%**
宇宙伽玛暴、中子星及相关物理研究	1	1%	2	1%	1	2%	2	14%
南极天文和射电天文								
南极天文中心	**1**	**1%**		**0%**				
星系宇宙学和暗能量研究团组	**7**	**4%**	**5**	**3%**	**6**	**13%**	**2**	**14%**
星系中的恒星形成研究团组	**19**	**10%**	**14**	**10%**	**10**	**21%**		
分子云与恒星形成研究团组	**13**	**7%**	**32**	**22%**	**3**	**6%**	**1**	**7%**
毫米波和亚毫米波技术实验室	24	12%	11	7%	2	**4%**	1	**7%**
德令哈毫米波观测基地		**0%**	**1**	**1%**	**1**	**2%**		
高能时域天文研究团组	**1**	**1%**	**7**	**5%**	**1**	**2%**	**1**	**7%**
银河系气体分布与性质研究团组	**2**	**1%**	**1**	**1%**	**1**	**2%**		
天文望远镜技术实验室								
星系形成与大视场巡天研究团组	**3**	**2%**	**3**	**2%**	**3**	**6%**	**1**	**7%**
基于 SKA 的宇宙学研究			**4**	**3%**	**1**	**2%**		
应用天体力学和空间目标与碎片								
空间目标与碎片观测研究	**22**	**11%**		**0%**		**0%**	**1**	**7%**
卫星精密定轨及应用研究								
行星科学和深空探测								
近地天体探测和太阳系天体研究	6	3%	1	1%				
历算和天文参考系研究	2	1%						
太阳和太阳系等离子体研究	4	2%	5	3%	3	6%		
行星科学与深空探测实验室	10	5%	3	2%	6	13%	1	7%
天体化学和行星科学实验室		0%						
行星光谱学	4	2%	1	1%				
近地天体望远镜	4	2%						
总计	193	**100%**	147	**100%**	48	**100%**	14	**100%**

中国 2018 年度“十大天文科技进展”

（紫金山天文台相关部分）

1、暗物质粒子探测卫星顺利进入延寿运行阶段并获得超过 57 亿宇宙线数据

在宇宙的组成中，常规的物质仅占 5%，而暗物质占整个宇宙组成的 27%。自二十世纪三十年代暗物质被发现以来，天文学家们通过大量的天文观测不断的证明暗物质的存在，精度也在不断提高，然而这些证据均来自于引力观测，也就是观测的全部都是暗物质的引力性质。我们知道物质是由粒子组成的，而暗物质作为粒子的本质是什么，是一直困扰物理学家的一大难题。“什么是暗物质”被认为是 21 世纪最需要解答的科学问题。

当前，物理学家们主要通过三种方法进行暗物质粒子探测：对撞机、直接探测、间接探测。对撞机方法是将常规粒子（质子、电子等）加速到极高能量进行对撞机来模拟宇宙大爆炸直接将暗物质粒子产生出来进行探测。直接探测利用了暗物质粒子直接与介质原子核发射碰撞，通过探测碰撞反冲原子核产生的信号来研究暗物质粒子。而间接探测则是通过测量暗物质粒子湮灭或者衰变产生的常规次级粒子来间接反推暗物质粒子的性质。

在暗物质粒子间接探测领域，我国的科学家走在了世界前列。2015 年 12 月 17 日，我国于酒泉卫星发射基地成功发射了一颗暗物质粒子探测卫星“悟空”号。卫星由中国科学院战略性先导科技专项支持，是一个专注于暗物质粒子间接探测研究的卫星。卫星的有效载荷由四个子探测器组成，如图 1 所示，从上到下分别为塑闪阵列探测器（PSD）、硅微条径迹探测器（STK）、BGO 量能器（BGO）、中子探测器（NUD）。其中，PSD 由 84 根塑料闪烁体交替排列的阵列组成，主要用于测量粒子电荷和对伽玛射线进行反符合，其电荷分辨能力与当前国际先进水平相当。STK 由 7 万多路 242 微米宽的硅微条探测器组成，其位置分辨能力可达 30-40 微米，与人的头发丝相当，是四个探测器中最精细的一个。主要用于测量粒子径迹或方向，同时亦可测量粒子电荷。BGO 量能器是有效载荷的核心探测器，由 308 根 60cm 长的 BGO 晶体组成。它负责着能量测量、e/p 鉴别以及触发系统。其能量测量精度世界领先，其动态范围更是达到了 10^5 量级。如果将其比作显微镜的话，它既可以看清出人的每一个细胞又可以测量出人的身高。最下面的 NUD 探测器由 4 块掺硼塑料闪烁体组成，主要功能是探测粒子在 BGO 中产生的次级中子来辅助 e/p 鉴别。通过四个子探测器的联合工作，可以精确的测量粒子的能量、方向、电荷、粒子种类。如此高的探测器性能使得悟空可对宇宙线电子、伽马射线，这些暗物质粒子衰变或者湮灭的次级粒子进行高分辨率的精确测量，并可对质子等宇宙射线进行高统计量的直接探测。

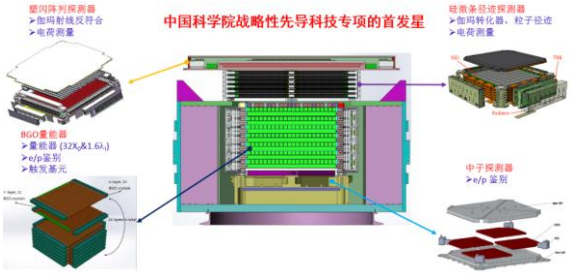

图 1 悟空号卫星有效载荷探测器结构

卫星在完成 3 个月在轨测试后，与 2016 年 3 月 17 日正式交付使用。卫星的在轨运行任务由中国科学院国家空间科学中心的地面支撑系统和中国科学院紫金山天文台的科学应用系统及卫星测控的相关单位共同完成。自 2015 年 12 月 20 日接收到第一帧科学数据至 2018 年 12 月 31 日，卫星累计接收数据 17000 余轨，完成了 6 遍全天区的扫描。卫星每天收集约 500 万例的高能宇宙线事例，迄今总数已经已逾 57 亿个(如图 2 左所示)。目前悟空号合作组共处理生成了超过 120TB 的科学数据。基于这些数据悟空号已经对电子、质子等宇宙射线的能谱进行了精确测量，一些成果已经发表，并引起了强烈的社会反响。

悟空号的设计寿命为三年。在这三年的运行中，悟空的运行非常稳定。图 2 右显示的是悟空每天的运行取数情况，从图中可以看出在在轨运行期间，除一次高压复位重启外，悟空基本上每天都可以获取超过五百万个事例，即使在 2017 年 9 月 X 级太阳大耀斑期间，卫星也从未中断运行一天。这充分反映了卫星设计建造的可靠性极高。经过三年的运行，悟空号的探测器依然处于满分状态。在轨标定的结果表明，悟空号 4 个子探测器的工作非常稳定。现在和上天时相比，所有子探测器的性能指标几乎没有明显变化，有效载荷共七万多路的电子学通道中没有增加任何新的坏道，完全具备延寿运行的条件。2019 年 1 月 4 日，中国科学院国家空间科学中心在北京组织召开了暗物质粒子探测卫星拓展观测论证评审会，评审专家听取了中国科学院紫金山天文台做的《暗物质粒子探测卫星拓展观测分析报告》和中科院微小卫星创新研究院做的《暗物质粒子探测卫星在轨运行分析报告》，经讨论认为（1）暗物质粒子探测卫星在轨运行三年，取得了丰硕的科学成果和社会效益。后续拓展实验目标明确，任务具体，计划安排合理可行；(2)暗物质粒子探测卫星具备延寿运行两年的能力；(3) 工程其他系统具备支撑延寿运行两年的能力。专家组同意通过悟空号延寿 2 年运行的评审。

至此，暗物质粒子探测卫星完成了三年的设计寿命，顺利进入到 2 年延寿运行阶段。从卫星三年的状态变化分析，在卫星完成 2 年延寿运行之后，仍有望继续延寿运行。期待卫星发布更多高质量的科学产出。

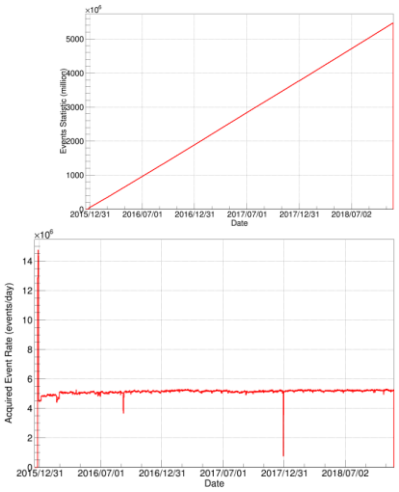

图 2 DAMPE 数据获取累计图（左），每天事例率图（右）

2、引力波事件电磁辐射对应体的研究取得系列进展

以紫金山天文台为主的一个团队近年来在引力波事件电磁对应体相关研究方面取得了一系列成果。通过分析 Hubble，VLT，Gemini，Keck 等望远镜历史数据，在“长短暴”GRB 060614，短暴 GRB 050709 中发现了巨新星（Li-Paczynski macronova/kilonova）候选体；并最早采用结构化喷流模型来解释短暴的余辉数据，提出“结构化喷流的偏轴辐射可以显著的提高短暴/引力波事件的成协率”。

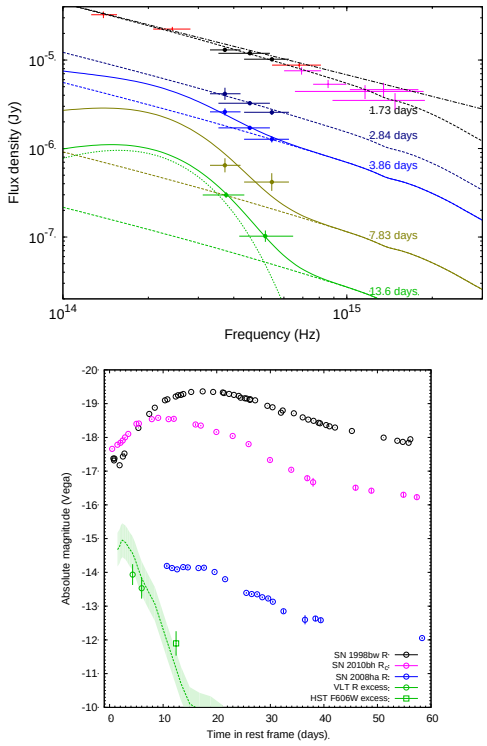

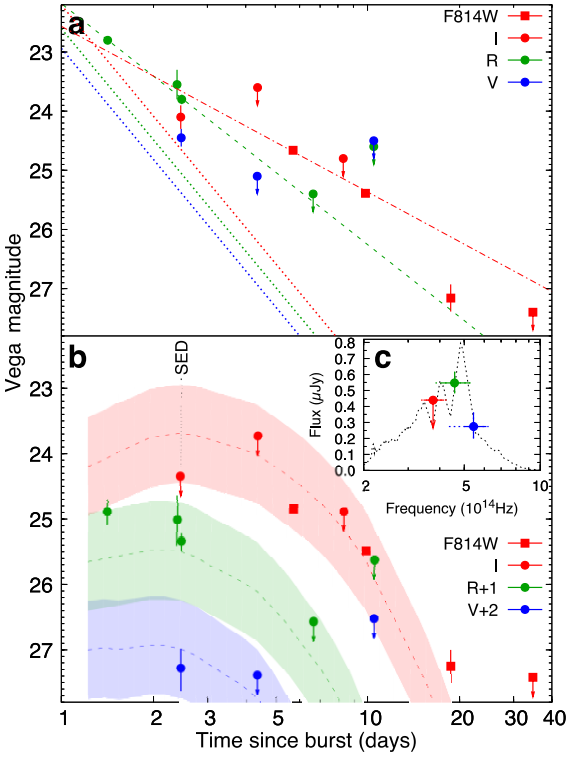

图 1：左上：GRB 060614 光学余辉的能谱演化，注意在 3.8 天之后能谱显著变陡（Jin et al. 2015），左下：GRB 060614 中巨新星光变与超新星有显著区别。右：GRB 050709 的光变曲线，I 波段和 R 波段的衰减行为迥异，意味着 I 波段存在一个新的能谱成分；并且 2.5 天处的 VLT I, R, V 波段测得的流量是线状结构，与余辉模型 不符（Jin et al. 2016）。

GRB 060614 同时具有长、短暴的部分特征，Nature 曾同时刊发 4 篇论文讨论其起源但无法达成一致，因而被称为“长短暴”。而我们系统分析光学能谱，发现早期可以很好地拟合为幂律谱，但 3.8 天之后能谱显著变陡，意味着数据中除余辉还包含着另一个能谱很软的新成分（见图 1 左），该成分与巨新星模型预言一致，晚期温度约为 2700 K (Jin et al. 2015)，显著的低于超新星，而与巨新星理论模型所预言的~2500 K (Barnes & Kasen 2013)一致，且光变曲线和晚期温度（见图 1 左）都与后来发现的 GW170817 成协的巨新星 AT2017gfo 一致。GRB 050709 是人类首次探测到光学对应体的短暴，该光学信号一直被解释为伽玛暴余辉辐射。而我们发现 VLT 在暴后 2.5 天测得的光学能谱呈“线状”，与余辉的连续能谱显著不同，而与一些巨新星模型预言一致；此外， 相邻 I 和 R 波段，其衰减行为却大相径庭， 意味着 I 波段存在一个能谱很软的成分（见图 1 右），该成分与巨新星的行为一致。我们还首次对巨新星与短暴/长短暴的关联性进行了统计分析，发现每个短暴/长短暴可能都伴随着一个巨新星，这表明巨新星普遍存在（Jin et al. 2016），是引力波事件的极具前景的电磁辐射对应体候选体。在首例中子星引力波事件 GW170817 就探测到了明亮巨新星 AT2017gfo 的事实支持了我们的推断。最近我们的研究又发现在 GRB 070809 的余辉中也存在巨新星信号。

几乎在 GW170817 发现的同时，Jin et al. (2018 ApJ; arXiv:1708.07008)分析了 GRB 150424A 以及 GRB 160821B 的数据，没有发现明确的巨新星信号，但发现了明显的喷流拐折，统计得到短暴的典型半张角约为 0.1 弧度，进而得到近邻宇宙的中子星并合率约为~1000 Gpc^{-3} yr^{-1}。我们还指出，由于 aLIGO/Virgo 等第二代引力波探测器对中子星并合事件的有效观测距离较近，因此在结构化喷流模型下（见图 2）偏轴的伽玛暴尽管较弱，但依然有望被探测到，这会显著提高短暴和引力波事件的成协率；但在均匀

喷流模型下，由于强的相对论集束效应，偏轴事例无法可靠提高短暴和引力波事件的成协率。因此结构化喷流模型有助于理解在首例中子星并合引力波事件 GW170817 中就看到了短暴 GRB 170817A 这个让人“意外”的事实。值得指出的是：紫金山天文台的研究组还最早用结构化喷流模型来解释短暴的余辉数据（Jin et al. 2007 ApJL），目前这类模型已被广泛的用于对 GRB 170817A 余辉数据的解读。我们得到的中子星并合率也与引力波探测给出的中子星并合率一致。

该工作主要得到国家自然科学基金杰青、重点、面上及中科院前沿科学重点研究计划、国际合作重点项目和 B 类先导专项等项目的资助。

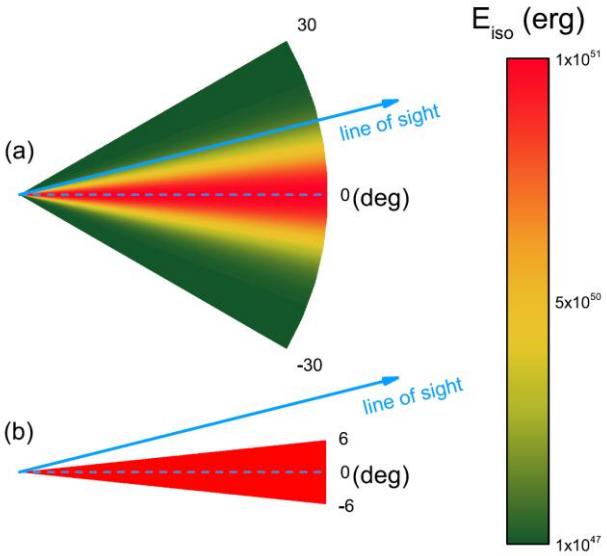

图 2：偏轴情形下的 sGRB 探测前景；(a)为结构化喷流模型，(b)为均匀喷流模型。